DISSERTATION

Carrier dynamics and gain in 1.3μm InGaAsN/GaAsP/GaAs laser diodes

Submitted by

Ovidio Antón

Electrical and Computer Engineering Department

In partial fulfillment of the requirements

for the degree of Doctor of Philosophy

Colorado State University

Fort Collins, Colorado

Summer 2006

Reproduced with permission of the copyright owner. Further reproduction prohibited without permission.

UMI Number: 3233319

INFORMATION TO USERS

The quality of this reproduction is dependent upon the quality of the copy submitted. Broken or indistinct print, colored or poor quality illustrations and photographs, print bleed-through, substandard margins, and improper alignment can adversely affect reproduction.

In the unlikely event that the author did not send a complete manuscript and there are missing pages, these will be noted. Also, if unauthorized copyright material had to be removed, a note will indicate the deletion.

UMI®

UMI Microform 3233319

Copyright 2006 by ProQuest Information and Learning Company. All rights reserved. This microform edition is protected against unauthorized copying under Title 17, United States Code.

ProQuest Information and Learning Company
300 North Zeeb Road
P.O. Box 1346
Ann Arbor, MI 48106-1346

Reproduced with permission of the copyright owner. Further reproduction prohibited without permission.

COLORADO STATE UNIVERSITY

May 17th, 2006

WE HEREBY RECOMMEND THAT THE DISSERTATION PREPARED UNDER OUR SUPERVISION BY OVIDIO H. ANTÓN ENTITLED CARRIER DYNAMICS AND GAIN IN 1.3μm INGAASN/GAASP/GAAS LASER DIODES ACCEPTED AS FULFILLING IN PART REQUIREMENTS FOR THE DEGREE OF DOCTOR OF PHILOSOPHY.

Committee on Graduate Work

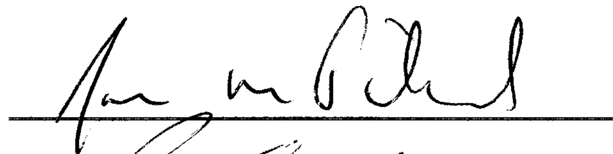

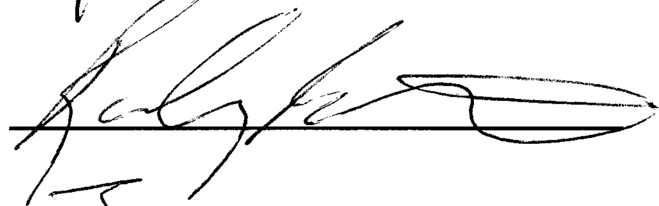

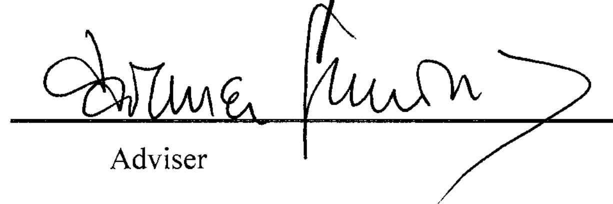

Adviser

Department Head

Reproduced with permission of the copyright owner. Further reproduction prohibited without permission.

ABSTRACT OF DISSERTATION

Carrier dynamics and gain in 1.3μm InGaAsN/GaAsP/GaAs laser diodes

This dissertation investigates the impact of nitrogen incorporation on the intrinsic processes that affects the threshold current and frequency response of 1.3μm InGaAsN/GaAsP/GaAs single quantum well (SQW) lasers. This study is accomplished through the analysis of the below threshold carrier lifetime and material gain and the frequency response above threshold in two identical laser structures that only differ in the incorporation of nitrogen. The above and below threshold frequency responses results are analyzed with a complete rate equation model of the laser diode that contains intrinsic material processes as well as external parasitics associated with the diode device.

The below threshold analysis coupled with the gain results provide the framework to understand the behavior of the threshold current in the 10-80°C temperature range in the nitrogen-containing structures in relation to that of the nitrogen free counterparts. This study was instrumental to find a three times increase in the monomolecular recombination and C_w parameter, and a ~30% decrease in the effective threshold differential gain in dilute nitride materials due to nitrogen incorporation. It was found that their combined effects could account for the majority of the increase in the threshold current and the decrease in the effective temperature T_o in dilute nitride lasers.

The study above threshold was motivated by the need to understand the potential of the dilute nitride laser for direct high speed modulation. In these studies the frequency response of the laser diode is obtained using selective femtosecond optical injection. As an innovation to the setup, we implemented this technique with pulse bias in order to

Reproduced with permission of the copyright owner. Further reproduction prohibited without permission.

prevent device damage and to reach 80°C in the active area. We show that single quantum well InGaAsN lasers reach –3dB bandwidths of 8.5GHz at 10°C, and their bandwidth reduces by 40% at 80°C. We analyze the modulation responses to extract the resonance frequency and damping. We utilize the rate equation model that incorporates carrier transport and electrical parasitics to show for the first time that the damping is affected by parasitics even under optical modulation. Further, the model permits to study the threshold effective differential gain of the devices. Within the uncertainties of the analysis, it is found that the effective differential gain shows a decrease with nitrogen incorporation similar to that observed from the analysis below threshold and furthermore, an identical temperature behavior. The results of this work are exploited to provide guidelines into the design of optimized laser structures with temperature insensitive threshold currents and bandwidths exceeding 10GHz, outperforming the existing 1.3μm InP-based technology.

Ovidio H. Antón
Department of Electrical and Computer Engineering
Colorado State University
Fort Collins, CO 80523
Summer 2006

Reproduced with permission of the copyright owner. Further reproduction prohibited without permission.

ACKNOWLEDGMENTS

I would like to thank my advisor, professor Carmen Menoni for her support and involvement over the years of my dissertation work. I also acknowledge her trust and encouragement during my stay in the labs.

I also acknowledge the constructive comments of professors J. Sites, J.M. Pikal, R. Bartels and A.A. Maciejewsky who served in my committee.

This dissertation and publications associated with it involve the collective effort of a number of people. It is appreciated the help of our collaborators Dr. Jeng-Ya Yeh and professor Luke Mawst, from University of Wisconsin-Madison, and professor Nelson Tansu from Lehigh University, for the fabrication of the test lasers. I would like to thank professor J. M. Pikal of University of Wyoming for helpful discussions about his dissertation and technical publications.

Among the people in our lab I should recognize the continuous support of Dr. Dinesh Patel, who not only helped me in the sample preparation but who also thought me how to look things from different perspective. I thank Li Fang Xu for collaborating with her data and participation with the calculation of the material electronic structure. Discussions with Dr. Georgiy Vaschenko are greatly appreciated.

I would like to thank professor Mario Marconi who unconditionally shared his time and vast experience in optical phenomena to ensure the success of our femtosecond experiments.

Lastly, I would like to acknowledge the support of Agilent Technologies through Agilent Fellowship who partially supported this work.

Reproduced with permission of the copyright owner. Further reproduction prohibited without permission.

I want to thank my friends Jorgito, Federico, Gabriela, Richi, Dolores, Fernando, Luciana, Jorge and Manuel for their support. I also appreciate the support of M. Julia Tavelli during last years.

My wife Laura and my children Marcos and Rocío have been the constant source of support throughout these many years. Without their constant encouragement I would not have made it to this point. I whish to acknowledge my parents, in laws, brothers and Ester and Nestor for their always extraordinary support. Thanks.

Reproduced with permission of the copyright owner. Further reproduction prohibited without permission.

To Laura, Marcos and Rocío for their never ending support

Reproduced with permission of the copyright owner. Further reproduction prohibited without permission.

Table of contents

Chapter **Page**

1. Basics in the understanding of quantum well 1.3μm laser diodes..............1

1. Introduction.......... 2

1.1. InGaAsN compounds for quantum well mid-infrared lasers..........4

1.2. The physics of laser diodes 6

1.2.1. Behavior below threshold..........6

1.2.1.1. The threshold condition 12

1.2.2. The high speed behavior of laser diodes above threshold..........17

1.3. Motivation: State of the art in the research of InGaAsN lasers 24

1.4. Objective and scope of this dissertation 27

References for Chapter 1..........30

2. Laser frequency response..........37

2.1. Introduction: Model of the laser carrier-gain dynamics..........38

2.1.1. Rate equations and device electrical parasitics 39

2.1.2. Small signal model 45

2.1.3. Q-χ coupling 49

2.1.4. Frequency domain 51

2.2. Subthreshold frequency response..........51

2.3. Small signal diode impedance..........57

2.4. Analysis above threshold.......... 62

Reproduced with permission of the copyright owner. Further reproduction prohibited without permission.

2.4.1. Optical modulation response..65

2.5. Temperature analysis...72

2.5.1. Temperature analysis below threshold.......................................73

2.5.1.1. Device current versus temperature.....................................73

2.5.1.2. Effective differential carrier lifetime analysis.......................83

2.5.2. Frequency response versus temperature above threshold..................86

2.6. Summary and conclusions on the model simulations 93

References for Chapter 2..96

3. Experimental details...101

3.1. Description of the laser samples...102

3.2. Experimental conditions...106

3.2.1. Active area temperature..106

3.3. Experiments below threshold..109

3.3.1. Subthreshold impedance measurements.....................................109

3.3.2. Subthreshold frequency response...114

3.3.3. Amplified spontaneous emission..118

3.4. Experiments above threshold 122

3.4.1. Optical frequency response 122

3.4.2. Electrical frequency response 129

References for Chapter 3...133

4. Analysis below threshold 135

4.1. Introduction...136

4.2. Analysis of differential carrier lifetime in InGaAsN QW lasers..............137

Reproduced with permission of the copyright owner. Further reproduction prohibited without permission.

4.2.1. Study of electrical parasitics in wide-stripe InGaAsN lasers..........137

4.2.2. Frequency response analysis..........142

4.3. Effective differential carrier lifetime analysis..........146

4.3.1. Effective carrier density in the quantum well..........147

4.4. Gain analysis 151

4.4.1. Gain spectra: bias and temperature behavior 152

4.4.2. Material gain analysis..........155

4.4.3. Effective differential gain and transparency carrier density 159

4.4.4. Below and above threshold differential gain comparison..........165

4.5. Analysis of the threshold current and T_0 166

4.6. Chapter summary 170

References for Chapter 4..........172

5. Above threshold behavior of InGaAs(N) lasers..........175

5.1. Introduction..........176

5.2. Results of optical modulation frequency response..........178

5.3. Analysis of the device parameters 182

5.4. Study of the device and material carrier dynamics..........187

5.5. Mechanism causing the bandwidth reduction in InGaAsN..........191

5.6. Chapter summary 195

References for Chapter 5..........197

6. Conclusions..........200

Appendix 1..........206

Appendix 2..........208

Reproduced with permission of the copyright owner. Further reproduction prohibited without permission.

Appendix 3……………………………………………………………………………210

Appendix 4……………………………………………………………………………211

Appendix 5……………………………………………………………………………212

Appendix 6……………………………………………………………………………213

Appendix 7……………………………………………………………………………216

Reproduced with permission of the copyright owner. Further reproduction prohibited without permission.

Chapter 1

Basics in the understanding of quantum well 1.3 μm laser diodes

This chapter describes the physics of gain and carrier dynamics that define temperature and speed performance of mid-infrared quantum well telecom lasers. This is accomplished by studying the laser active area with the typical carrier-photon reservoir model. By solving the corresponding rate equations for this model, the characteristic temperature T_0 and the laser frequency bandwidth are calculated as a function of the physical laser parameters.

Reproduced with permission of the copyright owner. Further reproduction prohibited without permission.

1. Introduction

1.3μm laser diodes are the subject of constant research and development as they are key components of optical fiber communication links, such as metropolitan area networks (MAN). The performance metric that is expected from a laser diode-based transmitter for communications comprises: high speed and high temperature operation. Distributed feedback (DFB) AlInGaAs/InP quantum well lasers are used nowadays for this type of applications [1], but the high cost and availability of the packaged devices are the factor that limit their scope of use. Vertical integration is another attractive alternative that makes possible optical interconnects. Unfortunately InP-based technology cannot produce efficient distributed Bragg reflectors (DBR) for vertical cavity surface emitting lasers (VCSELs) and wafer bonding to GaAs has to be used, dramatically increasing the cost [2].

The optimum solution for a 1.3μm transmitter is to implement it with a single diode laser that can be directly grown on substrate technology that permits reliable and cheap vertical integration and supports high speed electronics. Gallium arsenide, GaAs, is the only material that is suitable for this purpose. Volume production of 1.3μm GaAs-based laser diodes would produce a dramatic impact in telecomm by enabling the full deployment of more than 10's Gb/s fiber optic links down to the final user and lowering the cost for optical interconnects [3].

Devices that nearly meet speed and temperature specifications are made of InGaAs quantum well (QW) structures. Bandwidths of 30-40GHz have been demonstrated in InGaAs QW lasers [4-7]. In addition, temperature insensitive InGaAs QW lasers have been demonstrated [5, 8]. This technology has enabled VCSEL fabrication and

Reproduced with permission of the copyright owner. Further reproduction prohibited without permission.

integration with GaAs high speed mature technology [3, 9]. In spite of these desirable features, the emission wavelength of InGaAs/GaAs-QW lasers is restricted to reach as long as λ=1200nm. This ultimate wavelength is obtained by adding 35 % Indium to the GaAs, which produces a maximum compressive strain in a typical 60-80Å dislocation-free film grown on GaAs [10, 11]. The attractive performance characteristics of InGaAs motivated researchers to look for non-conventional ways to increase the emission wavelength to 1.3μm.

Suggested in 1992 to red-shift the emission of GaAs [12], the dilution of nitrogen in InGaAs made possible to realize emission in InGaAs quantum well beyond 1200nm and produce the first InGaAsN laser (referred to as 'dilute nitride') by Kondow in 1996 [13, 14]. Since its invention there has been a great deal of research on the understanding of the physics of dilute nitride materials [15-20] and their improvements as devices [21-28].

Other avenues have also been explored to realize emission wavelengths on InGaAs in the 1.3-1.5μm range. For example, the dilution of antimony produced a red-shift in the GaAs emission when used in combination with diluted nitrides for $\lambda \rightarrow 1.5\mu m$ [29]. Emission in the 1.3μm region can also be achieved through the growth of InAs clusters on InGaAs or GaAs [30]. This growth process has given rise to the development of zero dimensional confinement quantum dots (QD) laser structures. Laser devices have already been fabricated out of this material [31-34]. In spite of much effort devoted to realize GaAs-based laser materials, their devices have not yet reached the performance characteristics of the InGaAs QW lasers.

Reproduced with permission of the copyright owner. Further reproduction prohibited without permission.

1.1. InGaAsN compounds for quantum well mid-infrared lasers

The methodology to select the emission wavelength in III-V semiconductors consists of choosing binary or ternary materials which when mixed provide the desired bandgap wavelength and lattice constant to facilitate growth of epilayers on a suitable substrate. This is accomplished by using the III-V compounds roadmap of Figure 1.1 in which different III-V compounds are evaluated in terms of their bandgap energy versus their lattice constant. The most common substrates utilized in high speed lasers and electronics are gallium arsenide (GaAs) and indium phosphide (InP). However, GaAs is the most mature and cheaper technology for optoelectonics applications. For example, GaAs technology enables the development of inexpensive, fast and reliable 850nm VCSEL based optical interconnects [3].

The open circle in Figure 1.1 demarks the maximum possible wavelength reached by InGaAs grown on GaAs under maximum compressively strain. For comparison, the dotted circle identifies the InP-based material for λ=1.3μm lasers. The filled circle indicates InGaAsN grown on GaAs substrates.

Contrary to what was expected, alloying of gallium nitride, GaN, with a bandgap of ~3.4eV and GaAs produced a red instead of a blue-shift in the photoluminescence (PL) [12]. The same effect was observed in InGaAsN compounds. This phenomenon has been explained by a repulsion of the InGaAs conduction band states with a resonant nitrogen level that induces a reduction of about 100meV per percent of nitrogen incorporation, when below 3% [15]. This repulsion produces in turn a significant increase in the electron effective mass, m_e^* [35, 36].

Reproduced with permission of the copyright owner. Further reproduction prohibited without permission.

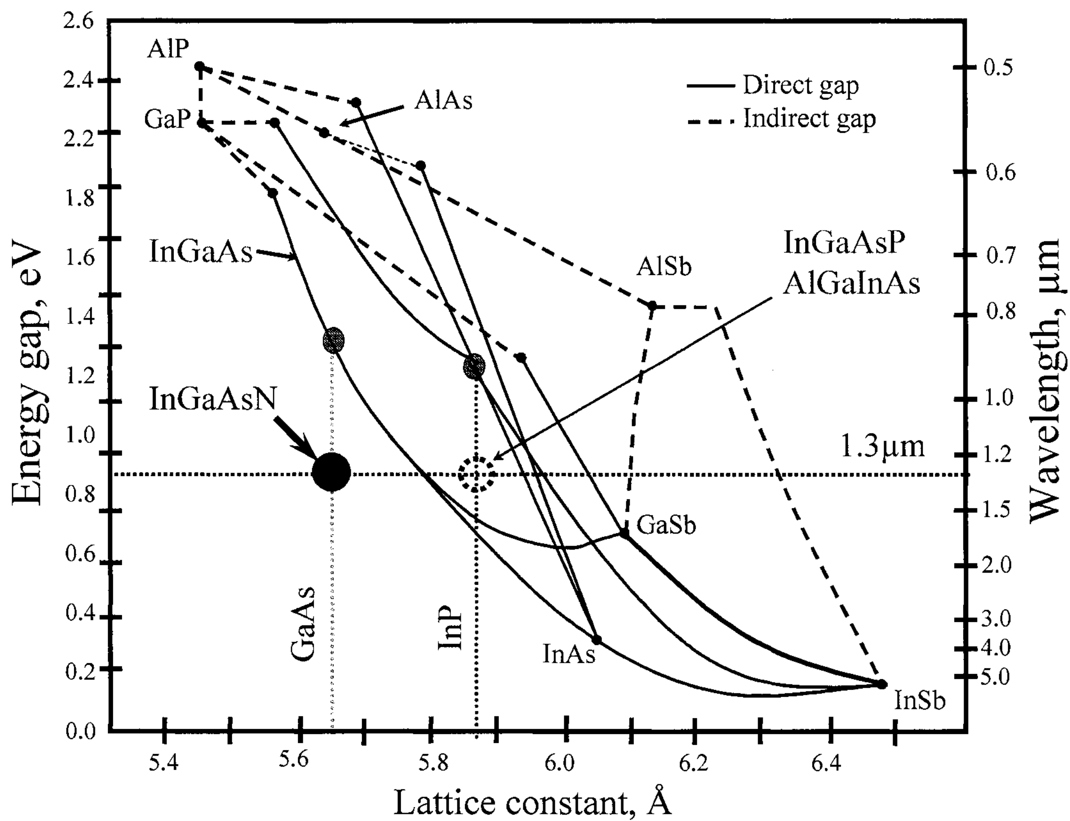

Figure 1.1.- III-V semiconductor compound roadmap.

Besides the electronic changes, the addition of nitrogen reduces the lattice constant in InGaAsN material, thereby compensating the effect of Indium and thus relaxing the compressive strain characteristic of the InGaAs alloy. However, there is no complete freedom in the addition of nitrogen to a III-V compound. The strategy to get the best InGaAs material resides in using the highest amount of In and least (~1%) nitrogen. this differs from early work were the nitrogen content was 2-3% [13, 23, 37, 38]. This approach maximizes elastic strain, thus quantum well lasers made out of these materials contain generally one quantum well or at most three if suitable strain compensating layers are used.

Reproduced with permission of the copyright owner. Further reproduction prohibited without permission.

1.2. The physics of laser diodes

This section provides the formalism to understand the static and dynamic behavior of laser diodes. Furthermore, it provides the framework to the models that were developed in this dissertation and that are used to analyze the results of the carrier lifetime, gain and above threshold behavior of the 1.3 μm InGaAsN laser diodes

1.2.1. Behavior below threshold

The behavior of an ideal quantum well laser diode below threshold is customarily explained using a reservoir model schematically shown for a single quantum well (SQW) heterostructure in Figure 1.2. The optical mode is laterally contained by the separate confinement heterostructure (SCH) region and longitudinally by the two-mirror Fabry-Perot cavity. Optical gain, G, is produced in the cavity by the stimulated processes taking place in the SQW as depicted in the figure. The confined optical mode experiences optical mirror and waveguide losses, α_m and α_i, and optical modal gain G [39],

$$G = \Gamma \cdot g$$

Based on Figure 1.2, the laser diode can be envisioned as a reservoir where carriers are injected and converted through the process of spontaneous and stimulated recombination into photons, thereby filling up a photon reservoir. In this model the carrier and photon densities as well as the current density injected into the laser are represented by fluxes into and out of the carrier and photon reservoirs [40, 41].

Reproduced with permission of the copyright owner. Further reproduction prohibited without permission.

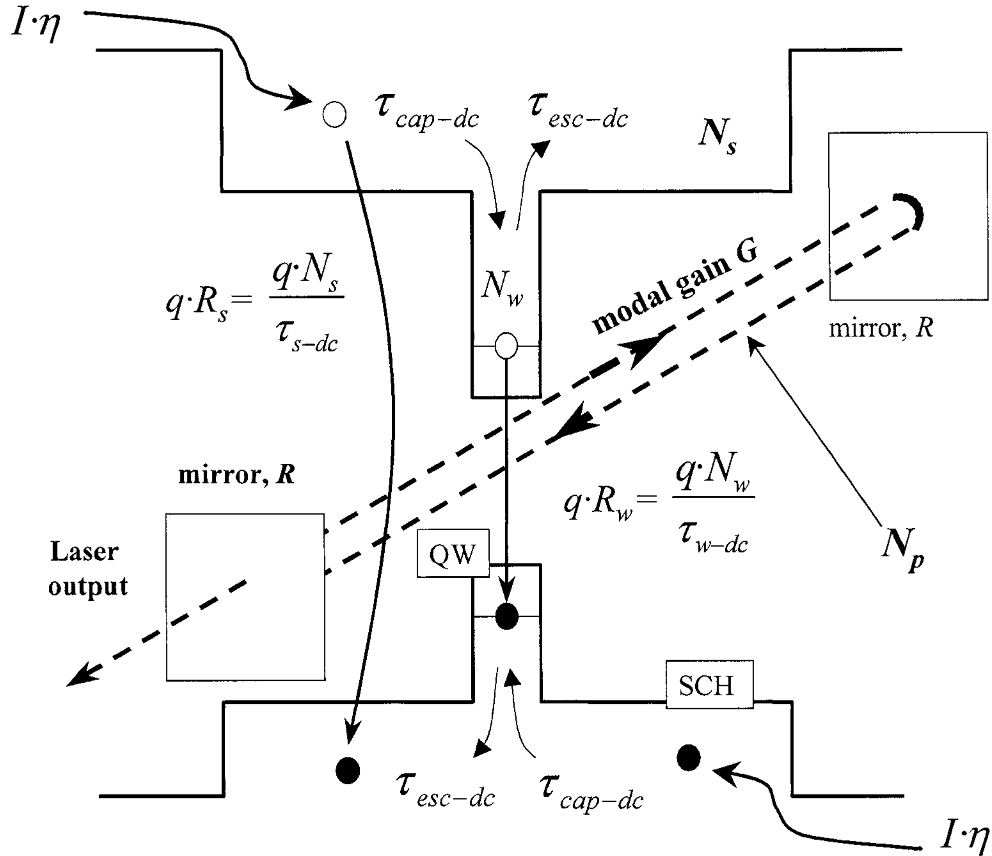

Figure 1.2.- Reservoir model of a single quantum well heterostructure laser. The injection efficiency, the carrier capture, escape and recombination mechanisms define the threshold current.

In Figure 1.2, three reservoirs are defined: the carrier density reservoir in the bulk separate confinement heterostructure (SCH) N_s, that in the quantum well (QW) N_w and the photon density in the optical mode N_p. In this ideal laser the interaction between carriers and photons is expressed by the rate equations given in (1.1).

$$\begin{aligned}
\frac{dN_s}{dt} &= \frac{\eta}{qV}I - \frac{N_s}{\tau_{cap-dc}} - \frac{N_s}{\tau_{s-dc}} + \frac{N_w}{\tau_{esc}}\Gamma_q \\
\frac{dN_w}{dt} &= \frac{N_s}{\tau_{cap}\Gamma_q} - \frac{N_w}{\tau_{qw-dc}} - \frac{N_w}{\tau_{esc-dc}} - v_g g N_p \\
\frac{dN_p}{dt} &= \frac{\Gamma\beta}{\tau_{qw-dc}}N_w - \frac{N_p}{\tau_p} + \Gamma v_g g N_p
\end{aligned} \tag{1.1}$$

Reproduced with permission of the copyright owner. Further reproduction prohibited without permission.

In relation to Figure 1.2, $q \cdot R_w$ and $q \cdot R_s$ are the recombination currents per unit volume in the SCH and QW, which are expressed in equations (1.1) in terms of the carrier lifetimes $\tau_{w\text{-}dc}$ and $\tau_{s\text{-}dc}$, as $N_w/\tau_{w\text{-}dc}$ and $N_s/\tau_{s\text{-}dc}$, respectively. The carrier capture/escape processes that connect the QW and SCH reservoirs are depicted by their time constants $\tau_{cap\text{-}dc}$ and $\tau_{esc\text{-}dc}$, respectively. The *-dc* subscript denotes large-signal parameters. The stimulated process couples N_p and N_w through the material peak gain g, as shown in (1.10) second and third rows. τ_p is the photon lifetime. V, q, Γ and Γ_q are the active area volume, electron charge, optical mode confinement factor and the ratio of QW and SCH volumes respectively.

As shown in Figure 1.2, the bias current I is injected into the active area with a current injection efficiency η. η accounts for the current leakage in the heterobarrier and in the laser structure external to the active area, and thus expresses the ratio of the laser active region current I_s+I_w to the total device current I [42]. These currents are given by $q(1-\Gamma_q)\text{V}\cdot R_s$ and $q\Gamma_q\text{V}\cdot R_w$, where $(1-\Gamma_q)\text{V}$ and $\Gamma_q\text{V}$ are the volumes in the SCH and QW, respectively. I_s can contribute to a significant part of I_{th} in 1.3μm lasers [43], and we considered it in detail in Chapter 2. For the following conceptual analysis, though, we assume $I_s=R_s=0$.

R_w is customarily expressed in terms of the QW carrier lifetime $\tau_{w\text{-}dc}$ [44] as:

$$R_w(N_w) = \frac{N_w}{\tau_{w-dc}} = AN_w + BN_w^2 + CN_w^3 \tag{1.2}$$

The recombination parameters A_w, B_w and C_w in an ideal QW laser are associated with monomolecular, bimolecular and Auger recombination as done in bulk laser diode materials [44]. R_s is expressed in similar fashion, though we leave its analysis for Chapter

Reproduced with permission of the copyright owner. Further reproduction prohibited without permission.

2. $\tau_{w\text{-}dc}$ is habitually measured by photoluminescence measurements in laser materials at different optical injection intensities [39, 45]. In laser diodes, however, it is customarily to measure the turn-on time and the small signal frequency response. The latter, as the main tool in this thesis, permits to very accurately determine the laser time constants and recombination parameters at different laser biases [46]. Frequency response measurements allow to obtain the differential carrier lifetime τ_w, which plays a fundamental role in relating N_w to R_w and to the bias current, as explained below. τ_w is defined as follows,

$$\frac{1}{\tau_w} = \frac{dR_w}{dN_w} = A_w + 2B_w N_w + 3C_w N_w^2 \tag{1.3}$$

The study of τ_w can be performed from the model shown in equation (1.1) by introducing a small signal perturbation i to the current I. Following, the small signal representation of equations (1.1) is achieved through a first-order Taylor series expansion, described in detail in Chapter 2. The small signal variables n_s, n_w and n_p are perturbations to N_s, N_w and N_p and arise as a result of the current modulation $i(t)$. Equations (1.4) through (1.6) describe the small signal model in terms of the small signal parameters.

$$\dot{n}_s = \frac{\eta}{qV_s} i - \frac{n_s}{\tau_{cap}} - \frac{n_s}{\tau_s} + \Gamma_q \frac{n_w}{\tau_{esc}} \tag{1.4}$$

$$\dot{n}_w = \frac{n_s}{\Gamma_q \tau_{cap}} - \frac{n_w}{\tau_w} - \frac{n_w}{\tau_{esc}} - \frac{n_p}{\Gamma \cdot \tau_p} \tag{1.5}$$

$$\dot{n}_p = \beta \frac{n_w}{\tau_w} - \frac{n_p}{\tau_p} \tag{1.6}$$

Reproduced with permission of the copyright owner. Further reproduction prohibited without permission.

The small signal lifetimes are indicated as τ_w, τ_s, τ_{cap} and τ_{esc}, whose relationship with their respective *–dc* subscript parameters will be provided in Chapter 2. The differential carrier lifetime τ_w is the variable that permits to obtain the $N_w - I$ relationship from the experimental small signal frequency response. Therefore, the knowledge of τ_w allows the study of dominant carrier recombination processes intrinsic to the well (1.4-1.6) [46].

The small signal frequency response shown in (1.7) is obtained from the Fourier transform of (1.4) through (1.6). Its poles, $1/\tau$, $1/\tau_1$ and $1/\tau_p$ are given by the eigenvalues of the small signal model. The pole $1/\tau$ is directly related to $1/\tau_w$ through the ratio $R_{ac}=\tau_{cap}/\tau_{esc}$. In a typical quantum well laser diode, τ is one to two order of magnitude larger than τ_1 and τ_p thus yielding a frequency response $H_{sp}(f)$ with a single dominant pole $1/\tau$. As an example, when setting $R_{ac}=0$, the model solution retrieves τ_1 and τ_p that are much smaller than τ, and at the same time $\tau = \tau_w$. Therefore, the fit of the experimental frequency response traces permits to obtain τ that retrieves τ_w.

$$H_{sp}(f) = \frac{H_0}{(1+j2\pi f\tau)(1+j2\pi f\tau_1)(1+j2\pi f\tau_p)} \tag{1.7}$$

The model simulations for τ in (1.7) are performed assuming A_w, B_w and C_w in 1.3μm laser parameters given in Table 1.1 for T=10°C.

In a similar fashion, and by assuming $I_s=R_s=0$, we obtain the device current I as:

$$I \approx \frac{qV\Gamma_q}{\eta}\left(A_w N_w + B_w N_w^2 + C_w N_w^3\right) \tag{1.8}$$

Reproduced with permission of the copyright owner. Further reproduction prohibited without permission.

The results of the simulation at T=10°C retrieve the time constant τ versus device current I at room temperature are shown in Figure 1.3. Therefore, a good approximation for the laser's 3dB bandwidth is given by $1/2\pi\tau$. Notice how τ decreases with bias, which indicates larger recombination rates at higher carrier densities. On the other hand and ruled by the monomolecular recombination, τ reaches a top value in the limit $I \rightarrow 0$, which corresponds to $1/A_w$ as shown in Figure 1.3.

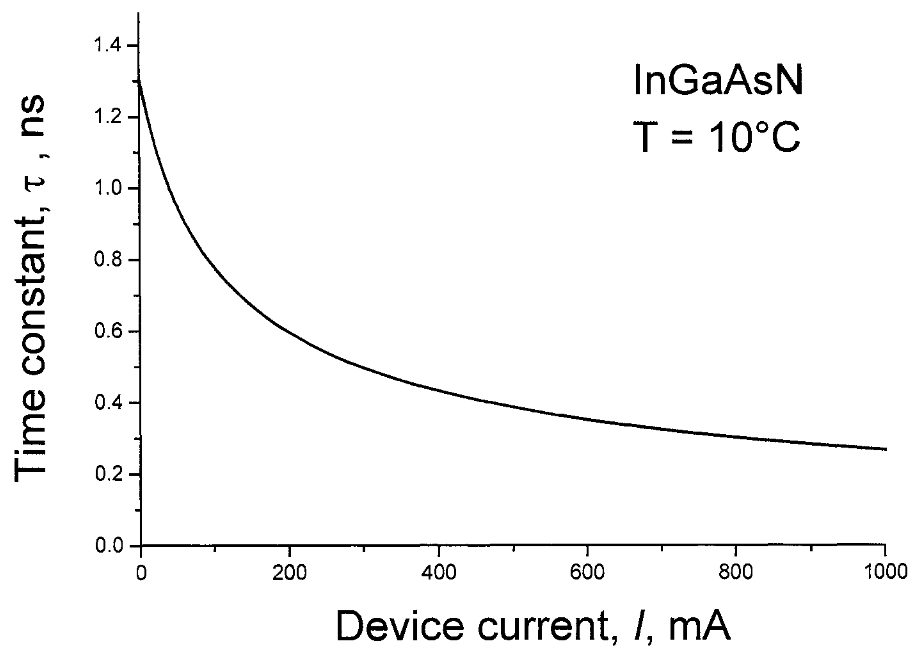

Figure 1.3.- Calculated time constant τ versus device current I at room temperature. The laser 3dB bandwidth at each bias current is given by $f_{3dB} \sim 1/2\pi\tau(I)$.

By introducing the parameter changes with temperature, we were able to repeat the previous calculations but as a function of the temperature, as described next.

Reproduced with permission of the copyright owner. Further reproduction prohibited without permission.

1.2.1.1. The threshold condition

The threshold condition occurs when the optical gain produced by the stimulated recombination of the carriers in the SQW [47] equals the total losses as shown in expression (1.9).

$$G_{th} = \alpha_i + \alpha_m = \alpha_i + \frac{1}{L}\ln\left(\frac{1}{R}\right) \tag{1.9}$$

In this expression G_{th} is the modal peak gain at threshold, L and R are the laser length and mirror reflectivity, respectively. G_{th} is extracted from (1.9) and is related to N_{th} by the following analysis.

The modal gain, $G(N_w,\lambda)$, is related to material's gain $g(N_w,\lambda)$ by (1.10) through the optical confinement factor Γ, given by the overlap of the QW dimension to the transverse optical field distribution [39].

$$G(\lambda, N_w) = \Gamma \cdot g(\lambda, N_w) \tag{1.10}$$

In the modeling of laser diodes, equation (1.10) is represented in terms of peak values, symbolized here by capital letters. It is customarily to represent, and most experiments confirm this in quantum well lasers, the modal peak gain in terms of a logarithmic dependence with N_w. The functional dependence of the peak modal gain G on N_w is generally expressed as in (1.11) in which N_{tr} and G_0 are the transparency carrier density and the gain parameter respectively [39, 47]. Observe that in (1.11) $G(N_{tr})=0$.

Reproduced with permission of the copyright owner. Further reproduction prohibited without permission.

$$G(N_w) = G_0 \cdot \ln\left(\frac{N_w}{N_{tr}}\right) \quad (1.11)$$

Figure 1.4 shows how I, N_w and G are related at three different temperatures. From this relationship and assuming that the total losses do not change with temperature, the threshold current is obtained at different temperatures. For simplicity we assumed R_s=0 and η=0.77. Nevertheless, Chapter 2 assumes all the exact values of η and R_s, the latter temperature and carrier density dependent [48].

The quantum well recombination parameters are shown on Table 1.1. The parameter A_w is adopted from our experimental work in identical laser structures [49], whereas B_w is obtained from the theoretical calculations performed by Tomic et al. in InGaAsN QW lasers [50]. Both A_w and B_w were assumed temperature invariant, which is accurate assumption, as observed in 1.3μm lasers by Pikal from 10-60°C [51]. The C_w parameter was adopted from InGaAs multiple quantum well lasers at room temperature [39], which followed an exponential dependence with a characteristic temperature T_c ~ 40K, in similar fashion to experimental findings in 1.3μm QW lasers [51]. Observe the dramatic increase on C_w in ~6 times from T=10 to 80°C, which will impact on the threshold current and T_0. The rest of the laser diode parameters are shown on Table 1.2.

The threshold current analysis assumes that the total losses are temperature insensitive, hence imposing a threshold gain G_{th} that is common for the three traces in Figure 1.4 at T=10, 40 and 80°C. The temperature changes in the gain are reflected by a reduction in G_0 and an increase in N_{tr} in Table 1.1 which were calculated by Tomic and O'Reilly in 1.3μm InGaAsN QW lasers [52]. In this case, equation (1.11) yields N_{th} that increases from ~$2.2 \cdot 10^{18}$ cm^{-3} (10°C) to $3.2 \cdot 10^{18}$ cm^{-3} (80°C), as shown in Figure 1.3 (a),

Reproduced with permission of the copyright owner. Further reproduction prohibited without permission.

which impact on I_{th} in a fashion shown in Fig. 1.3 (b). The N_w - I relationship was obtained from (1.8).

T	A_w $10^8 s^{-1}$	B_w $10^{-10} cm^{-3} s^{-1}$	C_w $10^{-30} cm^{-6} s^{-1}$	G_0 cm^{-1}	N_{tr} $10^{18} cm^{-3}$
10°C	7.7	1.2	3.88	61.1	1.42
40°C	7.7	1.2	8.21	64.1	1.66
80°C	7.7	1.2	22.3	62.8	1.99

Table 1.1. – Simulation parameters used in the differential carrier simulations. Parameters are adopted in 1.3μm lasers from refs. [39, 50, 51, 53].

Notice that the simulated traces in Figure 1.4 indicate that I_{th} increase in a supra-linear fashion with temperature. After simulations performed in the continuous temperature range we found a near exponential behavior of I - N_w that is typical of laser diodes [54]. Figure 1.5 shows the calculated I_{th} versus T obtained from the simulation of the results from Figure 1.4.

This behavior is commonly described by the empirical expression in (1.12), where T_0 is the characteristic temperature of the laser diode.

$$I_{th} = I_o \cdot e^{T/To} \tag{1.12}$$

The traces in Figure 1.5 are fitted with the exponential empirical formula given in (1.12) [55] from which the characteristic temperature T_0 is obtained as the inverse of the $ln(I_{th}) / T$ slope. We obtain T_0~100K which is mid-high value in of 1.3μm QW lasers [51].

Reproduced with permission of the copyright owner. Further reproduction prohibited without permission.

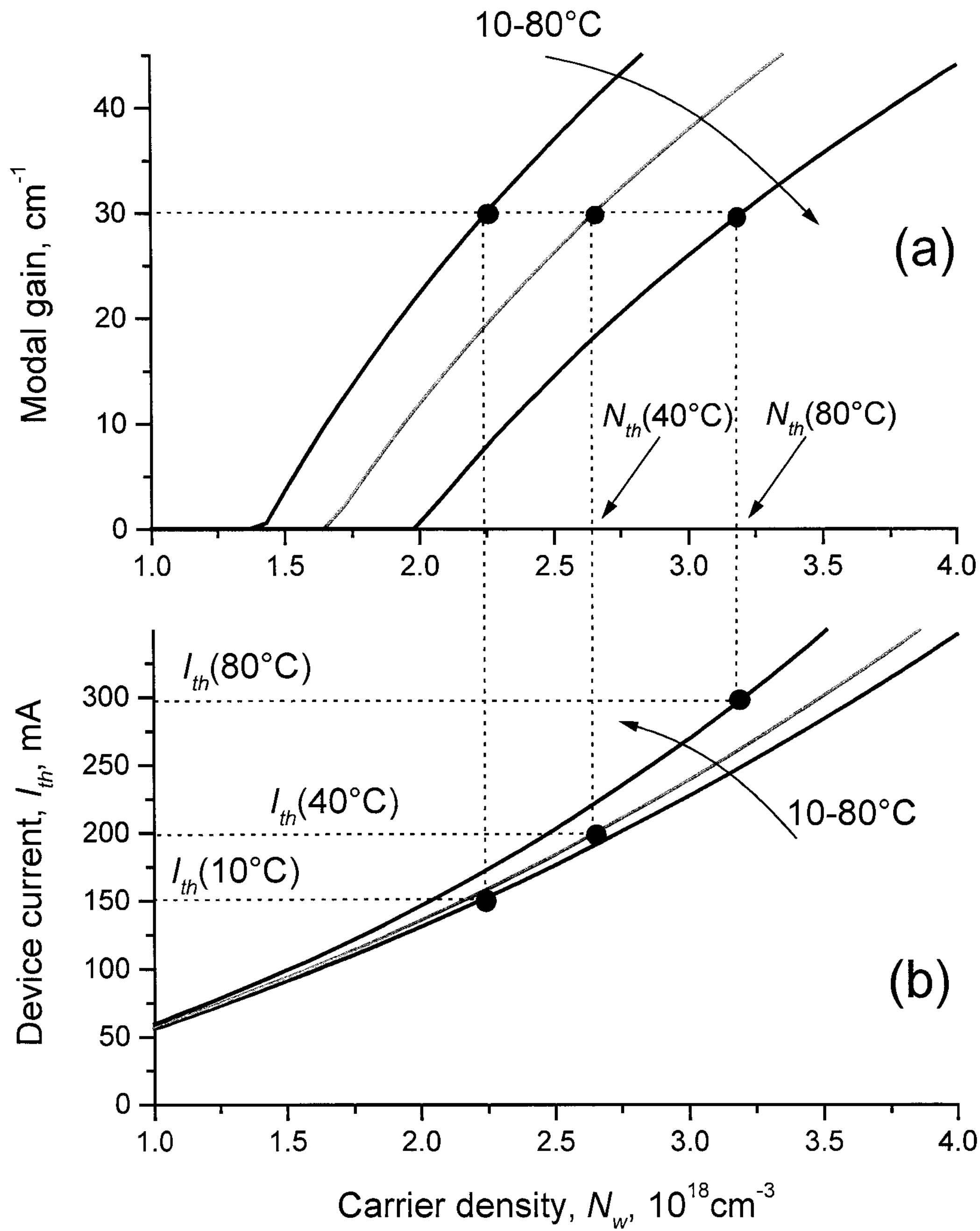

Figure 1.4.- Typical temperature dependent I - N_w and N_w -G relationships. Notice how the threshold current increases by the combined changes in the gain and material's recombination parameters in (a) and (b) respectively.

Reproduced with permission of the copyright owner. Further reproduction prohibited without permission.

However, a desirable laser would feature $T_0 \rightarrow \infty$ and would be depicted by a horizontal line $I_{th} - T$ in Figure 1.5, namely a temperature independent device performance. This particular case would require to have each parameter, i.e. A_w, B_w, C_w, G_0, N_{tr} and η insensitive to temperature. Or else, to have their effects to cancel each other.

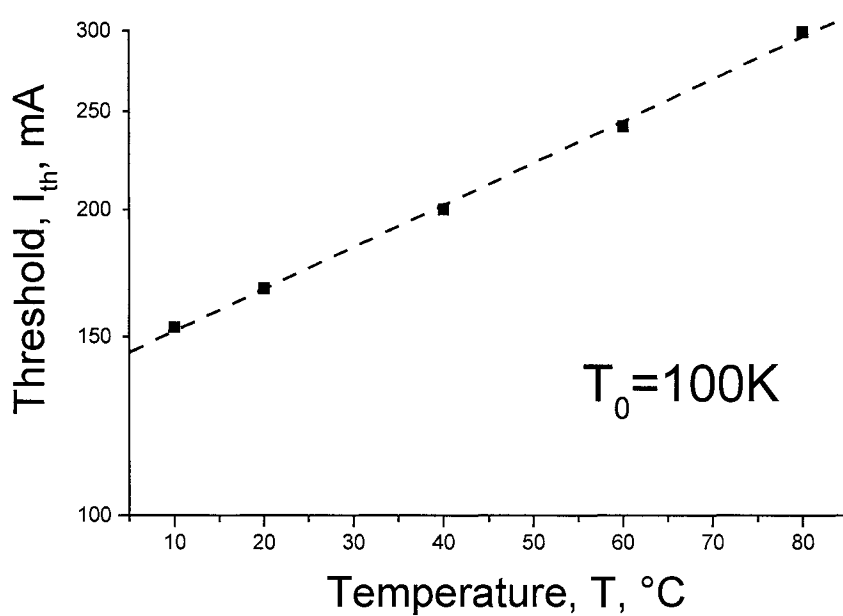

Figure 1.5.- Calculated threshold current I_{th} versus T following the parameters of Table 1.1 and simulations in Figure 1.5. A horizontal trace would represent a T-insensitive case in which $T_0 \rightarrow \infty$.

As it is of interest in laser diodes to find among the described laser parameter the one that has the larger effect into T_0, the theoretical study that follows the above introduction is carried out in Chapter 2. In fact, Chapter 2 carries out this analysis in full detail to study the separate impact of A_w, B_w,C_w, G_0, N_{tr}, R_{dc} or I_s on T_0, which provides the tools necessary for the experimental differential carrier lifetime analysis in Chapter 4.

Reproduced with permission of the copyright owner. Further reproduction prohibited without permission.

1.2.2. The high speed behavior of laser diodes above threshold

A performance parameter that is critical for direct modulation communication lasers is the modulation speed. The high speed potential of communication lasers is generally assessed from the analysis of above threshold frequency response. [56-62].

Similarly to the sub-threshold analysis, the frequency response for an ideal laser above threshold can be obtained from the solution of the rate equation model as shown by (1.13). Differently than in the subthreshold analysis, the gain clamps at threshold in an ideal laser to its value g_{th}, and the stimulated emission term is not negligible.

$$\begin{aligned}
\frac{dn_s(t)}{dt} &= \frac{\eta}{qV}i(t) - \frac{n_s}{\tau_{cap}} - \frac{n_s}{\tau_{sch}} + \frac{n_w}{\tau_{esc}}\Gamma_q \\
\frac{dn_w(t)}{dt} &= \frac{n_s(t)}{\tau_{cap}\Gamma_q} - \frac{n_w(t)}{\tau_{qw}} - \frac{1}{\Gamma\tau_p}n_p(t) - \frac{n_w(t)}{\tau_{esc}} - v_g a N_{p0} n_w(t) - v_g a_p N_{p0} n_p(t) \\
\frac{dn_p(t)}{dt} &= \Gamma v_g a N_{p0} n_w(t) + \Gamma v_g a_p N_{p0} n_p(t)
\end{aligned} \tag{1.13}$$

In (1.13) the bias point is defined by N_{p0} that is the optical mode photon density, proportional to the laser emitted power P_0. The N_{p0} - P_0 relationship is shown in (1.14) where hv is the emission photon energy.

$$N_{P0} = \frac{2\Gamma}{v_g V \alpha_m hv} P_0 \tag{1.14}$$

In this model, the first derivative of the threshold gain g_{th} necessary for the first order Taylor expansion is written in terms of the differential gain parameters a and a_p as in (1.15).

Reproduced with permission of the copyright owner. Further reproduction prohibited without permission.

$$dg = a \cdot N_w + a_p \cdot N_{P0} \tag{1.15}$$

The differential gain parameters a and a_p are described by equations (1.16) and (1.17), respectively. a and a_p are both affected by the gain compression factor ε that is extensively associated in the literature with carrier heating, and spectral and spatial hole burning, and is responsible for the differential gain reduction at biases well above threshold [47, 59, 63, 64]. ε was previously derived from the equations of energy transfer in semiconductor lasers operating above threshold [65] and is zero in an ideal laser. As it is shown below, ε produces an increase in the damping factor described below.

$$a = \frac{\partial g / \partial N_w}{1 + \varepsilon \cdot N_{PO}} \tag{1.16}$$

$$a_p = \frac{\varepsilon \cdot g_{th}}{1 + \varepsilon \cdot N_{PO}} \tag{1.17}$$

In order to obtain the laser frequency response, the three rate equation model is transformed into the frequency domain, with $j\omega$ as the imaginary frequency, as shown by (1.18) and the laser frequency response is obtained as the transfer $n_p(\omega)$ versus $i(\omega)$ solving by Cramer's rule [66].

$$\begin{pmatrix} \frac{1}{\tau_{cap}} + \frac{1}{\tau_{sch}} + j\omega & -\frac{\Gamma_q}{\tau_{esc}} & 0 \\ -\frac{1}{\tau_{cap}\Gamma_q} & \left(\frac{1}{\tau_{qw}} + \frac{1}{\tau_{esc}} + \mathrm{v}_g a N_{po} + j\omega\right) & \frac{1}{\Gamma\tau_p} + \mathrm{v}_g a_p N_{po} \\ 0 & -\Gamma \mathrm{v}_g a N_{po} & -\Gamma \mathrm{v}_g a_p N_{po} + j\omega \end{pmatrix} \cdot \begin{bmatrix} n_{sch}(\omega) \\ n_{qw}(\omega) \\ n_p(\omega) \end{bmatrix} = \frac{\eta_i}{qV} \begin{bmatrix} i(\omega) \\ 0 \\ 0 \end{bmatrix} \tag{1.18}$$

Reproduced with permission of the copyright owner. Further reproduction prohibited without permission.

The transfer function above threshold for a 3-rate equation system is shown by expression (1.19), where $\omega=2\pi f$.

$$H(f)=\frac{H_0}{(1+j2\pi f\tau_c)(f_r^2-f^2+jf\gamma)} \tag{1.19}$$

Equation (1.19) represents the frequency response in an ideal QW laser diode as a damped resonant behavior of frequency f_r and damping γ, followed by a real pole $1/2\pi\tau_c$ that arises from the transport processes in the SCH [39, 67]. This resonant behavior arises from the stimulated photon-carrier process above threshold, which does not occur below threshold.

Further analysis of (1.18) relates f_r, γ and τ_c to the laser parameters and bias point. It is found from the analytical solution of the model that when $\tau_{cap}\rightarrow 0$ $\tau_c\rightarrow 0$ in expression (1.19). This condition is experimentally equivalent of having $1/2\pi\tau_c>>f_r$, as was experimentally found in InAsP/InGaAsP/InP multiple quantum well (MQW) lasers [39] and is also verified in the lasers studied in this dissertation [68].

As first mentioned by Olshansky et al. [69], the laser's frequency bandwidth in (1.19) can be expressed as $f_{3dB\text{-}k}=2\pi/K$ when $f_r\rightarrow\infty$. $f_{3dB\text{-}k}$ is the K-limited bandwidth where K is defined in (1.20).

$$K=2\pi\frac{d\gamma}{df_r^2} \tag{1.20}$$

Smaller K values are desired for large bandwidth $f_{3dB\text{-}k}$. K increases with ε and R_{ac}, and can be approximated as in (1.21) for the limit $\tau_{cap} << 1/f_r$ [39].

Reproduced with permission of the copyright owner. Further reproduction prohibited without permission.

$$K \approx 4\pi^2\tau_p\left[1+\frac{\Gamma a_p}{a}(1+R_{ac})\right] = 4\pi^2\tau_p\left[1+\Gamma\frac{g_{th}\varepsilon(1+\varepsilon N_{P0})}{dg/dN_w(1+R_{ac})^{-1}}\right] \tag{1.21}$$

In order to study the laser bandwidth it is necessary to know the dependence of the resonance and damping with bias. As observed in (1.20), it is desirable to have f_r as large as possible. The solution of eigenvalues in (1.19) permits to obtain f_r^2 in the realistic limit $\tau_{cap} << 1/f_r$ as shown in (1.22).

$$f_r^2 \cong \frac{v_g \cdot a \cdot N_{PO}}{4\pi^2\tau_p(1+\tau_{cap}/\tau_{esc})} = \frac{v_g \cdot dg/dN_w}{4\pi^2\tau_p(1+\tau_{cap}/\tau_{esc})} \cdot \frac{N_{PO}}{1+\varepsilon N_{P0}} \tag{1.22}$$

Expression (1.22) shows that f_r^2 and therefore the laser bandwidth are affected by dg/dN_w and $(1+R_{ac})$. In fact the combined effect of these material parameters can not be separated. For this reason it is convenient to define an effective differential gain a_{eff} as shown in (1.23).

$$a_{eff} \cong \frac{a}{1+\tau_{cap}/\tau_{esc}} = \frac{dg/dN_w}{(1+\tau_{cap}/\tau_{esc})(1+\varepsilon N_{P0})} \tag{1.23}$$

The effect of the compression factor ε is observed in the sublinear dependence of f_r^2 with N_{p0} in (1.22). The slope of f_r^2 - N_{P0} depends exclusively on the effective differential gain parameter a_{eff} defined as in (1.23) when $\varepsilon \cdot N_{P0} \rightarrow 0$.

The damping factor, γ is found to linearly depend on N_{P0}. The slope γ - N_{P0} is determined by a_{eff} and ε, as shown in (1.22). Therefore in an ideal laser, the experimental determination of $\gamma - N_{po}$ allows to obtain ε by measuring a_{eff}.

Reproduced with permission of the copyright owner. Further reproduction prohibited without permission.

$$\gamma \cong v_g\, a_{eff}\left[1+\Gamma\frac{g_{th}\varepsilon(1+\varepsilon N_{P0})}{a_{eff}}\right]N_{PO} + \frac{1/\tau_w}{1+\tau_{cap}/\tau_{esc}} \quad (1.24)$$

The analysis just presented shows that in very limiting situations it is possible to extract parameters such as differential gain dg/dN_w and a_p from the measured frequency response. As it will be shown in Chapter 2, the situation is further complicated by the contributions of parasitics to the frequency responses.

Figure 1.6 shows the simulated frequency response traces (solid lines) at different photon densities P_0=0.5 mW, 2 mW and 6 mW for a Fabry Perot edge emitting laser with typical parameters given on Table 1.2. Two cases were analyzed: R_{ac}=0 (solid line) and R_{ac}=0.5 (dotted line). The former depicts perfect carrier capture in the QW, whereas the latter is typical of a real single quantum well InGaAsN laser diode. R_{ac}= 0.5 causes a reduction of ~30% in the bandwidth.

Description	Name	Value
Stripe width	L_s	100μm
Laser length	L	500μm
QW width	L_w	60Å
Active area volume	V	$3\cdot10^{-8}$ cm^{-3}
Electrical confinement factor	Γ_q	0.02
Spontaneous emission factor	β	$8.7\cdot10^{-5}$
Optical confinement factor	Γ	0.018
Compression factor	ε	10^{-17} cm^3
Photon lifetime	τ_p	4.6ps
SCH lifetime	τ_s	5ns

Table 1.2. – Typical parameters given for a Fabry-Perot cavity edge-emitting laser.

Reproduced with permission of the copyright owner. Further reproduction prohibited without permission.

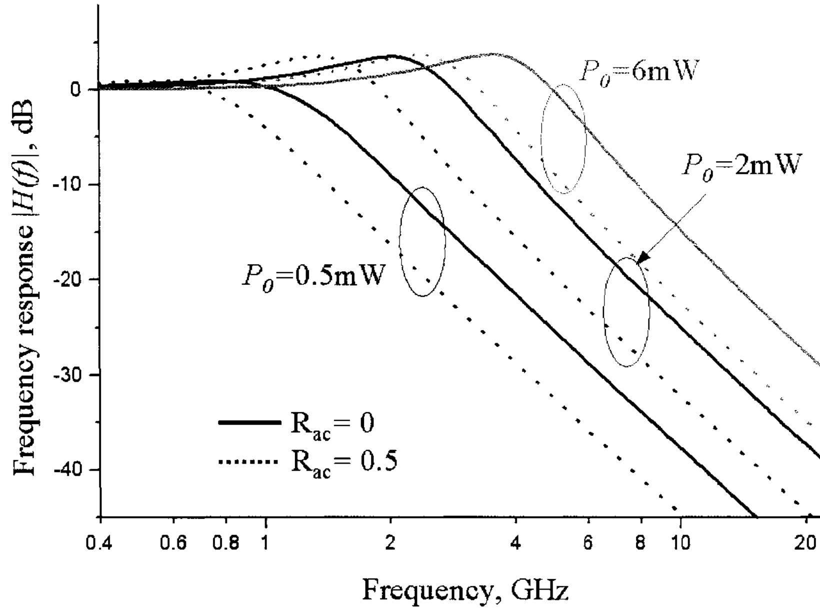

Figure 1.6.- Frequency response traces obtained with (1.20) at biases P_0=0.5 mW, 2 mW and 6 mW with the rest of the parameters shown on Table 1.2 . R_{ac}=0 corresponds to the solid line traces while R_{ac}=0.5 is shown by the dotted line traces.

The resonance frequency and damping extracted from the traces of Figure 1.6 are plotted in Figure 1.7 versus the single facet output power P_0. The sublinear dependence of f_r^2 and γ with P_0 is observed in the 40mW range, where $\varepsilon \cdot N_{P0}$ reaches values of ~0.15 at the maximum power. The case of K-limited bandwidth is depicted in Figure 1.8. At large biases (P_0=80 mW) although f_r ~12 GHz, due to a large K-factor, f_{3dB} reaches only 7.5 GHz. Instead, when K reduces to one half f_{3dB} doubles to 15 GHz.

Typical experimental cases have engineered lasers with QW-SCH doping or by changing the QW number to achieve reduced K [59, 67]. The values used in the simulations were R_{ac} =0.5 and ε from Table 1.2.

Reproduced with permission of the copyright owner. Further reproduction prohibited without permission.

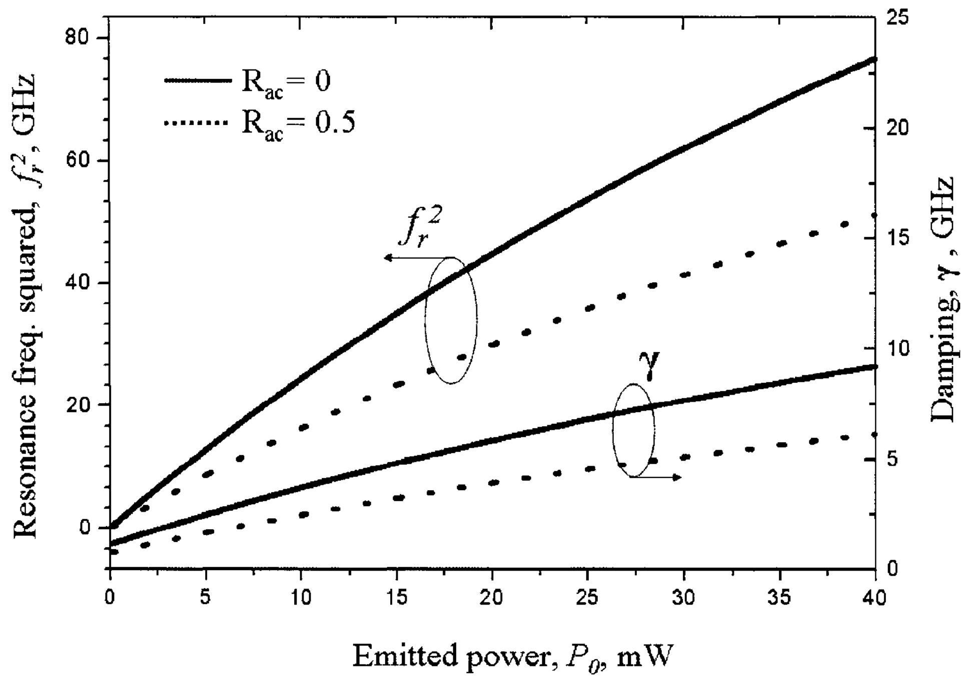

Figure 1.7.- Resonance frequency squared f_r^2 and damping γ versus P_0 from the calculations from (1.21-1.22) with parameters of Table 1.2.

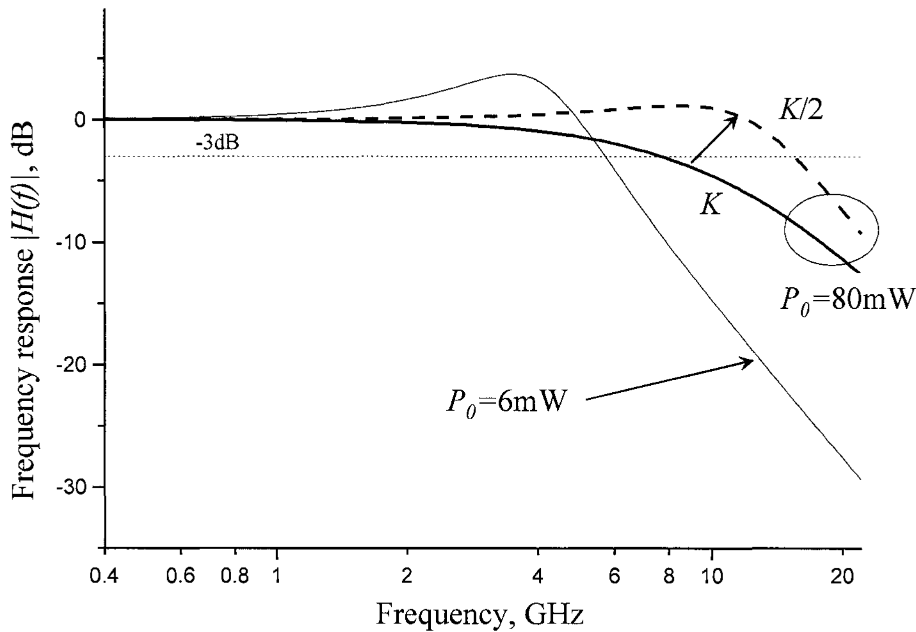

Figure 1.8.- Frequency response traces simulated at P_0=6 mW and P_0=80 mW. Dashed traces lines are computed by reducing K by one half. Notice the increase of f_{3dB} from 7.5 to 15GHz.

Reproduced with permission of the copyright owner. Further reproduction prohibited without permission.

The importance of dg/dN_w, R_{ac} and ε on affecting the bandwidth of the laser diode was discussed so far. Temperature also affects these parameters, and consequently the laser resonance, damping and 3dB frequencies are thus temperature sensitive. Chapter 2 carries out the temperature analysis of the laser bandwidth based on all the concepts previously defined.

1.3. Motivation: State of the art in the research of InGaAsN lasers

Long wavelength InGaAsN materials are relatively new and their behavior has been mainly predicted by theoretical modeling. Although there is extensive experimental work already performed in InGaAsN devices and aimed at improving their output characteristics, there is a lack of basic studies capable of unveiling the fundamental processes that occur at the device and at the material level due to the nitrogen incorporation. As an example, it is not yet known what are the physical processes that lead to the reduction of the characteristic temperature T_0. Consequently, there is not yet a defined guideline that would steer device and material engineering to improve T_0 for example.

Dilute nitride lasers have evolved from basic heterostructures with relative high amount of nitrogen emitting near 1.2μm under tens of kA/cm^2 pulsed operation [14] to a very low nitrogen composition tensile barriers structures with much lower current densities ($J_{th} < 300$A/cm^2) [24].

InGaAsN materials grown as QW structures with emission wavelength at 1.3μm have been predicted to posses many advantages over similar InP structures, such as superior differential gain $a=dg/dN_w$ [50], higher T_0 [70][18-20] and higher frequency response

Reproduced with permission of the copyright owner. Further reproduction prohibited without permission.

[9, 71]. The large conduction band discontinuity (ΔE_c>0.4eV) between QW and SCH provides an unprecedented electron confinement [17-20, 72].

Figure 1.9 shows two typical InGaAs and InGaAsN structures in which the changes due to nitrogen in the conduction and valence bands have been highlighted. Notice that the predicted higher electron confinement is contrasted by the smaller hole confinement as nitrogen is added to the InGaAs material. This effect increases hole escape and lowers T_0 by reducing η_{inj}, as experimentally demonstrated by Tansu et al. [73]. Hole thermionic escape directly impacts in the ratio R_{dc} as previously discussed [74]. As it will be shown in the next chapters, this has serious implications in the below and above threshold frequency response of InGaAsN laser diodes.

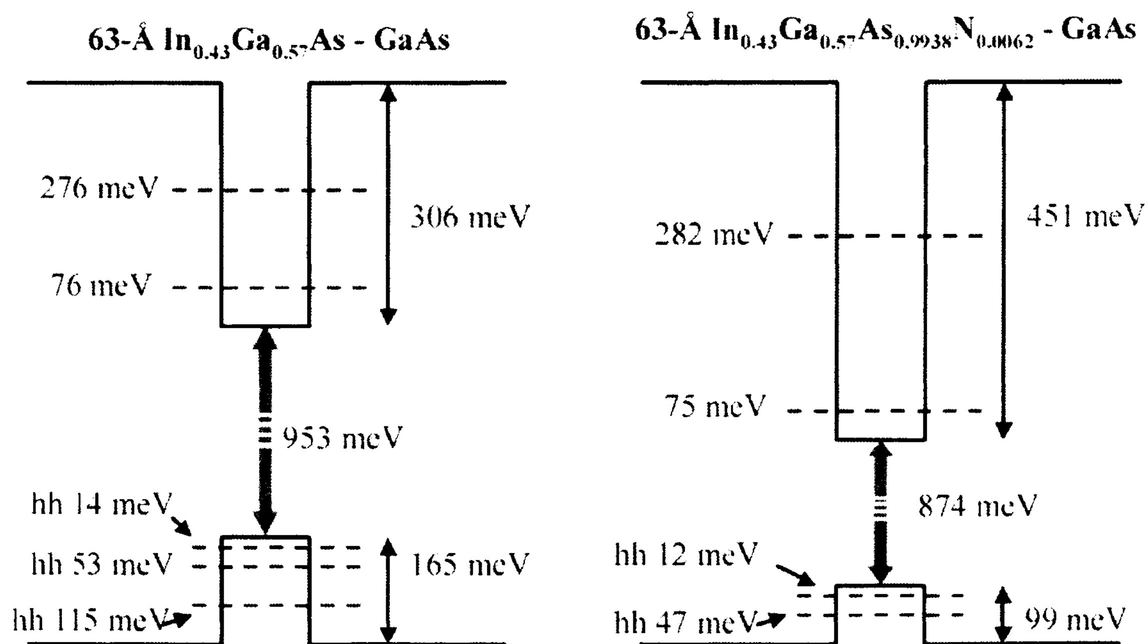

Figure 1.9.- Typical identical InGaAs host (a) and InGaAsN dilute nitride (b) structures, where the wavelength shift occurs from $\lambda = 1190$nm to $\lambda = 1295$nm, respectively [73].

Reproduced with permission of the copyright owner. Further reproduction prohibited without permission.

Nitrogen incorporation is predicted to affect carrier recombination in the material. Specifically, an increase in the monomolecular recombination is predicted. The work described in this dissertation and described in Chapter 4 is the first to univocally identified this effect in device structures.

These results are supported by Photoluminescence (PL) measurements directly performed in the material [75].

Other work modeled and studied Auger recombination in 1.3μm InGaAsN lasers [50, 52, 54, 76], which is found to contribute to ~55% of the threshold current in 1.3μm InGaAsN QW lasers.

Gain measurements were also performed on 1.3μm InGaAsN lasers [77-79]. Most of these studies have found a more than 2 times reduction in dg/dI due to the incorporation of nitrogen. However, until now there are no reports that show the effect of nitrogen incorporation in the differential gain dg/dN_w. This is because the I-N_w relationship is not known in InGaAsN lasers. Contrarily to theoretical predictions [17, 20, 52, 80], recent experimental evidence suggests that the incorporation of nitrogen may not alter significantly the gain to radiative current relationship in dilute nitride lasers, which suggest that dg/dN_w may not be significantly affected.

Chapter 4 of this dissertation is devoted to the analysis of gain and differential gain in the nitrogen containing laser structures. This analysis relies on a comprehensive laser model that includes electrical parasitics presented in Chapter 2.

The incorporation of the effects of carrier transport and current injection efficiency results to be key in the temperature study of the threshold current. Contrary to previous speculations about what causes T_0 in InGaAsN lasers, the thorough analysis of Chapter 4

Reproduced with permission of the copyright owner. Further reproduction prohibited without permission.

permits to formulate the issue of T_0 in terms of device and material separately in InGaAsN lasers. This in turn allows to individualize the main contributor to the reduction in T_0 in InGaAsN lasers.

This work has also investigated the high frequency modulation response of InGaAsN laser diodes. Although 1.3μm InGaAsN lasers were expected to surpass the 20Gb/s operation [71], they have occasionally reached 10Gb/s at T=20°C [81, 82]. The reasons that prevent these devices from operating at higher speeds and temperatures are still unclear. Theory predicts modulation bandwidths [71] in InGaAsN QW lasers larger than in InP-based lasers. Experiments such as frequency response and relative intensity noise (RIN) measurements were performed in 1.3μm InGaAsN QW lasers and show a reduction in the effective differential gain of more than 50% due to the incorporation of nitrogen [83, 84]. These findings were linked to the interaction of nitrogen with the host InGaAs material [85]. However, carrier transport also plays a role as shown by equation (1.22). Chapters 4 and 5 will show that neglecting $R_{dc}=\tau_{cap\text{-}dc}/\tau_{esc\text{-}dc}$ and $R_{ac}=\tau_{cap}/\tau_{esc}$ is not appropriate in InGaAsN lasers as it could lead to a misinterpretation of the physics of the material. Further, the incorporation of carrier transport is key to decouple the material from the device behavior with temperature. This analysis carried out in Chapter 5 will elucidate for the first time in InGaAsN lasers what is the effect of nitrogen in the temperature dependence of the device bandwidth.

1.4. Objective and scope of this dissertation

The experiments and modeling that are described in this dissertation have been motivated by the following questions:

Reproduced with permission of the copyright owner. Further reproduction prohibited without permission.

1.- What causes the reduction in T_0 when nitrogen is added in InGaAsN lasers?

2.- Is this a material issue, such as reduction in differential gain and transparency carrier density?

3.- Is this a device issue, such as carrier leakage?

4.- Why does the frequency bandwidth reduces when nitrogen is added in InGaAsN lasers?

5.- Is it an issue of low material's differential gain at threshold, or could carrier transport play an dominant role?

None of these fundamental questions have been answered with a solid analysis of experimental data yet. The work presented in this dissertation aims at answering all these questions. Furthermore, it attempts to re-engineer 1.3μm and longer wavelength InGaAsN materials and their laser structures.

The core of the study presented here relies on using identical single quantum well (SQW) $In_{0.40}Ga_{0.60}As_{1-x}N_x$ laser devices that differ in the nitrogen incorporation (x=0, x=0.005) in the quantum well.

The entire work is divided into below and above threshold experiments and their analysis. This chapter has provided so far the general notions on what rules on the temperature behavior of threshold and frequency bandwidth in SCH-QW lasers. In more detail, a general rate equation model that considers the device electrical parasitics, along with the carrier transport equations is fully developed on Chapter 2. This model provides the full support for the below and above threshold analyses.

Reproduced with permission of the copyright owner. Further reproduction prohibited without permission.

Details of the experiments that are used to investigate the below and above threshold laser diode response will be described in Chapter 3. The results of the experiments provide the impedance, frequency response and amplified spontaneous emission (ASE) below threshold, while retrieving the optical frequency response above threshold. These measurements were carried out at baseplate temperatures ranging from 10°C to 80°C.

Chapters 4 and 5 provide the analysis of the results obtained below and above threshold, respectively, that fully separate the device from the material parameters, as a function of the temperature and nitrogen incorporation. The analysis of results and conclusion in Chapter 4 will provide the answers to questions 1-3, whereas Chapter 5 will answer to questions 4-6. Chapter 6 presents the conclusions of this dissertation and suggested future work.

Reproduced with permission of the copyright owner. Further reproduction prohibited without permission.

References for Chapter 1

[1] K. Nakahara, T. Tsuchiya, T. Kitatani, K. Shinoda, T. Kikawa, F. Hamano, S. Fujisaki, T. Taniguchi, E. Nomoto, M. Sawada, and T. Yuasa, "12.5-Gb/s direct modulation up to 115 degrees C in 1.3-mu m InGaAlAs-MQW RWG DFB lasers with notch-free grating structure," *Journal of Lightwave Technology*, vol. 22, pp. 159-165, 2004.

[2] V. Jayaraman, M. Mehta, A. W. Jackson, S. Wu, Y. Okuno, J. Piprek, and J. E. Bowers, "High-power 1320-nm wafer-bonded VCSELs with tunnel junctions," *IEEE Photonics Technology Letters*, vol. 15, pp. 1495-1497, 2003.

[3] R. Michalzik, K. J. Ebeling, M. Kicherer, F. Mederer, R. King, H. Unold, and R. Jager, "High-performance VCSELs for optical data links," *Ieice Transactions on Communications*, vol. E84B, pp. 1255-1264, 2001.

[4] J. D. Ralston, S. Weisser, I. Esquivias, E. C. Larkins, J. Rosenzweig, P. J. Tasker, and J. Fleissner, "Control of Differential Gain, Nonlinear Gain, and Damping Factor for High-Speed Application of Gaas-Based Mqw Lasers," *IEEE Journal of Quantum Electronics*, vol. 29, pp. 1648-1659, 1993.

[5] K. Czotscher, E. C. Larkins, S. Weisser, W. Benz, J. Daleiden, J. Fleissner, M. Maier, J. D. Ralston, and J. Rosenzweig, "Uncooled high-temperature (130 degrees C) operation of InGaAs-GaAs multiple quantum-well lasers at 20 Gb/s," *IEEE Photonics Technology Letters*, vol. 9, pp. 575-577, 1997.

[6] G. Morthier, R. Schatz, and O. Kjebon, "Extended modulation bandwidth of DBR and external cavity lasers by utilizing a cavity resonance for equalization," *IEEE Journal of Quantum Electronics*, vol. 36, pp. 1468-1475, 2000.

[7] S. Weisser, E. C. Larkins, K. Czotscher, W. Benz, J. Daleiden, I. Esquivias, J. Fleissner, J. D. Ralston, B. Romero, R. E. Sah, A. Schonfelder, and J. Rosenzweig, "Damping-limited modulation bandwidths up to 40 GHz in undoped short-cavity In0.35Ga0.65As-GaAs multiple-quantum-well lasers," *IEEE Photonics Technology Letters*, vol. 8, pp. 608-610, 1996.

[8] N. Tansu, Y. L. Chang, T. Takeuchi, D. P. Bour, S. W. Corzine, M. R. T. Tan, and L. J. Mawst, "Temperature analysis and characteristics of highly strained InGaAs-GaAsP-GaAs (lambda > 1.17 mu m) quantum-well lasers," *IEEE Journal of Quantum Electronics*, vol. 38, pp. 640-651, 2002.

[9] J. S. Harris, "GaInNAs, a new material for long wavelength VCSELs," *Journal of the Korean Physical Society*, vol. 39, pp. S306-S312, 2001.

[10] N. Tansu, J. Y. Yeh, and L. J. Mawst, "Extremely low threshold-current-density InGaAs quantum-well lasers with emission wavelength of 1215-1233 nm," *Applied Physics Letters*, vol. 82, pp. 4038-4040, 2003.

[11] T. Takeuchi, Y. L. Chang, A. Tandon, D. Bour, S. Corzine, R. Twist, M. Tan, and H. C. Luan, "Low threshold 1.2 mu m InGaAs quantum well lasers grown under low As/III ratio," *Applied Physics Letters*, vol. 80, pp. 2445-2447, 2002.

[12] M. Weyers, M. Sato, and H. Ando, "Red Shift of Photoluminescence and Absorption in Dilute Gaasn Alloy Layers," *Japanese Journal of Applied Physics Part 2-Letters*, vol. 31, pp. L853-L855, 1992.

Reproduced with permission of the copyright owner. Further reproduction prohibited without permission.

[13] M. Kondow, S. Nakatsuka, T. Kitatani, Y. Yazawa, and M. Okai, "Room-temperature pulsed operation of GaInNAs laser diodes with excellent high-temperature performance," *Japanese Journal of Applied Physics Part 1-Regular Papers Short Notes & Review Papers*, vol. 35, pp. 5711-5713, 1996.

[14] M. Kondow, S. Natatsuka, T. Kitatani, Y. Yazawa, and M. Okai, "Room-temperature continuous-wave operation of GaInNAs/GaAs laser diode," *Electronics Letters*, vol. 32, pp. 2244-2245, 1996.

[15] W. Shan, W. Walukiewicz, J. W. Ager, E. E. Haller, J. F. Geisz, D. J. Friedman, J. M. Olson, and S. R. Kurtz, "Band anticrossing in GaInNAs alloys," *Physical Review Letters*, vol. 82, pp. 1221-1224, 1999.

[16] J. D. Perkins, A. Mascarenhas, Y. Zhang, J. F. Geisz, D. J. Friedman, J. M. Olson, and S. R. Kurtz, "Nitrogen-activated transitions, level repulsion, and band gap reduction in GaAs1-xNx with x < 0.03," *Physical Review Letters*, vol. 82, pp. 3312-3315, 1999.

[17] X. Marie, J. Barrau, T. Amand, H. Carrere, A. Arnoult, C. Fontaine, and E. Bedel-Pereira, "Band structure and optical gain in InGaAsN/GaAs and InGaAsN/GaAsN quantum wells," *IEE Proceedings-Optoelectronics*, vol. 150, pp. 25-27, 2003.

[18] A. Lindsay, S. Tomic, and E. P. O'Reilly, "Derivation of a 10-band k center dot p model for dilute nitride semiconductors," *Solid-State Electronics*, vol. 47, pp. 443-446, 2003.

[19] M. M. E. Fahmi, A. Khan, J. A. Griffin, G. L. Harris, L. H. Robins, A. G. Birdwell, Y. S. Kang, D. J. Smith, T. Steiner, and S. N. Mohammad, "Nitrogen-activated bowing of dilute InyGa1-yAs1-xNx based on photoreflectance studies," *Journal of Applied Physics*, vol. 94, pp. 7576-7580, 2003.

[20] J. M. Ulloa, J. L. Sanchez-Rojas, A. Hierro, J. M. G. Tijero, and E. Tournie, "Effect of nitrogen on the band structure and material gain of InyGa1-yAs1-xNx-GaAs quantum wells," *IEEE Journal of Selected Topics in Quantum Electronics*, vol. 9, pp. 716-722, 2003.

[21] B. Borchert, A. Y. Egorov, S. Illek, M. Komainda, and H. Riechert, "1.29 mu m GaInNAs multiple quantum-well ridge-waveguide laser diodes with improved performance," *Electronics Letters*, vol. 35, pp. 2204-2206, 1999.

[22] K. D. Choquette, J. F. Klem, A. J. Fischer, O. Blum, A. A. Allerman, I. J. Fritz, S. R. Kurtz, W. G. Breiland, R. Sieg, K. M. Geib, J. W. Scott, and R. L. Naone, "Room temperature continuous wave InGaAsN quantum well vertical- cavity lasers emitting at 1.3 mu m," *Electronics Letters*, vol. 36, pp. 1388-1390, 2000.

[23] A. W. Jackson, R. L. Naone, M. J. Dalberth, J. M. Smith, K. J. Malone, D. W. Kisker, J. F. Klem, K. D. Choquette, D. K. Serkland, and K. M. Geib, "OC-48 capable InGaAsN vertical cavity lasers," *Electronics Letters*, vol. 37, pp. 355-356, 2001.

[24] N. Tansu, N. J. Kirsch, and L. J. Mawst, "Low-threshold-current-density 1300-nm dilute-nitride quantum well lasers," *Applied Physics Letters*, vol. 81, pp. 2523-2525, 2002.

[25] D. Gollub, S. Moses, M. Kamp, and A. Forchel, "1.4 mu m continuous-wave GaInNAs distributed feedback laser diodes," *Electronics Letters*, vol. 39, pp. 1815-1816, 2003.

Reproduced with permission of the copyright owner. Further reproduction prohibited without permission.

[26] J. Y. Yeh, N. Tansu, and L. J. Mawst, "Long wavelength MOCVD grown InGaAsN-GaAsN quantum well lasers emitting at 1.378-1.41 mu m," *Electronics Letters*, vol. 40, pp. 739-741, 2004.

[27] S. R. Bank, M. A. Wistey, L. L. Goddard, H. B. Yuen, V. Lordi, and J. S. Harris, "Low-threshold continuous-wave 1.5-mu m GaInNAsSb lasers grown on GaAs," *IEEE Journal of Quantum Electronics*, vol. 40, pp. 656-664, 2004.

[28] O. Anton, G. Vaschenko, D. Patel, G. Y. Robinson, C. S. Menoni, and J. Pikal, "Small signal response of 1.3 mm InAsP/InGaAsP quantum well laser diodes obtained with a THz-bandwidth frequency comb," *IEEE Journal of Quantum Electronics*, vol. 40, pp. 982-988, 2004.

[29] V. Gambin, W. Ha, M. Wistey, H. Yuen, S. R. Bank, S. M. Kim, and J. S. Harris, "GaInNAsSb for 1.3-1.6-mu m-long wavelength lasers grown by molecular beam epitaxy," *IEEE Journal of Selected Topics in Quantum Electronics*, vol. 8, pp. 795-800, 2002.

[30] N. N. Ledentsov, V. M. Ustinov, A. Y. Egorov, A. E. Zhukov, M. V. Maksimov, I. G. Tabatadze, and P. S. Kopev, "Optical-Properties of Heterostructures with Ingaas-Gaas Quantum Clusters," *Semiconductors*, vol. 28, pp. 832-834, 1994.

[31] K. Otsubo, N. Hatori, M. Ishida, S. Okumura, T. Akiyama, Y. Nakata, H. Ebe, M. Sugawara, and Y. Arakawa, "Temperature-insensitive eye-opening under 10-Gb/s modulation of 1.3-mu m p-doped quantum-dot lasers without current adjustments," *Japanese Journal of Applied Physics Part 2-Letters & Express Letters*, vol. 43, pp. L1124-L1126, 2004.

[32] P. Bhattacharya, K. Kamath, J. Phillips, and D. Klotzkin, "Self-organized growth of In(Ga)As/GaAs quantum dots and their opto-electronic device applications," *Bulletin of Materials Science*, vol. 22, pp. 519-529, 1999.

[33] D. Bimberg and N. Ledentsov, "Quantum dots: lasers and amplifiers," *Journal of Physics-Condensed Matter*, vol. 15, pp. R1063-R1076, 2003.

[34] P. Bhattacharya, "Quantum well and quantum dot lasers: From strained-layer and self-organized epitaxy to high-performance devices," *Optical and Quantum Electronics*, vol. 32, pp. 211-225, 2000.

[35] M. H. Gass, A. J. Papworth, T. B. Joyce, T. J. Bullough, and P. R. Chalker, "Measurement of the effective electron mass in GaInNAs by energy-loss spectroscopy," *Applied Physics Letters*, vol. 84, pp. 1453-1455, 2004.

[36] G. Lin and C. P. Lee, "Comparison of 1300 nm quantum well lasers using different material systems," *Optical and Quantum Electronics*, vol. 34, pp. 1191-1200, 2002.

[37] S. Sato, "Low threshold and high characteristic temperature 1.3 mu m range GaInNAs lasers grown by metalorganic chemical vapor deposition," *Japanese Journal of Applied Physics Part 1-Regular Papers Short Notes & Review Papers*, vol. 39, pp. 3403-3405, 2000.

[38] N. Tansu and L. J. Mawst, "Low-threshold strain-compensated InGaAs(N) (lambda=1.19-1.31 mu m) quantum-well lasers," *IEEE Photonics Technology Letters*, vol. 14, pp. 444-446, 2002.

[39] L. A. Coldren and S. W. Corzine, *Diode lasers and Photonic Integrated Circuits*: Wiley series in microwave and optical engineering, 1995.

Reproduced with permission of the copyright owner. Further reproduction prohibited without permission.

[40] C. Y. Tsai, F. P. Shih, T. L. Sung, T. Y. Wu, and C. H. Chen, "A small-signal analysis of the modulation response of high- speed quantum-well lasers: Effects of spectral hole burning, carrier heating, and carrier diffusion-capture-escape," *IEEE Journal of Quantum Electronics*, vol. 33, pp. 2084-2096, 1997.

[41] K. L. Lau, "Dynamics of Quantum Well Lasers," in *Quantum Well Lasers*, P. Zory, Ed.: New York: Academic Press Inc., 1993.

[42] H. C. Casey, "Temperature-Dependence of the Threshold Current-Density in Inp-Ga0.28in0.72as0.6p0.4 (Lambda = 1.3 Mu-M) Double Heterostructure Lasers," *Journal of Applied Physics*, vol. 56, pp. 1959-1964, 1984.

[43] J. M. Pikal, C. S. Menoni, H. Temkin, P. Thiagarajan, and G. Y. Robinson, "Carrier lifetime and recombination in long-wavelength quantum- well lasers," *IEEE Journal of Selected Topics in Quantum Electronics*, vol. 5, pp. 613-619, 1999.

[44] R. Olshansky, C. B. Su, J. Manning, and W. Powazinik, "Measurement of Radiative and Nonradiative Recombination Rates in Ingaasp and Algaas Light-Sources," *IEEE Journal of Quantum Electronics*, vol. 20, pp. 838-854, 1984.

[45] J. Yang, B. B. Elenkrig, D. T. Cassidy, D. M. Bruce, and I. M. Templeton, "Application of Polarization Resolved Photoluminescence to the Study of Quantum-Well Intermixing in Ingaasp Systems (Vol 10, Pg 483, 1995)," *Semiconductor Science and Technology*, vol. 10, pp. 886-886, 1995.

[46] R. Olshansky, J. Lacourse, T. Chow, and W. Powazinik, "Measurement of Radiative, Auger, and Nonradiative Currents in 1.3-Mu-M Ingaasp Buried Heterostructure Lasers," *Applied Physics Letters*, vol. 50, pp. 310-312, 1987.

[47] S. L. Chuang, *Physics of optoelectronic devices*, 1995.

[48] N. Tansu and L. J. Mawst, "Temperature sensitivity of 1300-nm InGaAsN quantum-well lasers," *IEEE Photonics Technology Letters*, vol. 14, pp. 1052-1054, 2002.

[49] O. Anton, C. S. Menoni, J. Y. Yeh, L. J. Mawst, J. M. Pikal, and N. Tansu, "Increased monomolecular recombination in MOCVD grown 1.3-mu m InGaAsN-GaAsP-GaAs QW lasers from carrier lifetime measurements," *IEEE Photonics Technology Letters*, vol. 17, pp. 953-955, 2005.

[50] S. Tomic, E. P. O'Reilly, R. Fehse, S. J. Sweeney, A. R. Adams, A. D. Andreev, S. A. Choulis, T. J. C. Hosea, and H. Riechert, "Theoretical and experimental analysis of 1.3-mu m InGaAsN/GaAs lasers," *IEEE Journal of Selected Topics in Quantum Electronics*, vol. 9, pp. 1228-1238, 2003.

[51] J. Pikal, "Temperature dependence of Carrier Lifetime, Recombination and Gain in 1.3μm InAsP/InGaAsP Multiple Quantum Well Lasers," in *Electrical Engineering*: Colorado State University, 1999.

[52] S. Tomic and E. P. O'Reilly, "Gain characteristics of ideal dilute nitride quantum well lasers," *Physica E-Low-Dimensional Systems & Nanostructures*, vol. 13, pp. 1102-1105, 2002.

[53] S. T. Ng, W. J. Fan, Y. X. Dang, and S. F. Yoon, "Comparison of electronic band structure and optical transparency conditions of InxGa1-xAs1-yNy/GaAs quantum wells calculated by 10-band, 8-band, and 6-band k center dot p models," *Physical Review B*, vol. 72, 2005.

Reproduced with permission of the copyright owner. Further reproduction prohibited without permission.

[54] A. D. Andreev and G. G. Zegrya, "Auger recombination in strained quantum wells," *Semiconductors*, vol. 31, pp. 297-303, 1997.
[55] G. P. Agrawal and N. K. Dutta, *Semiconductor Lasers*. New York: Van Nostrand Reinhold, 1993.
[56] J. Eom, C. B. Su, J. Lacourse, and R. B. Lauer, "Simultaneous Measurement of Spontaneous Emission Rate, Nonlinear Gain Coefficient, and Carrier Lifetime in Semiconductor-Lasers Using a Parasitic-Free Optical Modulation Technique," *Applied Physics Letters*, vol. 56, pp. 518-520, 1990.
[57] D. Vassilovski, T. C. Wu, S. Kan, K. Y. Lau, and C. E. Zah, "Unambiguous Determination of Quantum Capture, Carrier Diffusion, and Intrinsic Effects in Quantum-Well Laser Dynamics Using Wavelength-Selective Optical Modulation," *IEEE Photonics Technology Letters*, vol. 7, pp. 706-708, 1995.
[58] R. Paiella, G. Hunziker, K. J. Vahala, and U. Koren, "Measurement of the interwell carrier transport lifetime in multiquantum-well optical amplifiers by polarization-resolved four-wave mixing," *Applied Physics Letters*, vol. 69, pp. 4142-4144, 1996.
[59] I. Esquivias, S. Weisser, B. Romero, J. D. Ralston, and J. Rosenzweig, "Carrier dynamics and microwave characteristics of GaAs-based quantum-well lasers," *IEEE Journal of Quantum Electronics*, vol. 35, pp. 635-646, 1999.
[60] M. Dutta and M. A. Stroscio, *Advances in semiconductor lasers and applications to optoelectronics*. Singapore ; River Edge, NJ: World Scientific, 2000.
[61] X. Jin and S. L. Chuang, "Microwave modulation of a quantum-well laser with and without external optical injection," *IEEE Photonics Technology Letters*, vol. 13, pp. 648-650, 2001.
[62] P. Bhattacharya and S. Ghosh, "Tunnel injection In0.4Ga0.6As/GaAs quantum dot lasers with 15 GHz modulation bandwidth at room temperature," *Applied Physics Letters*, vol. 80, pp. 3482-3484, 2002.
[63] T. Keating, X. Jin, S. L. Chuang, and K. Hess, "Temperature dependence of electrical and optical modulation responses of quantum-well lasers," *IEEE Journal of Quantum Electronics*, vol. 35, pp. 1526-1534, 1999.
[64] R. Nagarajan, M. Ishikawa, T. Fukushima, R. S. Geels, and J. E. Bowers, "High-Speed Quantum-Well Lasers and Carrier Transport Effects," *IEEE Journal of Quantum Electronics*, vol. 28, pp. 1990-2008, 1992.
[65] C. Y. Tsai, Y. H. Lo, R. M. Spencer, and L. F. Eastman, "Nonlinear Gain Coefficients in Semiconductor Quantum-Well Lasers - Effects of Carrier Diffusion, Capture, and Escape," *IEEE Journal of Selected Topics in Quantum Electronics*, vol. 1, pp. 316-330, 1995.
[66] "Cramer's Rule, http://www.mathwords.com/c/cramers_rule.htm."
[67] R. Nagarajan, T. Fukushima, M. Ishikawa, J. E. Bowers, R. S. Geels, and L. A. Coldren, "Transport Limits in High-Speed Quantum-Well Lasers - Experiment and Theory," *IEEE Photonics Technology Letters*, vol. 4, pp. 121-123, 1992.
[68] O. Anton, D. Patel, C. S. Menoni, J. Y. Yeh, T. T. Van Roy, L. Mawst, J. Pikal, and N. Tansu, *in press, IEEE Journal of Selected Topics in Quantum Electronics*, 2005.

Reproduced with permission of the copyright owner. Further reproduction prohibited without permission.

[69] R. Olshansky, P. Hill, V. Lanzisera, and W. Powazinik, "Universal Relationship between Resonant-Frequency and Damping Rate of 1.3 Mu-M Ingaasp Semiconductor-Lasers," *Applied Physics Letters*, vol. 50, pp. 653-655, 1987.
[70] C. K. Kim and Y. H. Lee, "Thermal characteristics of optical gain for GaInNAs quantum wells at 1.3 mu m," *Applied Physics Letters*, vol. 79, pp. 3038-3040, 2001.
[71] J. C. L. Yong, J. M. Rorison, M. Othman, H. D. Sun, M. D. Dawson, and K. A. Williams, "Simulation of gain and modulation bandwidths of 1300nm RWG InGaAsN lasers," *IEE Proceedings-Optoelectronics*, vol. 150, pp. 80-82, 2003.
[72] J. C. L. Yong, J. M. Rorison, and I. H. White, "1.3-mu m quantum-well InGaAsP, AlGaInAs, and InGaAsN laser material gain: A theoretical study," *IEEE Journal of Quantum Electronics*, vol. 38, pp. 1553-1564, 2002.
[73] N. Tansu and L. J. Mawst, "The role of hole leakage in 1300-nm InGaAsN quantum-well lasers," *Applied Physics Letters*, vol. 82, pp. 1500-1502, 2003.
[74] N. Tansu and L. J. Mawst, "Current injection efficiency of InGaAsN quantum-well lasers," *Journal of Applied Physics*, vol. 97, 2005.
[75] A. Kaschner, T. Luttgert, H. Born, A. Hoffmann, A. Y. Egorov, and H. Riechert, "Recombination mechanisms in GaInNAs/GaAs multiple quantum wells," *Applied Physics Letters*, vol. 78, pp. 1391-1393, 2001.
[76] R. Fehse, S. Tomic, A. R. Adams, S. J. Sweeney, E. P. O'Reilly, A. Andreev, and H. Riechert, "A quantitative study of radiative, Auger, and defect related recombination processes in 1.3-mu m GaInNAs-based quantum-well lasers," *IEEE Journal of Selected Topics in Quantum Electronics*, vol. 8, pp. 801-810, 2002.
[77] M. Hofmann, A. Wagner, C. Ellmers, C. Schlichenmeier, S. Schafer, F. Hohnsdorf, J. Koch, W. Stolz, S. W. Koch, W. W. Ruhle, J. Hader, J. V. Moloney, E. P. O'Reilly, B. Borchert, A. Y. Egorov, and H. Riechert, "Gain spectra of (GaIn)(NAs) laser diodes for the 1.3-mu m- wavelength regime," *Applied Physics Letters*, vol. 78, pp. 3009-3011, 2001.
[78] D. J. Palmer, P. M. Smowton, P. Blood, J. Y. Yeh, L. J. Mawst, and N. Tansu, "Effect of nitrogen on gain and efficiency in InGaAsN quantum-well lasers," *Applied Physics Letters*, vol. 86, 2005.
[79] L. Shterengas, J. Y. Yeh, L. Mawst, N. Tansu, and G. Belenky, "Linewidth-enhancement factors of InGaAs and InGaAsN single-quantum-well diode lasers," presented at Conference on Lasers and Electro-Optics, CLEO '04., San Francisco, 2004.
[80] J. Hader, S. W. Koch, J. V. Moloney, and E. P. O'Reilly, "Gain in 1.3 mu m materials: InGaNAs and InGaPAs semiconductor quantum-well lasers," *Applied Physics Letters*, vol. 77, pp. 630-632, 2000.
[81] G. Steinle, F. Mederer, M. Kicherer, R. Michalzik, G. Kristen, A. Y. Egorov, H. Riechert, H. D. Wolf, and K. J. Ebeling, "Data transmission up to 10Gbit/s with 1.3 mu m wavelength InGaAsN VCSELs' (vol 37, pg 632, 2001)," *Electronics Letters*, vol. 37, pp. 803-803, 2001.
[82] A. Martinez, J. G. Provost, B. Dagens, V. Sallet, D. Jahan, K. Merghem, L. Ferlazzo, J. Landreau, O. Le Gouezigou, J. C. Harmand, and A. Ramdane, "9.7

Reproduced with permission of the copyright owner. Further reproduction prohibited without permission.

GHz small-signal bandwidth of three-quantum well GalnNAs/GaAs laser diodes operating at 1.35 mu m," *Electronics Letters*, vol. 40, pp. 425-427, 2004.
[83] L. Shterengas, G. L. Belenky, J. Y. Yeh, L. J. Mawst, and N. Tansu, "Differential gain and linewidth-enhancement factor in dilute-nitride GaAs-based 1.3-mu m diode lasers," *IEEE Journal of Selected Topics in Quantum Electronics*, vol. 11, pp. 1063-1068, 2005.
[84] J. S. Harris, "GaInNAs long-wavelength lasers: progress and challenges," *Semiconductor Science and Technology*, vol. 17, pp. 880-891, 2002.
[85] M. Hetterich, M. D. Dawson, A. Y. Egorov, D. Bernklau, and H. Riechert, "Electronic states and band alignment in GalnNAs/GaAs quantum-well structures with low nitrogen content," *Applied Physics Letters*, vol. 76, pp. 1030-1032, 2000.

Reproduced with permission of the copyright owner. Further reproduction prohibited without permission.

CHAPTER 2

Modeling of the carrier dynamics in InGaAsN and InGaAs lasers below and above threshold

This chapter is devoted to the development of a rate equation analysis to model the laser dynamics to small signal perturbations. The model couples for the first time the full effects of electrical parasitics of the *p-n* laser diode, the circuitry external to the device and the typical carrier equations in its active area.

The numerical solutions to this model allow to obtain expressions of the electrical response, the impedance as well as the optical response below and above threshold. This analysis is the tool to fit the experimental data described in Chapters 4 and 5 in terms of physical parameters, and separate them from the device behavior.

The results and analysis presented on this chapter are based on "Frequency response of strain-compensated InGaAsN/GaAsP/GaAs SQW lasers", O. Anton, D. Patel, C.S. Menoni, J. Y. Yeh, T. Van Roy, L. J. Mawst, J. Pikal and N. Tansu, that is published in IEEE Journal of Selected Topic on Quantum Electronics **11**, 1079-1088, (2005). The manuscript was written by O. Anton and edited by C.S. Menoni.

Reproduced with permission of the copyright owner. Further reproduction prohibited without permission.

2.1. Introduction: Model of the laser carrier-gain dynamics

The study of the dynamic behavior of laser diodes has evolved since its invention. Since the early days, the resonant behavior observed on heterostructure laser diodes when its bias current is switched from zero to somewhere above threshold was explained by the interaction between two reservoirs: the carrier density, responsible for the laser gain, and the density of photons in the fundamental lasing mode [1, 2]. With the advent of broader bandwidth laser diodes necessary for telecomm applications, electrical parasitics were included into the model to describe the behavior of packaged devices. This analysis was based on admittance and S-parameters [3-5]. The developed models were used to analyze either double heterostructure or multiple well lasers. The latter were intended to reach higher speeds but suffered from carrier transport effects [6-8]. By being able to explain some discrepancies between theory and experiments, the effect of carrier transport was formally incorporated in heterostructure quantum well lasers [7, 9, 10]. In this way state filling and transport between bulk and quantum well states in the sub-micron width (typically ~3000Å) separate confinement heterostructure (SCH) that optically confines the mode were incorporated. Although not a first principle approach, like those described by [11, 12], the rate equation analysis provides a simple and direct way to analyze the laser's frequency response and impedance in bandwidths of up to tens of gigahertz [7, 13-21].

Below threshold, the concept of carrier transfer between bulk and QW states has been incorporated in the differential carrier lifetime analysis to obtain the carrier density in the QW and study the recombination processes in 1.3μm multiple quantum well lasers [22]. Further, the analysis of new InGaAsN laser structures with considerable amount of

Reproduced with permission of the copyright owner. Further reproduction prohibited without permission.

parasitics was taken into account by a more complex rate equation model [23], to isolate the monomolecular recombination.

Based on these introductory examples, this chapter presents a novel rate equation analysis of the small signal laser behavior that includes the laser diode electrical parasitics and external circuitry.

The analysis below threshold retrieves the quantum well differential carrier lifetime τ_w versus device bias introduced on Section 1.2.1 as shown on Section 2.2. This is fundamental in the calculation of the carrier density N_w versus bias I relationship from experimental results obtained in Section 4.

Above threshold, Section 2.4 describes the model introduced in Section 1.2.2 that allows obtaining important parasitics-free device parameters and material parameters versus temperature, based on the results from the optical frequency response measurements obtained on Chapter 5.

The MATLAB algorithms implemented to carry out the simulations are given in Appendix 1 through 5.

2.1.1. Rate equations and device electrical parasitics

A typical quantum well semiconductor laser comprises a heterostructure active region sandwiched in between two p^+ and n^+ claddings of a diode's p-n junction. The active region is formed by an undoped separate confinement heterostructure (SCH) that serves as host to one or more quantum wells, which are surrounded by (quantum) barriers. In this thesis, a single quantum well (SQW) configuration described in detail on Section 3.1 is utilized to build the laser diodes.

Reproduced with permission of the copyright owner. Further reproduction prohibited without permission.

Figure 2.1 sketches the laser diode cross sectional area in which a top narrow metal stripe serves as the *p*-contact, whereas a metal deposition on the whole substrate creates the *n*-contact. In this analysis and the experiments in following chapters, we will deal with laser diodes with two top stripe widths: narrow and wide. Their characteristics parameters are shown in Table 2.1. The central region, located right below the *p*-contact is named active area. In this region is where all the device current is intended to flow and generate through stimulated emission the laser optical mode out of the plane. The two regions at the stripe sides are not contributing to the device operation and thereby are called passive regions. Notice that the distributed resistances and capacitances in the passive regions are inexistent in buried heterostructure lasers characterized in previous works [17, 22]. As they significantly alter the device operation, the parasitics effects of the passive area are considered in the next analysis.

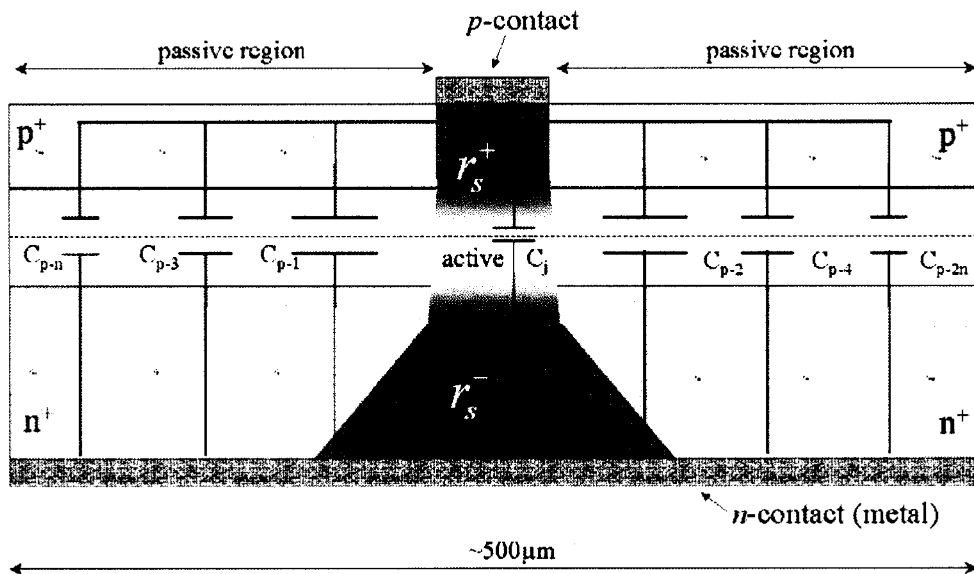

Figure 2.1.- Schematic of a stripe laser diode as those used in this work, which includes the parasitic capacitances and resistances in the stripe laser diodes. $C_{p-1}+C_{p-2}+...+C_{p-2n}$ and C_j are the capacitances parasitic capacitances in the passive and active area, respectively.

Reproduced with permission of the copyright owner. Further reproduction prohibited without permission.

Figure 2.1 shows how the passive region acts as the dielectric of a diode junction distributed capacitor formed in between the p^+ and n^+ claddings, $C_{p-1}...C_{p-2n}$. As a practical approach, this distributed parasitic capacitance in the passive region is lumped into an equivalent bias dependent capacitor $C_p=\Sigma C_{p-i}$ as shown in Figure 2.2. There is also a capacitance that arises in the diode junction active region, which is identified as C_j.

In a similar way, the p^+ and n^+ distributed cladding resistances r_{si}^+ and r_{si}^- are combined in the cladding resistor r_s.

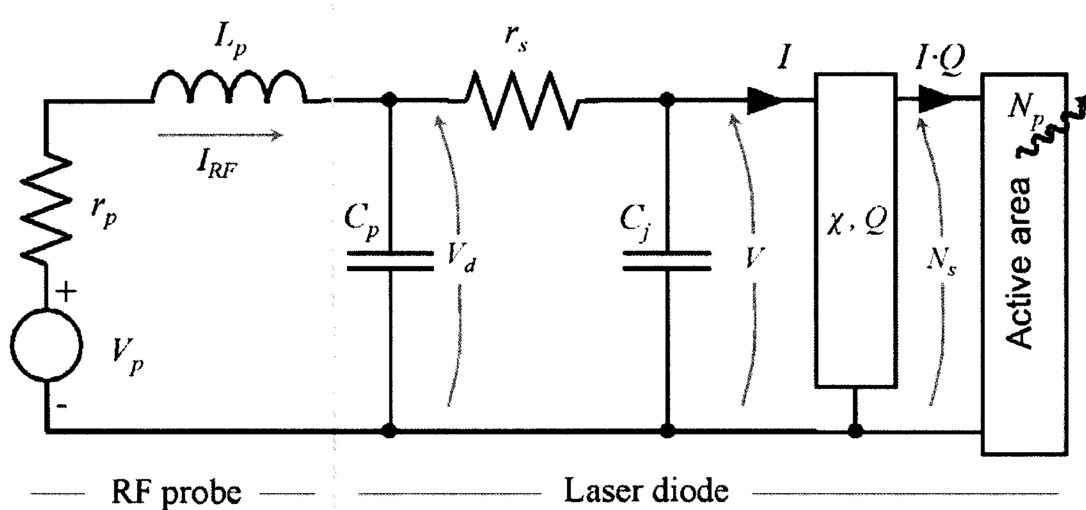

Figure 2.2.- Small signal circuit of the laser diode and electrical parasitics with its driving circuitry. The driving circuitry is represented by v_p-L_p-r_p . The parasitics C_j-C_p-r_s feed the intrinsic active area through the χ-Q network.

The laser driving circuitry is shown on the left side of Figure 2.2, captioned as *RF probe*. Although there are different types of driving circuitries that depend on the device stripe dimensions and bias current (subthreshold or above threshold), the *RF probe* can be accurately summarized as a Thévenin equivalent circuit depicted by v_p-L_p-r_p in Figure 2.2. The open circuit voltage is represented as v_p and the probe impedance given by

Reproduced with permission of the copyright owner. Further reproduction prohibited without permission.

$r_p+j2\pi f L_p$. Typical values of L_p and r_p are shown on Table 2.1.

Description	Name	Wide stripe	Narrow stripe
Stripe width	L_s	100μm	3.5μm
Laser length	L	500μm	500μm
QW width	L_w	60Å	60Å
SCH width	L_{sch}	3000Å	3000Å
Active area volume	V	$3\cdot10^{-8}$ cm^{-3}	10^{-11} cm^{-3}
QW-to-SCH Volume ratio	Γ_q	0.02	0.02
Spontaneous emission factor	β	$8.7\cdot10^{-5}$	$8.7\cdot10^{-5}$
Optical confinement factor	Γ	0.018	0.018
Optical compression factor	ε	$1.5\cdot10^{-17}$cm^3	$1.5\cdot10^{-17}$cm^3
Photon lifetime	τ_p	4.6ps	4.6ps
SCH lifetime	τ_s	5ns	5ns
Current injection efficiency	η	0.85-0.88	0.85-0.88
Parasitic inductance	L_p	~1nH	~1nH
Parasitic capacitance	C_p+C_j	~100pF	~40pF
Cladding resistance	r_s	~0.3Ω	1Ω

Table 2.1.- Typical parameters in wide and narrow stripe InGaAsN (InGaAs) lasers and driving circuitry.

C_j and C_p represent the capacitances of the diode junction at the active and passive areas, respectively, which are bias dependent. According to Figure 2.2, C_j and C_p are separated by r_s, which scales with the *p*-contact stripe dimension. As r_s is one order of magnitude smaller than the capacitive reactance of either C_j or C_p in ~1GHz frequency range, C_j and C_p can be lumped as a single capacitor. This is discussed more in detail later on Section 2.3.

As shown in Figure 2.2, the network C_j-C_p-r_s feeds the laser current I through the

Reproduced with permission of the copyright owner. Further reproduction prohibited without permission.

transfer box Q-χ. Equation (2.1) and (2.2) represent the parasitic circuit C_j-C_p-r_s and v_p-L_p-r_p from Kirchoff's method. V_d and I_{RF} are the laser device voltage and current, respectively.

The parameter Q is defined as $Q=\eta/qV$, where η is the current injection efficiency and q and V are the electron charge and the active area volume, respectively, defined in Table 2.1. The physical processes that rule on χ and other parameters of the circuit of Figure 2.2 and Figure 2.3 considerably change when switching from below to above threshold operation. For this reason, both below and above threshold analyses are separately described in Sections 2.2 and 2.4, respectively.

As described in Chapter 1, the laser active region is consisting of a bulk reservoir (SCH) and a two dimensional quantum well (QW) as shown in Figure 2.3. The typical rate equations that relate the QW and SCH reservoirs [24] are written in equations (2.3) through (2.5) in terms of the carrier densities N_w and N_{sch} and photon density N_p.

The bracketed term in equation (2.3) is equivalent to the input current in the parasitic-free model of Chapter 1, which is equivalent to $I \cdot Q$ shown on Figure 2.2.

In the rate equations for the active area, N_w and N_s are connected by the thermionic carrier capture and escape represented by $\tau_{cap\text{-}dc}$ and $\tau_{esc\text{-}dc}$, respectively, shown in Figure 2.2 and equations (2.3) and (2.4). In addition, it is shown that the carrier recombination processes, represented by the recombination rates $R_w=N_w/\tau_{w\text{-}dc}$ and $R_s=N_s/\tau_{s\text{-}dc}$, are taking place in the QW and SCH regions, respectively. The time constants $\tau_{w\text{-}dc}$ and $\tau_{s\text{-}dc}$ are the carrier lifetimes in the QW and SCH, respectively. $\tau_{w\text{-}dc}$ play an important role place in this study as then relate the recombination current and carrier density in the QW material, as is shown next in the small signal model.

Reproduced with permission of the copyright owner. Further reproduction prohibited without permission.

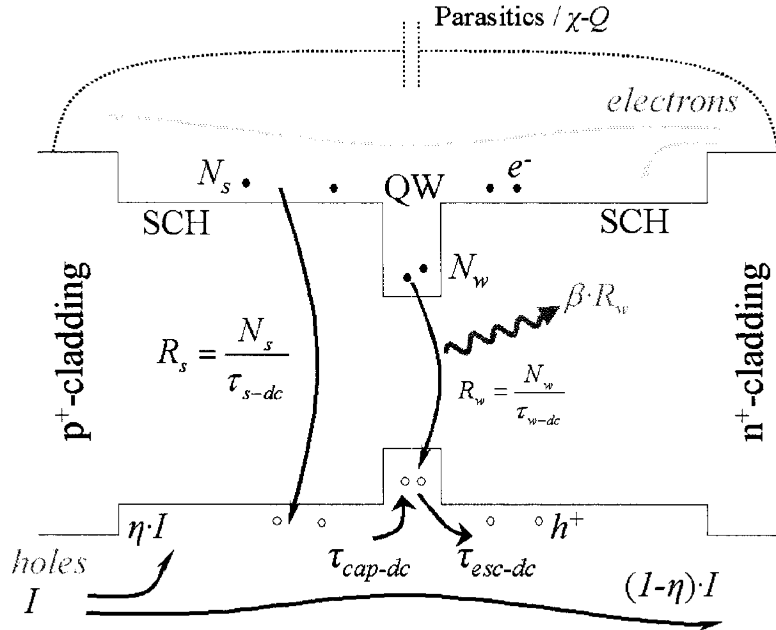

Figure 2.3.- Schematics of the carrier dynamics in the intrinsic laser diode. The injected current $\eta \cdot I$ is formed by the recombination paths R_w and R_s. $\tau_{cap\text{-}dc}$ and $\tau_{esc\text{-}dc}$ define the carrier dynamics in between QW and SCH.

Observe that in the term $(1\text{-}\eta)\cdot I$ in Figure 2.2 represents the heterobarrier leakage current, which adversely affect the laser performance [25].

Although the device input current in Figure 2.2 is denoted by I_{RF}, the device bias is represented for clarity by I, as they are identical under DC conditions. For simplicity, we represent η/qV of Equation 1.2 as Q in (2.3).

The spontaneous emission factor β relates R_w and N_p in (2.5), whereas the material peak gain g links N_w and N_p via the factor $\Gamma v_g g N_p$ in (2.4) and (2.5). Γ and v_g are the optical mode confinement and group velocity in the optical mode. Typical values for v_g, Γ and β in InGaAsN/GaAs are given in Table 2.1.

Reproduced with permission of the copyright owner. Further reproduction prohibited without permission.

$$L_p \dot{I}_{RF} = V_p - r_p I_{RF} - V_d \tag{2.1}$$

$$C_P \dot{V}_d = I_{RF} - \frac{V_d}{r_s} + \frac{V}{r_s} \tag{2.2}$$

$$\dot{N}_s = Q\left(\frac{V_d - V}{r_s} - C_j \dot{V}\right) - \frac{N_s}{\tau_{cap_dc}} - R_s + \Gamma_q \frac{N_w}{\tau_{esc-dc}} \tag{2.3}$$

$$\dot{N}_w = \frac{N_s}{\Gamma_q \tau_{cap_dc}} - R_w - \frac{N_w}{\tau_{esc_dc}} - v_g g \cdot N_p \tag{2.4}$$

$$\dot{N}_p = \frac{\Gamma\beta}{\tau_{qw-dc}} N_w - \frac{N_p}{\tau_p} + \Gamma v_g g N_p \tag{2.5}$$

2.1.2. Small signal model

In this dissertation, the study of the laser dynamics is conducted based on frequency response and impedance measurements below and above threshold. These types of measurements are performed by applying small signal perturbations to a variable chosen as the model input, such as V_p, and measuring the fluctuations on an output variable, such as I_{RF} or N_p. A typical perturbation is a sinusoidal modulation $e^{j\omega t}$, superimposed to the input variable V_P. A Dirac-delta perturbation is used for optical excitation described in Section 2.4.

In order to provide the tools for the analysis of these data, the expressions for impedance and frequency response must be obtained from the set of equations previously described. This is done next by moving a step further and rewriting the previous model in terms of small signal variables and their parameters.

Reproduced with permission of the copyright owner. Further reproduction prohibited without permission.

The small signal analysis is conducted by superimposing perturbations $i_{RF}(t)$, $v_d(t)$, $n_s(t)$, $n_w(t)$ and $n_p(t)$ to the steady state values I_{RF}, V_d, N_s, N_w and N_p, respectively. As the perturbations are small in comparison to the steady state variables, the dynamic behavior of the model is described by a first order Taylor expansion of the model given in terms of as $i_{RF}(t)+I_{RF}$, $v_d(t)+V_d$, $n_s(t)+N_s$, $n_w(t)+N_w$, $n_p(t)+N_p$, respectively.

To clarify the small signal analysis consider a function $f(x)$ where its first order Taylor expansion around x_0 is $f(x_0)+df/dx|_{x0}\cdot(x-x_0)$. $f(x_0)$ is the steady state or *DC* bias point, such as I, whereas $(x-x_0)$ is called the small signal perturbation, such as i.

The model of small signal variables can be separated from that of the steady state values and is called small signal model. As the laser's gain dynamics are different below and above threshold, the carrier-photon interaction in the quantum well, n_w-n_p, has to be represented by different expressions. Below threshold, the modal gain changes with the carrier density in the well as described in Chapter 1. Carrier recombination is the dominant processes in the quantum well and the reservoir N_w only sees a leak path to N_p through $R_w=N_w/\tau_{w\text{-}dc}$. Equations (2.6)-(2.8) and (2.9a) (2.10a) show the standard representation of the laser carrier-photon dynamics in the laser active region under small signal perturbations around a bias point below threshold. This is obtained from the first term in the Taylor expansion of (2.3) through (2.5), as in Refs. [24, 26] This model is entirely written in terms of the small signal variables and their *AC* parameters.

$$L_p \dot{i}_{RF} = v_p - r_p i_{RF} - v_d \tag{2.6}$$

$$C_P \dot{v}_d = i_{RF} - \frac{v_d}{r_s} + \frac{v}{r_s} \tag{2.7}$$

Reproduced with permission of the copyright owner. Further reproduction prohibited without permission.

$$\dot{n}_s = Q\left(\frac{v_d}{r_s} - \frac{v}{r_s} - C_j\dot{v}\right) - \frac{n_s}{\tau_{cap}} - \frac{n_s}{\tau_s} + \Gamma_q\frac{n_w}{\tau_{esc}} \tag{2.8}$$

$$\dot{n}_w = \frac{n_s}{\Gamma_q\tau_{cap}} - \frac{n_w}{\tau_w} - \frac{n_w}{\tau_{esc}} - \frac{n_p}{\Gamma\cdot\tau_p} \tag{2.9a}$$

$$\dot{n}_p = \beta\frac{n_w}{\tau_w} - \frac{n_p}{\tau_p} \tag{2.10a}$$

Expressions (2.6) and (2.7) are identical to (2.1) and (2.2) as the parameters involved are linear passive elements. Nevertheless, C_p and C_j are bias dependent, as discussed later on in Section 2.3. The large signal parameters that used the *–dc* subscript: $\tau_{s\text{-}dc}$, $\tau_{w\text{-}dc}$, $\tau_{cap\text{-}dc}$ and $\tau_{esc\text{-}dc}$ are now represented by their small signal or *AC* equivalents τ_s, τ_w, τ_{cap} and τ_{esc}, which are bias dependent. The rest of parameters q, Γ, Γ_q, τ_p are the same in both *DC* and *AC* models and are bias independent. η is considered bias independent, however the total injected carrier into the QW depends not only on the carrier recombination parameters but also on the balance of carrier densities between QW and SCH imposed by R_{dc}, as described in section 2.5.

The interest of the sub-threshold rate equation model is to obtain the quantum well carrier density N_w versus bias I relationship. This is done through integration of the differential carrier lifetime τ_w in (2.11) as it was described on equation (1.4). Section 2.2 is devoted to the differential carrier lifetime analysis.

$$\frac{1}{\tau_w} = \frac{dR_w}{dN_w} \tag{2.11}$$

Reproduced with permission of the copyright owner. Further reproduction prohibited without permission.

Chapter 1 already discussed the importance of the capture and escape processes in either the *DC* steady state model or the *AC* small signal regime. These time constants have not been measured for InGaAsN, but have been calculated. Based on calculations of the band offsets of InGaAsN/GaAs that show the hole confinement reduces when nitrogen is added, τ_{cap} and τ_{esc} were calculated for holes for InGaAsN/GaAs and InGaAs/GaAs [27]. These calculated values, obtained for steady state conditions, and are symbolized as τ_{cap-dc} and τ_{esc-dc}. τ_{esc-dc}, depend on the quantum well carrier density N_w and *T*. τ_{cap-dc} was calculated by Yeh et al. [28] and found to be constant and equal to τ_{cap-dc} ~5.3ps, in InGaAsN and InGaAs lasers. From steady state conditions, (equations 2.3 and 2.4) it is found that $\tau_{cap-dc} / \tau_{esc-dc}$ represent the balance provided between N_w and N_s provided $\tau_w >> \tau_{esc}$ [22]. In fact it is this ratio $R_{dc} = \tau_{cap-dc} / \tau_{esc-dc}$ that affects the laser response, more than the individual values of τ_{cap-dc} and τ_{esc-dc}. As it represents the balance in between N_s and N_w [22], the calculated ratio $R_{dc}=\tau_{cap-dc}/\tau_{esc-dc}$.

In the small signal analysis of Equations (2.6) through (2.10) the different time constants however, represent dynamic instead of static values. It is therefore appropriate to define a dynamic *AC* ratio, denoted by $R_{ac} = \tau_{cap} / \tau_{esc}$. Tsai et al. [29] developed an analysis based on the interaction between bulk and quantum confined states in QW lasers that allows to calculate the dynamic constants from the static ones that can be measured with other methods. For the InGaAsN and InGaAs laser structures studied in this work, $R_{ac} / R_{dc} \approx 1.5$.

Differently than the sub-threshold analysis, the small signal model above threshold is shown in equations (2.9b)-(2.10b) but still conserving (2.6)-(2.8).

Reproduced with permission of the copyright owner. Further reproduction prohibited without permission.

$$\dot{n}_w = \frac{n_s}{\Gamma_q \tau_{cap}} - \frac{n_w}{\tau_w} - \frac{n_w}{\tau_{esc}} - v_g a N_{P0} \cdot n_w + \frac{n_p}{\Gamma \cdot \tau_p} + v_g a_p N_{P0} \cdot n_p \tag{2.9b}$$

$$\dot{n}_p = \Gamma v_g a N_{P0} \cdot n_w + \Gamma v_g a N_{P0} \cdot n_p \tag{2.10b}$$

The strong photon-carrier interaction is manifested in (2.9b)-(2.10b) by the differential gain dg at threshold, expanded in partial derivatives of N_w and N_p in terms of the parameters a and a_p. The gain is nearly clamped to g_{th} at threshold as described in (1.4). The expression of the differential gain dg at threshold in (1.14) is shown again in equation (2.12).

$$dg = a \cdot N_w + a_p \cdot N_{P0} \tag{2.12}$$

As discussed in Chapter 1, the compression term in (1.15) and (1.16) is only valid for the above threshold analysis, for high photon densities.

Experimental evidence supports the introduction of a compression term that is only valid at high photon densities N_{P0}. In this case the differential gain parameter a does not represent a material's parameter any longer. Modifications to (2.12) to account for gain compression are shown in equations (1.16) and (1.17).

2.1.3. Q-χ coupling

As mentioned before, the key element that relates the electrical circuit with the intrinsic laser dynamics is the transfer factor χ, which is similar to an electrical

Reproduced with permission of the copyright owner. Further reproduction prohibited without permission.

transformer of ratio $\chi:1$. The parameter χ is frequency independent. Based on the model of Figure 2.2, the parameter χ can be visualized as the variation of carrier density in the SCH with laser diode voltage [30-32], $\chi=dN_s/dV$. In terms of small signal variables, the n_s-v relationship can be written as $\chi=n_s/v$ [13], where χ is obtained as dN_s/dV at each bias point [13]. In this work, χ is such that the ratio v/i calculated at $f\rightarrow 0$ (DC) from equations (2.8)-(2.10) equals the p-n junction differential resistance r_d, which is known from V-I (voltage versus current) diode measurements. An expression for χ given in (2.13), is obtained by inserting the solution of n_s/i by solving (2.8) - (2.10) for $t\rightarrow\infty$ and equating $\chi^{-1} \cdot n_s/i = r_d$. The parameter M, which accounts for a, a_p and N_{p0}, is obtained in Appendix 3 to keep (2.13) simple. Although there is no analytical expression for M, the numerical solution of the model (Appendix 3) yielded $M<10$ above threshold and zero below threshold in narrow-stripe lasers.

$$\chi = \frac{Q}{r_d}\left[\frac{1}{\tau_s} + \frac{\tau_{cap}/\tau_{esc}}{(\tau_w + \tau_{esc})(1+M)}\right]^{-1} \quad (2.13)$$

The temperature dependence of χ below and above threshold is found to be mainly linked to the variations of the dynamic resistance r_d. By utilizing the values given on Table 2.1, χ is found to be $<10^{18} cm^{-3}V^{1}$ for $I<I_{th}$ and $\sim 10^{19}$—$10^{20} cm^{-3}V^{1}$ for $I>I_{th}$. The latter was calculated for the narrow-stripe devices used above threshold.

Simulations shown later on, indicate that the values of χ produce a parasitics masking effect on the intrinsic dynamics processes at very low bias currents. Conversely, the values of χ obtained above threshold produce a decoupling between the active area and

Reproduced with permission of the copyright owner. Further reproduction prohibited without permission.

the electrical parasitics. Similar concepts and findings are discussed elsewhere in the study of electrical impedance in InGaAs/GaAs QW lasers at different biases [33].

2.1.4. Frequency domain

The last section developed the small signal model in the time domain. In order to provide solutions in the frequency domain and obtain expressions for the electrical impedance and frequency response of the laser diode, the model is rewritten in the frequency domain.

The frequency domain solutions of the model in (2.6) through (2.10) depend on whether the laser operating condition is below or above threshold. Below threshold the spontaneous emission is the main recombination mechanism in the quantum well. The current I imposes the laser bias point. Above threshold, the gain is nearly clamped to its threshold value g_{th} in a real laser diode [34], and the stimulated process rules over the laser operation. N_{P0}, proportional to the emitted power above threshold, dictates the bias point.

Next, the impedance and electrical frequency responses below threshold are obtained, followed by the calculation of above threshold frequency response by electrical and optical modulation.

2.2. Subthreshold frequency response

In the frequency domain, a new representation of (2.6) through (2.10) in the form of a 5x5 matrix after replacing v by n_s/χ is given in (2.14). By using Fourier analysis, the derivatives are replaced by $j\omega$, or imaginary unit times the angular frequency $\omega=2\pi f$.

Reproduced with permission of the copyright owner. Further reproduction prohibited without permission.

To obtain the frequency response and impedance of the laser diodes, equation (2.14) is solved by Cramer's rule [35]. Details on the algorithms are described on Appendix 2.

$$\begin{pmatrix} j\omega + r_p / L_p & 1/L_p & 0 & 0 & 0 \\ -1/C_p & j\omega + 1/(C_p r_s) & -1/(H_{21} C_p r_s) & 0 & 0 \\ 0 & \dfrac{-Q}{r_s(1+C_j Q/\chi)} & j\omega + \dfrac{Q/r_s + \chi(1/\tau_{cap} + 1/\tau_s)}{T + C_j Q} & \dfrac{-\Gamma_q}{\tau_{esc}(1+C_j Q/\chi)} & 0 \\ 0 & 0 & -1/(\Gamma_q \tau_{cap}) & j\omega + (1/\tau_w + 1/\tau_{esc}) & -1/\Gamma(1/\tau_p) \\ 0 & 0 & 0 & -\beta/\tau_w & j\omega + 1/\tau_p \end{pmatrix} \begin{bmatrix} i_{RF} \\ v_d \\ n_s \\ n_w \\ n_p \end{bmatrix} + \begin{bmatrix} v_p \\ 0 \\ 0 \\ 0 \\ 0 \end{bmatrix} \quad (2.14)$$

Solution of (2.14) allows to obtain the desired small signal Z_{ii} or S_{ij} parameters, which represent the laser impedance or frequency response, respectively, and which are described in detail in the following sections.

The small-signal electrical modulation frequency response of the laser diode is defined as the transfer function $H(f)=n_p(f)/v(f)$, at a given bias point. As shown in the experiments in Section 3.2, $v(f)$ is customarily the output voltage of a sinusoidal signal generator. The frequency response of the laser diode is obtained from the frequency domain expression of the rate equation model in (2.6) through (2.10) by Cramer's rule [35]. The terms that depend on stimulated power N_{p0} vanish in equation (2.14), below threshold.

Expression (2.15) shows the frequency response for electrical modulation, which contains five poles that are the eigenvalues of the model. Due to the model complexity, the values of the poles are found numerically at every bias point.

Reproduced with permission of the copyright owner. Further reproduction prohibited without permission.

$$H_{sp}(f) = \frac{dP_{sp}/dv_p\big|_{f\to 0}}{(1+j2\pi f\tau)} \cdot \frac{1}{(1+j2\pi f\tau_1)(1+j2\pi f\tau_2)(1+j2\pi f\tau_3)(1+j2\pi f\tau_p)} \qquad (2.15)$$

In (2.15) $dP_{sp}/dv_p\big|_{f\to 0}$ represents the incremental ratio of laser spontaneous emission to the modulation voltage. The poles τ_1 and τ_2 are mainly influenced by parasitics and external circuitry whereas τ_3 strongly depends on τ_{cap} and τ_{esc} and weakly on τ_w. The numerical solution (appendix 2) of equation (2.14) for InGaAsN lasers utilizing the parameters of Table 2.1 yields the reciprocal of τ_1, τ_2, τ_3 and τ_p >2GHz, >3GHz, >3GHz and ~50GHz in a bias range within a decade below I_{th}. Similar values are found in InGaAs lasers. For this calculation, the volume of the active area is scaled in length from that given by Table 2.1. At such high frequency these poles pose negligible effects on the measurements detailed in Section 3.2, performed in the 1GHz range.

The remaining dominant pole τ extracted from the analytical solution of equation (2.14) is the one that contains the information on the well differential lifetime τ_w. This is shown in the next example, where it is assumed τ_w=*500* and *1000ps*, r_d=*3Ω* and *1Ω,* for I=150mA and 7.5mA, respectively. In this case, constant values of τ_{cap}=5ps and τ_{esc}=12ps are assumed, whereas τ_s is shown on Table 2.1. Figure 2.4 shows the calculated frequency response traces, which are compared with similar ones calculated with the electrical parasitics removed (dotted) and with typical measured traces in InGaAsN BA lasers (dot symbols). The more dramatic effect of electrical parasitics at biases below 5-10 A/cm^2, is evidenced by the increase of τ.

In order to further study the effect of parasitics on τ, model simulations were run under different conditions, as shown next.

Reproduced with permission of the copyright owner. Further reproduction prohibited without permission.

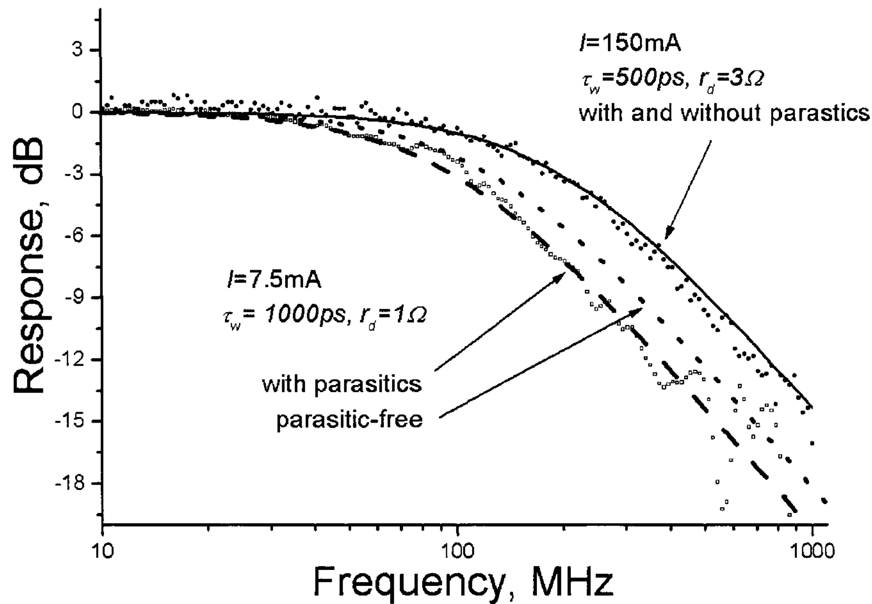

Figure 2.4.- Frequency response traces calculated at bias 7.5 and 150mA in InGaAsN broad area lasers with and without parasitics effects. The increase in τ caused by parasitics is more dramatic at low biases.

Figure 2.5 shows how the dominant pole τ changes its behavior with bias depending on the external circuitry and diode junction electrical parasitics. Three cases are observed: Ideal (C_p+C_j =0, r_p=1000Ω>> r_d), low bias parasitics dominated (C_p+C_j=100pF, r_p=1000Ω>>r_d) and low probe impedance (r_p=50Ω).

In the first case used as reference, τ represents τ_w of InGaAsN BA lasers. The second case, which was observed in Figure 2.4 in InGaAsN devices at 7.5mA, indicates a strong coupling between C_p-C_j and τ due to low values of χ. And finally, as an interesting example, the third case shows the circuitry effects of driving the laser directly with a 50Ω line (r_p~r_d) first reported by Olsahnsky et al. and misinterpreted as a reduction of τ_w at low biases [36]. To circumvent this effect, Pikal et al. implemented a new laser probe design in which r_p>>r_d [37].

Reproduced with permission of the copyright owner. Further reproduction prohibited without permission.

Figure 2.5 (d) shows a comparison of τ in BA laser with similar length RWG lasers. In both lasers, the differential carrier lifetime is the same, shown as the "*ideal*" behavior in (a). The simulation in RWG lasers comprised the parameters of Table 2.1, where r_d was scaled down with the stripe width. However, $C_p + C_j$ shown in Figure 2.1, was assumed 50pF to account for the size of the passive areas. Notice how the time constant τ in RWG lasers is affected by parasitics in all of the current range due to an extra contribution of r_d, making thereby the frequency response in RWG laser unreliable for the lifetime analysis. In the previous examples the model analysis assumed R_{ac}=0.05. This corresponds to a condition in which the effective capture is very efficient. In agreement with a much simpler analysis [38], τ is equivalent to τ_w when parasitics are not present and τ_{cap}/τ_{esc}=0 that is, an ideal parasitic-free laser diode where all the carriers recombine into the quantum well. In the InGaAsN laser however, a more realistic value of R_{ac} is 0.5-1.0.

In order to analyze the impact of R_{ac}, traces of τ versus I are simulated using (2.14) and R_{ac}=1 and R_{ac}=0, for which parasitics were turned off for simplicity. These traces shown in Figure 2.6 correspond to the same τ_w of the simulation in Figure 2.5(a). As can be seen from Figure 2.6 τ_w and the carrier density are overestimated when R_{ac} is underestimated.

This also shows that the analysis of τ to extract A, B and C recombination parameters is very sensitive to R_{ac}, as it impacts more dramatically the higher order B_w and C_w terms. In turn, the well carrier density N_w is overestimated, as addressed later on in the effective lifetime analysis section.

Reproduced with permission of the copyright owner. Further reproduction prohibited without permission.

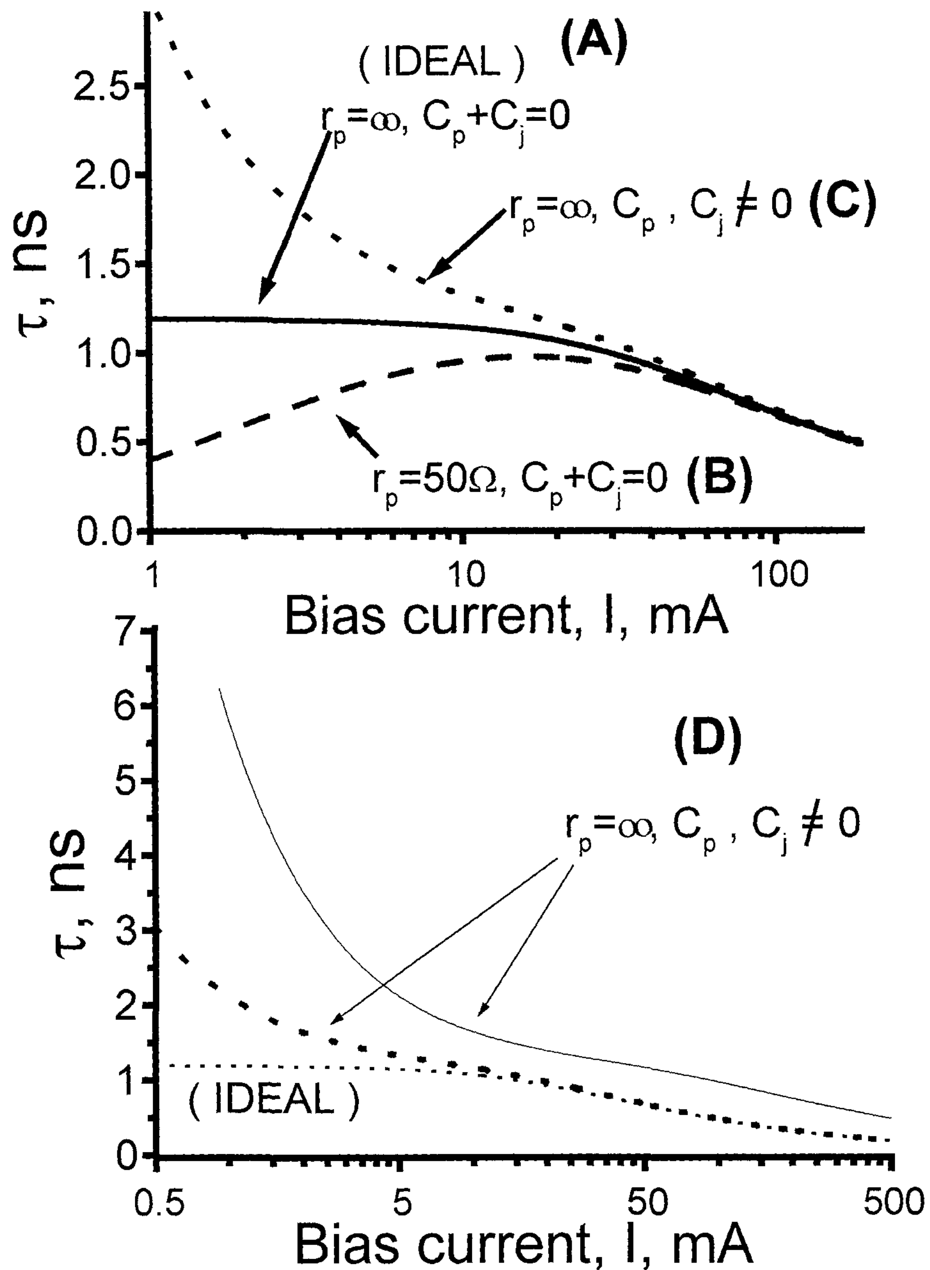

Figure 2.5.- Model simulation of the below threshold dominant pole τ versus I. For wide-stripe lasers $\tau(I)$ is calculated for different parasitic conditions: (a) Ideal -without parasitics (C_p+C_j =0, r_p>> r_d); (b) for C_p+C_j =0, r_p=50Ω and (c) for C_p+C_j=100pF, r_p>>r_d . $\tau_w(I)$ corresponds to the solid trace. Case (d) compares τ in narrow and wide-stripe lasers, where r_d ~50KΩ-50Ω (1-500 mA) respectively and $r_p \rightarrow \infty$.

Reproduced with permission of the copyright owner. Further reproduction prohibited without permission.

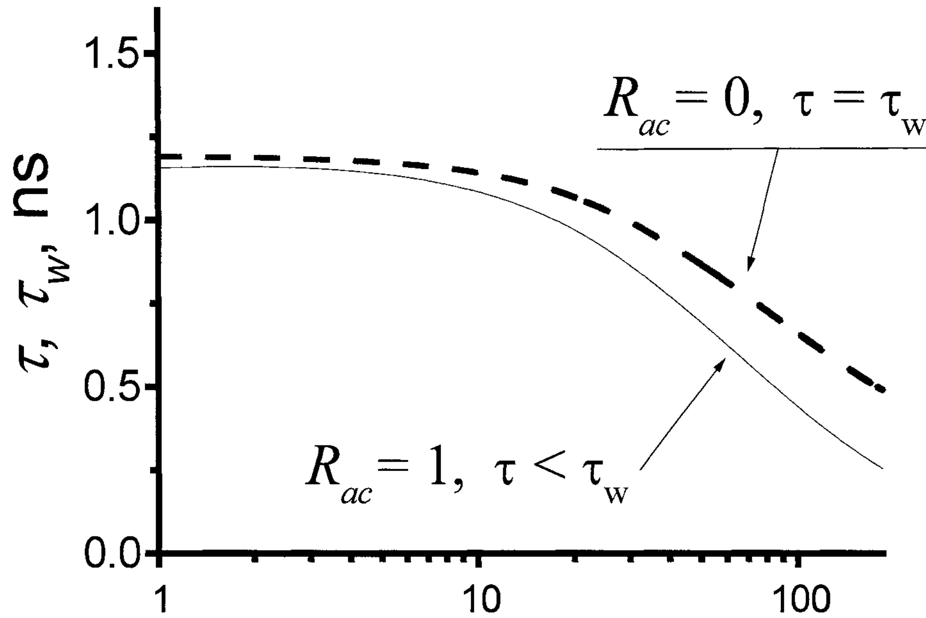

Figure 2.6.- Model simulation of τ versus I in InGaAsN wide-stripe lasers described by Table I for R_{ac}=0 (dashed) and R_{ac}=1 (solid). Parasitics are turned off.

As important as the variations of R_{ac} to τ_w is the accurate modeling of the parasitic capacitance C_j - C_p. Determination of device parameters such as $C_j + C_p$ can be independently obtained from the impedance analysis shown next.

2.3. Small signal laser diode impedance

As mentioned in Section 2.2, the solution of (2.14) can also retrieve an expression for the small-signal impedance response $Z(f)$. The impedance of a device is typically extracted from the bilinear transformation of the S_{11} parameter [39], which is measured at the laser contacts. A fit of the experimental impedance with the solution of this model in turn allows the extraction of the parasitic capacitances in the laser devices. These values

Reproduced with permission of the copyright owner. Further reproduction prohibited without permission.

are then fed in to the model to calculate the frequency response.

In reference to Figure 2.2, the laser impedance can be obtained from the transfer function $v_D(f)/i_{RF}(f)$ when disconnecting the RF probe r_p-L_p-v_p. The calculation of impedance reduces to that of a 3×3 matrix, thus yielding (2.14) three eigenvalues shown as the three poles in expression (2.16). In addition, a zero of value $(2\pi\tau_z)^{-1}$ is obtained, similarly to that predicted by Esquivias et al. [33] in InGaAs multiple quantum well lasers. The expression for $Z(f)=v_d(f)/i_{RF}(f)$ obtained from (2.14) is shown in (2.16).

$$Z_e(f) = r_d \frac{1 + j2\pi f\tau_Z}{(1 + j2\pi f\tau_p)\cdot(1 + j2\pi f\tau_A)\cdot(1 + j2\pi f\tau_B)} \tag{2.16}$$

In the model simulation, the diode's dynamic resistance r_d is obtained from I-V measurements, with typical value $r_d \sim 60\text{mV} / I$ in 500μm length InGaAs wide-stripe lasers [23]. The values of C_p and C_j are bias dependent as they arise from the *p-n* junction at the passive and active areas, respectively. The total parasitic capacitance $C_p + C_j$ versus bias I is known and shown in Figure 2.7 (circles) for typical 500μm length InGaAs BA lasers [40]. Simulations indicated that the model is sensitive to $C_p + C_j$ but instead insensitive to how it is distributed between C_p and C_j. This is explained by the relative small cladding resistance r_s, which makes them behave as if they were a unique capacitor $C_p + C_j$. The trace in Figure 2.7 represents the forward bias junction capacitance that corresponds to the forward bias model described by Liou et al. for a *p-I-n* diode [41].

Notice, in Figure 2.7, the asymptotic capacitance value of C_p+C_j C_I=100pF (refer formula in Figure 2.7) is the same as obtained from impedance measurements when reverse-biasing the diode to ~1-2V [23]. This capacitance corresponds to that of a

Reproduced with permission of the copyright owner. Further reproduction prohibited without permission.

capacitor formed by the 3000Å passive area (ε_{GaAs}~12·ε_0) and plate dimensions 500μm x 500μm, where L_s=100μm.

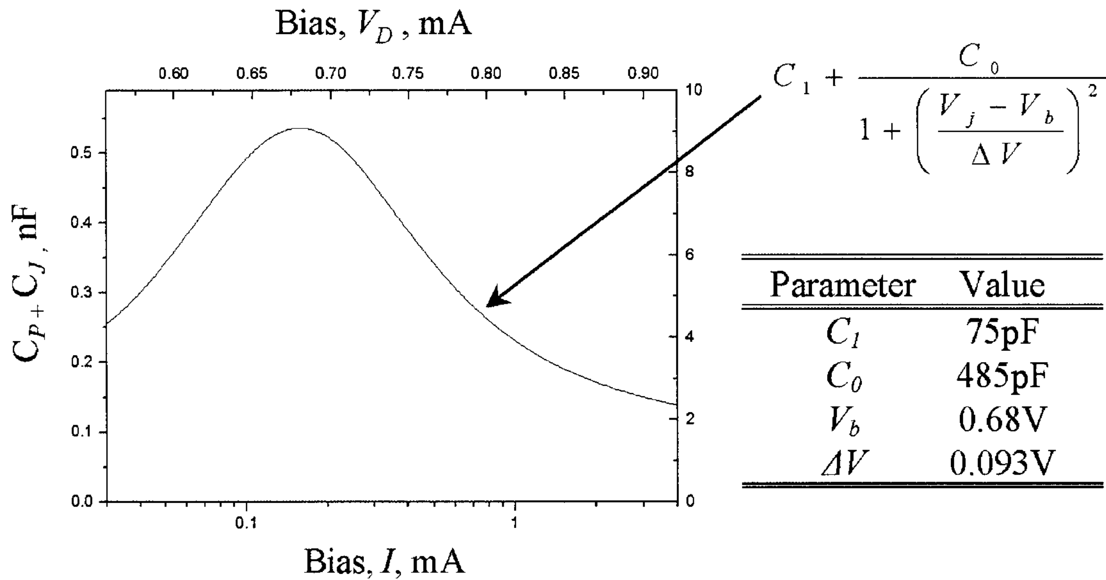

Parameter	Value
C_1	75pF
C_0	485pF
V_b	0.68V
ΔV	0.093V

Figure 2.7.- Typical behavior C_j +C_p versus bias current and voltage in wide-stripe InGaAs lasers at very low bias currents and T=20°C. The solid lines represent the fit.

A simulation of $Z(f)$ based on the model in (2.14) and using the parameters of Table 2.1 for InGaAsN BA lasers is shown on Figure 2.8. It is found that the effects of τ_B and τ_p are significant above 3GHz and 50GHz, respectively, whereas the effect of τ_Z is found to be above 1GHz as evidenced by the decrease in slope of $|Z|$-f above 1GHz. Since the impedance measurements are carried out in a frequency range of 1GHz (Section 3.2.1), the pole $(2\pi\tau_A)^{-1}$ is dominant, as shown in Figure 2.8. The experimental impedance analysis of poles and zero to obtain τ_{cap} / τ_{esc} parameters was performed by Esquivias et al. in InGaAs QW lasers [33].

Reproduced with permission of the copyright owner. Further reproduction prohibited without permission.

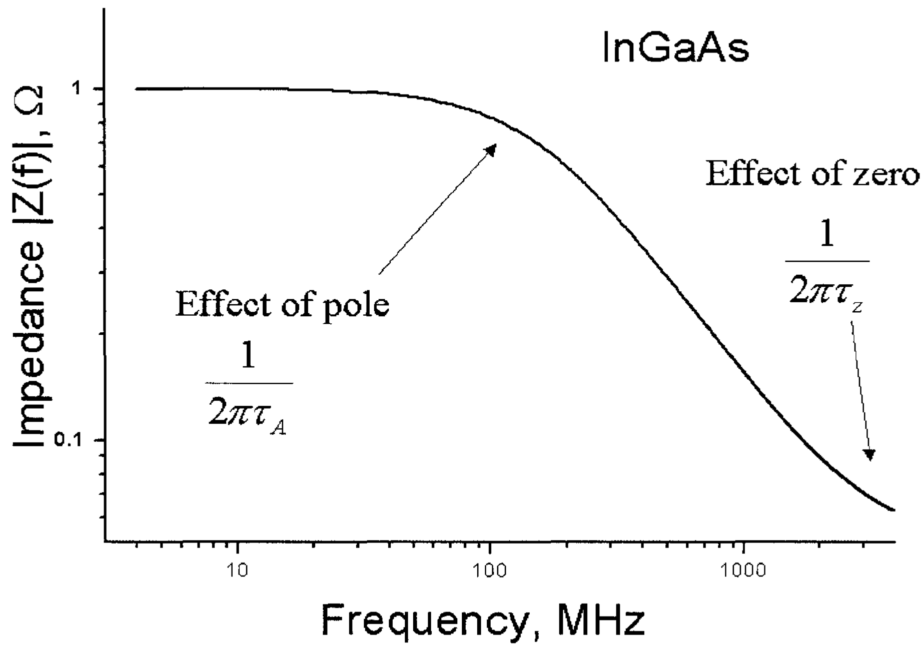

Figure 2.8.- Calculated impedance $Z(f)$ in InGaAsN wide-stripe laser with parameters of Table I at I=100mA dominated by pole $(2\pi\tau_A)^{-1}$.

Figure 2.9 shows the calculated traces of $\tau_A(I)$ compared with those measured in real devices, shown by the squares. Similarly to the traces of Figure 2.5, the increase in τ_A at low biases is due to the effect of parasitic values C_p-C_j, r_d and r_s. For comparison, we performed a parasitic-free simulation that retrieved a trace identified in Figure 2.9 as "τ_A ideal", which saturates at low currents in a similar manner as in the parasitic-free frequency response time constant τ in Figure 2.5 (a).

Based on the model it is found from the simulations that when $I \rightarrow 0$ the values of τ_A are fully representative of the electrical parasitics as shown by Figure 2.2. On the other hand, τ_A is more influenced by intrinsic device parameters and shows a behavior similar to τ in Figure 2.5 (a) at biases above 2-4mA, in the InGaAsN and InGaAs lasers investigated.

Reproduced with permission of the copyright owner. Further reproduction prohibited without permission.

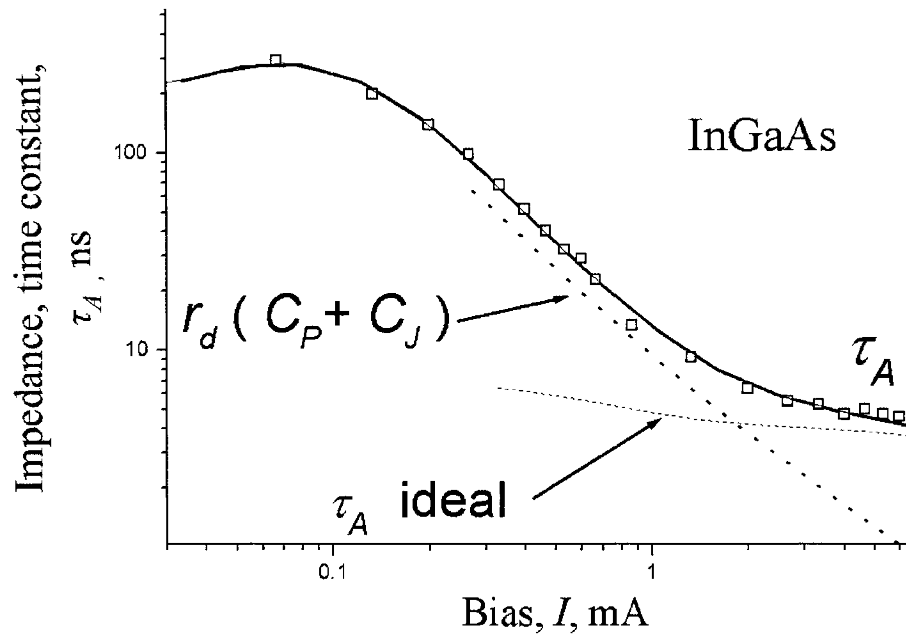

Figure 2.9.- Calculated τ_A versus I in InGaAsN wide-stripe laser with parameters of Table I. Notice the increase in τ_A at low biases due to the effect of the device parasitics, becoming similar to the asymptotic expression (2.17).

The parasitic circuit formed by $C_p + C_j$ and r_d behaves as a simple *R-C* circuit of time constant given in (2.17). This was experimentally corroborated in our previous work in InGaAsN lasers below J=10A/cm^2 [40], which is equivalent to I=5mA in 500µm x 100µm wide-stripe devices.

$$\tau_A\big|_{I\to 0} = r_d\,(c_p + c_j) \tag{2.17}$$

Further, based on the solution of the full model, we find the approximation for τ in the same laser devices is,

Reproduced with permission of the copyright owner. Further reproduction prohibited without permission.

$$\tau = \tau_{eff} + r_d (c_p + c_j) \tag{2.18}$$

where τ_{eff} is the effective differential lifetime. τ_{eff} is described later on in the effective lifetime analysis section, represents the combined differential lifetime of N_s and N_w.

These simulations anticipate that the parasitics effects are less pronounced at currents higher than ~4-5mA where $C_p + C_j$ adopts an asymptotic value. This condition ensures a more accurate analysis of the frequency response measurements as done in Section 4.2.1.

2.4. Analysis above threshold

Above threshold, the laser stimulated emission involves strong interactions between N_w and N_p that are accounted for by equations (2.9b) and (2.10b). As described on Section 2.1.3, the χ parameter in (2.13) considerably increases above threshold, implying a very weak coupling (negligible cross-talk) between the active area and the parasitics shown in Figure 2.2. This is observed in more detail in terms of the poles in the frequency response expression.

The frequency domain representation of the model above threshold is shown in (2.19). These equations are based on equations (2.6) through (2.8) and (2.9b)-(2.10b).

$$\begin{pmatrix} j\omega + r_p/L_p & 1/L_p & 0 & 0 & 0 \\ -1/C_p & j\omega + 1/(C_p r_s) & -1/(H_{21} C_p r_s) & 0 & 0 \\ 0 & \dfrac{-Q}{r_s(1 + C_j Q/\chi)} & j\omega + \dfrac{Q/r_s + \chi(1/\tau_{cap} + 1/\tau_s)}{\chi + C_j Q} & \dfrac{-\Gamma_q}{\tau_{esc}(1 + C_j Q/\chi)} & 0 \\ 0 & 0 & -1/(\Gamma_q \tau_{cap}) & j\omega + (1/\tau_w + 1/\tau_{esc} + P) & -1/\Gamma(1/\tau_p + A_p P) \\ 0 & 0 & 0 & -\Gamma P & j\omega - A_p P \end{pmatrix} \cdot \begin{bmatrix} i_{RF} \\ v_d \\ n_s \\ n_w \\ n_p \end{bmatrix} + \begin{bmatrix} v_p \\ 0 \\ 0 \\ 0 \\ 0 \end{bmatrix} \tag{2.19}$$

Reproduced with permission of the copyright owner. Further reproduction prohibited without permission.

For simplicity, equation (2.19) has been rewritten in terms of P and A_p given in (2.20) and (2.21), respectively, where P is proportional to the single facet emitted power P_0 and A_p is proportional to ε [24]. The parameters $h\nu$ and α_m are the laser emission photon energy and the mirror losses, respectively.

$$P = \frac{2\Gamma}{v_g \alpha_m h\nu_s} N_{P0} = \frac{2a\Gamma}{\alpha_m h\nu V} P_0 \tag{2.20}$$

$$A_p = \Gamma \frac{a_p}{a} \equiv \Gamma \frac{\varepsilon g_{th}}{dg / dN_w \big|_{th}} \tag{2.21}$$

Similarly to Section 2.2, the solution of (2.19) by Cramer's rule retrieves the five poles of the transfer function $H_{st}(f)$ above threshold given by (2.22).

$$H_{st}(f) = \frac{1}{(1 + j2\pi f\tau_1)(1 + j2\pi f\tau_2)} \cdot \frac{dP_0 / dv_p \big|_{f \to 0}}{(1 + j2\pi f\tau_c)(f_r^2 - f^2 + jf\gamma)} \tag{2.22}$$

In (2.22) the two principal poles, $f=\alpha+j\beta$ and $f=\alpha-j\beta$, arise from the strong carrier-photon interaction by the stimulated process in the laser active area and are customarily expressed by the relaxation frequency $f_r=\sqrt{\alpha^2 + \beta^2}$ and damping $\gamma=2\alpha$. In the parasitic-free case, the third pole $1/2\pi\tau_c$ represents the combined effects of the quantum well capture and carrier diffusion along the SCH [8]. However, parasitics are coupled to the active area through the Q-χ box in Figure 2.2. In fact, our model shows that the values of f_r, γ and τ_c are influenced by χ, L_p, C_p, C_j, r_s and r_p.

For the values of χ mentioned in Section 2.1.3 and obtained above threshold from (2.13), for narrow stripe lasers, the coupling between the active area and parasitics is

Reproduced with permission of the copyright owner. Further reproduction prohibited without permission.

weak. Therefore, the two poles $1/2\pi\tau_1$ and $1/2\pi\tau_2$ in this case arise solely from the external circuitry and parasitics.

The electrical modulation response calculated by the model with the laser parameters of Table 2.1 is shown on Figure 2.10, at P_0=2.2 and 5.6mW. Notice that the damped resonant behavior is masked by the response of a parasitic pole $(2\pi\tau_2)^{-1}$. The transport pole $(2\pi\tau_c)^{-1}$ is found to be ~30GHz, thereby representing a negligible effect to the measured traces.

The poles $1/2\pi\tau_1$ and $1/2\pi\tau_2$ typically observed in the electrical modulation traces fall in the 1-10GHz range. It is this characteristic that has led to the erroneous interpretation of them as the transport pole $1/2\pi\tau_c$ [42, 43].

The simulations shown are not affected by the detection noise, as it occurs in real measurements. When thermal noise is added, the laser frequency response gets buried into the noise floor making it impossible to fit with (2.22).

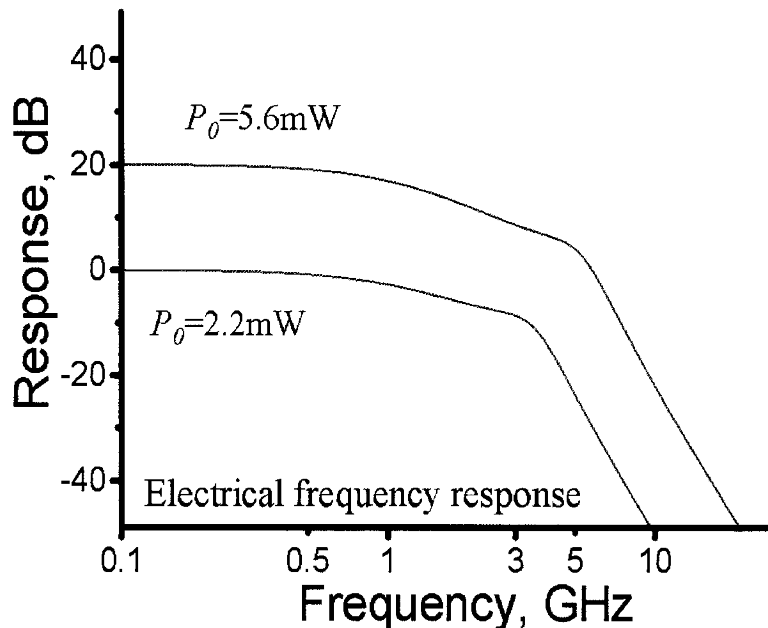

Figure 2.10.- Electrical modulation frequency response above threshold in narrow-stripe SQW InGaAs lasers, at emitted powers P_0=2.2mW and 5.6mW.

Reproduced with permission of the copyright owner. Further reproduction prohibited without permission.

2.4.1. Optical modulation response

It is possible to circumvent most, although not all of the effects of parasitics in the above threshold frequency response of a laser diode via the use of tunable optical source that modulates carriers in the laser's QW or SCH [17-21]. In the model (2.19), this situation corresponds to one in which the input is directly coupled to $\dot{n}_s$ as an optical perturbation $\delta(\omega)$, thus setting v_p=0. This is schematically shown in Figure 2.11 (a).

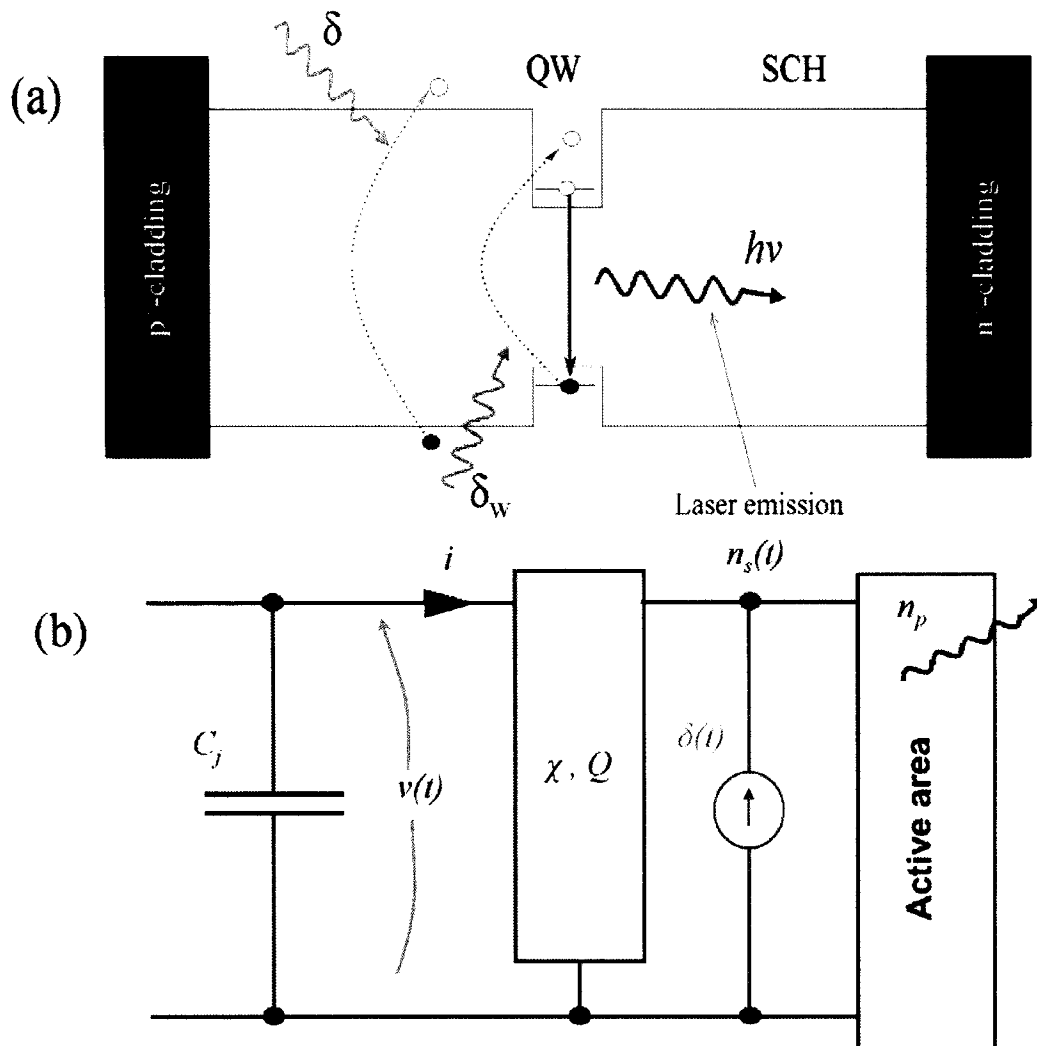

Figure 2.11.- (a) Schematic of the SCH (δ) and QW (δ_w) optical injection (b) Equivalent circuit, where δ(t) is depicted by a current source.

Reproduced with permission of the copyright owner. Further reproduction prohibited without permission.

This situation is modeled by adding the excitation source to the circuit of Figure 2.2, as shown on Figure 2.11 (b).

We focus the analysis to the modulation conditions provided by a short optical pulse from a tunable femtosecond laser as described in our previous work [17].

The time and frequency representations of the pulse excitation signal are shown in Figure 2.12 (a) and (b), respectively. The tunable pulses feature 81MHz repetition rate and FWHM~0.15ps. Their 81MHz-spaced frequency comb spectrum extends beyond 2000GHz [17].

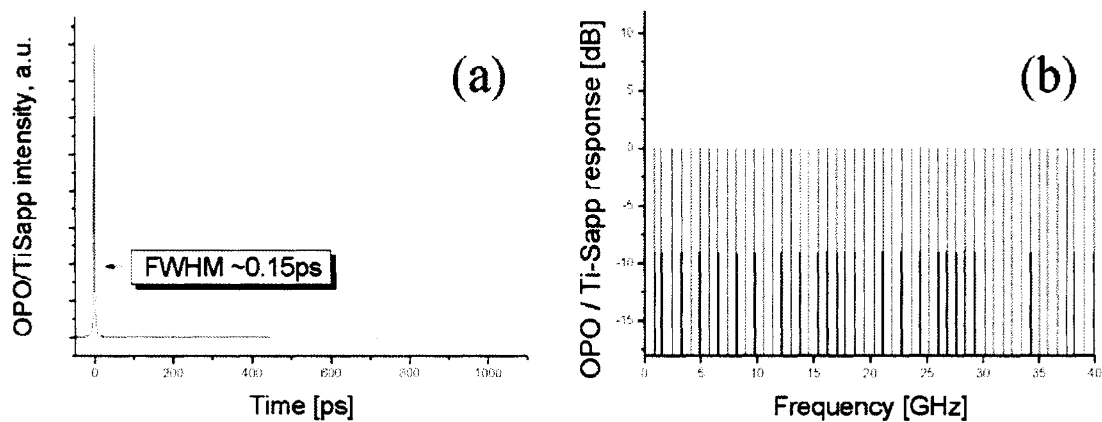

Figure 2.12.- Sub-picosecond pulse excitation from either optical parametric oscillator or Ti-Sapphire laser: (a) Time domain, (b) Frequency domain.

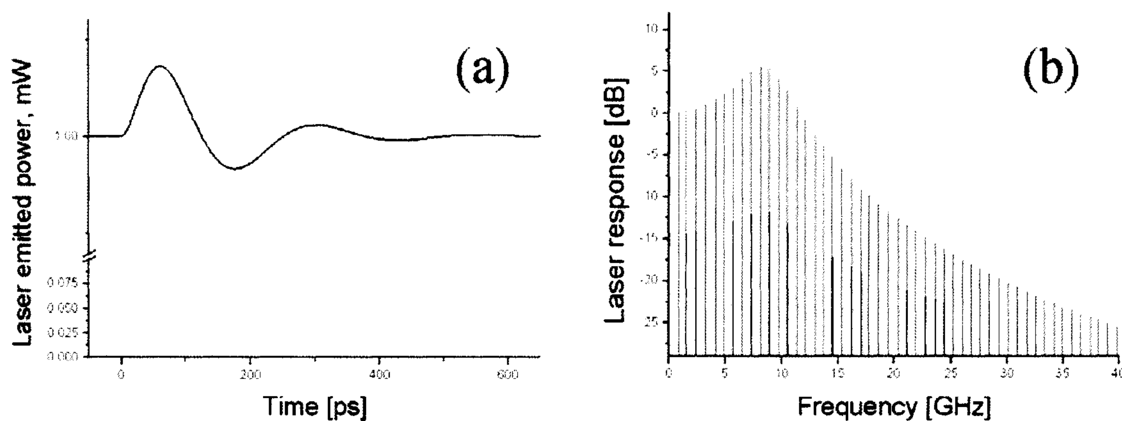

Figure 2.13.- Frequency response spectra: (a) Input Gaussian pulse, (b) Laser output response.

Reproduced with permission of the copyright owner. Further reproduction prohibited without permission.

Figure 2.13 (a) shows the typical time response of the laser above threshold, characterized by a damped resonant behavior. Subplot (b) shows the Fourier spectrum of (a), whose envelope, is shaped by the laser frequency response, calculated next.

For optical excitation the frequency response obtained by solving (2.19) is shown in (2.23), where the factor H_{zp} includes two new zeroes τ_{z1} and τ_{z2} and the two poles τ_1 and τ_2 as in (2.22) (Appendix 5). Interestingly, it is found that for the typical parameters of InGaAs and InGaAsN lasers, τ_{z1} and τ_{z2} nearly cancel out with τ_1 and τ_2, thereby yielding $H_{zp}\rightarrow 1$ and a response that only depends on f_r, γ and τ_c.

$$H_{opt-sch}(f) = H_{zp} \cdot \frac{dP_0 / dS_o\big|_{f\to 0}}{(1 + j2\pi f\tau_c)(f_r^2 - f^2 + jf\gamma)} \tag{2.23}$$

When the excitation wavelength is selected to produce photoabsorption in the quantum well, shown as δ_w in Figure 2.11 (a), n_w is modified and the solution to the model like in (2.23) simplifies as given by (2.24).

$$H_{opt-w}(f) = H_{zp} \cdot \frac{dP_0 / dS_o\big|_{f\to 0}}{(f_r^2 - f^2 + jf\gamma)} \tag{2.24}$$

The simulated optical frequency responses obtained using (2.23) and (2.24) are plotted on Figure 2.14. They are also compared with FR calculated from electrical modulation. Notice that there is a difference between the traces generated by (2.23) and (2.24) given by a single pole, whose 3dB value is $f_c = (2\pi\tau_c)^{-1}$. Depending on the value of χ above threshold, τ_c could be influenced by the device parasitics. In InGaAsN and InGaAs lasers, τ_c weakly depends on parasitics and its pole f_c is ~30GHz. This value was corroborated

Reproduced with permission of the copyright owner. Further reproduction prohibited without permission.

experimentally in 1.3μm InGaAsN lasers by the analysis of their optical modulation frequency response measurements [23].

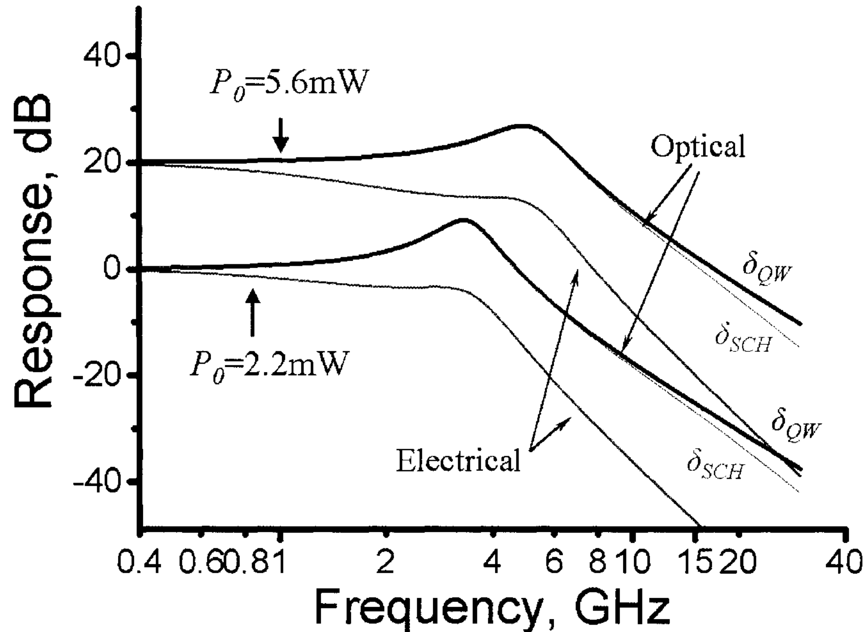

Figure 2.14.- Calculated frequency responses of InGaAsN and InGaAs SQW narrow-stripe lasers, for P_0=2.2mW and P_0=5.6mW, obtained with electrical (dotted lines) and optical (solid lines) modulation.

Similarly, the parameters γ and f_r in (2.23) and (2.24) which are the same as in the electrical modulation response in (2.22) can be affected by parasitics. This is shown in Figure 2.15 in which the QW-optical modulation frequency response is calculated (dotted lines) and compared with similar parasitic-free case (solid lines) in where $r_p=\infty$ and $C_j=C_p=0$. For optical excitation, the parasitic-free case corresponds to a situation in which the active area is completely decoupled from the diode circuit by $\chi\rightarrow\infty$. The parasitic effects in f_r are unnoticeable while they increase γ.

Reproduced with permission of the copyright owner. Further reproduction prohibited without permission.

The effect of parasitics is highlighted in Figure 2.16 where γ is plotted versus P_0 for InGaAs lasers. The increase of γ is of several times at threshold, and decays asymptotically to ~15% at higher biases. The same behavior of γ versus P_0 is observed in InGaAs lasers by Sharfin et al. [44].

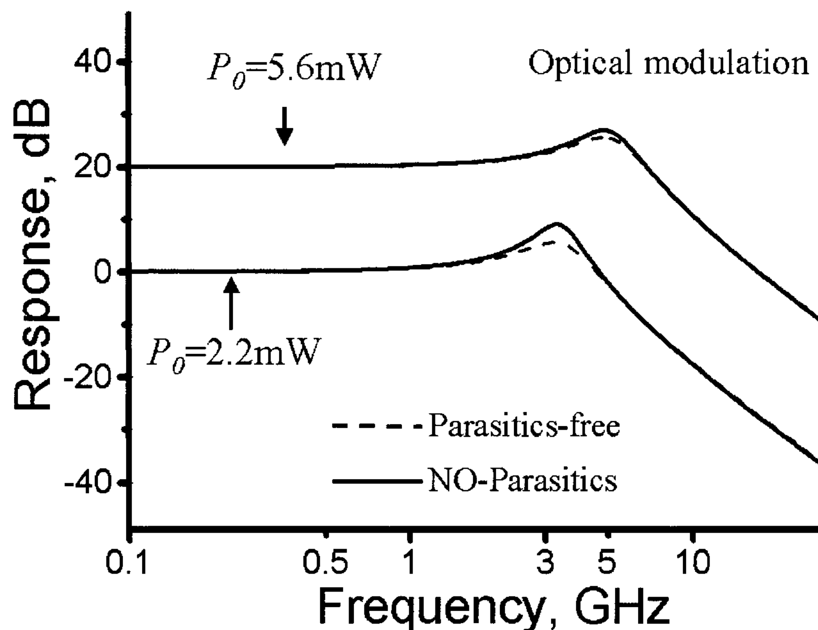

Figure 2.15.- Calculated frequency responses of InGaAs SQW narrow-stripe lasers above threshold for QW optical modulation at P_0=2.2mW and P_0=5.6mW. The parasitics significantly increase γ but not f_r, as shown by the parasitic-free lines (dashed).

These findings provide the analysis tools for extracting γ and the K-factor from the experiments as described in Chapter 5.

The simulation also allowed to obtain the relationship of f_r^2 versus P_0, which is parasitic-insensitive and thus coincides with the solution of the standard 3-rate equation analysis [24]. The asymptotic expression of f_r^2 - P_0 in the limit when τ_{cap}, τ_{esc} << $1/f_r$ and assuming the coupling factor χ=10^{19}—$10^{20}cm^{-3}V^{1}$ as given on Section 2.1.3 for bias above threshold is shown in (2.25). The parameter a_{eff} is the effective differential gain

Reproduced with permission of the copyright owner. Further reproduction prohibited without permission.

and comprises the mixed effects of the threshold differential gain dg/dN_w, ε and $R_{ac}=\tau_{cap}/\tau_{esc}$. a_{eff} is obtained by solving the model in (2.19) and relating the slopes of f_r^2–P_0 in the limit $\tau_{cap}\rightarrow 0$.

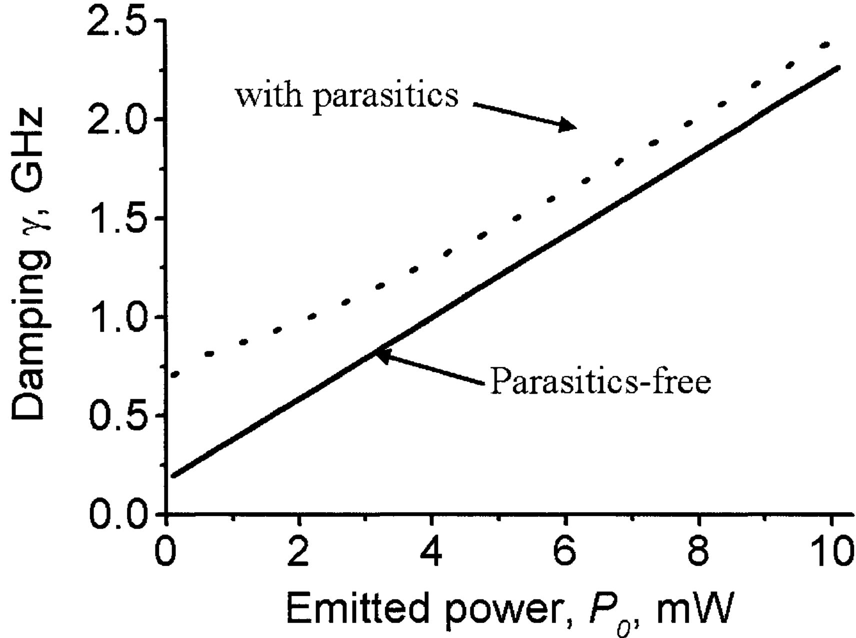

Figure 2.16.- Calculated γ versus P_0 in InGaAs SQW narrow- stripe lasers above threshold for QW optical modulation. γ increases more notoriously due to parasitics at low biases.

$$f_r^2 = \frac{v_g}{4\pi^2\tau_p} a_{eff} \cdot N_{P0} \tag{2.25}$$

The bias is represented by the quiescent photon density N_{P0} which is given by P_0 as:

$$N_{P0} = \frac{2\Gamma}{v_g V \alpha_m h\nu} P_0 \tag{2.26}$$

Equation (2.27) shows that the effect of R_{ac} and $\varepsilon \cdot N_{P0}$ are inseparable unless τ_{cap}/τ_{esc} is known [17] or when $N_{P0} << 1/\varepsilon$ (low emitted powers).

Reproduced with permission of the copyright owner. Further reproduction prohibited without permission.

$$a_{eff} = \frac{dg / dN_w}{(1+R_{ac})(1+\varepsilon N_{P0})} \tag{2.27}$$

The damping obtained from the model is shown in (2.28) by replacing A_p by the model parameters.

$$\gamma = \left\{ \frac{v_g\, a_{eff}}{2\pi} \left[1 + \Gamma \frac{g_{th}\varepsilon(1+\varepsilon N_{P0})}{a_{eff}} \right] N_{PO} + \frac{1/2\pi\tau_w}{1+R_{ac}} \right\} (1+U) \tag{2.28}$$

Equation (2.28) is equivalent to the parasitic-free damping expression in (1.23) with the addition of the factor *(1+U)*. *U*, which is obtained in Appendix 4 by numerical simulations, strongly depends on the parasitics $C_p + C_j$, r_d, η and the coupling factor χ, and weakly on R_{ac}, N_{P0}, dg/dN_w, ε and τ_w. As $C_p + C_j$ and η are constant above threshold, U is related to r_d, which depends on bias current as $\sim 1/I$. In this case, smaller values of U are obtained in laser diodes that operate at higher currents, which in turn make them less sensitive to parasitics. In a parasitics free laser in which $C_p + C_j = 0$, the value of U vanishes and (2.28) and (1.25) are equivalent. The cases η=0 and $\chi \rightarrow \infty$ are equivalent and would lead to U=0 or parasitic free γ by completely decoupling the active area from the external laser parasitics. However, the latter are impossible to realize in a real laser diode.

The numerically calculated values of U were 2.5 at P_0=0 and decayed asymptotically to 0.15 at high powers, as represented by the relationship between the traces in Figure 2.16. A similar effect of parasitics on γ was observed experimentally on InGaAs QW lasers [44].

Reproduced with permission of the copyright owner. Further reproduction prohibited without permission.

In similar way, parasitics affect the values of the *K*-factor. Equation (2.29) shows *K* that dictates the slope γ - f_r^2, which is now influenced by parasitics (1+*U*).

$$K \approx 4\pi^2\tau_p\left[1+\frac{\Gamma a_p}{a}(1+R_{ac})\right](1+U) = 4\pi^2\tau_p\left[1+\Gamma\frac{g_{th}\varepsilon(1+\varepsilon N_{P0})}{dg/dN_w(1+R_{ac})^{-1}}\right](1+U) \qquad (2.29)$$

As the expression of damping γ and K-factor are utilized to obtain the compression factor ε from the fit of experimental frequency response, it is important to have an accurate knowledge of $C_p + C_j$, r_d, η_{inj} and χ. The solutions of the model as well as equations (2.25) and (2.27) are the tools utilized for the data analysis in Chapter 5.

2.5. Temperature analysis

The description of the dynamics below and above threshold presented in the preceding section was carried out at constant temperature. However, the experiments described in Chapter 3 that retrieve the data for Chapters 4 and 5 cover a temperature range from *T*=10-80°C. Therefore, in order to provide the tools for the analysis in Chapters 4 and 5, we theoretically investigated the temperature dependence of many of the parameters that affect the quiescent conditions as well as the dynamic response of the laser diode.

In order to evaluate T_0, section 2.5.1 performs a complete simulation of the DC conditions of the laser diode that retrieve $I_{th} - T$ relationship in InGaAsN and InGaAs devices. This analysis relies on both experimentally known laser parameters, such as the carrier monomolecular recombination, as well as the calculated carrier thermionic escape and R_{dc}.

Reproduced with permission of the copyright owner. Further reproduction prohibited without permission.

Section 2.5.2 develops the AC small signal model above threshold, in order to provide the theoretical analysis tools for Chapter 5. The impact of *AC* capture and escape times that determine R_{ac}, along with the differential gain were investigated to find their connection with the temperature dependence of the laser bandwidth.

Interestingly, the AC small signal analysis, the effect of temperature on η and χ did not produce significant changes on how parasitics coupled to the intrinsic parameters. Notice that the DC analysis below threshold is inherently parasitics insensitive.

2.5.1. Temperature analysis below threshold

This section targets the study of the threshold current and characteristic temperature T_0 of a single quantum well $In_{0.4}Ga_{0.6}As_{1-x}N_x$ laser for x=0 and x=0.005. Following up with the analysis in Section 1.2.1, simulations were carried out in Section 2.5.1.1 to investigate the sensitivity of I_{th} and T_0 to the laser's device and material parameters through $I_{th} - T$ simulations. More in depth than in Chapter 1, this section includes the effects of the QW thermionic emission, R_{dc} as well as the recombination in the SCH, R_s.

To finalize the study below threshold, we present in Section 2.5.1.2 the effective lifetime analysis, which provides the essential tool for the analysis in Chapter 4 when R_{dc} is not experimentally known. The estimation errors in the recombination coefficients that accrue from this analysis are estimated.

2.5.1.1. Device current versus temperature

The analysis described next finds the $N_w - I$ relationship and T_0 in $In_{0.4}Ga_{0.6}As_{1-x}N_x$ laser diodes (x=0 and x=0.005) at different temperatures. More in depth than in Chapter

Reproduced with permission of the copyright owner. Further reproduction prohibited without permission.

1, this analysis comprises the detailed analysis of all the constituents of the active area current: $\tau_{cap\text{-}dc}$, $\tau_{esc\text{-}dc}$, A_w, B_w,C_w, A_s, B_s and C_s.

Equation (2.30) shows the complete expression of the device bias current I given by the recombination processes in the QW and SCH.

$$I = \frac{qV}{\eta}\left[\Gamma_q\left(A_w N_w + B_w N_w^2 + C_w N_w^3\right) + (1-\Gamma_q)\left(A_s N_s + B_s N_s^2 + C_s N_s^3\right)\right] \tag{2.30}$$

Equation (2.30) is the complete form of expression (1.9), which incorporates on its second term the effects of carrier build up and recombination in the SCH, R_s. Typical values of η are shown in Table 2.1 and we adopt 0.85 and 0.88 for InGaAsNand InGaAs lasers, respectively [45]. Since it represents the heterobarrier leakage current [46], it is not surprising the similarity in η in InGaAsN and InGaAs lasers as they have identical SCH cladding regions. These values of η are found similar than those in near infrared laser diodes [46].

The carrier density N_s in the SCH is unknown, however it keeps a relationship with N_w as it was demonstrated from the solution of the steady state rate equations by Pikal et al. [22]. In steady state regime and using equation (2.4) below threshold, N_s can be expressed in terms of N_w as in (2.31).

$$\frac{N_s}{\Gamma_q \cdot \tau_{cap-dc}} = N_w\left(\frac{1}{\tau_{w-dc}} + \frac{1}{\tau_{esc-dc}}\right) \tag{2.31}$$

Typical values of $\tau_{esc\text{-}dc}$ calculated in the studied $In_{0.4}Ga_{0.6}As_{1-x}N_x$ laser structures fall in the range 10-100ps [27] for T= 10-100°C range, which yields $R_{dc} = \tau_{esc\text{-}dc} / \tau_{w\text{-}dc} < 0.1$ and therefore equation (2.31) could be simplified as

Reproduced with permission of the copyright owner. Further reproduction prohibited without permission.

$$N_s \approx \Gamma_q R_{dc} N_w \tag{2.32}$$

Equation (2.32) shows that the ratio of SCH to QW carrier density is imposed by Γ_q and R_{dc}, where R_{dc} depends on N_w and T. For the typical values Γ_q=0.02 and $R_{dc} < 2$ shown later on, equation (2.32) yields N_s of less than 10% of N_w.

In this analysis we have adopted $\tau_{esc\text{-}dc}$ from the carrier thermionic emission study described by Tansu et al. in InGaAsN and InGaAs SQW lasers, which feature active SQW structures identical to those studied in this thesis [27]. Figure 2.17 shows the $R_{dc}=\tau_{cap\text{-}dc} / \tau_{esc\text{-}dc}$ based on the carrier thermionic escape in InGaAsN (a) and InGaAs (b) SQW lasers. $\tau_{cap\text{-}dc}$ was found to be constant at around 5.3ps and dominated by the ambipolar SCH diffusion time in both InGaAsN and InGaAs lasers for temperatures from 250-400K [45]. The escape time $\tau_{ersc\text{-}dc}$ is given by the quantum well thermionic emission rates for holes and electrons ($N_w/\tau_{e\text{-}ee}$ and $N_w/\tau_{e\text{-}hh}$), which contribute to the total escape time as $1/\tau_{esc\text{-}dc} = 1/\tau_{e\text{-}ee} + 1/\tau_{e\text{-}hh}$. Electron thermionic emission was found to be negligible in InGaAsN structures due to the large typical electron confinement $\Delta E_c > 0.4$eV (see Figure 1.9), thus yielding $R_{dc}=\tau_{cap\text{-}dc} / \tau_{e\text{-}hh}$ in Figure 2.17 (a). Instead, the electron heavy hole thermionic escape is found to be more pronounced than in InGaAs at higher carrier densities and temperatures due to the reduction in ΔE_v which results from the addition of nitrogen [45, 47-50]. This effect is observed when comparing Figure 2.17 (a) and (b). On the other hand, the rapid growth of R_{dc} in Figure 2.17 (b) above $3\text{-}4\cdot10^{18}$ cm^{-3} arises from the dominance of thermionic electron escape in InGaAs structures.

Consistently with Figure 2.3, larger values of $\tau_{esc\text{-}dc}$ and R_{dc} give rise to a carrier density build up in the SCH and therefore $R_s \neq 0$. Therefore, in order to compute I in

Reproduced with permission of the copyright owner. Further reproduction prohibited without permission.

(2.30), we utilized the SCH recombination parameters for GaAs to be $A_s=10^8$ 1/s and $B_s=1.2\cdot10^{-10}$cm^3/s for all the simulated temperatures [24, 45]. The effect of the term $C_s\cdot N^3_s$ was negligible in the analysis, as $C_s\sim3.5\cdot10^{-30}$ cm^6/s [24] and the carrier concentration in the SCH is not large. Therefore, the term $C\cdot N^3_s$ was discarded in the calculation of R_s.

The simulation results for I - N_w are shown in Figure 2.18 in InGaAs (a) and InGaAsN (b) SQW lasers at T=10, 40and 80°C. Based on the threshold gain g_{th} = 30cm^{-1} from Chapter 1, we calculated the threshold points (N_{th}, I_{th}) for each case. Notice that I_{th} in (a) is 2-3 times larger and also more temperature sensitive than in (b), which contrasts with what is experimentally observed in InGaAs(N) lasers [49, 51, 52]. Notice that the increase of I_{th} is due to a mixed contribution of the gain decrease with temperature and the change in the I-N_w traces in Figure 2.18 as well, rather than the separated effect of reduction in the injection efficiency due to current leakage [49, 52] or non-radiative recombination [53-55]. In order to clarify what are the potential effects of each one of the different current paths that contribute to the laser threshold current, we use our model to study I_{th} as a function of temperature.

As a first measure to study the effect of the different current paths into the device current, we broke up expression (2.30) into its different terms assuming $I=I_{th}(T)$. We regrouped those terms into the different recombination in the well and the total recombination path in the SCH.

Figure 2.19 shows the relative percent contribution of the different recombination paths in (2.30) in InGaAsN (a) and InGaAs (b) SQW lasers at threshold. The radiative

Reproduced with permission of the copyright owner. Further reproduction prohibited without permission.

and non radiative recombination paths in the QW are represented by $B_w N_w^2$ and $A_w N_w - C_w N_w^3$, respectively, whereas I_s represents the total recombination path in the SCH.

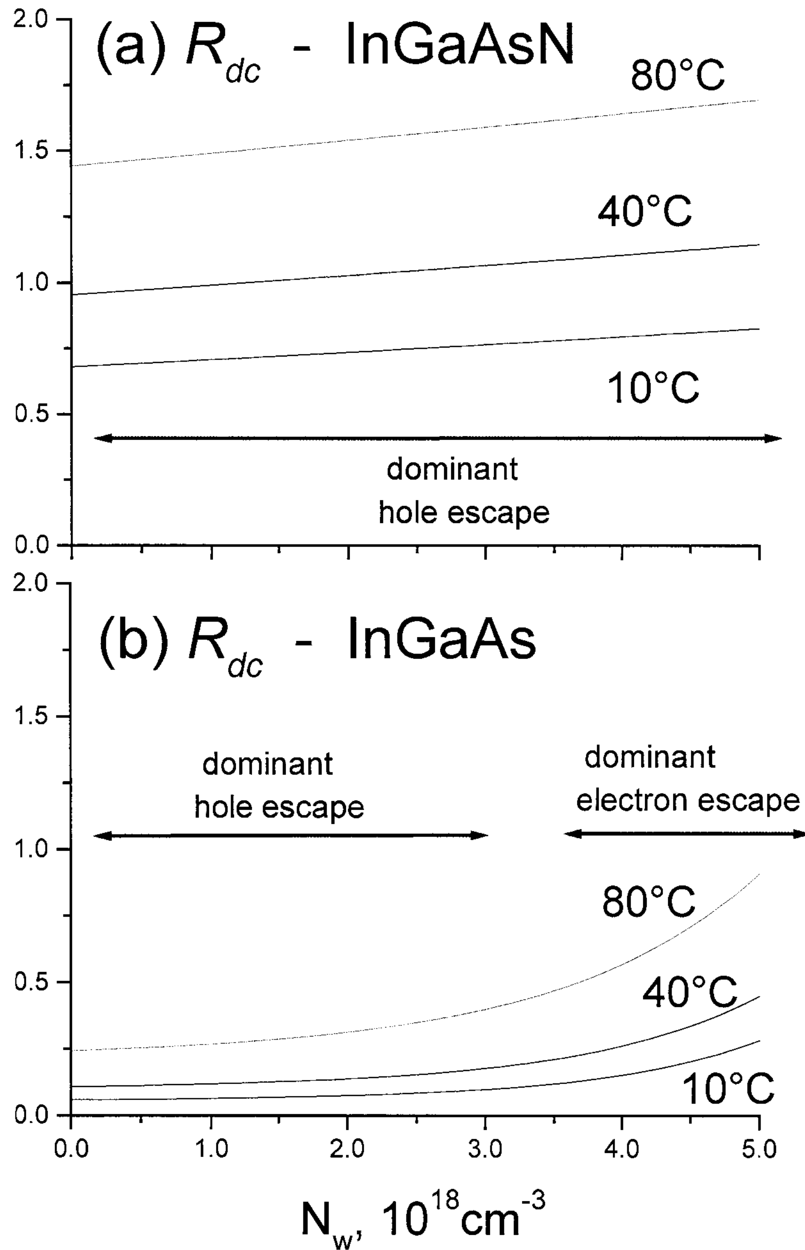

Figure 2.17. – Steady state ratio $R_{dc}=\tau_{cap\text{-}dc}/\tau_{esc\text{-}dc}$ versus N_w in InGaAsN (a) and InGaAs (b) SQW lasers in the range T=10-80°C from ref [45]. R_{dc} in (a) is larger than (b) due to larger hole thermionic escape. In (b) the thermionic electron escape becomes dominant above $3\text{-}4{\cdot}10^{18}$ cm^{-3}.

Reproduced with permission of the copyright owner. Further reproduction prohibited without permission.

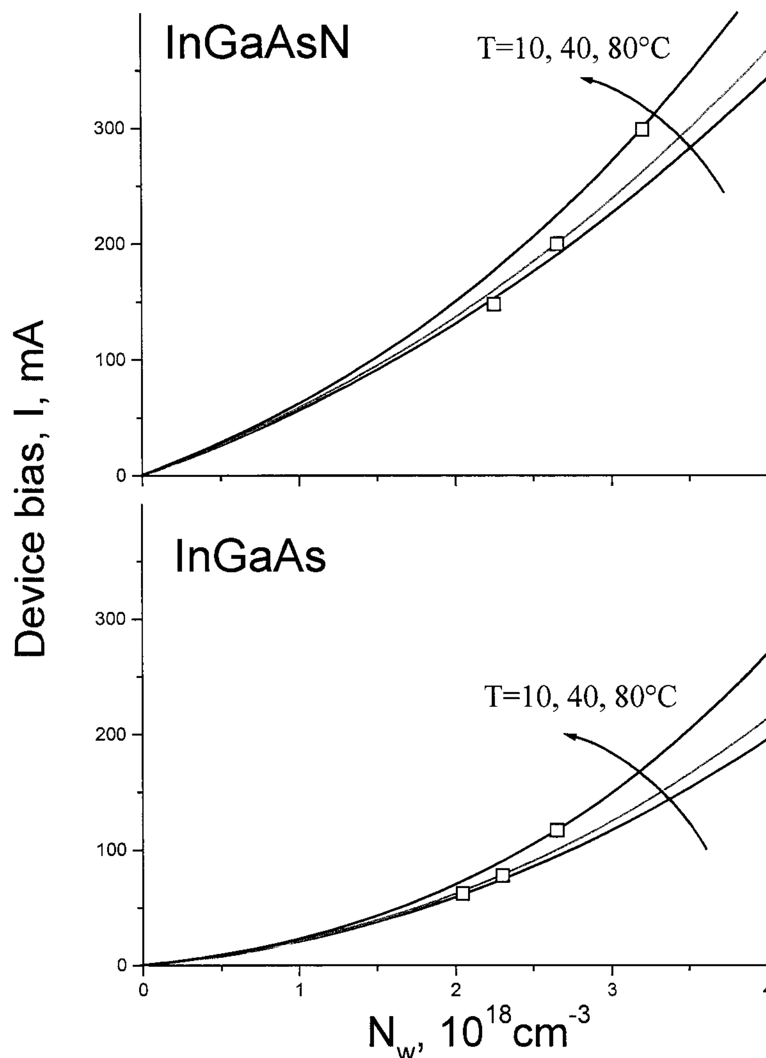

Figure 2.18. – Simulated device bias current I versus carrier density N_w in InGaAsN (a) and InGaAs (b) SQW lasers at T=10, 40 and 80°C. It is indicated in each trace the threshold point obtained from the gain relation $g_{th} = 30\text{cm}^{-1}$ from Chapter 1.

It is also plotted in dotted line the total non radiative recombination path in the QW, $A_wN_w + C_wN_w^3$, which increases considerably from subplot (b) to (a) due to the increase on A_w.

It can be observed in Figure 2.19 (a) that I_A+I_C represents 60-70% of I_{th} over the full temperature range in InGaAsN lasers, which is mainly influenced by the monomolecular

Reproduced with permission of the copyright owner. Further reproduction prohibited without permission.

recombination I_A (40-60% I_{th}). This is consistent with previous experimental findings in 1.3μm InGaAsN lasers, in which a 3-4 times increase in the monomolecular recombination is associated with the nitrogen incorporation [40, 56, 57]. The significant growth of C_w and the third order dependence with N_w makes $C_w \cdot N_w^3$ to contribute to 30% of I_{th} at T=100°C. On the other hand, subplot (b) shows that I_{th} is dominated by the term $B_w N_w^2$ in InGaAs lasers, where the monomolecular recombination takes a second place up to T~90°C. Above 90°C, $C_w \cdot N_w^3$ becomes important (~30% I_{th}) due to the same reasons given in (a).

Figure 2.19 shows in both cases that the SCH recombination path I_s barely contributes to I_{th} over the full temperature range. In fact, subplot (a) shows that I_s adds up to 10% of I_{th}, more significant than the 2-5% found in InGaAs (b). This is attributed to the larger R_{dc} (Figure 2.17) and consequent carrier build up and recombination in the SCH in (a). Still, I_s is much smaller than the total current I_{th}, as was previously speculated from equation (2.32).

From the analysis of the traces in Figure 2.19 we infer that the monomolecular recombination rules over I_{th} in InGaAsN lasers. It is nor clear though, what would be the direct impact in T_0 of each one of the recombination paths. In order to answer this, we further investigate I_{th} and T_0 in InGaAsN lasers by removing, one at a time, each one of the parameters of the model.

By repeating the simulation done above in InGaAsN devices, the following analysis obtains the traces of $I_{th} - T$ by suppressing one of the effects of either A_w, B_w ,C_w or τ_{esc-dc}. To explore all the possibilities, we simulated also the cases in which the gain parameter or the transparency carrier density are temperature insensitive.

Reproduced with permission of the copyright owner. Further reproduction prohibited without permission.

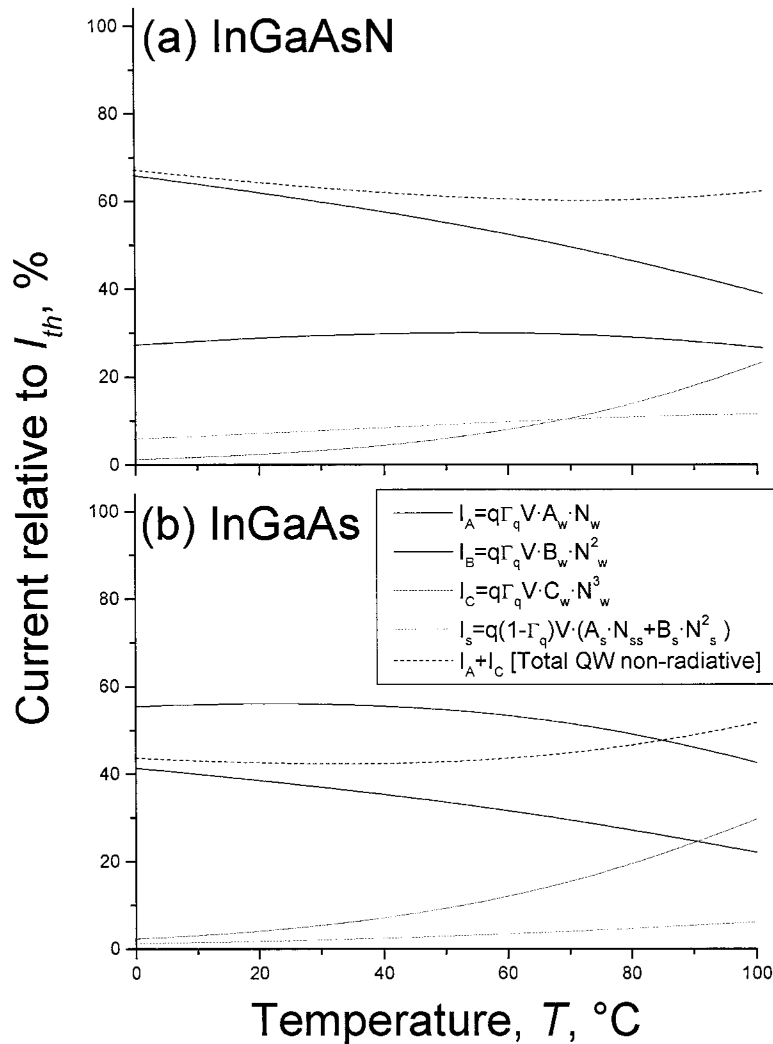

Figure 2.19. – Different recombination paths, percent, that contribute to I_{th} (100%) versus T in InGaAsN (a) and InGaAs (b) SQW lasers. The dotted line represents the current for the total non-radiative recombination path $A_wN_w + C_wN_w^3$ in the QW. I_S represents the SCH recombination current.

Figure 2.20 shows $I_{th} - T$ calculated from (2.30) and (2.32), in which the semi-logarithmic plot permits to directly visualize T_0 as the inverse of the slope. The black trace (solid) represents the threshold current I_{th} in the InGaAsN, followed by the same

Reproduced with permission of the copyright owner. Further reproduction prohibited without permission.

calculation by equating either A_w, B_w, or C_w to zero, as represented by the red, green and blue (solid) traces, respectively.

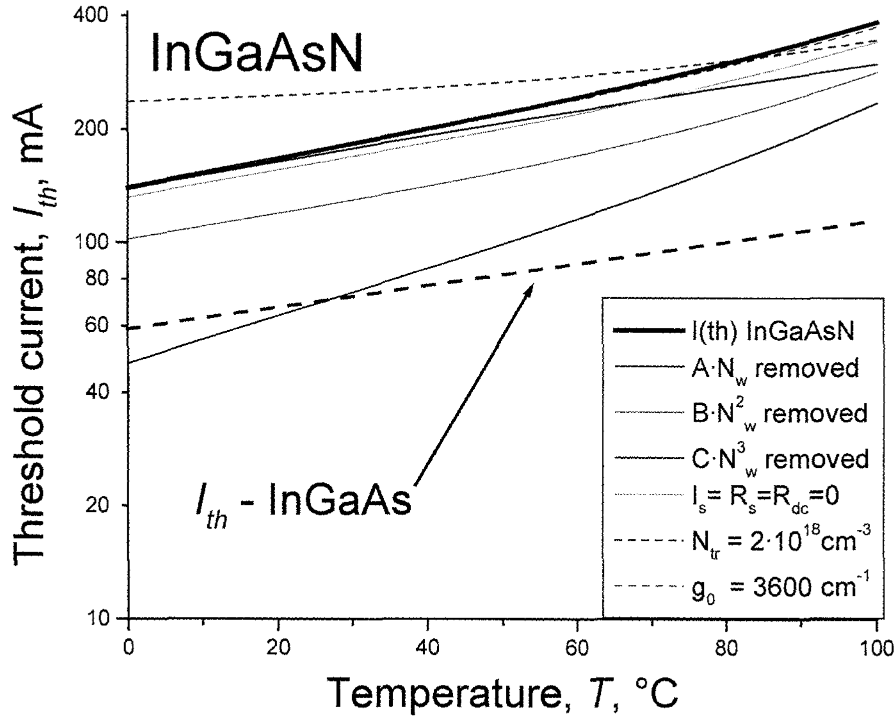

Figure 2.20. –Analysis of the sensitivity of I_{th} -T behavior to the suppression of either $A_w{\cdot}N$, $B_w{\cdot}N^2$, $C_w{\cdot}N^3$ and R_s (or R_{dc}=0) in InGaAsN SQW lasers.

Then we iterated for I_s=0, which is equivalent to R_{dc}=0 or A_s=B_s=0, as shown by the solid trace in cyan. Finally, we assumed for completeness two cases in which either N_{tr} or g_0 were temperature insensitive and fixed to the values in references [48, 55] 3600cm^{-1} and 2·10^{18}cm^{-3}, respectively. As a comparison, we plotted I_{th} – T in InGaAs lasers (dashed).

We observe in Figure 2.20 that fixing G_0 has no impact in either I_{th} or T_0. In similar way, the suppression of I_s causes little improvement in I_{th} and T_0. It is more notorious,

Reproduced with permission of the copyright owner. Further reproduction prohibited without permission.

though, the suppression of $C_wN_w^3$ leads to direct increase on T_0, as found elsewhere [54, 58].

It is observed also that the suppression of $B_wN_w^2$ reduces I_{th} in ~30% but keeps T_0 unchanged. On the other hand, and confirming our suspicion, the suppression of I_A considerably reduces I_{th}, which becomes comparable to that of InGaAs lasers at low temperatures. In this case however, the trace is even steeper (lower T_0), meaning that the monomolecular recombination does not explain the reduction in T_0. Interestingly, we find that by fixing N_{tr} to $2 \cdot 10^{18}$cm^{-3} (compare to N_{tr} in Figure 1.4a) produces an increment in both I_{th} and T_0.

In conclusion, this analysis tells us that in theory the reduction on T_0 could be a combination of N_{tr} and C_w due to the nitrogen incorporation in InGaAsN lasers. To summarize our findings Table 2.2 shows I_{th} at T=20°C and T_0 obtained from the fit of each trace in Figure 2.20 with equation (1.12). These values allow us to more accurately identify the potential parameters that may reduce T_0 in InGaAsN SQW lasers, confirming C_w as the main candidate of lower T_0, followed in importance by N_{tr}. B_w plays a less significant role and its effect mainly reduces I_{th}, whereas the effect g_0 is negligible in both I_{th} and T_0. Finally, we found that the effect of neglecting N_s (R_{dc}=0) produces changes of ~5% in both I_{th} and T_0.

Although the case where N_s =0 does not considerably impact on I_{th} and T_0, it has fundamental importance for the data analysis in Chapter 4. For that reason we dedicate the following section to the study of the of the effective recombination parameters in the data analysis when assuming $R_{dc}=0$.

Reproduced with permission of the copyright owner. Further reproduction prohibited without permission.

Parameter changed	I_{th}, mA (20°C)	T_0 (K)
Normal case	164	97
A_w=0	61	61
B_w=0	115	94
C_w=0	164	132
R_{dc}=0 or A_s= B_s=0	152	103
$N_{tr} = 2 \cdot 10^{18} cm^{-3}$	242	257
$g_0 = 3600\ cm^{-1}$	164	101

Table 2.2.- Parameter sensitivity of I_{th} (20°C) and T_0 in InGaAsN lasers.

2.5.1.2 Effective differential carrier lifetime analysis

The effective differential lifetime analysis is widely used in the literature and only assumes a single carrier density in the active area, N_{eff} [59]. In practical cases, the fundamental reason that justifies the effective carrier lifetime analysis is the difficulty to measure the capture to escape ratio R_{dc} [22], which is unknown in most of the practical cases. Therefore, the effective carrier lifetime analysis becomes the only tool to provide an estimation of the effective carrier density in the quantum well [59].

The effective lifetime analysis model results from a simplification to the active area model of equations (2.3) and (2.4) when assuming R_{dc}=0 and thus N_s=0. Under this assumption N_w no longer represents the carrier density in the QW so we rename it as the effective carrier density N_{eff}. As it accounts for the carrier density in the active area all, N_{eff} is an overestimation to N_w, unless $R_{dc} \rightarrow 0$ in where $N_{eff} = N_w$.

The effective rate equations model is now simplified and then the device current in

Reproduced with permission of the copyright owner. Further reproduction prohibited without permission.

(2.30) simplifies to

$$I = \frac{qV_w}{\eta}\left[A_{eff}N_{eff} + B_{eff}N_{eff}^2 + C_{eff}N_{eff}^3\right] \tag{2.33}$$

In a similar way, we obtain an expression of the differential lifetime τ_{eff} instead of that in (2.11) as

$$\frac{1}{\tau_{eff}} = A_{eff} + 2B_{eff}N_{eff} + 3C_{eff}N_{eff}^2 \tag{2.34}$$

We analyzed theresults form the previous section by simultaneously fitting I in (2.30) and τ in (2.15), with equations (2.33) and (2.34). The fit retrieved A_{eff}, B_{eff}, C_{eff} and N_{eff}. We found that N_{eff} overestimated N_w from Figure 2.18 in up to 20%, which is due to the small effect of I_s on I_{th} found above. In order to check the validity of the effective analysis, we compared A_{eff}, B_{eff}, C_{eff} with A_w, B_w and C_w in InGaAsN and InGaAs lasers.

Table 2.3 shows the results of the effective analysis performed to the InGaAsN (a) and InGaAs (a) lasers simulated above.

Again, the limit $R_{dc}\rightarrow 0$ yields the effective carrier parameters A_{eff}, B_{eff}, and C_{eff} identical to A_w, B_w, and C_w used in the simulation (Table 1.1). Notice that A_{eff}, B_{eff}, and C_{eff} in InGaAs lasers are still like A_w, B_w, and C_w due to the low values in R_{dc}. However, the fit in InGaAsN lasers retrieve A_{eff}, B_{eff}, and C_{eff} that show a distorted representation of the physical of the real recombination processes, due to the considerable thermionic escape and carrier build up in the SCH.

Reproduced with permission of the copyright owner. Further reproduction prohibited without permission.

(a) InGaAsN			
T	A_{eff} $10^8 s^{-1}$	B_{eff} $10^{-10} cm^{-3} s^{-1}$	C_{eff} $10^{-30} cm^{-6} s^{-1}$
10°C	7.3	2.26	5.8
40°C	7.5	2.3	1.7
80°C	7.9	2.5	12
T	A_w	B_w	C_w
10°C	7.7	1.5	3.9
40°C	7.7	1.5	8.2
80°C	7.7	1.5	22.3

(b) InGaAs			
T	A_{eff} $10^8 s^{-1}$	B_{eff} $10^{-10} cm^{-3} s^{-1}$	C_{eff} $10^{-30} cm^{-6} s^{-1}$
10°C	2	1.6	3.7
40°C	2.1	1.6	9.1
80°C	2.2	1.5	26.6
T	A_w	B_w	C_w
10°C	2.2	1.5	3.9
40°C	2.2	1.5	8.2
80°C	2.2	1.5	22

Table 2.3.- Effective carrier lifetime analysis to the modeled InGaAsN (a) and InGaAs (b) lasers. If R_{dc}=0 then $N_s = 0$ and A_{eff}, B_{eff}, and C_{eff} become A_w, B_w, and C_w identical those used in the simulation (Table 1.1)

With exception of the recombination parameters, the presented analysis was accurate enough to obtain the carrier density in the QW, which is used in Chapter 4 for the experimental lifetime and gain analysis.

Reproduced with permission of the copyright owner. Further reproduction prohibited without permission.

2.5.2. Frequency response versus temperature above threshold

The analysis above threshold is oriented to study the impact of temperature on the device bandwidth. As shown in Section 2.4.1, both f_r and γ are are influenced by R_{ac}, which follows the temperature dependence in Figure 2.17 as R_{ac} = 1.5·R_{dc} in this work ([29], Figure 2.21). In addition, model calculations predict a change in the material's differential gain at threshold decreases with temperature as shown in Figure 2.22. This in turn would affect $f_r - T$.

For the simulation, we assumed the differential gain at threshold dg/dN_w obtained from ref. [60] in InGaAsN SQW lasers, as shown in Figure 2.22. By using the model in (2.19) with the parameters of Table 2.1, the slope of f_r^2 versus P_0 is calculated as shown in Figure 2.24 in InGaAsN SQW lasers.

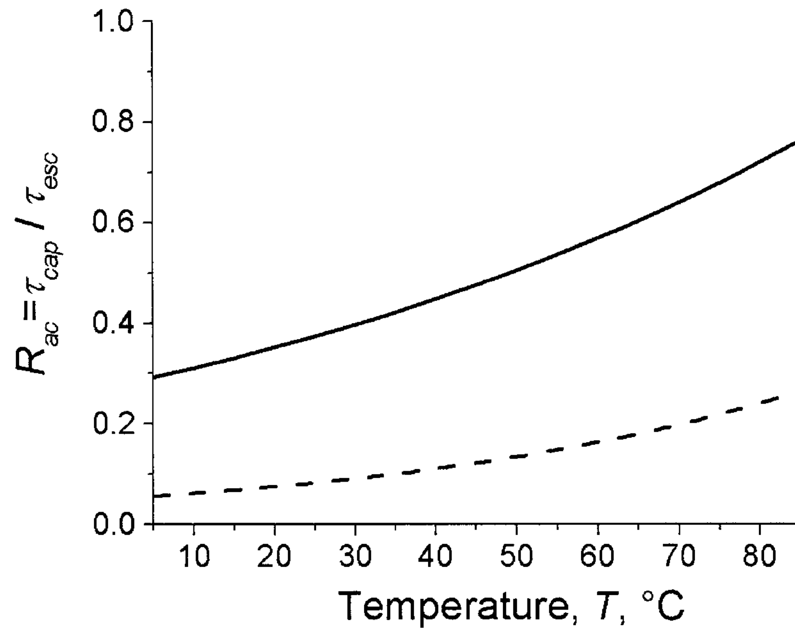

Figure 2.21. – R_{ac} at threshold versus T in InGaAsN (solid) and InGaAs (dash) SQW lasers in the range T=10-80°C. R_{ac} is obtained as 1.5 times the values of Figure 2.17 at N_{th} assumed to rise 3-4·10^{18}cm^{-3} at T=10-80°C.

Reproduced with permission of the copyright owner. Further reproduction prohibited without permission.

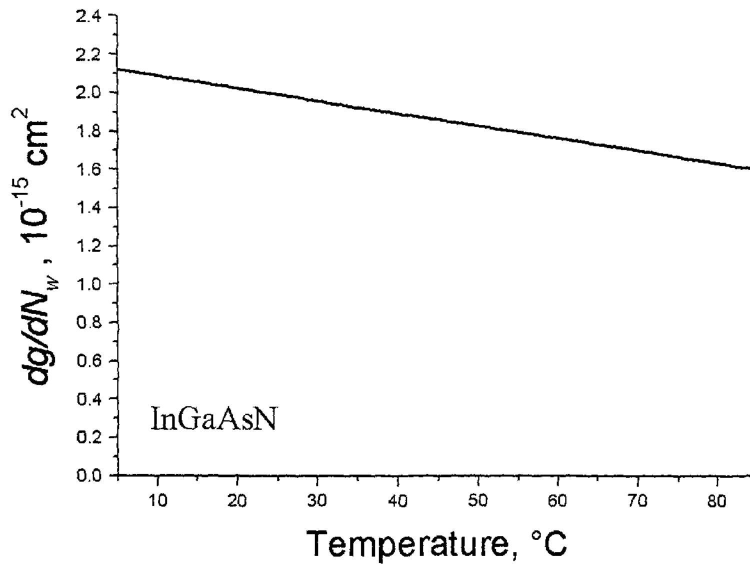

Figure 2.22. – Differential gain at threshold, dg/dN_w versus temperature T from ref. [60] in InGaAsN SQW lasers.

Using expressions (2.25) to (2.28) we analyze next the sensitivity to temperature of f_r and γ. For the simulation, we used the parameters in Table 2.1.

In the first set of simulations, we studied how the f_r^2 - P_0 behavior changes due to the sole effect of either dg/dN_w and R_{ac} at threshold, and the compression factor ε.

In the absence of gain compression (ε=0) f_r^2 - P_0 behavior is linear, as shown in Figure 2.23 (all the traces), assuming R_{ac}=0. The solid trace depicts the case in which dg/dN_w is temperature insensitive. On the other hand, the dotted lines show f_r^2 obtained by assuming dg/dN_w shown in Figure 2.21, which caused a reduction of up to 20% in the slope f_r^2 - P_0 at T=80°C.

Reproduced with permission of the copyright owner. Further reproduction prohibited without permission.

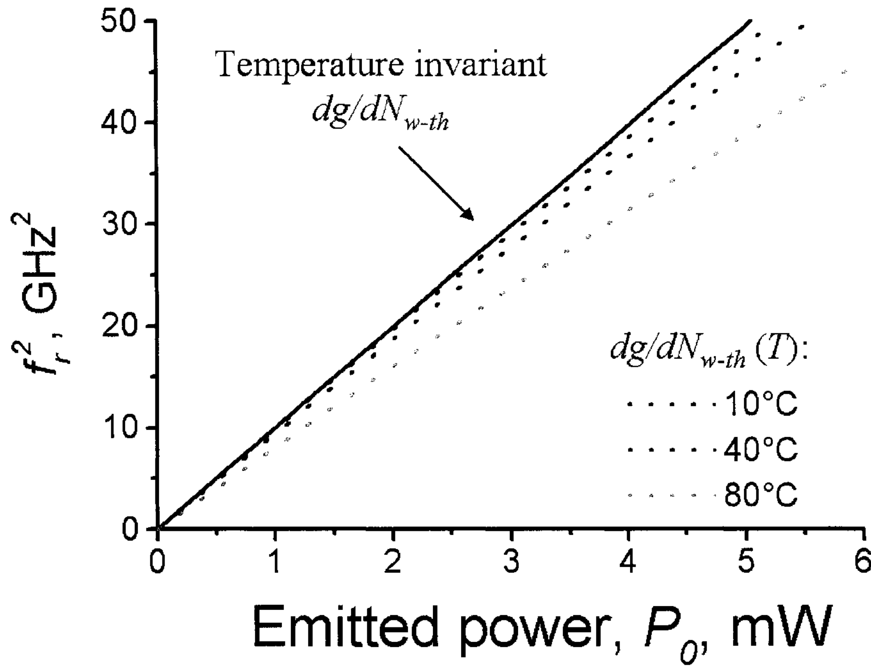

Figure 2.23. – f_r^2 versus P_0 in InGaAsN SQW lasers at T=10, 40 and 80°C. The dotted lines indicated the effect of the reduction on $dg/dN_{w\text{-}t}$. at threshold with T.

The next simulation studied the effect of carrier transport in the behavior of f_r^2 - P_0. The solid traces in Figure 2.24 were obtained in the absence of carrier transport, that is R_{ac}=0. It is found a decrease in the slope of f_r when the threshold value of R_{ac} of Figure 2.21 is incorporated to the simulation, which was evidenced by a reduction on 35-50% in f_r^2 at P_0 = 5mW.

The next simulation considers the impact of the compression factor ε on f_r^2 - P_0. Figure 2.25 shows the simulation of f_r^2 considering the variation of dg/dN_w with temperature and assuming R_{ac}=0. The solid traces were obtained by assuming $\varepsilon=10^{-17}$cm^3 as given in Table 2.1, which were identical to those in which ε=0. In order to observe changes in f_r^2 - P_0 due to ε, we further repeated the simulation with $\varepsilon=10^{-18}$cm^3 (dotted lines) and could observe as change in less than 5% on f_r^2 at P_0 = 5mW.

Reproduced with permission of the copyright owner. Further reproduction prohibited without permission.

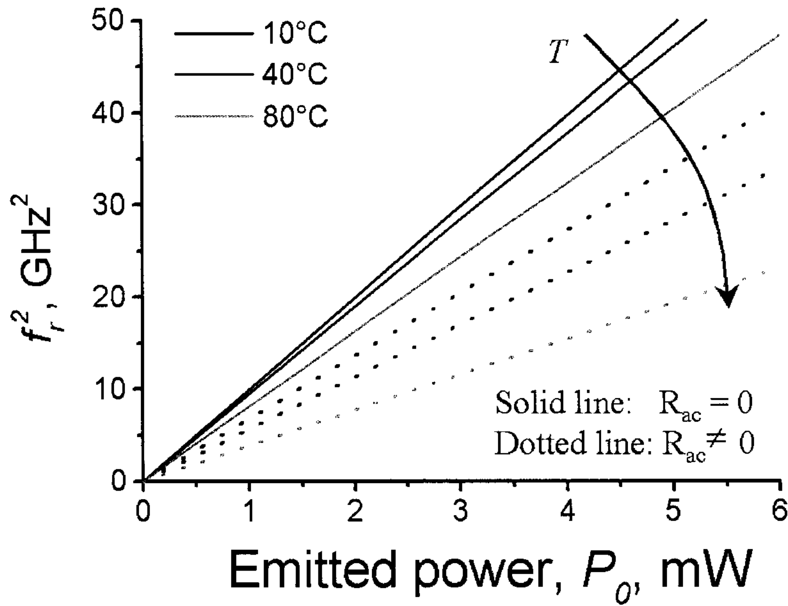

Figure 2.24. – f_r^2 versus P_0 in InGaAsN SQW lasers in the range T=10, 40 and 80°C, when the threshold value R_{ac} varies with T. The dotted lines show a dramatic reduction on f_r^2 due to carrier transport.

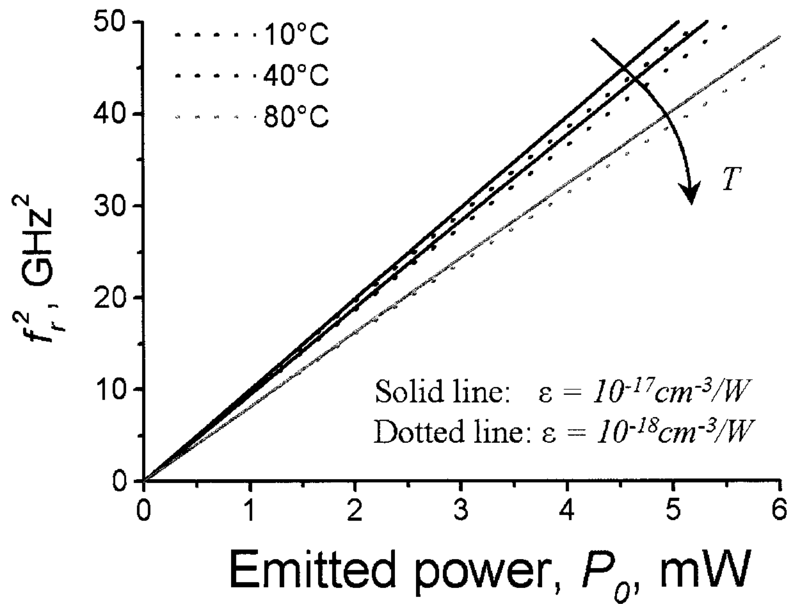

Figure 2.25. – f_r^2 versus P_0 in InGaAsN SQW lasers at T=10, 40 and 80°C with two different values of compression factor ε. f_r^2 is not sensitive to ε.

Reproduced with permission of the copyright owner. Further reproduction prohibited without permission.

Comparison of the results in last three cases show that the slope of f_r^2 - P_0, which is imposed by the effective differential gain at threshold a_{eff} (2.27), is insensitive to ε and was moderately affected by the predicted changes on dg/dN_w [60]. However, the slope f_r^2 - P_0 was dramatically reduced due to the changes on R_{ac} with temperature. These findings are experimentally confirmed in Chapter 5.

The second set of simulations is carried out to analyze the effect of dg/dN_w, R_{ac} and ε in the γ - P_0 behavior. This investigation was performed by obtaining $\gamma - P_0$ for changes on the $dg/dN_w(1+R_{ac})$ and on ε separately. As found in Section 2.4, the damping γ depends on the electrical parasitics for this reason we performed the study of damping versus $dg/dN_w(1+R_{ac})$ or ε by comparing back to back simulations with and without parasitics. These situations are described by a coupling factor χ to be 10^{19}-10^{20}cm^{-3}V^{-1} and ∞, respectively. The purpose of this comparison is to show how our model will be utilized in Chapter 5 to correct the value of γ to its equivalent parasitic-free value appropriate for the study of carrier dynamics.

Figure 2.26 (a) shows γ - P_0 for the case in which ε=0 and $dg/dN_w(1+R_{ac})$ is temperature invariant (solid line) or changes with temperature as previously shown in Figure 2.21 and Figure 2.22. Interestingly, the changes in the slope γ - P_0 in the parasitic free case (a) are similar to those in f_r^2 - P_0 for the combined effects of dg/dN_w and R_{ac} at threshold. This behavior is different when ε is not zero, as shown next. Figure 2.26 (b) shows γ - P_0 when including parasitics ($\chi \neq \infty$), showing the increase in γ similar to Figure 2.16 and observed in the experimental data. Before commenting further, let us find γ when ε changes.

Reproduced with permission of the copyright owner. Further reproduction prohibited without permission.

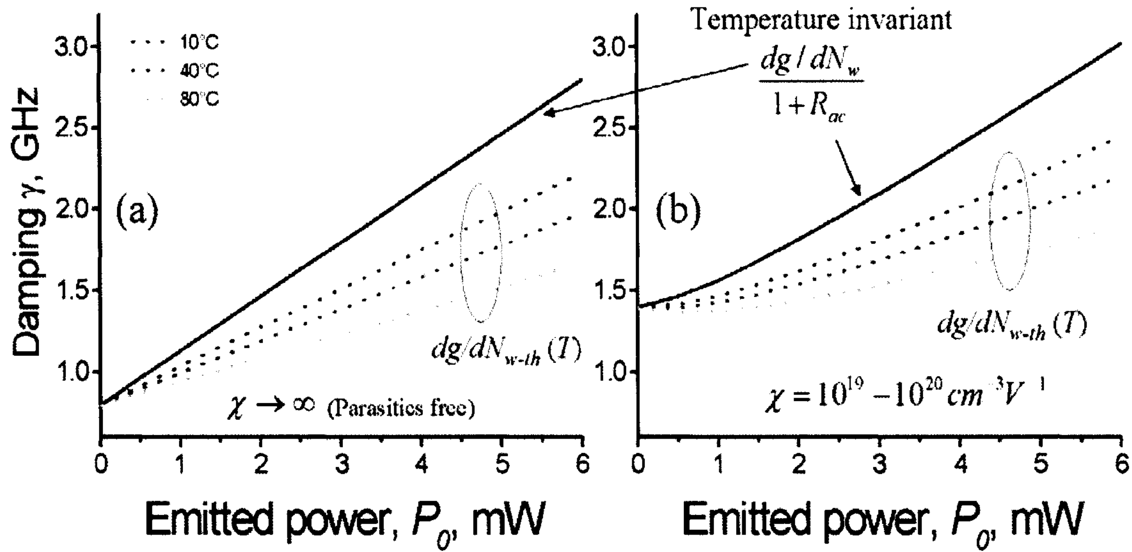

Figure 2.26. – Damping γ versus P_0 in InGaAsN SQW lasers at T=10, 40 and 80°C with ε=0 and temperature dependent dg/dN_w and R_{ac} at threshold.

Figure 2.27 shows the damping simulation with $\varepsilon=10^{-17}cm^3$ and $5\cdot10^{-17}cm^3$.The threshold value of $dg/dN_w(1+R_{ac})$ was constant and obtained from Figure 2.21 and Figure 2.22 at T=10°C. The traces in (a) show to be sensitive to ε, as γ increases ~100% when ε increases in five times, which is much more notorious than in f_r^2.

In conclusion, γ is found to be sensitive to $dg/dN_w(1+R_{ac})$ at threshold and to ε, which permits to find ε as the former can be obtained from the slope f_r^2 - P_0.

The simulations performed above provide the guidelines to the data analysis performed later in Chapter 5 above threshold. Figure 2.23 through Figure 2.25 provide the study of threshold differential gain and carrier transport, provided that the effect of ε is found to be negligible, which id experimentally confirmed in Chapter 5. On the other hand, Figure 2.27 and Figure 2.28 show the potential of our developed model to connect obtain the parasitic free damping (a) from the experimental data (b) by numerical

Reproduced with permission of the copyright owner. Further reproduction prohibited without permission.

calculations in reverse order. This is done in Chapter 5 to obtain ε from the damping factor.

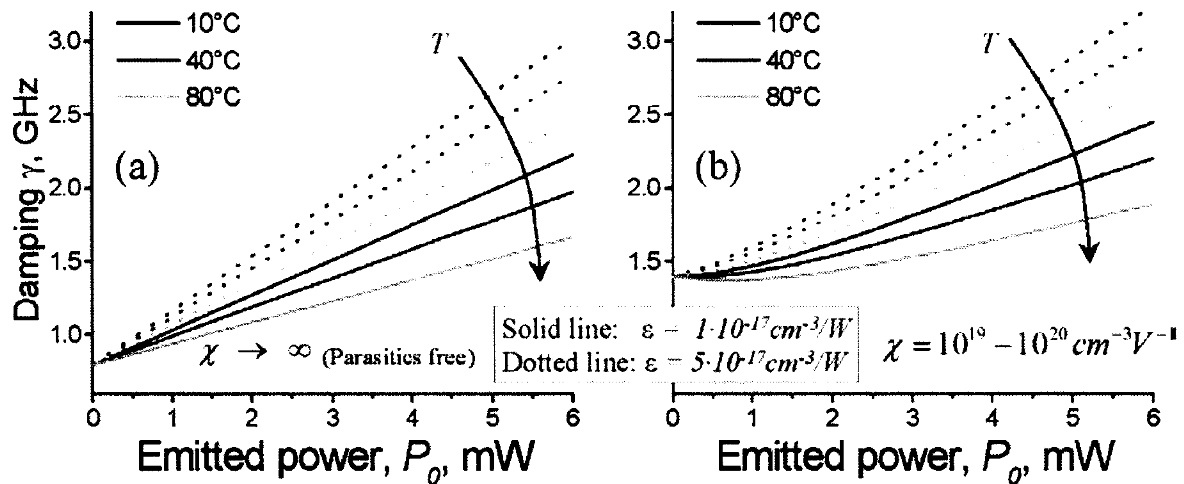

Figure 2.27. – Damping γ versus P_0 in InGaAsN SQW lasers at T=10, 40 and 80°C with ε=10^{-17}cm^3 and $5\cdot10^{-17}$cm^3 and dg/dN_w and R_{ac} fixed to their threshold values at T=10°C.

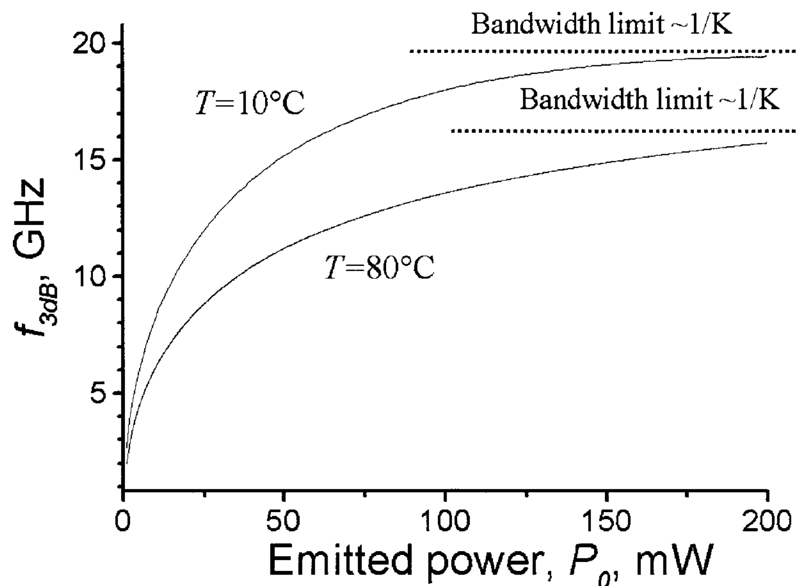

Figure 2.28. – Bandwidth f_{3dB} versus emitted power P_0 in InGaAsN SQW lasers at T=40°C. Same parameters were used for the simulation. Upper line shows.

Reproduced with permission of the copyright owner. Further reproduction prohibited without permission.

As a complimentary calculation, we found the bandwidth f_{3dB} by combining the temperature dependent γ and f_r^2 on equation (2.25). The values of f_{3dB} are shown at exaggerated biases in Figure 2.28 to make evident the asymptotic limit known as K-limited bandwidth f_{3dB-k} [61].

The K analysis is used on Chapter 5 to put f_{3dB-k} in InGaAsN in prospective to commercial devices.

2.6. Summary and conclusions of the model simulations

This chapter developed the simulation tools that permit to analyze the experimental impedance and frequency responses from which the carrier dynamics in SQW InGaAs(N) laser diodes is studied. Specific tools were developed separately for the analysis below and above threshold, that permitted to study the threshold current and the laser bandwidth versus temperature, respectively.

Below threshold, we developed a rate equation model that accounts for the diode electrical parasitics, the carrier recombination parameters A_w, B_w and C_w in the QW as well as the carrier transport and recombination in SCH. The model retrieved the laser diode differential carrier lifetime and the time constants that dictate the frequency response below threshold.

We then used our model to answer the questions of this thesis work, which were formulated at the end of Chapter 1 as 1 through 3. Using the model results and typical calculated gain in InGaAsN material, we performed a temperature analysis of the threshold current and obtained T_0. We then studied the sensitivity of T_0 to all the different parameters and found that nitrogen induced larger A_{eff} produces an increase on I_{th} but

Reproduced with permission of the copyright owner. Further reproduction prohibited without permission.

does not significantly changes T_0. Instead, we found that the increase of C_w and N_{tr} due to nitrogen incorporation causes a reduction in T_0 in dilute nitride lasers. This analysis took place assuming all parameters were known. Instead, R_{dc} is now experimentally known and we had to develop an alternative analysis.

We developed also the analysis in which R_{dc} is not experimentally known, as it is the case of Chapter 4. We developed an effective differential carrier lifetime analysis, in which we assumed a carrier density N_{eff} that replaced N_w. The effective analysis produced an overestimation in the QW carrier density as R_{dc} increased, which in theory could be up to ~20%. It was found that the effective recombination parameters B_{eff} and C_{eff} resulting from this analysis do not represent physical mechanisms. Instead, the effective analysis could relate A_{eff}~A_w, $N_{tr\text{-}eff}$ and dg/dN_{eff} to T_0 and I_{th}, becoming instrumental for the correct interpretation of the experimental data in Chapter 4.

The developed rate equation model above threshold provided the tools to study the optical modulation frequency response considering the effect of electrical parasitics. In this way, the damping in real laser diodes was simulated with this model, which incorporated electrical parasitics. Based on the intrinsic material parameters, such as threshold differential gain and compression factor calculated in dilute nitrides, we were able to simulate the laser frequency response under electrical and optical modulation. From those simulations we found electrical measurements to be unsuited for the analysis, as they were highly shaped by electrical parasitics. Instead, we found that optical excitation measurements recommendable for the experimental analysis, as done in Chapter 5.

The simulation of optical modulation response above threshold was used to answer

Reproduced with permission of the copyright owner. Further reproduction prohibited without permission.

questions 4-6 formulated at the end of Chapter 1. From the above threshold analysis we found three major contributors to the laser bandwidth: differential gain, transport factor and gain compression factor. By having these calculated parameters, we simulated the frequency response for InGaAsN and InGaAs SQW lasers. The analysis indicated that, for typical measurement conditions like those in Chapter 5, the compression factor did not alter nor limit the laser frequency response. Therefore, the reduction in the differential gain and enlargement on the carrier transport were responsible for causing the reduction in bandwidth due to nitrogen incorporation. Moreover, the model solution indicated that both effects were inseparable, unless R_{ac} is known. Following, R_{ac} and dg/dN_w were combined into the effective differential gain a_{eff}. We found a_{eff} to reduce f_{3db} in InGaAsN lasers due to nitrogen incorporation and to shape its temperature behavior.

Reproduced with permission of the copyright owner. Further reproduction prohibited without permission.

References for Chapter 2

[1] D. A. Kleinman, "Maser Rate Equations + Spiking," *Bell System Technical Journal*, vol. 43, pp. 1505-+, 1964.

[2] K. Y. Lau, P. L. Derry, and A. Yariv, "Ultimate Limit in Low Threshold Quantum Well Gaalas Semiconductor-Lasers," *Applied Physics Letters*, vol. 52, pp. 88-90, 1988.

[3] R. Olshansky, W. Powazinik, P. Hill, V. Lanzisera, and R. B. Lauer, "Ingaasp Buried Heterostructure Laser with 22 Ghz Bandwidth and High Modulation Efficiency," *Electronics Letters*, vol. 23, pp. 839-841, 1987.

[4] R. S. Tucker and D. J. Pope, "Circuit Modeling of the Effect of Diffusion on Damping in a Narrow-Stripe Semiconductor-Laser," *IEEE Journal of Quantum Electronics*, vol. 19, pp. 1179-1183, 1983.

[5] R. S. Tucker and D. J. Pope, "Microwave Circuit Models of Semiconductor Injection-Lasers," *IEEE Transactions on Microwave Theory and Techniques*, vol. 31, pp. 289-294, 1983.

[6] K. Y. Lau, N. Barchaim, P. L. Derry, and A. Yariv, "High-Speed Digital Modulation of Ultralow Threshold (Less-Than 1 Ma) Gaas Single Quantum-Well Lasers without Bias," *Applied Physics Letters*, vol. 51, pp. 69-71, 1987.

[7] R. Nagarajan, T. Fukushima, S. W. Corzine, and J. E. Bowers, "Effects of Carrier Transport on High-Speed Quantum-Well Lasers," *Applied Physics Letters*, vol. 59, pp. 1835-1837, 1991.

[8] K. L. Lau, "Dynamics of Quantum Well Lasers," in *Quantum Well Lasers*, P. Zory, Ed.: New York: Academic Press Inc., 1993.

[9] R. Olshansky, V. Lanzisera, C. B. Su, W. Powazinik, and R. B. Lauer, "Frequency-Response of an Ingaasp Vapor-Phase Regrown Buried Heterostructure Laser with 18 Ghz Bandwidth," *Applied Physics Letters*, vol. 49, pp. 128-130, 1986.

[10] W. Rideout, W. F. Sharfin, E. S. Koteles, M. O. Vassell, and B. Elman, "Well-Barrier Hole Burning in Quantum-Well Lasers," *IEEE Photonics Technology Letters*, vol. 3, pp. 784-786, 1991.

[11] M. Grupen and K. Hess, "Iib-1 the Self-Consistent Simulation of the Modulation Responses of Quantum-Well Lasers," *IEEE Transactions on Electron Devices*, vol. 40, pp. 2105-2106, 1993.

[12] W. W. Chow, H. C. Schneider, S. W. Koch, C. H. Chang, L. Chrostowski, and C. J. Chang-Hasnain, "Nonequilibrium model for semiconductor laser modulation response," *IEEE Journal of Quantum Electronics*, vol. 38, pp. 402-409, 2002.

[13] I. Esquivias, S. Weisser, B. Romero, J. D. Ralston, and J. Rosenzweig, "Carrier dynamics and microwave characteristics of GaAs-based quantum-well lasers," *IEEE Journal of Quantum Electronics*, vol. 35, pp. 635-646, 1999.

[14] C. Silfvenius, G. Landgren, and S. Marcinkevicius, "Carrier transport effects in

Reproduced with permission of the copyright owner. Further reproduction prohibited without permission.

1.3 mu m multiple quantum well InGaAsP laser design," *Japanese Journal of Applied Physics Part 1-Regular Papers Short Notes & Review Papers*, vol. 38, pp. 1227-1229, 1999.

[15] T. Keating, X. Jin, S. L. Chuang, and K. Hess, "Temperature dependence of electrical and optical modulation responses of quantum-well lasers," *IEEE Journal of Quantum Electronics*, vol. 35, pp. 1526-1534, 1999.

[16] P. Bhattacharya and S. Ghosh, "Tunnel injection In0.4Ga0.6As/GaAs quantum dot lasers with 15 GHz modulation bandwidth at room temperature," *Applied Physics Letters*, vol. 80, pp. 3482-3484, 2002.

[17] O. Anton, G. Vaschenko, D. Patel, G. Y. Robinson, C. S. Menoni, and J. Pikal, "Small signal response of 1.3 mm InAsP/InGaAsP quantum well laser diodes obtained with a THz-bandwidth frequency comb," *IEEE Journal of Quantum Electronics*, vol. 40, pp. 982-988, 2004.

[18] J. Eom, C. B. Su, J. Lacourse, and R. B. Lauer, "Simultaneous Measurement of Spontaneous Emission Rate, Nonlinear Gain Coefficient, and Carrier Lifetime in Semiconductor-Lasers Using a Parasitic-Free Optical Modulation Technique," *Applied Physics Letters*, vol. 56, pp. 518-520, 1990.

[19] D. Vassilovski, T. C. Wu, S. Kan, K. Y. Lau, and C. E. Zah, "Unambiguous Determination of Quantum Capture, Carrier Diffusion, and Intrinsic Effects in Quantum-Well Laser Dynamics Using Wavelength-Selective Optical Modulation," *IEEE Photonics Technology Letters*, vol. 7, pp. 706-708, 1995.

[20] R. Paiella, G. Hunziker, K. J. Vahala, and U. Koren, "Measurement of the interwell carrier transport lifetime in multiquantum-well optical amplifiers by polarization-resolved four-wave mixing," *Applied Physics Letters*, vol. 69, pp. 4142-4144, 1996.

[21] X. Jin and S. L. Chuang, "Microwave modulation of a quantum-well laser with and without external optical injection," *IEEE Photonics Technology Letters*, vol. 13, pp. 648-650, 2001.

[22] J. M. Pikal, C. S. Menoni, H. Temkin, P. Thiagarajan, and G. Y. Robinson, "Carrier lifetime and recombination in long-wavelength quantum- well lasers," *IEEE Journal of Selected Topics in Quantum Electronics*, vol. 5, pp. 613-619, 1999.

[23] O. Anton, D. Patel, C. S. Menoni, J. Y. Yeh, T. T. Van Roy, L. Mawst, J. Pikal, and N. Tansu, "Frequency response of strain-compensated InGaAsN/GaAsP/GaAs SQW lasers," *IEEE Journal of Selected Topics in Quantum Electronics*, 2005.

[24] L. A. Coldren and S. W. Corzine, *Diode lasers and Photonic Integrated Circuits*: Wiley series in microwave and optical engineering, 1995.

[25] G. P. Agrawal and N. K. Dutta, *Semiconductor Lasers*. New York: Van Nostrand Reinhold, 1993.

[26] O. Anton, "Optical modulation response of 1.3μm InAsP Lasers," in *Electrical Engineering*: Colorado State University, 2002.

[27] N. Tansu and L. J. Mawst, "The role of hole leakage in 1300-nm InGaAsN

Reproduced with permission of the copyright owner. Further reproduction prohibited without permission.

quantum-well lasers," *Applied Physics Letters*, vol. 82, pp. 1500-1502, 2003.

[28] J. Y. Yeh and L. J. Mawst, "Modelling of thermionic processes in 1.3μm InGaAsN/GaAsP/GaAs SQW laser heterostructures," University of Wisconsin, Madison 2004.

[29] C. Y. Tsai, Y. H. Lo, and L. F. Eastman, "Carrier Dc and Ac Capture and Escape Times in Quantum-Well Lasers," *IEEE Photonics Technology Letters*, vol. 7, pp. 599-601, 1995.

[30] S. L. Chuang, *Physics of optoelectronic devices*, 1995.

[31] G. E. Shtengel and D. A. Ackerman, "Internal Optical Loss Measurements in 1.3-Mu-M Ingaasp Lasers," *Electronics Letters*, vol. 31, pp. 1157-1159, 1995.

[32] S. C. Kan and K. Y. Lau, "Intrinsic Equivalent-Circuit of Quantum-Well Lasers," *IEEE Photonics Technology Letters*, vol. 4, pp. 528-530, 1992.

[33] I. Esquivias, S. Weisser, B. Romero, and J. D. Ralston, "Carrier capture and escape times in In0.35Ga0.65As-GaAs multiquantum-well lasers determined from high-frequency electrical impedance measurements," *IEEE Photonics Technology Letters*, vol. 8, pp. 1294-1296, 1996.

[34] P. M. Smowton and P. Blood, "Fermi level pinning and differential efficiency in GaInP quantum well laser diodes," *Applied Physics Letters*, vol. 70, pp. 1073-1075, 1997.

[35] E. W. Weisstein, *Cramer's Rule*: MathWorld - A Wolfram Web Resource, http://mathworld.wolfram.com/CramersRule.html.

[36] R. Olshansky, C. B. Su, J. Manning, and W. Powazinik, "Measurement of Radiative and Nonradiative Recombination Rates in Ingaasp and Algaas Light-Sources," *IEEE Journal of Quantum Electronics*, vol. 20, pp. 838-854, 1984.

[37] J. M. Pikal, C. S. Menoni, H. Temkin, P. Thiagarajan, and G. Y. Robinson, "Impedance independent optical carrier lifetime measurements in semiconductor lasers," *Review of Scientific Instruments*, vol. 69, pp. 4247-4248, 1998.

[38] G. E. Shtengel, D. A. Ackerman, P. A. Morton, E. J. Flynn, and M. S. Hybertsen, "Impedance-Corrected Carrier Lifetime Measurements in Semiconductor-Lasers," *Applied Physics Letters*, vol. 67, pp. 1506-1508, 1995.

[39] J. D. Kraus and D. A. Fleisch, *Electromagnetics*.

[40] O. Anton, C. S. Menoni, J. Y. Yeh, L. J. Mawst, J. M. Pikal, and N. Tansu, "Increased monomolecular recombination in MOCVD grown 1.3-mu m InGaAsN-GaAsP-GaAs QW lasers from carrier lifetime measurements," *IEEE Photonics Technology Letters*, vol. 17, pp. 953-955, 2005.

[41] J. J. Liou and F. A. Lindholm, "Capacitance of Semiconductor P-N-Junction Space-Charge Layers - an Overview," *Proceedings of the IEEE*, vol. 76, pp. 1406-1422, 1988.

[42] R. Nagarajan, T. Fukushima, M. Ishikawa, J. E. Bowers, R. S. Geels, and L. A. Coldren, "Transport Limits in High-Speed Quantum-Well Lasers - Experiment and Theory," *IEEE Photonics Technology Letters*, vol. 4, pp. 121-123, 1992.

[43] X. Zhang, A. L. GutierrezAitken, D. Klotzkin, P. Bhattacharya, C. Caneau, and

Reproduced with permission of the copyright owner. Further reproduction prohibited without permission.

R. Bhat, "0.98 mu m multiquantum well tunnelling injection lasers with ultra-high modulation bandwidths," *Electronics Letters*, vol. 32, pp. 1715-1717, 1996.

[44] W. F. Sharfin, J. Schlafer, W. Rideout, B. Elman, R. B. Lauer, J. Lacourse, and F. D. Crawford, "Anomalously High Damping in Strained Ingaas-Gaas Single Quantum-Well Lasers," *IEEE Photonics Technology Letters*, vol. 3, pp. 193-195, 1991.

[45] N. Tansu and L. J. Mawst, "Current injection efficiency of InGaAsN quantum-well lasers," *Journal of Applied Physics*, vol. 97, 2005.

[46] P. M. Smowton and P. Blood, "The differential efficiency of quantum-well lasers," *IEEE Journal of Selected Topics in Quantum Electronics*, vol. 3, pp. 491-498, 1997.

[47] J. M. Ulloa, J. L. Sanchez-Rojas, A. Hierro, J. M. G. Tijero, and E. Tournie, "Effect of nitrogen on the band structure and material gain of InyGa1-yAs1-xNx-GaAs quantum wells," *IEEE Journal of Selected Topics in Quantum Electronics*, vol. 9, pp. 716-722, 2003.

[48] X. Marie, J. Barrau, T. Amand, H. Carrere, A. Arnoult, C. Fontaine, and E. Bedel-Pereira, "Band structure and optical gain in InGaAsN/GaAs and InGaAsN/GaAsN quantum wells," *Iee Proceedings-Optoelectronics*, vol. 150, pp. 25-27, 2003.

[49] S. T. Ng, W. J. Fan, Y. X. Dang, and S. F. Yoon, "Comparison of electronic band structure and optical transparency conditions of InxGa1-xAs1-yNy/GaAs quantum wells calculated by 10-band, 8-band, and 6-band k center dot p models," *Physical Review B*, vol. 72, 2005.

[50] N. Tansu, J. Y. Yeh, and L. J. Mawst, "Experimental evidence of carrier leakage in InGaAsN quantum-well lasers," *Applied Physics Letters*, vol. 83, pp. 2112-2114, 2003.

[51] N. Tansu and L. J. Mawst, "Temperature sensitivity of 1300-nm InGaAsN quantum-well lasers," *IEEE Photonics Technology Letters*, vol. 14, pp. 1052-1054, 2002.

[52] N. Tansu, J. Y. Yeh, and L. J. Mawst, "Low-threshold 1317-nm InGaAsN quantum-well lasers with GaAsN barriers," *Applied Physics Letters*, vol. 83, pp. 2512-2514, 2003.

[53] R. Fehse, S. Jin, S. J. Sweeney, A. R. Adams, E. P. O'Reilly, H. Riechert, S. Illek, and A. Y. Egorov, "Evidence for large monomolecular recombination contribution to threshold current in 1.3 mu m GaInNAs semiconductor lasers," *Electronics Letters*, vol. 37, pp. 1518-1520, 2001.

[54] A. D. Andreev and E. P. O'Reilly, "Theoretical study of Auger recombination in a GaInNAs 1.3 mu m quantum well laser structure," *Applied Physics Letters*, vol. 84, pp. 1826-1828, 2004.

[55] S. Tomic, E. P. O'Reilly, R. Fehse, S. J. Sweeney, A. R. Adams, A. D. Andreev, S. A. Choulis, T. J. C. Hosea, and H. Riechert, "Theoretical and experimental analysis of 1.3-mu m InGaAsN/GaAs lasers," *IEEE Journal of Selected Topics in Quantum Electronics*, vol. 9, pp. 1228-1238, 2003.

Reproduced with permission of the copyright owner. Further reproduction prohibited without permission.

[56] D. J. Palmer, P. M. Smowton, P. Blood, J. Y. Yeh, L. J. Mawst, and N. Tansu, "Effect of nitrogen on gain and efficiency in InGaAsN quantum-well lasers," *Applied Physics Letters*, vol. 86, 2005.

[57] A. Kaschner, T. Luttgert, H. Born, A. Hoffmann, A. Y. Egorov, and H. Riechert, "Recombination mechanisms in GaInNAs/GaAs multiple quantum wells," *Applied Physics Letters*, vol. 78, pp. 1391-1393, 2001.

[58] R. Fehse, S. Tomic, A. R. Adams, S. J. Sweeney, E. P. O'Reilly, A. Andreev, and H. Riechert, "A quantitative study of radiative, Auger, and defect related recombination processes in 1.3-mu m GaInNAs-based quantum-well lasers," *IEEE Journal of Selected Topics in Quantum Electronics*, vol. 8, pp. 801-810, 2002.

[59] G. E. Shtengel, D. A. Ackerman, and P. A. Morton, "True Carrier Lifetime Measurements of Semiconductor-Lasers," *Electronics Letters*, vol. 31, pp. 1747-1748, 1995.

[60] S. Tomic and E. P. O'Reilly, "Gain characteristics of ideal dilute nitride quantum well lasers," *Physica E-Low-Dimensional Systems & Nanostructures*, vol. 13, pp. 1102-1105, 2002.

[61] R. Olshansky, P. Hill, V. Lanzisera, and W. Powazinik, "Universal Relationship between Resonant-Frequency and Damping Rate of 1.3 Mu-M Ingaasp Semiconductor-Lasers," *Applied Physics Letters*, vol. 50, pp. 653-655, 1987.

Reproduced with permission of the copyright owner. Further reproduction prohibited without permission.

CHAPTER 3

Experimental Details

This dissertation chapter describes the experiments carried out in InGaAsN and InGaAs laser aimed at the investigation of the effect of nitrogen incorporation and temperature on gain, carrier density and modulation response. This chapter is divided into the description of the experiments performed below and above threshold. The former consists of the electrical frequency response and impedance measurements that provide the data to carry out the carrier lifetime analysis. In addition, amplified spontaneous emission measurements provided the basis for material gain analysis. Above threshold, the frequency response are obtained via femtosecond optical modulation under laser pulsed bias. Details of the laser diodes, as well as the pulse bias and light detection conditions are also provided.

Reproduced with permission of the copyright owner. Further reproduction prohibited without permission.

3.1. Description of the laser samples

This section describes in detail the laser diodes used in the work described in this dissertation. Two single quantum well (SQW) laser structures with only 0 and 0.5% nitrogen incorporation in the well were investigated in a temperature range of 10-80°C.

The laser structures were grown by metal-organic chemical vapor deposition (MOCVD) at University of Wisconsin-Madison by the group of Professor Luke Mawst [1-16]. These are denominated InGaAsN and InGaAs lasers, depending upon their nitrogen content of 0 and 0.5%, respectively. Nitrogen is utilized to red-shift the bandgap in the InGaAs alloy, therefore producing a shift from λ~1210nm to λ~1290nm. The Indium composition was 40% in both InGaAsN and InGaAs quantum wells. The laser structures are schematically shown on Figure 3.1. They consist of a single $In_{0.4}Ga_{0.6}As_{1-x}N_x$ quantum well 60Å thick surrounded by GaAsP tensile-strain barriers with 100Å-GaAs spacers. The 60Å quantum well is grown under compressive strain, which relaxes from ~2.8% down to ~2.7% when grown with 0.5% nitrogen incorporation. This structure is embedded in a 3000Å – GaAs separate confinement region (SCH), which comprises the intrinsic region of a p^+-n^+ diode delimited by highly doped AlGaAs claddings [4]. An schematic of the band structure of this sample is shown in Figure 3.1. The black region in Figure 3.1 represents a 30Å $GaAs_{0.66}P_{0.33}$ buffer layer, whose purpose is to optimize the cladding-SCH interface quality [4].

Reproduced with permission of the copyright owner. Further reproduction prohibited without permission.

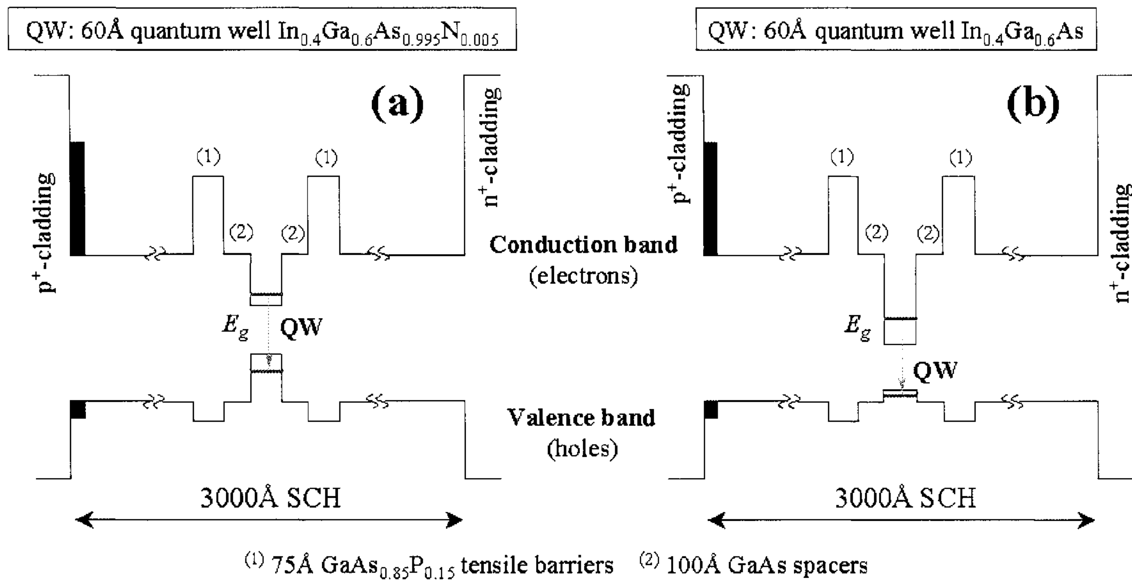

Figure 3.1.- Band diagram of the of the InGaAsN (a) and InGaAs (b) single quantum well (SQW) laser structures studied in this work. The nitrogen percentages in the quantum well are 0.5 and 0, respectively.

The laser structures were grown using Sato's approach [17] which requires the nitrogen to indium ratio to be kept to a minimum therefore reducing the amount of nitrogen required to shift the bandgap from λ~1.2μm to λ~1.29μm. This approach is intended to minimize some of the detrimental effects caused by high-nitrogen incorporation [12, 18]. This required the In content (In>35%) SQW InGaAs laser structures were grown prior to the nitrogen addition [11]. At this In content the QW has a ~2.8% strain.

InGaAs SQW laser structures were optimized to realize emission at λ=1.17-1.21μm, and their and very high characteristic temperature T_0 (~200K). This was accomplished by carefully selecting the cladding material composition and growth procedure [4].

Reproduced with permission of the copyright owner. Further reproduction prohibited without permission.

Once grown with nitrogen incorporation, a dramatic reduction in T_0 was observed that was attributed to am abrupt reduction on the hole confinement [7]. To overcome this, tensile strain barriers surrounding the quantum wells were added as shown in Figure 3.1, effectively improving the overall device performance in terms of T_0 [7]. However, the effect on frequency bandwidth of this SCH design has not yet been investigated. The InGaAsN and InGaAs band diagrams show a large conduction band discontinuity as well as an improved hole confinement provided by the GaAsP barriers.

The InGaAsN and InGaAs structures just described were fabricated into devices by depositing an alloy layer on the n^+ and p^+ claddings, as shown on Figure 3.2. By using appropriate etching masks, a top alloy layer is etched down to a stripe, which can feature a width of 3-4μm or 100μm, as shown by (a) and (b), respectively. Two types of devices were fabricated, according to their stripe width. The devices are identified as narrow-stripe laser (a) and wide-stripe laser (b). After the stripe sides are covered with silicon oxide (SiO_2), a top gold contact is deposited as is shown on Figures 3.2 (a) and (b).

Note the different ratios of passive to active widths of 1/100 and 1/5, shown on (a) and (b), respectively. As discussed on Chapter 2, this results in the narrow-stripe laser having larger parasitics values r_d and similar C_p+C_j, which in the carrier lifetime studies mask the behavior of τ-I. Conversely, the small lateral dimensions of the narrow-stripe devices ensure a good optical mode confinement, which makes them suitable for subthreshold gain and above threshold modulation measurements.

Reproduced with permission of the copyright owner. Further reproduction prohibited without permission.

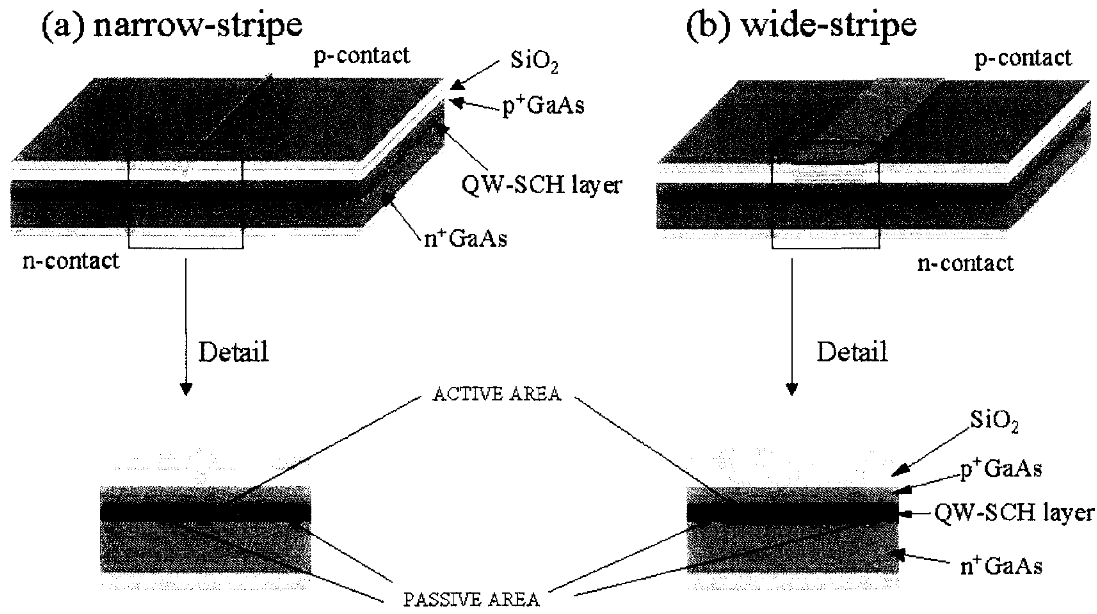

Figure 3.3.- Laser device geometry in (a) narrow-stripe and (b) wide-stripe . Note the different passive/active area ratios, 1/100 and 1/5, respectively as discussed on Chapter 2 and Figure 2.1.

Description	Name	Value
Wide (narrow) stripe width	L_s	100μm (3.5-4μm)
Laser length	L	490-570μm
QW width	L_w	60Å
SCH width	L_{sch}	3000Å
Wide (narrow) stripe SCH volume	V_s	60 (2.4) 10^{-12}cm^{-3}
Spontaneous emission factor	β	$8.7\cdot10^{-5}$
Internal losses	α_i	6-15 cm^{-1}
Mirror losses	α_m	~22 cm^{-1}
Optical confinement factor	Γ	0.018
QW to SCH volume ratio	Γ_q	0.02
Parasitic inductance	L_p	~1nH
Parasitic capacitance (I>5mA)	C_p+C_j	~100pF
Current injection efficiency	η or η_{inj}	0.58-0.79 (see Chapter 2)
Wide (narrow) stripe cladding resistance	r_s	<0.2Ω (<1Ω)

Table 3.1.- Typical parameters in wide and narrow-stripe InGaAsN and InGaAs lasers and driving circuitry.

Reproduced with permission of the copyright owner. Further reproduction prohibited without permission.

Despite their different widths, the narrow-stripe and wide-stripe lasers have the same length. In similar way, all the laser devices are as-cleaved, namely their facet mirror reflectivity is that imposed by the semiconductor air interface, of the order of 0.32. Other relevant parameters of the laser devices are shown in Table 3.1.

3.2. Experimental conditions

3.2.1 Active area temperature

The different experiments were carried out under different pulse or DC bias conditions which are summarized in Table 3.2. In order to accurately know the active area temperature in each particular experiment, we experimentally determined the Joule heating on each particular case. Therefore, a study based on laser spectral emission was performed on narrow and wide-stripe lasers.

By using the Advantest 8584 optical spectrum analyzer, the spectral emission of one of the laser modes was tracked above threshold, for different injection conditions and baseplate temperature settings, using different pulsewidths, from 100ns (Joule heating) up to DC bias (complete heating). In this procedure, the laser amplified spontaneous emission (ASE) was measured above threshold. The red shift in the wavelength of one of the oscillation peaks qualitatively indicates the active area change in temperature. The experiment was conducted in two steps: (i) measure λ versus T with 100ns pulses and $<1\%$ duty cycle, and (ii) measure λ versus I at different pulse widths. Part (i) was accomplished in narrow and in wide-stripe lasers with stripe dimensions 3.5x500 and 100x500 μm^2 respectively and parameters as given in Table 3.1. When biasing both types

Reproduced with permission of the copyright owner. Further reproduction prohibited without permission.

of lasers with <500ns pulses and 1% duty cycle, we measured λ versus T and found a thermal slope of ~0.88Å/K in InGaAsN and InGaAs lasers. This intrinsic parameter was similar to that in InP based lasers [19]. By increasing the pulsewidth to that of the experimental conditions in Table 3.2 we obtained the wavelength fluctuation in each case. Then the ratio of λ/T and λ/I slopes obtained from (i) and (ii), respectively, retrieved thermal conductance values of ~0.025-0.037°C/mA and 0.022°C/mA in narrow and wide-stripe lasers, respectively, under operating conditions of Table 3.2.

Based on these findings, the experimental conditions of the lifetime and impedance measurements in Table 3.2 raised the active area temperature from 0 to up to 4.4°C in both cases. This heating is small compared with the difference in the baseplate temperature ranges of 10, 20, 40, 60 and 80°C, and also is comparable with the accuracy of the thermo-electric cooler (TEC) at the baseplate (~1.5°C). Therefore, we assumed a compromise and have added 2°C average to the baseplate and assumed an uncertainty of ±2°C for the active area temperature, as shown in Table 3.2.

The amplified spontaneous emission measurements (ASE) were performed on narrow-stripe lasers. A pulsewidth of 2μs, shown on Table 3.2, was only utilized at very low currents, under 2mA, in order to obtain reasonable signal-to-noise ratios. Instead pulses as narrow as ~400ns and duty cycle <2% were used for the measurements up to the threshold current. Under these circumstances, the heating in the active area was negligible, thus we assumed the same temperatures as in the baseplate.

The measurements above threshold were performed with bias currents that reached 60mA in InGaAsN narrow stripe lasers. The wavelength shift results measured at 10μs

Reproduced with permission of the copyright owner. Further reproduction prohibited without permission.

pulsewidth and 2% duty cycle led to a maximum heating of approximately 1.2°C, wich is still within the uncertainty of the TEC.

Measurement	**Stripe/Device**		**Pulse width**	**Baseplate temperature**				
				10°C	**20°C**	**40°C**	**60°C**	**80°C**
Lifetime Impedance	wide wide	InGaAsN /InGaAs	120μs	12	22	42	62	82
ASE	narrow	InGaAsN /InGaAs	0.4-2μs	10	20	40	60	80
Frequency response	narrow	InGaAsN /InGaAs	10μs	10	20	40	60	80

Table 3.2 - True active area temperature in the narrow-stripe and wide-stripe lasers. The active area temperature is shown in the yellow background.

Typical threshold currents for InGaAsN and InGaAs laser over the range of temperature of the experiments are summarized in Tables 3.3 and 3.4.

Wide-stripe SQW lasers		
T, °C	Threshold current, *Ith*, mA	
	InGaAsN	InGaAs
10	211	73
20	246	80
40	333	93
60	451	119
80	611	159
T_0	**65K**	**90K**

Table 3.3.- Threshold current I_{th} in InGaAsN and InGaAs wide-stripe lasers, where L=580 and 530μm, respectively.

Reproduced with permission of the copyright owner. Further reproduction prohibited without permission.

Narrow-stripe SQW lasers				
T, °C	Threshold current, Ith, mA		dP_0/dI, W/A (per facet)	
	InGaAsN	InGaAs	InGaAsN	InGaAs
10	10.4	8.2	0.197	0.180
20	11.7	9.4	0.193	0.177
40	14.6	10.8	0.143	0.171
60	19.3	13.2	0.112	0.166
80	29.6	17.0	0.072	0.160
T_0	**66K**	**102K**		

Table 3.4.- Threshold current I_{th} and differential slope dP_0/dI in InGaAsN and InGaAs SQW lasers, where L=570 and 520µm, respectively.

3.3. Experiments below threshold

This section describes the subthreshold impedance and frequency response measurements in InGaAsN and InGaAs SQW wide-stripe lasers. Details about their experimental setups are described in 3.3.1 and 3.3.2. In addition to impedance measurements, the typical current-voltage measurements are described in 3.3.1.

Section 3.3.3 described the experiments on amplified spontaneous emission (ASE) measurements, which were performed on narrow-stripe lasers.

3.3.1. Subthreshold impedance measurements

Figure 3.3 shows the setup for electrical impedance measurements performed on wide-stripe lasers. The test laser is placed in a custom designed probe, in between a flexible arm and a baseplate which contacts its anode and cathode, respectively. The space in between the probe arm and baseplate is adjustable in the order of 0-0.5mm by a

Reproduced with permission of the copyright owner. Further reproduction prohibited without permission.

stage (not shown). The baseplate temperature is set within a temperature range T=10-80°C in five steps at 10, 20, 40, 60 and 80°C. It is controlled to ±1°C accuracy by a thermoelectric cooler (TEC) and an electronic sensor shown in the figure connected to an ILX controller.

As shown in Figure 3.3 (b), the probe is soldered to a 50Ω microstrip line built with a low-loss dielectric material, which is terminated in a SMA connector on the left. As shown in Figure 3.3 (a), a 30cm transmission line connects this assembly with PORT 1 of a Agilent 8753 vector network analyzer (VNA). The network analyzer is set to measure the S_{11} parameter from 1MHz to 1GHz in a log-scale, versus bias currents up to 20% below threshold. The laser is DC biased through the internal bias tee provided by the network analyzer. The electrical diode impedance is obtained from the S_{11} parameter by bilinear transformation [20].

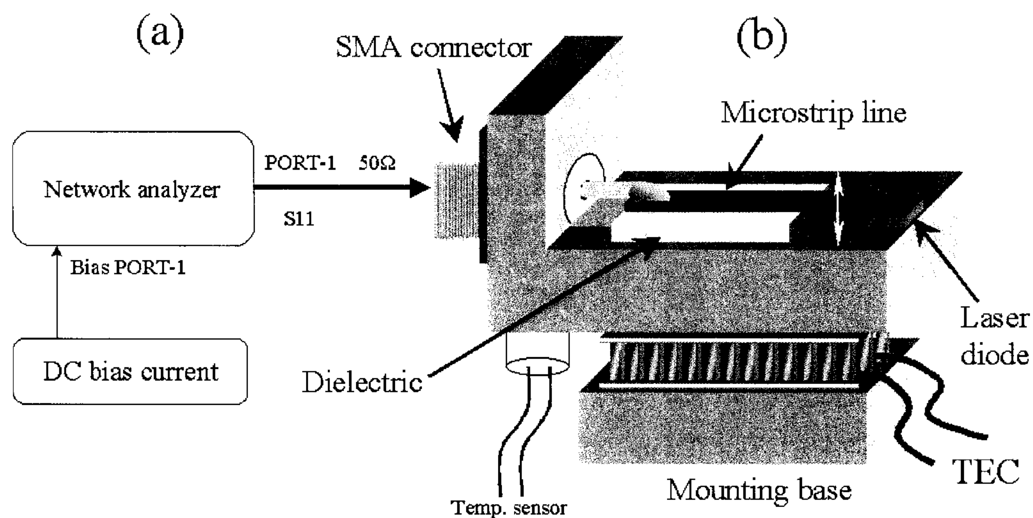

Figure 3.3.- (a) Setup for electrical impedance measurements on wide-stripe lasers. (b) Detail of the probe arm touching the test laser.

Reproduced with permission of the copyright owner. Further reproduction prohibited without permission.

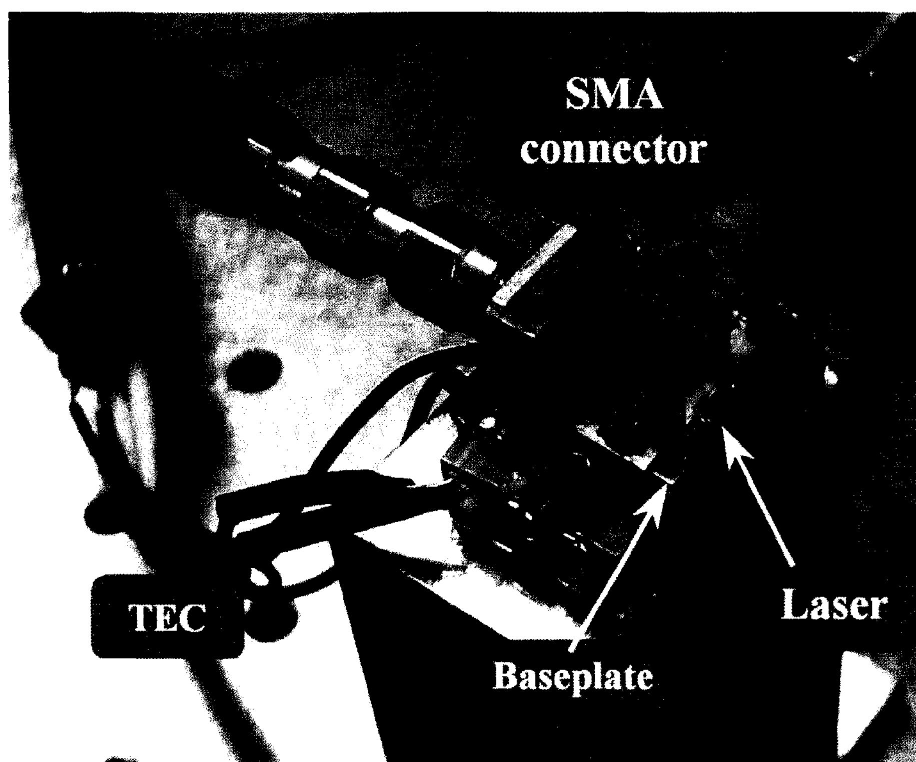

Figure 3.4.- (c) Photograph of the baseplate for electrical impedance measurements.

Prior to the measurement of S_{11}, the network analyzer is calibrated by a standard procedure in three steps. These steps consist of performing measurements of an open and short circuit, which are obtained by keeping the probe to 100μm above and touching the baseplate, respectively. The last step consists in measuring a 50Ω low-parasitics resistor with gold contacts at its top and bottom, which is placed at the end of the probe instead of the test laser.

Figure 3.5 shows typical impedance traces in terms of real and imaginary parts, as directly obtained from the network analyzer. Although each pair of traces seems to represent a complex process, most of them are simply fitted by a single pole expression similar to that of a parallel *R-C* circuit.

Reproduced with permission of the copyright owner. Further reproduction prohibited without permission.

In addition to the impedance experiment, the current-voltage (*I-V*) measurements were obtained using the same setup. A HP 4145A semiconductor parameters analyzer was connected to the SMA probe connector of Figure 3.3 (b). Fast current ramps of I=0-100mA were run while measuring the diode voltage. The setup was previously calibrated by running a short circuit measurement as the one described above.

A typical *I-V* trace for InGaAs wide-stripe laser is shown in Figure 3.6. The fit of *I-V* measurements using equation (3.1) provides accurate values of the dynamic resistance $r_d = dV/dI$ and the cladding resistance r_s.

$$I = I_s \cdot \left[e^{\frac{(V - I \cdot r_s) \cdot q}{k_B T \cdot n}} - 1 \right] \tag{3.1}$$

In (3.1), I_s is the saturation current, n is the typical ideality factor for a *p-n* junction and k_B the Boltzmann constant, where k_B /q is ~0.086mV/K [21].

These parameters are added to the electrical diode impedance traces for the study of electrical parasitics described on Section 2.3. The parasitics are obtained in Section 4.2.1 by utilizing the algorithms implemented in Matlab, as shown on Appendix 2.

Reproduced with permission of the copyright owner. Further reproduction prohibited without permission.

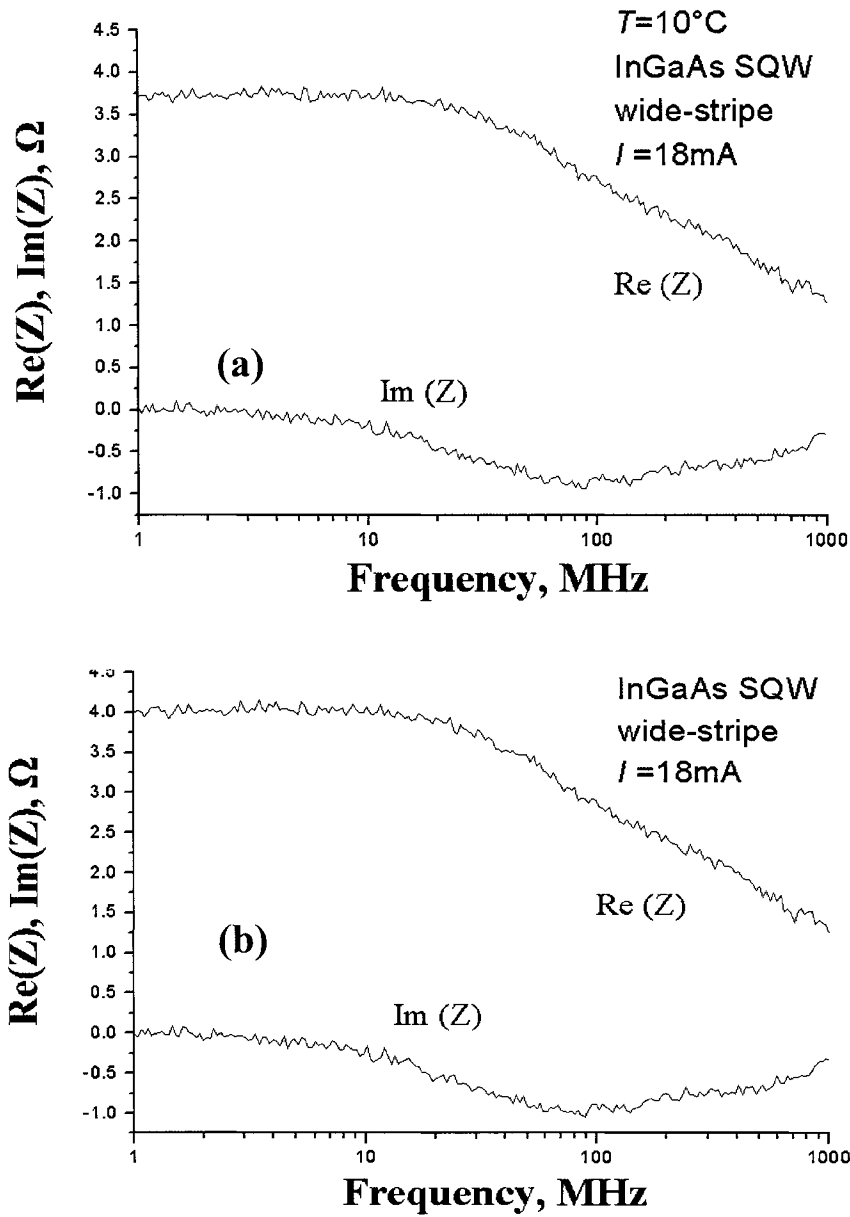

Figure 3.5.- Typical raw impedance data from S11 measurements versus frequency in wide-stripe InGaAs SQW lasers at (a) T=10°C and (b) T=80°C.

Reproduced with permission of the copyright owner. Further reproduction prohibited without permission.

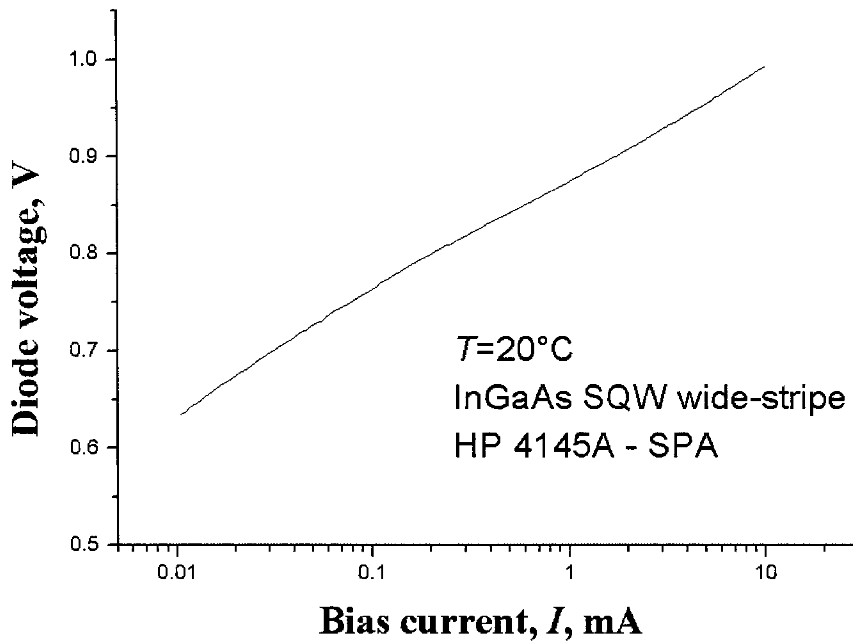

Figure 3.6.- Typical I-V traces in InGaAs wide-stripe SQW lasers at room temperature, obtained with HP 4145A semiconductor parameter analyzer.

3.3.2. Subthreshold frequency response

Frequency response measurements were taken in wide-stripe lasers at currents below 200mA and in a temperature range similar to that of the impedance experiments. Current pulses were utilized to bias the laser diode, in order to avoid excessive heating that could deteriorate the device.

Similar to impedance measurements, the frequency response was measured using the network analyzer in a frequency range up to 1GHz. However in this case S_{12} is measured. The wide-stripe test laser was mounted on a baseplate similar than that of impedance measurements for these experiments. Some changes were implemented in the probe arm

Reproduced with permission of the copyright owner. Further reproduction prohibited without permission.

that contacts the laser anode. Inserted in the microstrip line was a high frequency 500Ω series resistor. Figure 3.7 (a) shows the 50Ω resistor connected to a 5nF capacitor that normalizes the impedance at the SMA input connector to ~50Ω. The SMA connector was connected to a bias tee and then to Port-1 of the Agilent 8753 network analyzer, as is shown in Figure 3.7 (b).

Above I=20mA, the frequency response was measured under pulsed bias. Bias pulses of 120μs with 10% duty cycle were coupled through the external bias tee and launched into the test laser. This was done to avoid laser deterioration. The real active area temperatures at which measurements were performed are shown on Table 3.1. The network analyzer was set to a logarithmic frequency sweep from 10MHz to 1GHz and its bandwidth was set to IF=10Hz to minimize the thermal noise at the VNA's input stage. The network analyzer was triggered by the bias pulses in order to sample only when the test laser is turned on. Below I=20mA, the frequency response was measured with DC bias, similarly to impedance, in a frequency range of 1MHz to 1GHz.

Although the duty cycle of the bias pulses avoided laser damage, the pulse length allowed the laser active area to reach its thermal steady state, that is, the active area's temperature is similar to that as under DC bias, as described in the impedance measurements.

Reproduced with permission of the copyright owner. Further reproduction prohibited without permission.

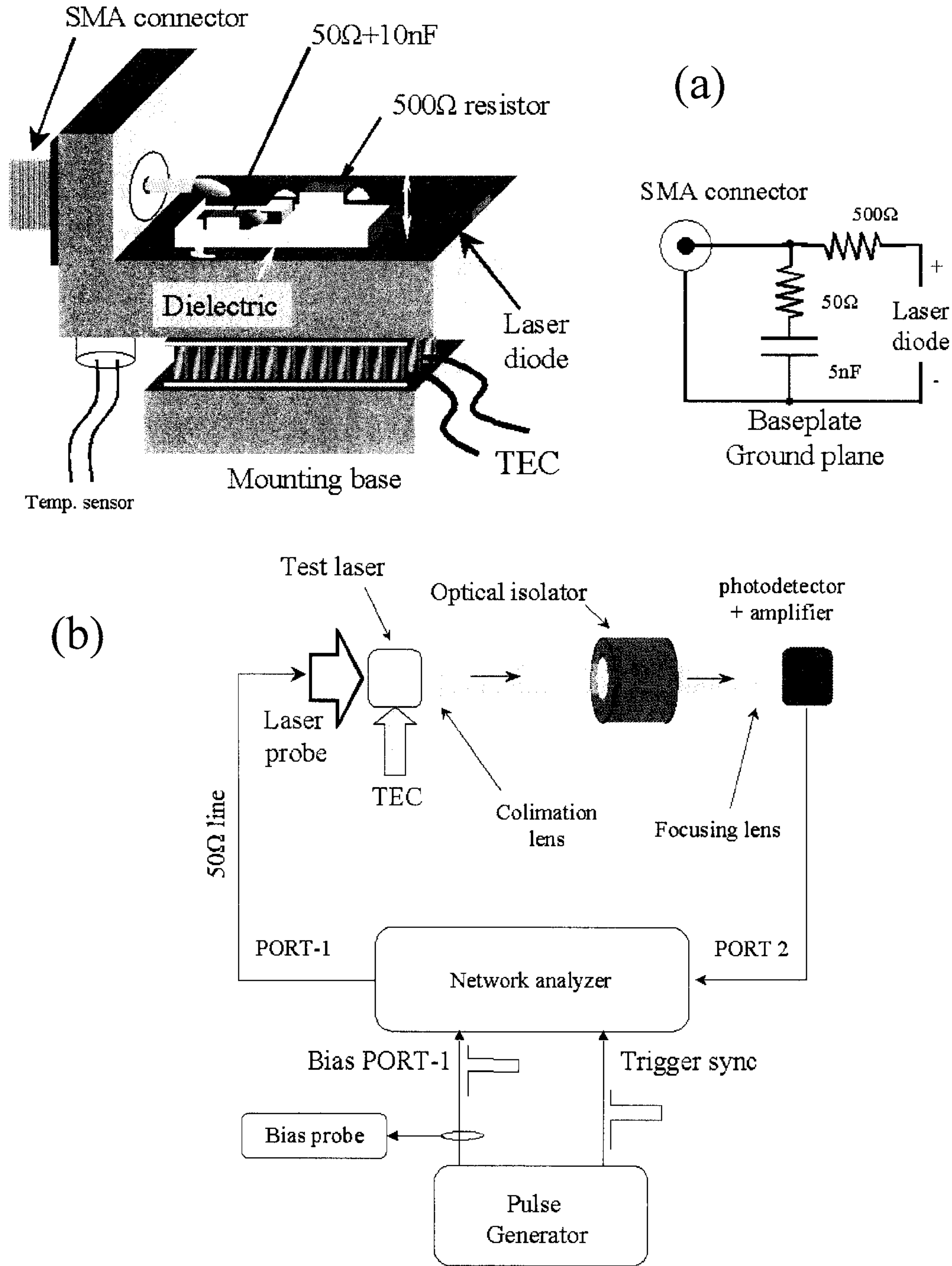

Figure 3.7.- (a) Setup for frequency response measurements on wide-stripe lasers. (b) Detail of the circuit in the probe's arm.

Reproduced with permission of the copyright owner. Further reproduction prohibited without permission.

The bias tee consisted of a modified Picosencond-Labs 5550, in which the DC port bandwidth was increased by reducing the value of its first inductor. The resulting bias tee design accommodates the 100KHz bandwidth to permit the bias pulses to reach the laser. At the same time, the bias tee combined the bias with the laser 1MHz-1GHz RF modulation.

The test laser spontaneous emission was collimated with a large numerical aperture lens of 3mm focal length. The beam was refocused by a second lens into a 100μm diameter New Focus 1611 InGaAs photodetector, which was connected to the Port-2 of the 8753 network analyzer.

The frequency response of the laser diode was obtained form the S_{21} parameter versus frequency measured by the VNA after being calibrated. The calibration procedure consisted of coupling a custom designed SMA adaptor plugged into to the probe that replaced the test laser, and then performing a loop S_{21} measurement with cables and bias tee included. Although the photodetector was not included in the calibration loop, its frequency response is known to be flat within 1dB in the measurement range. Typical frequency response traces for InGaAsN and InGaAs lasers are shown in Figure 3.8.

As simple single pole fit of the data was performed to least squares obtain the time constant τ. The software tools developed to analyze the measured FR traces is briefly outlined in Appendix 2.

Reproduced with permission of the copyright owner. Further reproduction prohibited without permission.

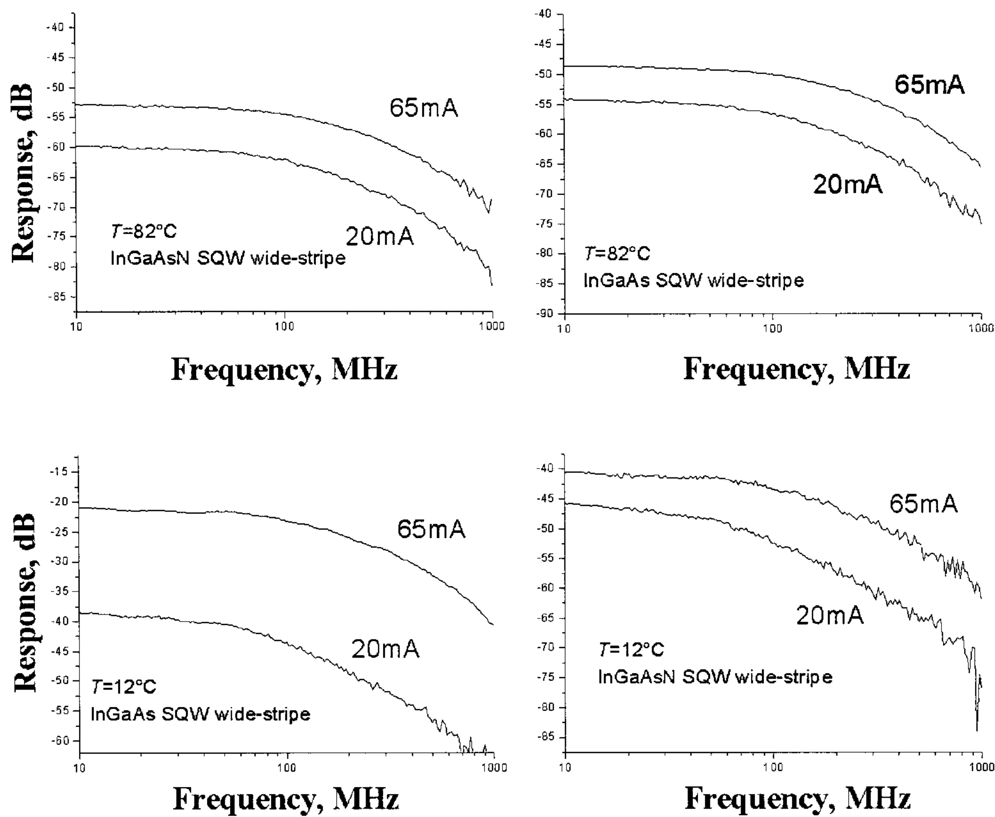

Figure 3.8.- Typical frequency response traces in InGaAsN and InGaAs wide-stripe lasers below threshold at (a) T=10°C and (b) T=80°C

Combined with the impedance measurements of Section 3.3.1, the frequency response experiments below threshold provide the necessary information to conduct the differential carrier lifetime analysis in InGaAsN and InGaAs wide-stripe lasers in Section 4.2.

3.3.3. Amplified spontaneous emission

ASE measurements were performed in InGaAsN and InGaAs narrow-stripe devices under pulses bias current. The test lasers were mounted on a clip baseplate connected as

Reproduced with permission of the copyright owner. Further reproduction prohibited without permission.

shown in Figure 3.9. The baseplate was controlled in temperature with the same setup as that in Sections 3.3.1 and 3.3.2. Temperature values were set identically as previously.

Current pulses of <2μs and 2% duty cycle biased the test lasers, whose peak current amplitude was monitored by a current probe as shown in Figure 3.9. The amplified spontaneous emission at the laser facet was collected by a 0.55 numerical aperture lens, coupled into a single-mode SF-28 fiber and measured by using an Optical Spectrum Analyzer (OSA) as shown in Figure 3.9. The OSA was set to a resolution of 0.01nm, span of 100nm and centered at λ=1300nm (λ=1200nm) for the InGaAsN (InGaAs) narrow-stripe lasers.

Figure 3.10 shows typical raw traces obtained from the optical spectrum analyzer. There is a shift of ~75meV in the emission maximum due to the addition of nitrogen into the quantum well as seen in (a)-(c)-(e). As the temperature is increased there is a red shift and broadening in the ASE, as in the sequence (b)-(d)-(f) for InGaAsN. The inset in (a) shows the oscillation period ~5Å of the Fabry –Perot laser cavity that is given by (3.2), where L is the cavity length, n the effective index of refraction (n~4.2 [22]), and λ the laser emission wavelength.

$$\Delta\lambda = \frac{\lambda^2}{2nL} \tag{3.2}$$

The ASE traces were analyzed to obtain modal gain by utilizing the Hakki and Paoli technique [23], as done in Section 4.4 by utilizing the Matlab-implemented algorithm described on Appendix 6. The analysis of these results provides a complete set of traces

Reproduced with permission of the copyright owner. Further reproduction prohibited without permission.

of gain versus wavelength λ, obtained at different bias currents and temperatures, which are further studied in Section 4.4.2.

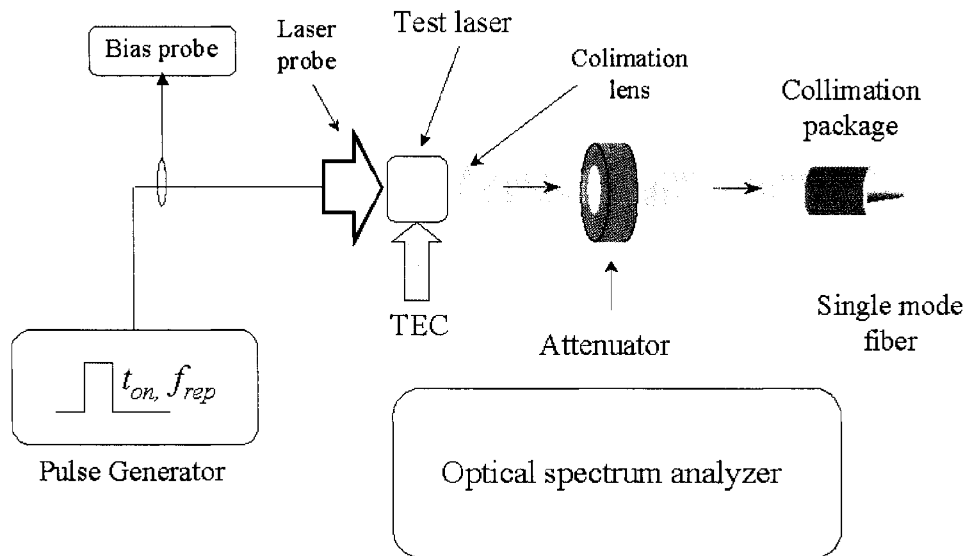

Figure 3.9.- Setup of Amplified Spontaneous Emission measurements in narrow-stripe lasers.

Reproduced with permission of the copyright owner. Further reproduction prohibited without permission.

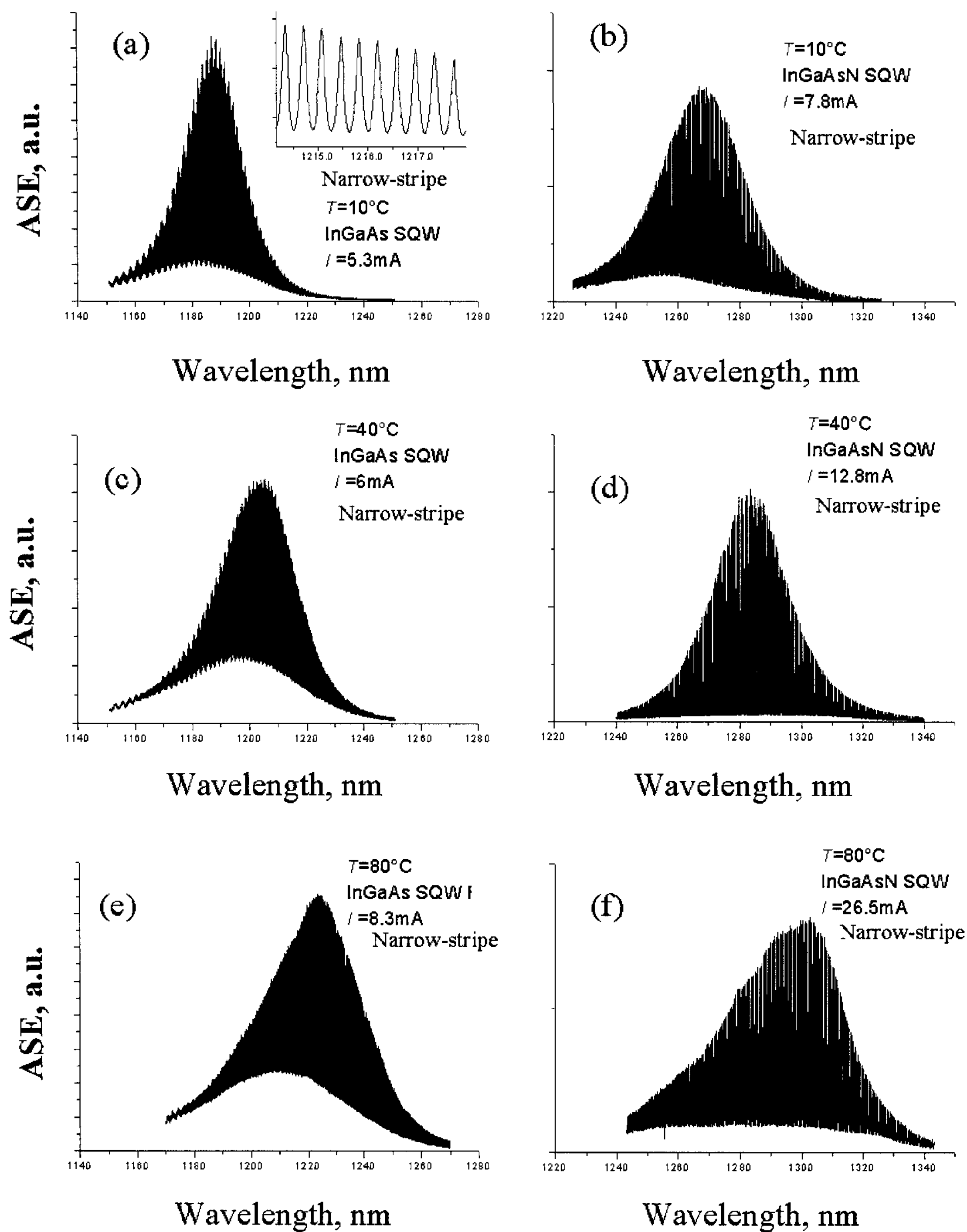

Figure 3.10.- Typical Amplified Spontaneous Emission traces obtained in InGaAsN and InGaAs SQW narrow-stripe lasers at T= 10, 40 and 80°C and at different bias points.

Reproduced with permission of the copyright owner. Further reproduction prohibited without permission.

3.4. Experiments above threshold

This section is devoted to describe the frequency response measurements performed above threshold in 1.3μm InGaAsN and 1.2μm InGaAs SQW narrow-stripe lasers versus bias and temperature. Frequency responses were obtained using optical and electrical injection. However the latter were not useful to obtain the relevant resonance frequency and damping parameters due to the influence of parasitics. These traces are however useful to validate the model described in Chapter 2.

I start by discussing in Section 3.4.1 the optical injection measurements, which use a technique developed in our group.

3.4.1. Optical frequency response

The frequency response of narrow-stripe laser devices was obtained above threshold by optical injection. Previously developed for the characterization of 1.3μm InAsP/InGaAsP/InP MQW laser diodes [24]. This approach uses short optical pulses of tunable wavelength to photogenerate carriers and perturb the carrier population in different regions of the laser active area. By utilizing a spectrum analyzer connected to a photodetector, this technique measures the laser impulse response in the frequency domain and then extracts the frequency response from its envelope.

In this scheme, a small signal perturbation is produced by sub-picosecond optical pulses impinging into the laser active area, as it is sketched on Figure 2.12. The pulses are generated at a repetition rate of ~81MHz by either an Optical Parametric Oscillator (OPO) or Ti:sapp laser, covering wavelength ranges of λ=1040-1350nm and

Reproduced with permission of the copyright owner. Further reproduction prohibited without permission.

λ~780-820nm, respectively. Further details on the pulse generation and shaping are described in previous works [24-26]. The pulse time and frequency domain representations of the input signal to the device are shown on Figure 2.13.

The pulses are impinged into one of the laser's facets by the setup shown on Figure 3.11, in where the excitation beam creates electron-hole pairs by reaching one of the bandgaps of the laser structure (Figure 2.13 (a)). The geometry was necessary because the narrow-stripe lasers have absorbing GaAs layers that prevent accessing the active area through the device's side as done in InAsP [24].

The modulation into the facet was achieved by utilizing λ~800nm (*hv*~1.55eV) from the Ti:Sapp for SCH injection or λ~1100nm (*hv*~1.23eV) from the OPO for injection into the quantum well. The optical pulses were focused on the back facet of the laser diode by a lens of 19mm focal length attached to a X-Y-Z positioner.

This scheme produced a local modulation in the active area, where the modulation index and therefore signal at the laser output was reduced in comparison with that of the side-injection scheme [24]. Nevertheless, the signal level provided in the experiments by the transimpedance photodetector is large enough to ensure measurement of frequency response up to 12GHz.

Reproduced with permission of the copyright owner. Further reproduction prohibited without permission.

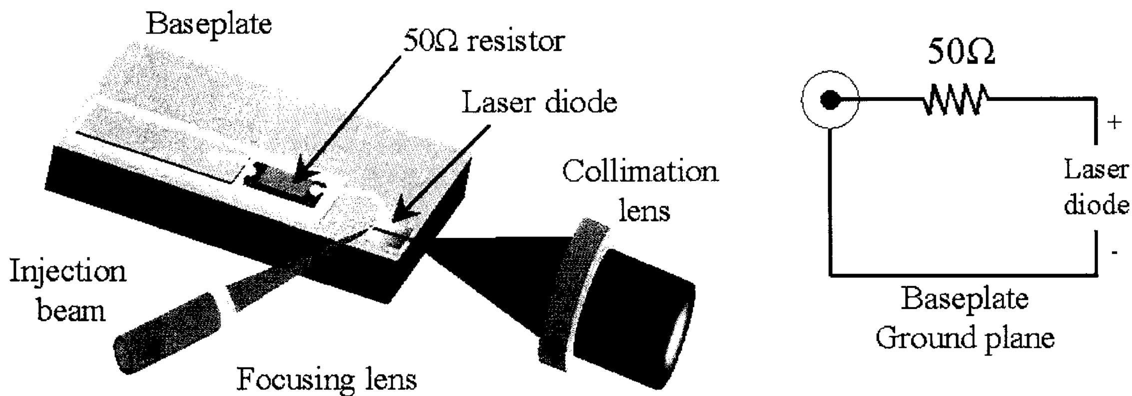

Figure 3.11.- Setup geometry of optical modulation frequency response in narrow-stripe laser diodes. The OPO or Ti:Sapphire is impinged on one facet whereas the laser emission is measured from the other.

In theory, the model described in Section 2.1.2 describes the laser's small signal perturbations. At the experimental level, the small signal modulation conditions are set by adjusting the intensity of the optical pulses to a level where the laser diode output and the peak wavelength shifts in less than 5% and 0.8Å, respectively, as shown by Figure 3.13.

Figure 3.12 shows the schematics of the frequency response measurements with optical modulation. After impinging into the laser back facet, the laser output beam was collimated by a first lens of 2.9mm focal length and 0.55 numerical aperture (N.A.) held by a XYZ stage. The beam traveled through a low pass optical filter (LPF) that rejects wavelengths shorter than 1150nm, followed by an optical isolator that prevents any optical feedback. At the end, the beam was focused into a New Focus 1567 photodetector by a 10mm focal-length lens positioned by a XYZ stage.

Reproduced with permission of the copyright owner. Further reproduction prohibited without permission.

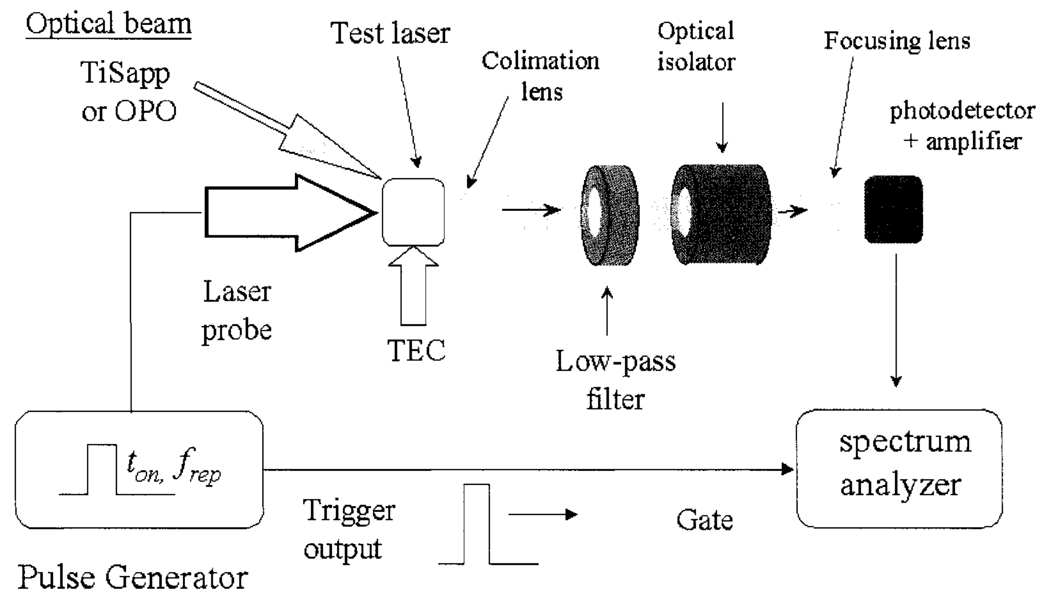

Figure 3.2.- Schematics of the optical modulation frequency response setup. (a) After passing through an optical isolator and LPF, the laser output is impinged into a photodetector/spectrum analyzer.

The electrical output of the photodetector is shown in Figure 3.14 (a), where its shape is identical to that of the bias pulses. The superimposed arrows correspond to the laser impulse response shown in detail on Figure 2.13 (a).

The photodetector output, with typical signal levels of –85dBm to –30dBm, was connected to a HP8563 spectrum analyzer. The spectrum analyzer span is set to 70MHz-12GHz under gated operation [27]. To gain insight into the gated detection scheme, Figure 3.14 (b) and (c) show the detected signal inside the spectrum analyzer. The spectrum analyzer analyzes the incoming signal one frequency at a time, downconverting it to an intermediate frequency f_{IF} shown in Figure 3.14 (b).

Reproduced with permission of the copyright owner. Further reproduction prohibited without permission.

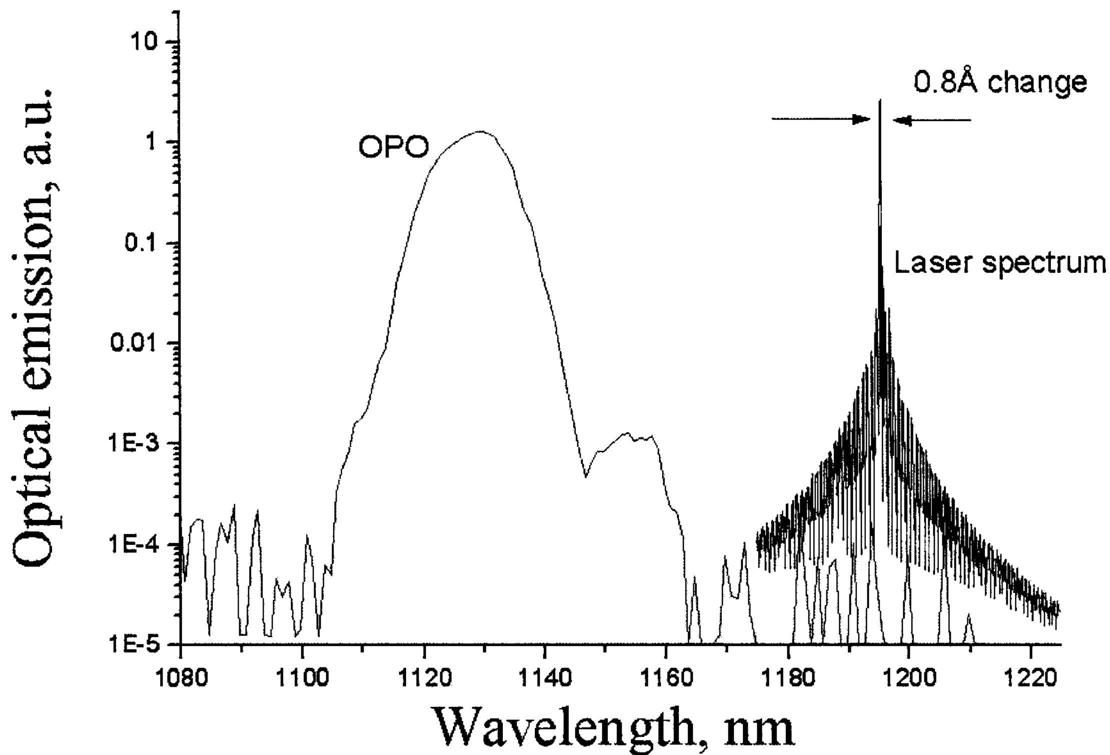

Figure 3.13.- Typical laser emission and OPO spectra. The OPO features larger photon energy than that of the laser emission, producing absorption in the laser QW. When either OPO or Ti:Sapp are impinged into the laser facet, the laser emission changes in less than 1Å in wavelength and 5% in intensity.

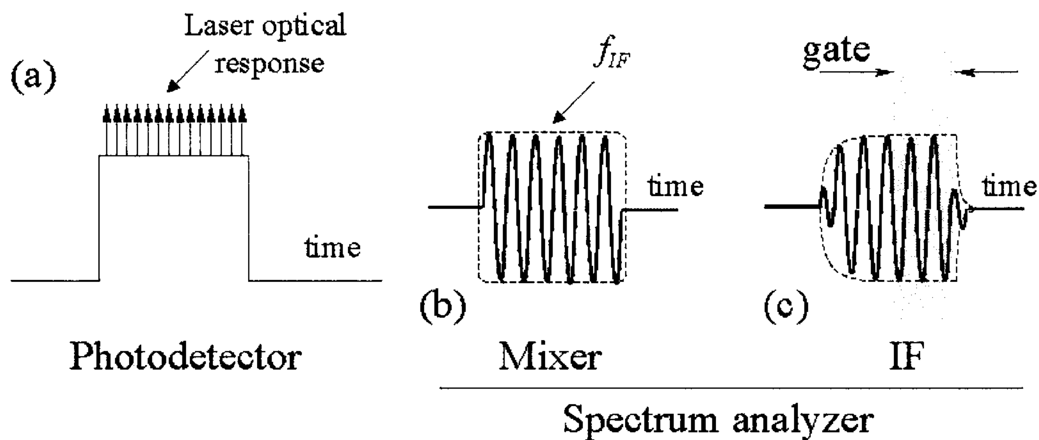

Figure 3.14.- Electrical waveforms for 10μs bias pulses: (a) photodetector output, (b) spectrum analyzer: mixer's output, and (c) IF signal, for 6μs gate time.

Reproduced with permission of the copyright owner. Further reproduction prohibited without permission.

The signal is smoothed by the response of the IF bandwidth, which acts as a low pass filter. Therefore, the IF bandwidth has to be large enough to provide a flat envelope in (c) during the gating process (shaded), but at the same time it must be small enough to minimize the noise floor [27]. The trade off indicated that, for typical 10μs bias pulses, the IF bandwidth must be set to 100KHz.

Figure 3.15 shows typical raw traces obtained at T=10°C and 80°C in InGaAs SQW narrow-stripe lasers from the spectrum analyzer under optical OPO injection.

Crosstalk signal was not observed when injecting with the Ti:Sapp laser, as the 1150nm low-pass filter (LPF) strongly attenuates the beam (λ=800nm).

The complete system is calibrated by impinging the attenuated injection beam into the photodetector and measuring its frequency response. This was done by adding two mirrors and a 100 times attenuator to deflect the OPO beam to the photodetector's fiber. The calibration frequency response shown on Figure 3.16 served as the calibration reference for each one of the measured traces.

The test narrow-stripe lasers were mounted on a baseplate controlled by a thermoelectric cooler (TEC). The baseplate was set to five different temperatures: T=10, 20, 40, 60 and 80°C to ±1°C, in similar fashion to the experiments described above. Detailed values of the device threshold current I_{th} and slope efficiency dP_0/dI are shown on Table 3.4 for the set of narrow-stripe devices characterized above threshold. Pulsed bias was used to perform these measurements under identical conditions than in frequency response measurements as described in Table 3.2.

Reproduced with permission of the copyright owner. Further reproduction prohibited without permission.

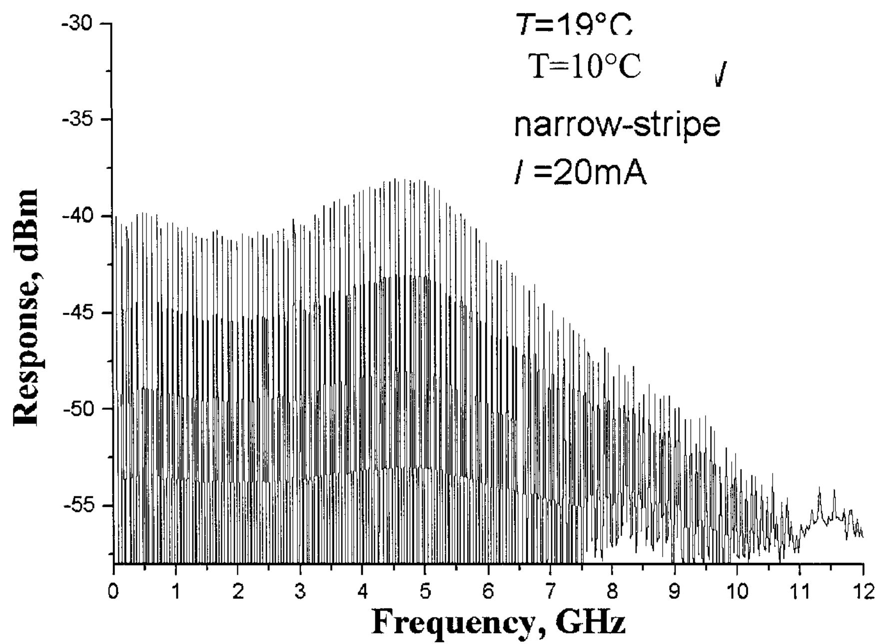

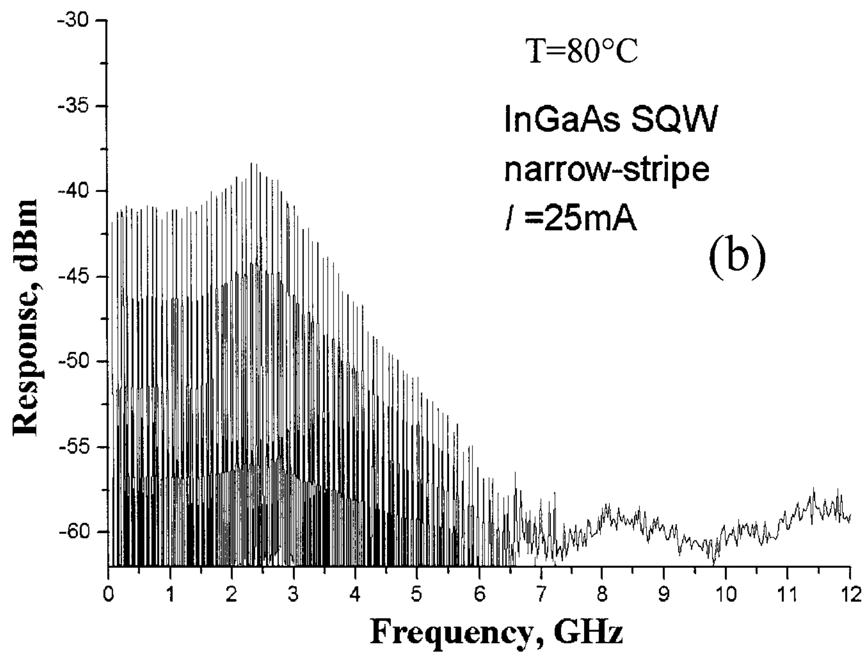

Figure 3.15.- Typical measured traces with spectrum analyzer and OPO injection in InGaAs narrow-stripe SQW lasers at (a) T=10°C and (b) T=80°C. Similar traces were observed in InGaAsN narrow-stripe lasers.

Reproduced with permission of the copyright owner. Further reproduction prohibited without permission.

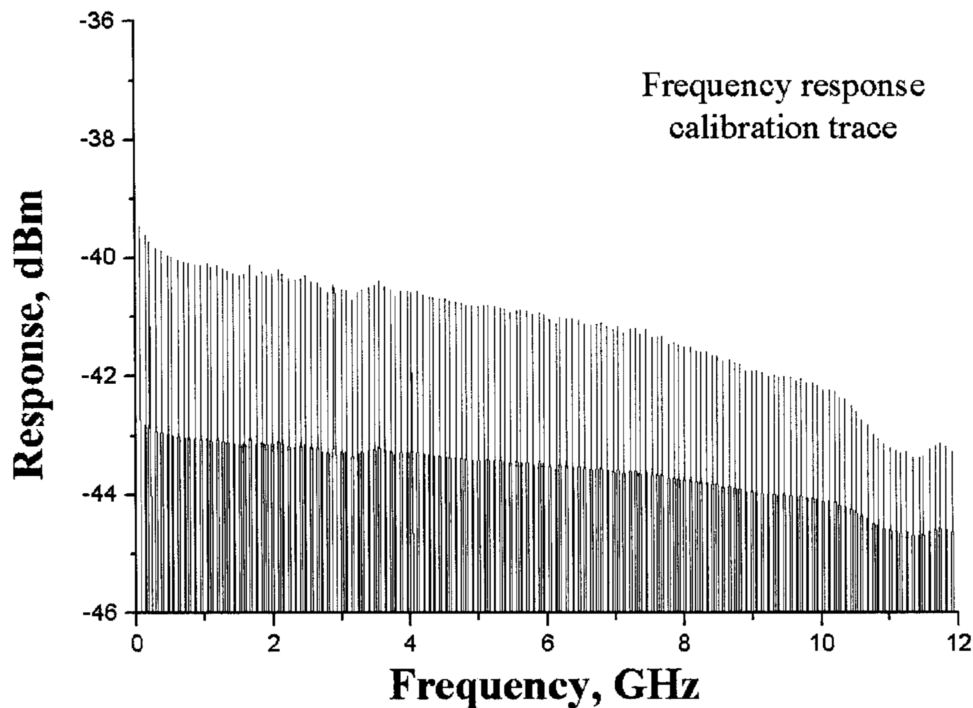

Figure 3.16.- Calibration frequency response traces obtained by impinging the attenuated OPO beam onto the high speed photodetector.

3.4.2 Electrical frequency response

In the optical modulation measurements described on Figure 3.11, the circuitry bonded to the laser diode was used only to provide the bias pulses. However, this circuitry was carefully designed to couple electrical modulation to the laser diode as well. Figure 3.17 shows details about the microstrip line that is connected to the laser diode through a 50Ω resistor. This low inductance resistor provides the impedance match to the laser diode on the right side to the transmission line within a bandwidth of approximately 10GHz. The parasitics inductance of the wire bond is in the order of L_p=1nH.

Reproduced with permission of the copyright owner. Further reproduction prohibited without permission.

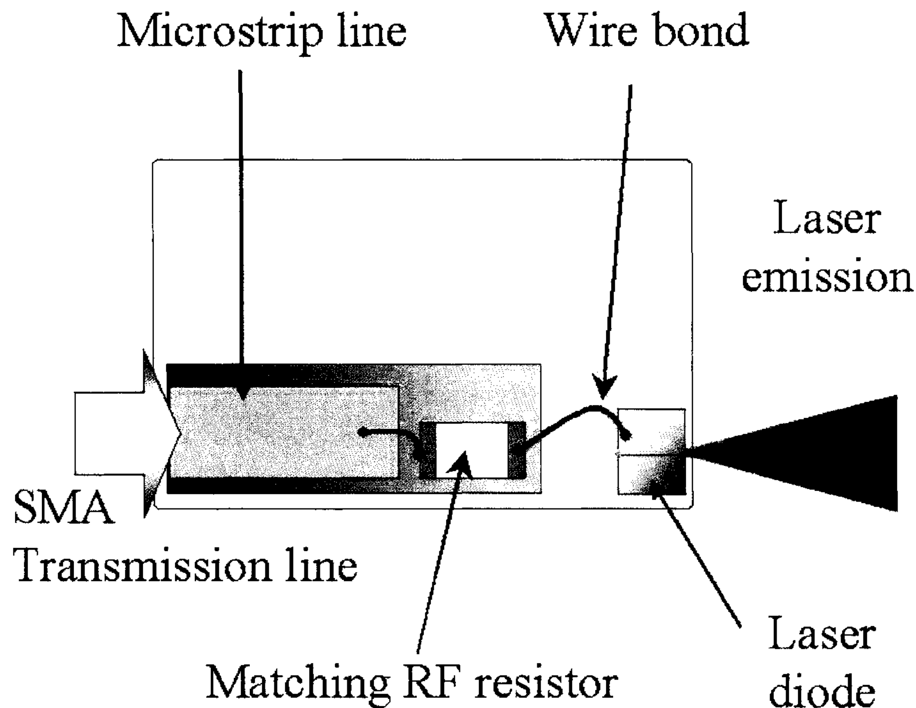

Figure 3.17.- Detailed schematics of the laser probe on Figure 3.11. A microstrip line couples the bias and modulation into the laser diode through an impedance matching resistor.

Similarly to Section 3.4.1, this transmission line supplies the bias pulses and the RF modulation to the laser which are identical to that used in the optical experiments. Figure 3.18 shows the details of the experiment to measure the frequency response by electrical modulation. The laser probe is connected to a 40GHz Agilent 8722 VNA, with a geometry that resembles the schematics in Figure 3.7.

In this case, a 30cm cable connects the probe to PORT-1 at the VNA. The VNA has an internal bias tee that permitted the 10μs bias pulses to reach the test laser at the same time that the RF modulation was provided.

Reproduced with permission of the copyright owner. Further reproduction prohibited without permission.

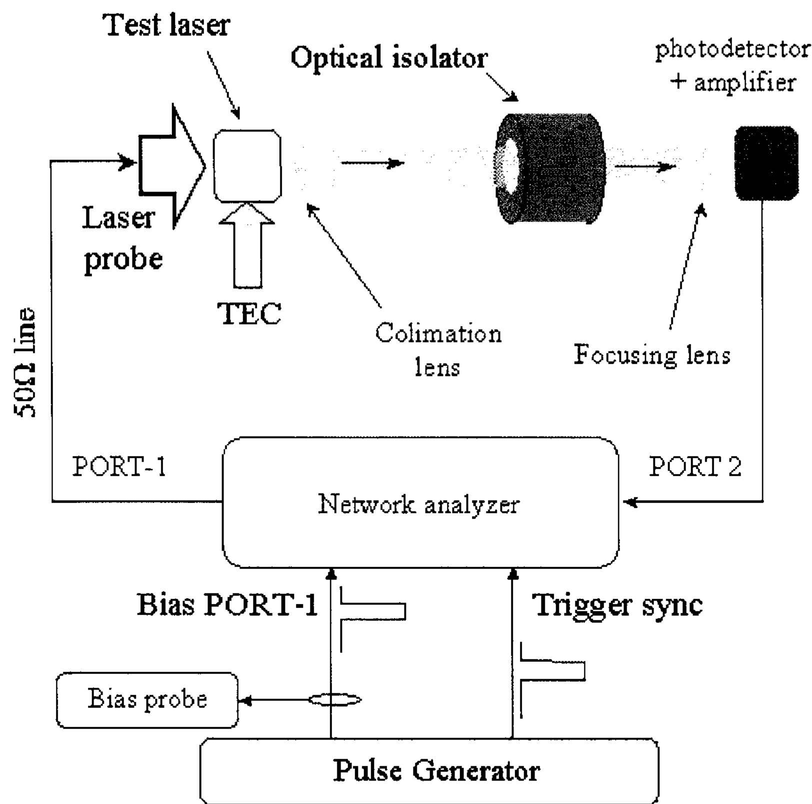

Figure 3.18.- Electrical frequency response setup. The bias is launched into the bias port of the VNA. The VNA works in triggered mode.

The laser beam is collimated and refocused into a SMF-28 single mode fiber, after passing through an optical isolator. The fiber is connected to a New Focus 1411 Schottky InGaAs photodetector with 25GHz bandwidth. The VNA is set to measure S_{21} after connecting the photodetector to its PORT-2 in a logarithmic sweep from 70MHz to 12GHz. The frequency response was obtained from the S_{21} traces versus bias and temperature, under identical experimental conditions as in Section 3.4.1. Typical electrical modulation S_{21} traces are shown in Figure 3.19 . The influence of the parasitics in these traces shadow the resonant behavior.

Reproduced with permission of the copyright owner. Further reproduction prohibited without permission.

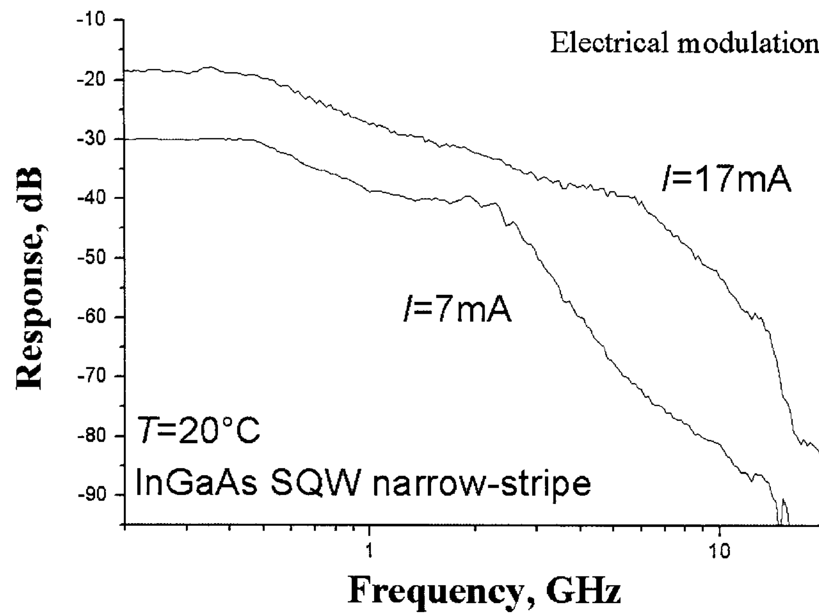

Figure 3.19.- Typical electrical frequency response traces in InGaAs narrow-stripe SQW lasers. Observe the masking effect of parasitics in both traces. The parasitics affect InGaAsN laser in identical manner.

Reproduced with permission of the copyright owner. Further reproduction prohibited without permission.

References Chapter 3

[1] N. Tansu, Y. L. Chang, T. Takeuchi, D. P. Bour, S. W. Corzine, M. R. T. Tan, and L. J. Mawst, "Temperature analysis and characteristics of highly strained InGaAs-GaAsP-GaAs (lambda > 1.17 mu m) quantum-well lasers," *IEEE Journal of Quantum Electronics*, vol. 38, pp. 640-651, 2002.

[2] N. Tansu, N. J. Kirsch, and L. J. Mawst, "Low-threshold-current-density 1300-nm dilute-nitride quantum well lasers," *Applied Physics Letters*, vol. 81, pp. 2523-2525, 2002.

[3] N. Tansu and L. J. Mawst, "High-performance strain-compensated InGaAs-GaAsP-GaAs (lambda=1.17 mu m) quantum-well diode lasers," *IEEE Photonics Technology Letters*, vol. 13, pp. 179-181, 2001.

[4] N. Tansu and L. J. Mawst, "Low-threshold strain-compensated InGaAs(N) (lambda=1.19-1.31 mu m) quantum-well lasers," *IEEE Photonics Technology Letters*, vol. 14, pp. 444-446, 2002.

[5] N. Tansu and L. J. Mawst, "Temperature sensitivity of 1300-nm InGaAsN quantum-well lasers," *IEEE Photonics Technology Letters*, vol. 14, pp. 1052-1054, 2002.

[6] N. Tansu and L. J. Mawst, "Design analysis of 1550-nm GaAsSb-(In)GaAsN type-II quantum-well laser active regions," *IEEE Journal of Quantum Electronics*, vol. 39, pp. 1205-1210, 2003.

[7] N. Tansu and L. J. Mawst, "The role of hole leakage in 1300-nm InGaAsN quantum-well lasers," *Applied Physics Letters*, vol. 82, pp. 1500-1502, 2003.

[8] N. Tansu, A. Quandt, M. Kanskar, W. Mulhearn, and L. J. Mawst, "High-performance and high-temperature continuous-wave-operation 1300 nm InGaAsN quantum well lasers by organometallic vapor phase epitaxy," *Applied Physics Letters*, vol. 83, pp. 18-20, 2003.

[9] N. Tansu, J. Y. Yeh, and L. J. Mawst, "Low-threshold 1317-nm InGaAsN quantum-well lasers with GaAsN barriers," *Applied Physics Letters*, vol. 83, pp. 2512-2514, 2003.

[10] N. Tansu, J. Y. Yeh, and L. J. Mawst, "Experimental evidence of carrier leakage in InGaAsN quantum-well lasers," *Applied Physics Letters*, vol. 83, pp. 2112-2114, 2003.

[11] N. Tansu, J. Y. Yeh, and L. J. Mawst, "Extremely low threshold-current-density InGaAs quantum-well lasers with emission wavelength of 1215-1233 nm," *Applied Physics Letters*, vol. 82, pp. 4038-4040, 2003.

[12] N. Tansu, J. Y. Yeh, and L. J. Mawst, "Improved photoluminescence of InGaAsN-(In)GaAsP quantum well by organometallic vapor phase epitaxy using growth pause annealing," *Applied Physics Letters*, vol. 82, pp. 3008-3010, 2003.

[13] N. Tansu, J. Y. Yeh, and L. J. Mawst, "Physics and characteristics of high performance 1200 nm InGaAs and 1300-1400 nm InGaAsN quantum well lasers obtained by metal-organic chemical vapour deposition," *Journal of Physics-Condensed Matter*, vol. 16, pp. S3277-S3318, 2004.

Reproduced with permission of the copyright owner. Further reproduction prohibited without permission.

[14] N. Tansu, D. Zhou, and L. J. Mawst, "Low-temperature sensitive, compressively strained InGaAsP active (lambda=0.78-0.85 mu m) region diode lasers," *IEEE Photonics Technology Letters*, vol. 12, pp. 603-605, 2000.

[15] J. Y. Yeh, N. Tansu, and L. J. Mawst, "Long wavelength MOCVD grown InGaAsN-GaAsN quantum well lasers emitting at 1.378-1.41 mu m," *Electronics Letters*, vol. 40, pp. 739-741, 2004.

[16] J. Y. Yeh and L. J. Mawst, "Modelling of thermionic processes in 1.3μm InGaAsN/GaAsP/GaAs SQW laser heterostructures," University of Wisconsin, Madison 2004.

[17] S. Sato, "Low threshold and high characteristic temperature 1.3 mu m range GaInNAs lasers grown by metalorganic chemical vapor deposition," *Japanese Journal of Applied Physics Part 1-Regular Papers Short Notes & Review Papers*, vol. 39, pp. 3403-3405, 2000.

[18] T. Takeuchi, Y. L. Chang, A. Tandon, D. Bour, S. Corzine, R. Twist, M. Tan, and H. C. Luan, "Low threshold 1.2 mu m InGaAs quantum well lasers grown under low As/III ratio," *Applied Physics Letters*, vol. 80, pp. 2445-2447, 2002.

[19] J. Pikal, "Temperature dependence of Carrier Lifetime, Recombination and Gain in 1.3μm InAsP/InGaAsP Multiple Quantum Well Lasers," in *Electrical Engineering*: Colorado State University, 1999.

[20] J. D. Kraus and D. A. Fleisch, *Electromagnetics.*

[21] G. P. Agrawal and N. K. Dutta, *Semiconductor Lasers*. New York: Van Nostrand Reinhold, 1993.

[22] L. A. Coldren and S. W. Corzine, *Diode lasers and Photonic Integrated Circuits*: Wiley series in microwave and optical engineering, 1995.

[23] B. W. Hakki and T. L. Paoli, "Gain Spectra in Gaas Double-Heterostructure Injection Lasers," *Journal of Applied Physics*, vol. 46, pp. 1299-1306, 1975.

[24] O. Anton, G. Vaschenko, D. Patel, G. Y. Robinson, C. S. Menoni, and J. Pikal, "Small signal response of 1.3 mm InAsP/InGaAsP quantum well laser diodes obtained with a THz-bandwidth frequency comb," *IEEE Journal of Quantum Electronics*, vol. 40, pp. 982-988, 2004.

[25] O. Anton, "Optical modulation response of 1.3μm InAsP Lasers," in *Electrical Engineering*: Colorado State University, 2002.

[26] O. Anton, D. Patel, C. S. Menoni, J. Y. Yeh, T. T. Van Roy, L. Mawst, J. Pikal, and N. Tansu, "Frequency response of strain-compensated InGaAsN/GaAsP/GaAs SQW lasers," *IEEE Journal of Selected Topics in Quantum Electronics*, 2005.

[27] "Hewlett Packard Application Note Number 150."

Reproduced with permission of the copyright owner. Further reproduction prohibited without permission.

CHAPTER 4

Analysis below threshold

This chapter is devoted to the study of the impact of nitrogen incorporation and temperature on the differential lifetime and gain of 1.3μm InGaAsN laser diodes. These studies provide insight on key material properties that influence the laser threshold current. Furthermore, because these studies are carried out at different temperatures, they allow to explore the influence of the mechanisms controlling T_0, the characteristic parameter that measures the temperature sensitivity of the laser threshold current.

Reproduced with permission of the copyright owner. Further reproduction prohibited without permission.

4.1. Introduction

Understanding the output behavior of semiconductor lasers relies in part in knowing the carrier density at different injection conditions. As shown in Chapter 2, the carrier density and gain parameters can be extracted within the reservoir model, if the device parasitics and transport parameters of the materials conforming the active region are known.

In this chapter we use the model of Chapter 2 to analyze the results of modulation response measurements below threshold from which the effective differential carrier lifetime is obtained. The results of these experiments coupled with those of gain measurements allow to obtain for the first time the material's gain parameters. In turn, these results allow to draw conclusions on the impact of nitrogen on the gain and effective differential gain at the threshold current I_{th}, which are compared with those from above threshold study in Chapter 5. Further conclusions are drawn on the high temperature behavior of the gain parameters and threshold current of the dilute nitride lasers. This analysis is relevant to unveil the changes in the device parameters produced by the nitrogen incorporation in dilute nitrides and in turn to assess how well these devices compare to 1.3μm InP-based laser diodes.

The experimental study of I_{th} - T allowes us to find the answers to what are the detrimental effects of nitrogen incorporation in dilute nitride lasers. Section 4.4.3 connects the changes in the differential gain dg/dN_{eff}, monomolecular recombination A_{eff} and other parameters with the reduction on the temperature performance in dilute nitride lasers. Section 4.4.4 compares dg/dN_{eff} with that obtained in Chapter 5, which shows similar trends with temperature and nitrogen incorporation. We found also a link between

Reproduced with permission of the copyright owner. Further reproduction prohibited without permission.

the reduction of dg/dN_{eff} and that of T_0. In a similar way the increase of A_{eff} increases I_{th} in dilute nitride lasers. The analysis also pointed to C_{eff} as an important player in reducing T_0 in dilute nitrides. The effective analysis (R_{dc}=0), as shown in Chapter 2, is justified as as the contribution due to carrier recombination in the separate confinement region of the structure is at most 10% at the highest temperature.

4.2. Analysis of differential carrier lifetime in InGaAsN wide-stripe QW lasers

This section describes the analysis of the measured time constant τ extracted from the fit of the modulation responses below threshold at different biases and temperatures. There are complications in this analysis that arise from the fact that the measured τ is masked by parasitic effects at very low bias. Thus, we first describe how with the help of impedance measurements it is possible to limit the bias range to extract a τ_{eff} from the data that is truly representative of the differential lifetime. The $\tau_{eff} - I$ behavior is then analyzed to extract the carrier density N_{eff}. This analysis as shown in chapter 2, is justified as for the characteristic transport parameters calculated following the analysis of Ref. [1], the contribution of the SCH carrier density to the total current is less than 10% at the highest temperature.

4.2.1. Study of electrical parasitics in wide-stripe InGaAsN lasers

The electrical parasitics of wide-stripe InGaAs(N) lasers were evaluated from impedance measurements as described in 3.2.1, from which $r_d \cdot (C_p + C_j)$, where r_d is the diode differential resistance and $C_p + C_j$ the total diode capacitance, was obtained. Complimentary *I-V* measurements described in Section 3.2.1 yielded the diode

Reproduced with permission of the copyright owner. Further reproduction prohibited without permission.

differential resistance $r_d=dV/dI$. Figure 4.1 shows typical impedance traces at T=22°C in InGaAsN and InGaAs wide-stripe laser diodes at I=6mA and I=30mA, obtained with the technique described in section 3.2.1. These traces are fitted with expression (2.16), which is repeated here for completion, from which a single dominant pole is obtained.

$$Z_e(f) = r_d \frac{1 + j2\pi f\tau_Z}{(1 + j2\pi f\tau_p)\cdot(1 + j2\pi f\tau_A)\cdot(1 + j2\pi f\tau_B)} \qquad \text{(4.1) and (2.16)}$$

As was predicted by the analysis in Section 2.2, the fit of the experimental traces with (4.1) indicated, within ±10% errors bars, the absence of poles other than τ_A in the 1GHz frequency range of the measurements. The extracted τ_A versus bias I for InGaAsN and InGaAs wide-stripe lasers is plotted in Figure 4.2 in a range $I<0.1\cdot I_{th}$. Although measurements at higher biases were performed, the magnitude of τ_A reaches a plateau at about 5mA, which according to Section 2.3 indicates the transition between parasitics dominated and intrinsic behavior in the laser diode.

Figure 4.3 shows r_d versus bias I obtained from I-V measurements. I-V measurements also provide the cladding resistance r_s (Table 2.1), which is given by the typical diode I-V equation in (4.2) [2].

$$I = I_s \cdot \left\{ \exp\left[\frac{(V - I\cdot r_s)q}{k_B T\cdot n} \right] - 1 \right\} \qquad (4.2)$$

The parameters in (4.2) were explained in Section 3.2.1. The solid and dashed lines in Figure 4.3 are the fit to the experimental data with (4.2), showing r_d for InGaAsN and InGaAs, respectively.

Reproduced with permission of the copyright owner. Further reproduction prohibited without permission.

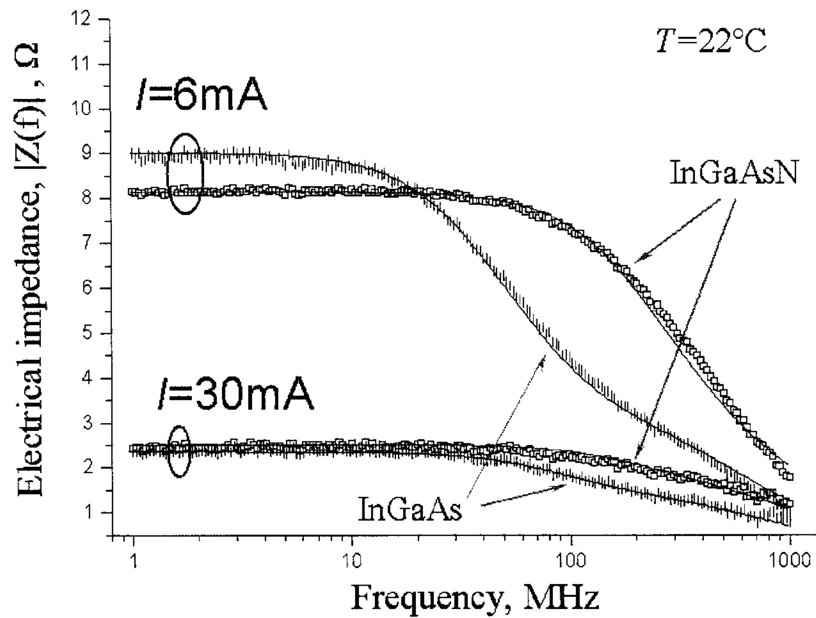

Figure 4.1.- Electrical impedance traces at I=6mA and I=30mA in InGaAsN and InGaAs 500μm x 100μm wide-stripe laser diodes at T=22°C.

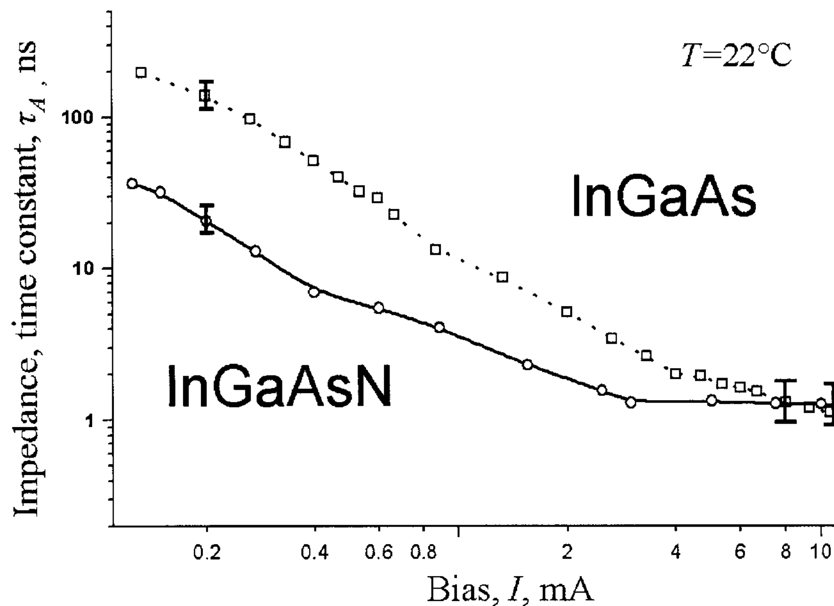

Figure 4.2.- Impedance time constant τ_A versus bias I at T=22°C. InGaAsN (InGaAs) laser traces are shown in solid (dashed) lines. The current range is 5% (12%) of I_{th} for InGaAsN (InGaAs).

Reproduced with permission of the copyright owner. Further reproduction prohibited without permission.

Similar values of r_d versus I were obtained from the low frequency impedance traces ($f \rightarrow 0$) by following (2.18). It is interesting to note that for the particular wide-stripe devices investigated the InGaAs lasers show a higher r_d at all biases.

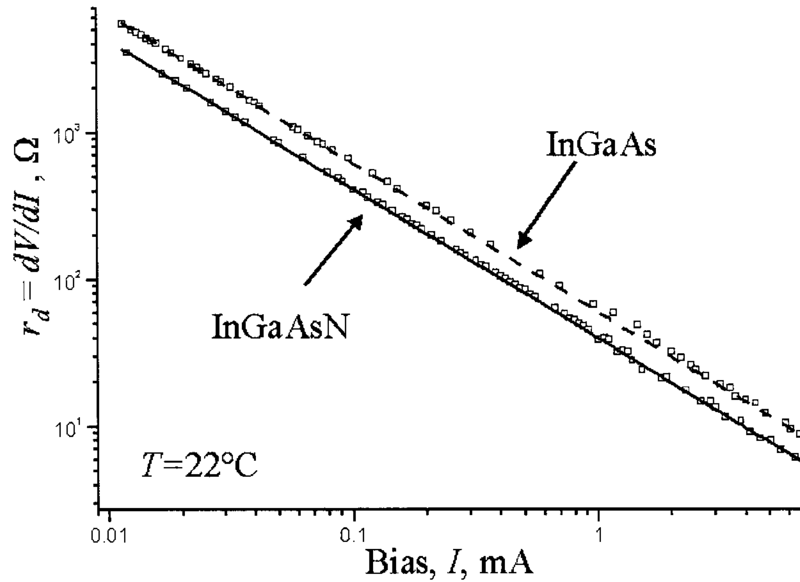

Figure 4.3.- r_d versus bias I obtained from I-V measurements at T=22°C. InGaAsN (InGaAs) wide-stripe laser traces are shown in solid (dashed) lines.

As predicted by the impedance analysis of Section 2.3, the value of the frequency response time constant τ in a parasitic free laser saturates when the bias reduces to zero, as was shown in Figure 2.9 (ideal case). In a similar way, the impedance time constant τ_A should saturate too. However, the experimental traces of Figure 4.2 show that τ_A monotonically increases as I goes to zero. This is an indication of the significant presence of parasitic effects.

Based on the model in Section 2.3, the behavior of τ_A observed from experiments can be accounted for the effects of C_p+C_j. This in turn allows to extract C_p+C_j from the

Reproduced with permission of the copyright owner. Further reproduction prohibited without permission.

fit of τ_A and r_d versus I of Figure 4.2 and Figure 4.3 respectively in the low-bias approximation (2.19).

$$\tau_A\big|_{I\to 0} = r_d(c_p + c_j) \tag{2.19}$$

The values of C_p+C_j are shown at very low biases in Figure 4.4 in InGaAsN and InGaAs wide-stripe lasers at T=22°C. The behavior of C_p+C_j is similar to that modeled in Chapter 2 in InGaAs wide-stripe lasers, based on the study by Liou et al. [3]. However, this is not the case in InGaAsN lasers within the bias range of the measurements, where (C_p+C_j) was practically independent of bias.

The single pole response of impedance measurements is also commonly used to extract the carrier lifetime. However, based on the discussion just presented, this is only valid if parasitic effects are negligible. Thus the analysis served to separate the bias regime where τ_A is only due to parasitics. The behavior of (C_p+C_j) is relevant for extracting the carrier lifetime. From the behavior of (C_p+C_j) of Figure 4.4, we conclude that beyond 5-10A/cm^2, where (C_p+C_j) asymptotically decays to ~105pF (±20%) at T=22°C, corresponds to a parasitic free behavior. It is important to point out that the parasitic dominated lifetime is limited to the range below 10% the threshold current.

The temperature dependence of (C_p+C_j) was obtained from reverse-bias impedance measurements. In fact, when reverse-biasing the diode to ~1-2V [4], the impedance measurements in InGaAsN and InGaAs wide-stripe lasers at 12, 42, 62 and 82°C indicated (C_p+C_j) equals to 110pF ±20%.

Reproduced with permission of the copyright owner. Further reproduction prohibited without permission.

We thus make $C_p + C_j$ =110pF at biases above I=5mA and at all temperatures in InGaAsN and InGaAs wide-stripe SQW laser diodes, in the following carrier lifetime analysis.

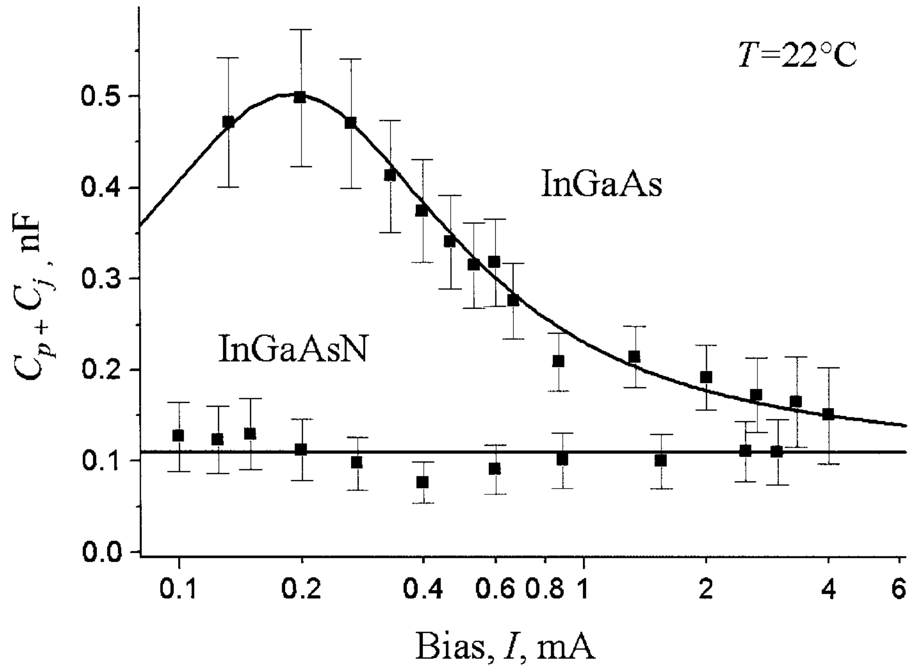

Figure 4.4.- Typical behavior C_p+C_j versus bias current and voltage in a wide-stripe SQW InGaAs lasers at very low bias currents and T=22°C.

4.2.2. Frequency response analysis

This section describes the analysis of the below threshold frequency responses of the InGaAs(N) lasers. The experimental traces are fitted with the solution of the model described in Section 2.1.4, in which the parasitic parameters have been determined as described in the previous section. The analysis retrieves an effective differential carrier lifetime and thus permits extracting an effective N_{eff} in the laser active region versus I and T.

Reproduced with permission of the copyright owner. Further reproduction prohibited without permission.

Figure 4.5 shows the frequency response traces obtained in InGaAsN and InGaAs SQW wide-stripe lasers at I=7 and 35mA and room temperature. The frequency response traces in InGaAsN feature always smaller time constant than similar ones in InGaAs lasers.

Figure 4.6 compares the frequency response traces obtained in InGaAsN and InGaAs at T=12 and 82°C and at the same bias I=30mA. The traces grouped by type of laser are vertically shifted for visual aid, as they are similar and overlap. These traces show a single dominant pole $1/2\pi\tau$, which is temperature insensitive.

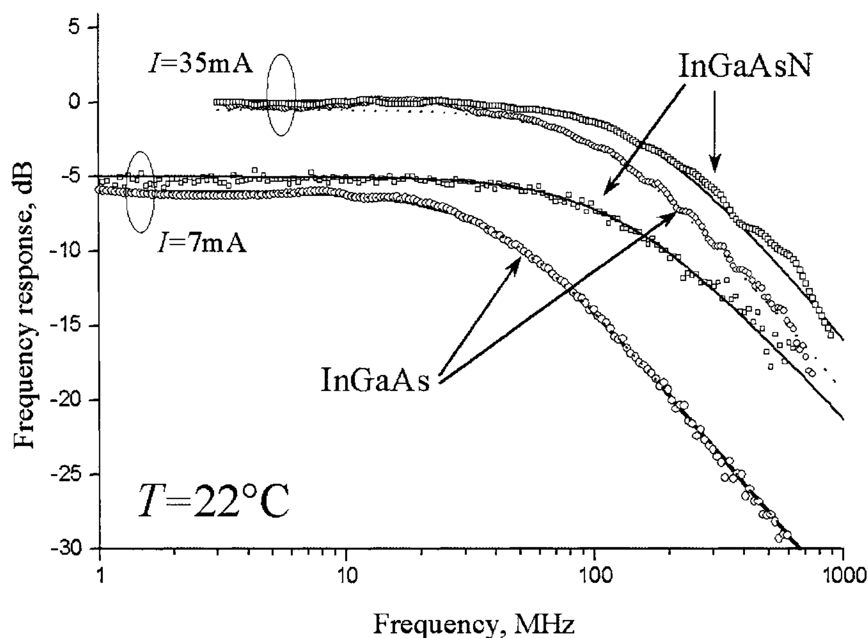

Figure 4.5.- Frequency response measurements in InGaAsN and InGaAs SQW wide-stripe lasers at I=7 and 35mA and T=22°C.

The frequency response time constant τ extracted in wide-stripe lasers is plotted in Figure 4.7 versus bias for temperatures of 12°C, 42°C and 82°C.

Reproduced with permission of the copyright owner. Further reproduction prohibited without permission.

A similar analysis to the one just described was applied to extract the dominant pole in the frequency response of narrow-stripe InGaAsN and InGaAs lasers in the current range from 5 mA to I_{th}. However, as explained in 4.2.1, the range of currents in which τ could accurately be extracted is narrower due to the significant role of parasitics. Figure 4.7 shows τ in InGaAsN (a) and InGaAs (b) narrow-stripe lasers. Notice how the electrical parasitics produce an increase of a factor of 2 in τ compared to wide-stripe lasers. Based on the large passive to active area size ratio, this huge effect of parasitics affecting τ in narrow-stripe lasers was predicted in Section 2.2. Due to the dominance of parasitics, the lifetime obtained from narrow-stripe devices was considered unsuited for the analysis of carrier lifetime.

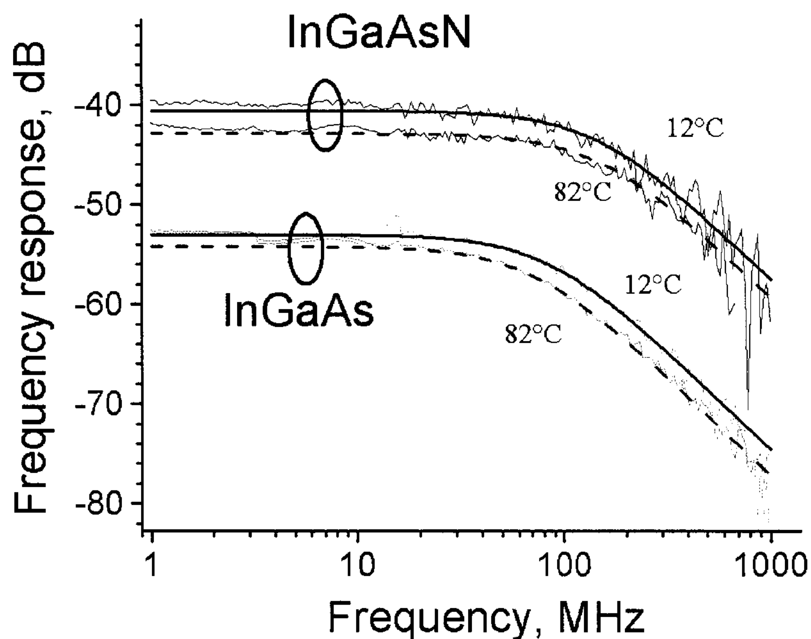

Figure 4.6.- Frequency response measurements in InGaAsN and InGaAs SQW wide-stripe lasers at I=30mA and T=12 and 82°C. For clarity, the traces at T=82°C have been displaced vertically by ~2dB.

Reproduced with permission of the copyright owner. Further reproduction prohibited without permission.

We have therefore concentrated in the rest of this section in the analysis of behavior of τ versus I above I=5mA in wide-stripe InGaAsN and InGaAs lasers.

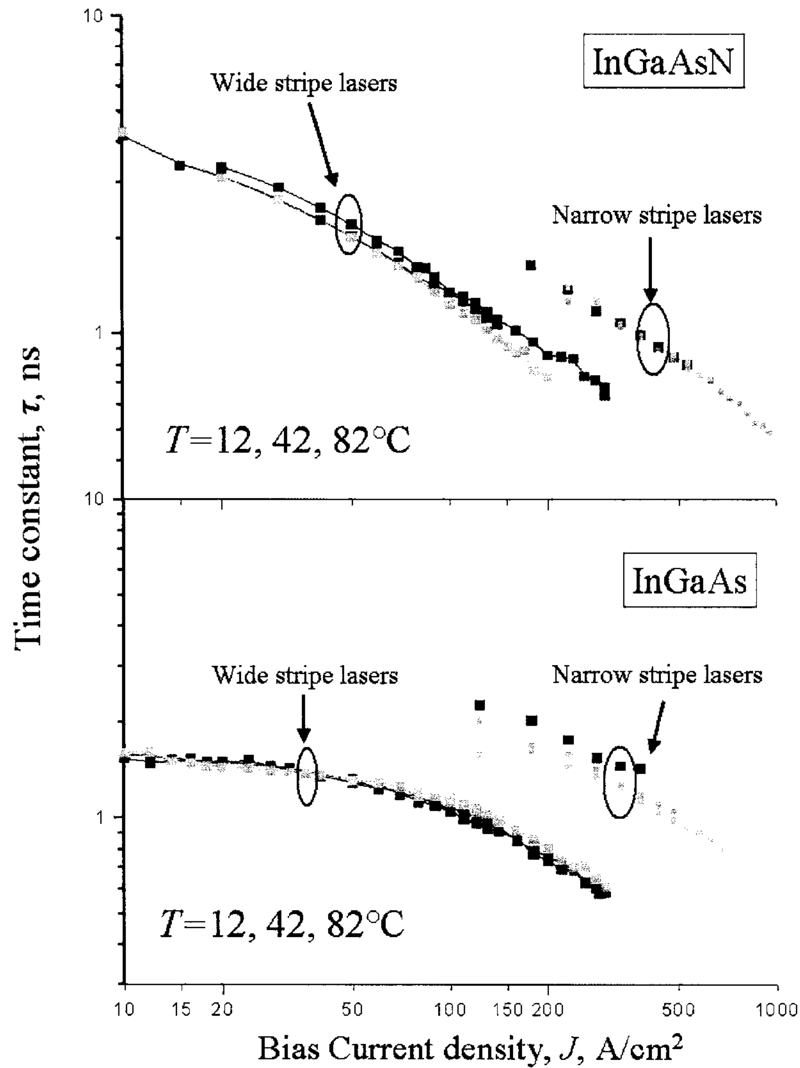

Figure 4.7.- τ versus I obtained from the fit of the frequency response measurements of InGaAsN (A) and InGaAs (b) SQW wide-stripe lasers at T=12°C, 42°C and 82°C. Similar results obtained in narrow-stripe lasers are also plotted to highlight the influence of parasitics.

Reproduced with permission of the copyright owner. Further reproduction prohibited without permission.

4.3. Effective differential carrier lifetime analysis

The effective differential carrier lifetime analysis described in Chapter 2 is carried out in this section to obtain the effective carrier density N_{eff} in InGaAsN and InGaAs wide-stripe SQW laser diodes versus temperature. N_{eff} represents the total carrier density in the laser active area: i.e. quantum well and SCH.

The effective differential carrier lifetime τ_{eff} was obtained from $\tau(I,T)$ (Figure 4.7) and from the impedance data in 4.2.1, by using the analysis from Section 2.2. These had an estimated accuracy of ±10% at all the measured temperatures. These errors arise from corrections in parasitics and from the fit of τ from the frequency response traces. Figure 4.8 shows $\tau_{eff}(I,T)$ obtained at T=12, 42 and 82°C. The traces show that τ_{eff} is smaller in InGaAsN than in InGaAs lasers in most of the bias current range, except near threshold.

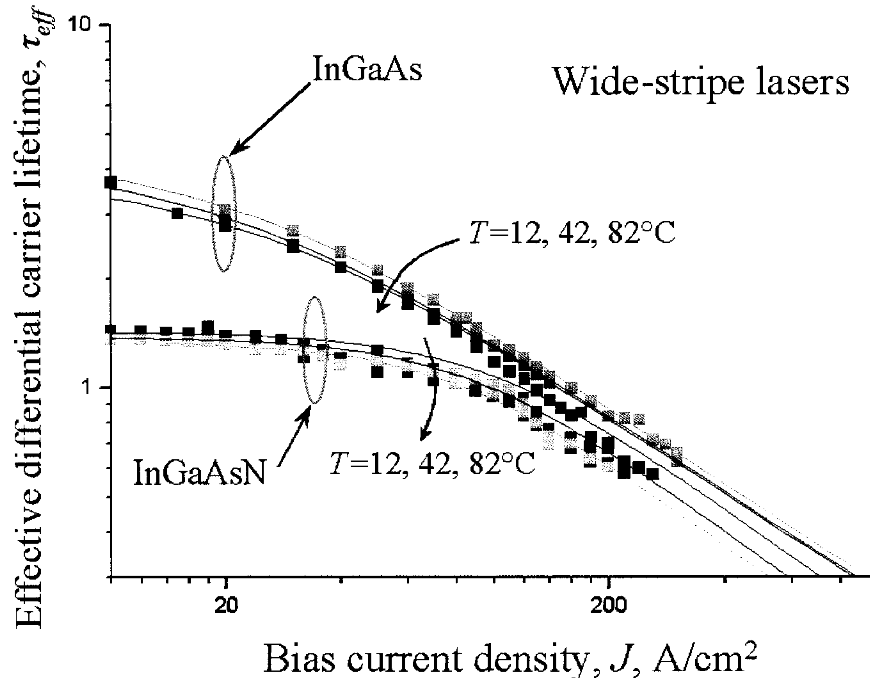

Figure 4.8.- τ_{eff} versus I and T obtained from model analysis [4] of the frequency response measurements in InGaAsN and InGaAs SQW wide-stripe lasers at T=12, 42 and 82°C.

Reproduced with permission of the copyright owner. Further reproduction prohibited without permission.

The ~3 times decrease in τ_{eff} in InGaAsN points to a 3 times stronger monomolecular recombination than in identical InGaAs lasers [5].

Further, these values of τ_{eff} are smaller than those measured in InP-based 1.3μm devices [6].

The next step in the analysis consisted of obtaining the effective carrier density, N_{eff} from the experimental τ_{eff} at different biases.

4.3.1. Effective carrier density in the quantum well

Based on the differential carrier lifetime analysis of Section 2.5.1.2 we obtained the $N_{eff} - J$ relationship at each measured temperature T, where J is the current density in A/cm^2. We utilized J instead of I to relate to the gain analysis performed in narrow-stripe lasers. N_{eff} was obtained by simultaneously fitting τ_{eff} and I (Figure 4.8) with equations (2.33) and (2.34).

Figure 4.9 shows $J(N_{eff})$ at different temperatures in the InGaAsN (a) and InGaAs (b) wide-stripe lasers with uncertainties of ±20%. Also shown in the figure are the experimental threshold points given on Tables 3.3 and 3.4 for wide and narrow-stripe lasers, respectively. Having similar lengths and identical structures, it would be expected that narrow and wide-stripe devices have the same threshold point. This is observed in InGaAsN lasers (in (a), squares and triangles) but not in InGaAs which had larger total losses than in typical narrow stripe lasers [7]. We corrected I_{th} in Figure 4.9 (b) in InGaAs lasers (circles: uncorrected, triangles: corrected) accordingly with the typical losses [7] by using the gain-current traces shown later in Section 4.4 and this analysis shows a closer agreement between the narrow and wide stripe lasers.

Reproduced with permission of the copyright owner. Further reproduction prohibited without permission.

Figure 4.9 reveals a N_{eff} threshold value ($N_{eff\text{-}th}$) varying from $2.5\text{-}4.5\cdot10^{18}cm^{-3}$ in InGaAsN and from $2.5\text{-}4\cdot10^{18}cm^{-3}$ in InGaAs lasers, however achieved in a more than twice the current in the former. This was conceptually and quantitatively pictured by the analysis in Section 2.5, which also requires the values of gain. We repeat a similar analysis than Section 2.5 later on in Section 4.5.

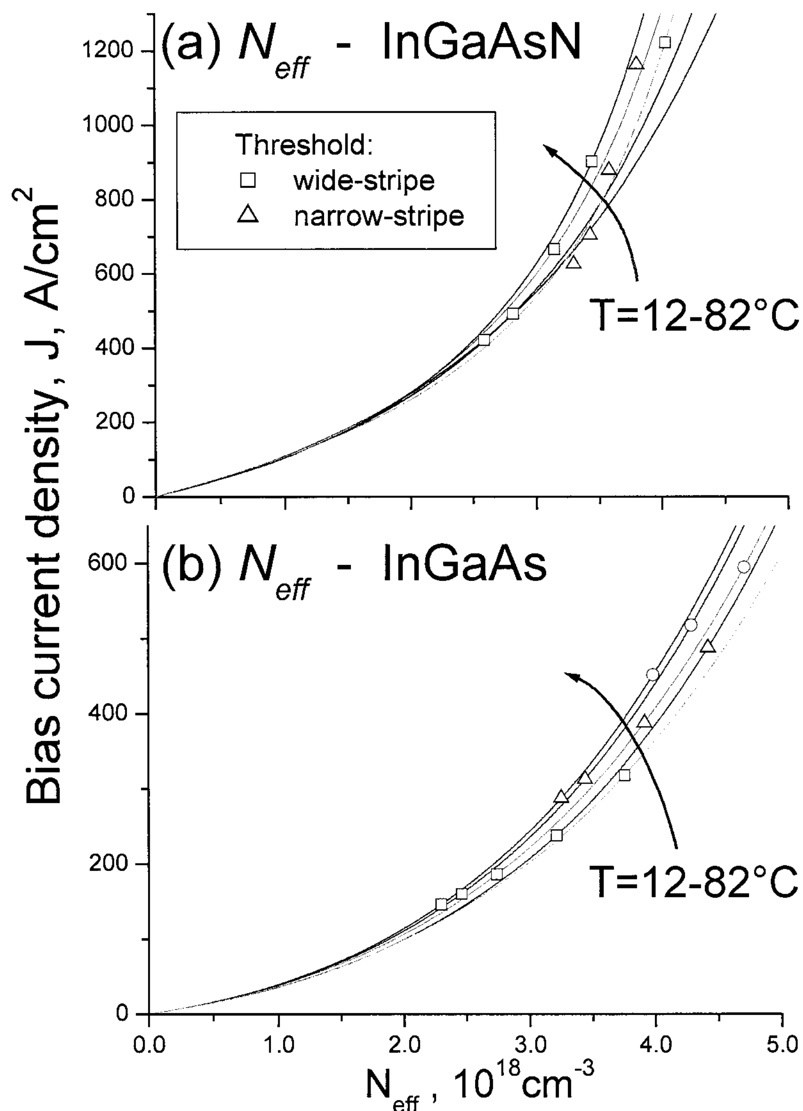

Figure 4.9.- Experimental effective carrier density N_{eff} versus J and T, obtained in InGaAsN and InGaAs wide-stripe SQW lasers at T=12-82°C. The threshold points for the narrow and wide stripe lasers are marked as triangles and squares respectively.

Reproduced with permission of the copyright owner. Further reproduction prohibited without permission.

In addition to N_{eff}, the effective analysis retrieved the effective expansion parameters A_{eff} , B_{eff}, C_{eff} which are shown in Figure 4.10 for InGaAsN and InGaAs lasers versus temperature. This analysis assumes the injection efficiency, η, constant and equal to its threshold value of 0.85 and 0.8 for InGaAsN and InGaAs respectively [1].

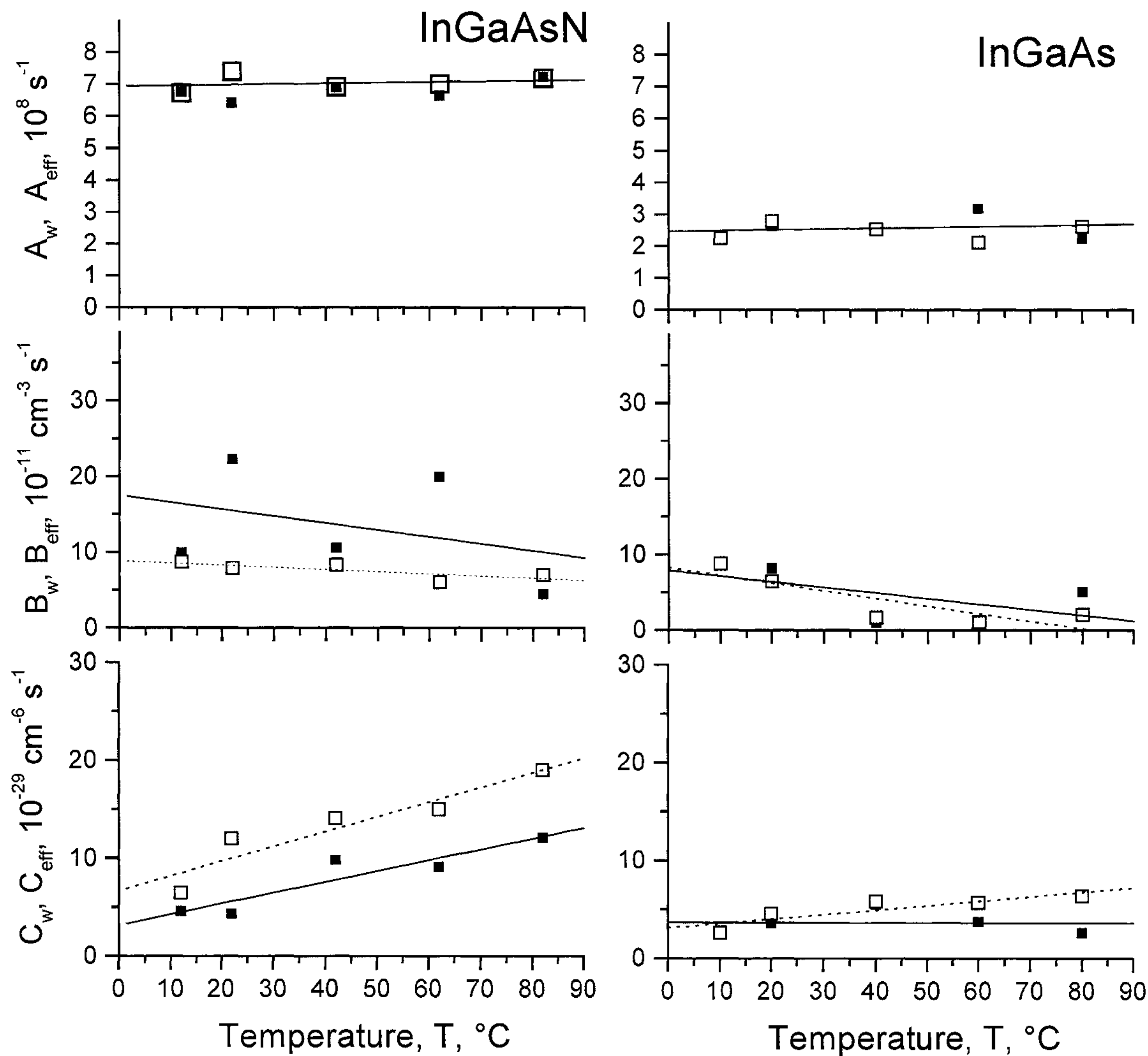

Figure 4.10.- Experimental effective expansion parameters A_{eff}, B_{eff} and C_{eff} in InGaAsN and InGaAs versus temperature (in solid). Also shown are (open square symbols) are A_w, B_w and C_w (filled square symbols) obtained from the fit of experimental lifetime (in open dots and dotted lines) assuming the calculated bias and temperature dependent R_{dc} from Section 2.5.1.

Reproduced with permission of the copyright owner. Further reproduction prohibited without permission.

We utilize these coefficients to assess the role of nitrogen incorporation on InGaAsN and draw a comparison with other 1.3 μm lasers.

The variation of A_{eff}, B_{eff} and C_{eff} with temperature is shown in Figure 4.10. As previously demonstrated [5], the A_{eff} terms is ~ ×3 larger in the nitrogen containing quantum well than in InGaAs, and in both is found to be temperature independent. The values of B_{eff} are comparable to those previously reported in different laser structures [2, 8, 17]. The uncertainty in the higher order terms is ~ 50%. Within this uncertainty, one can conclude that C_{eff} is larger by about a factor of 2 in InGaAsN that in InGaAs.

We compared A_{eff}, B_{eff} and C_{eff} with A_w, B_w and C_w obtained from the fit of experimental lifetime assuming the calculated R_{dc} from Section 2.5.1. This was implemented by the simultaneous fit of τ_{eff} - I (Figure 4.8) with equations (1.4), (2.30) and (2.32) as well as R_{dc}, A_s and B_s calculated in Section 2.5. This analysis is carried out to show that A_{eff} is not affected, hence it is representative of the material. Instead, as was shown in InAsP lasers the values of B_{eff} and C_{eff} provide a higher and lower limit respectively to the material's parameters. This correction is more significant in the nitrides.

It is important to point out that C_{eff} in the host 1.2μm InGaAs material is an order of magnitude larger than in 980nm $In_{0.85}Ga_{0.25}As/GaAs$ [8].

Our analysis confidently shows that the addition of nitrogen increases by ~3 times A_{eff}. Further, as the values of A_{eff} obtained in Figure 4.10 are weakly dependent on temperature and on R_{dc} (A_w~A_{eff}), we can assume that A_{eff} is connected with defect recombination, as we previously reported [5]. This effect is therefore 3 times larger in the InGaAsN than in InGaAs material. Experimental evidence shows a similar increase in monomolecular recombination due to the nitrogen presence in InGaAsN lasers [9, 10].

Reproduced with permission of the copyright owner. Further reproduction prohibited without permission.

We utilized the effective expansion parameters A_{eff}, B_{eff} and C_{eff} to obtain the recombination currents $I_{A\text{-}eff}$, $I_{B\text{-}eff}$ and $I_{C\text{-}eff}$, in similar fashion as done in Figure 2.19. Interestingly, we found that the contribution of $I_{A\text{-}eff}$ to the total current was ~75% and ~40-50% in InGaAsN and InGaAs, respectively.. The effective analysis indicated that I_A is about 3 times larger in InGaAsN than in InGaAs when compared with the rest of the recombination paths, which pointed to the monomolecular recombination as the mechanism responsible for the increase of I_{th} in InGaAsN lasers.

Summarizing, the $N_{eff} - I$ relationship was found for the first time in SQW 1.3μm InGaAsN laser diodes in a temperature range from 12 to 82°C. From these results $N_{th\text{-}eff}$ was obtained. Although these findings allowed us to estimate similar $N_{th\text{-}eff}$ in InGaAsN and InGaAs lasers, they do not suffice to explain the $I_{th} - T$ behavior and the origin of T_0 in InGaAsN lasers. Aiming to answer this question, we complement the analysis with the experimental gain study in narrow stripe lasers, shown next.

4.4. Gain analysis

This section is dedicated to the analysis of the amplified spontaneous emission data obtained in InGaAsN and InGaAs narrow-stripe SQW lasers below threshold and in the temperature range of 12-82°C. As explained before, it was necessary to use narrow-stripe laser diodes to avoid filamentation seen in wide-stripe lasers, which would distort the gain spectra.

From the analysis of the gain spectra and using the N_{eff}- J relationship obtained in the previous section and shown in Figure 4.9, the transparency and differential gain parameters were obtained. This analysis relies on the assumption that the injection efficiency is the same in narrow and wide stripe lasers.

Reproduced with permission of the copyright owner. Further reproduction prohibited without permission.

4.4.1. Gain spectra: bias and temperature behavior

We measured the amplified spontaneous emission (ASE) spectra in narrow-stripe lasers as described in Chapter 3. Figure 4.11 shows ASE spectra in InGaAsN (a) and InGaAs (b) narrow-stripe lasers versus bias and at different temperatures from T=12 to 82°C.

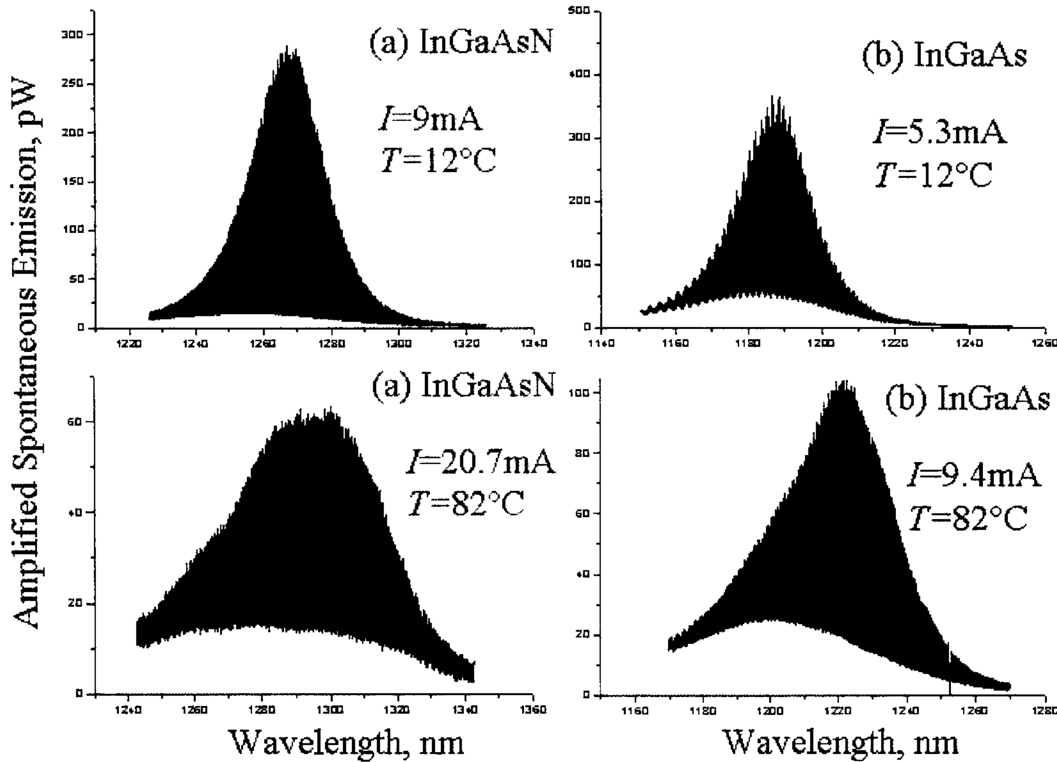

Figure 4.11.- Amplified spontaneous emission traces obtained in InGaAsN (a) and InGaAs (b) narrow-stripe SQW lasers at T=12 and 82°C.

The net modal gain in the laser cavity is obtained from the ASE traces by the Hakki-Paoli technique [11] implemented by the software shown in Appendix 6, represented by the RHS in (4.3).

$$G(\lambda) = \frac{1}{L}\ln\left(\frac{\sqrt{r}-1}{\sqrt{r}+1}\right) + \alpha_m + \alpha_i \qquad (4.3)$$

Reproduced with permission of the copyright owner. Further reproduction prohibited without permission.

In (4.3) $G(\lambda)$ is the material gain and $\Gamma G(\lambda)$ is the modal gain. The parameter r is the wavelength-dependent local ratio of maximum/minimum amplitude in the ASE spectra traces. α_m is the distributed mirror loss, which for the as-cleaved 500μm edge emitting laser of facet reflectivity R_m=0.32 is 22cm^{-1}, as shown on Table 3.1. The internal losses are represented by α_i. $\alpha_i+\alpha_m$ are obtained from the flat asymptotic value that the net modal gain in (4.3) adopts in its RHS.

Using a numerical algorithm written in Matlab^R (Appendix 6) the oscillation maxima and minima were identified every ~5Å, which is the mode spacing to obtain the gain spectra.

Figure 4.12 shows the net modal gain G - ($\alpha_m+\alpha_i$) versus wavelength λ in InGaAsN (a, c and e) and InGaAs (b, d and f) narrow-stripe lasers, and T=12, 42 and 82°C. The peak of the spectra is red-shifted from InGaAs to InGaAsN by ~75meV due to the addition of nitrogen. Internal losses, α_i of 4 cm^{-1} and 15 cm^{-1} were obtained from the longer wavelength asymptote of the total losses and using α_m= 22 cm^{-1} to within ±40% in InGaAsN and InGaAs SQW narrow-stripe lasers, respectively. The dilute nitride lasers spectra showed similar spectral range and bias shift as in other works performed at room temperature and shown on Table 3.1 [7, 12]. The total losses measured on InGaAs lasers were larger than typical values of ~6-10 cm^{-1} found on similar devices [7], due to what we believe is a reduction in the facet reflectivity arising from damage during sample preparation . The larger losses were consistent with a threshold current larger than typical values in similar lasers [7] shown on Table 3.1.

The data of Figure 4.12 also show that the maximum of the modal gain, or peak modal gain Γg, increases more rapidly with bias in InGaAs than in InGaAsN lasers. The

Reproduced with permission of the copyright owner. Further reproduction prohibited without permission.

peak material gain g is a fundamental physical parameter that determines the threshold bias point in the laser.

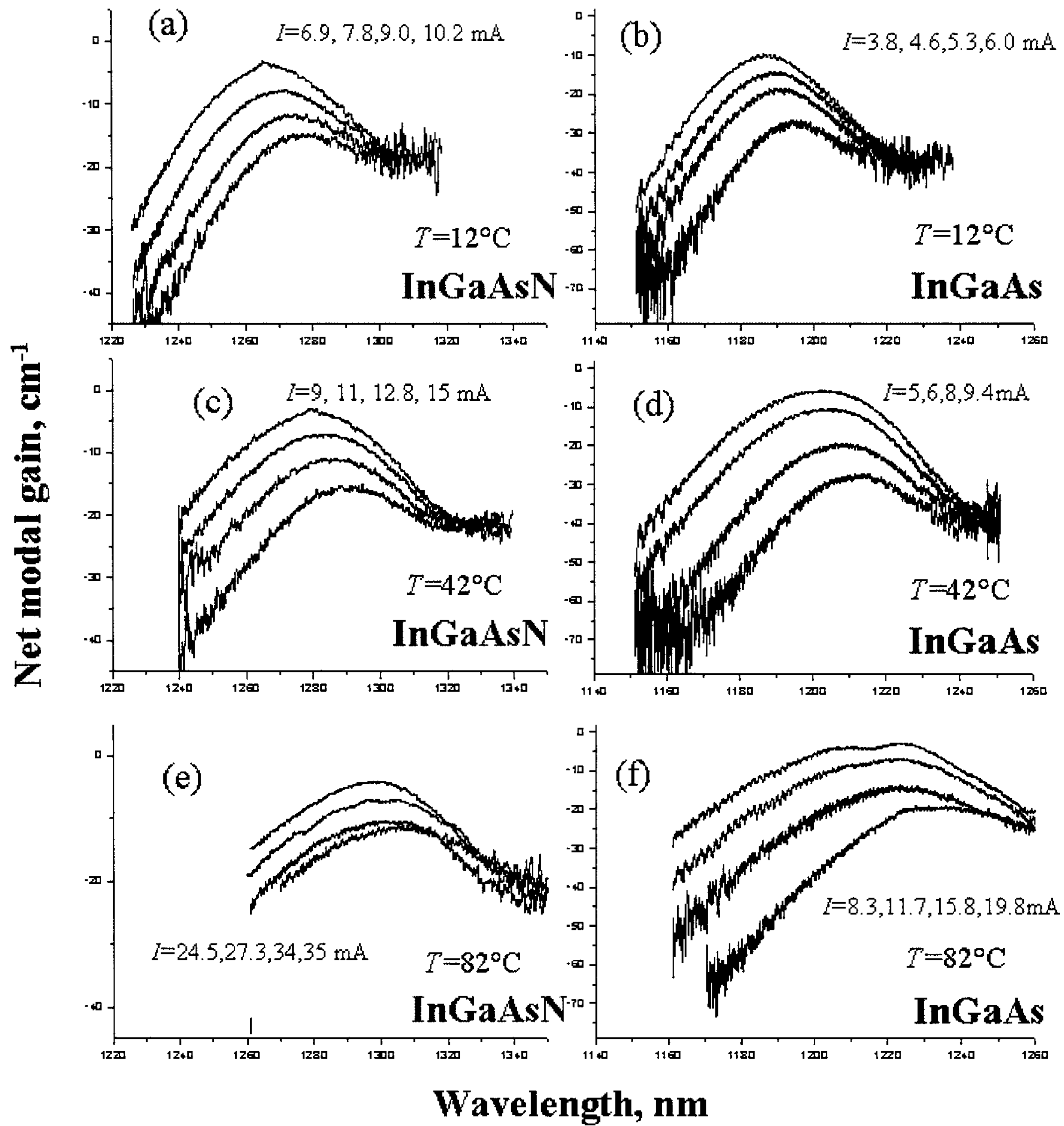

Figure 4.12.- Net modal gain spectra obtained in InGaAsN (a)-(c)-(e) and InGaAs (b)-(d)-(f) narrow-stripe SQW lasers at different biases and T=12-82°C.

Reproduced with permission of the copyright owner. Further reproduction prohibited without permission.

All the data shown corresponds to TE polarization ASE signal, as we could measure no signal in the TM polarization. This means that the contribution of the first confined electron to light-hole transition to the gain is insignificant.

4.4.2. Material gain analysis

The gain spectra obtained at different bias and temperatures were analyzed by performing a parabolic fit near the maximum to obtain the peak gain *g*. Figures 4.13 (a) and (b) show the values of *g(I,T)* for InGaAsN and InGaAs narrow-stripe SQW lasers, respectively. These traces were fitted by the logarithmic approximation shown in (4.4) (solid trace), from which the values I_{tr} and g_{0I} were obtained (Table 4.1).

$$g = g_{0I} \ln(I / I_{tr}) \tag{4.4}$$

Comparison of Figure 4.13 (a) and (b) reveals a notorious reduction of the peak gain slope with bias at threshold in InGaAsN with respect to that in InGaAs lasers. This reduction is more notorious with temperature.

An increase in I_{tr} with the incorporation of nitrogen is also observed, which correlates with the ~2 times increase in threshold current. Similar experimental work shows a comparable increase in the device current span when 0.5% nitrogen is added into InGaAs lasers diodes [7]. I_{tr} is the transparency current in (4.4). Its temperature behavior is shown in Figure 4.14.

Reproduced with permission of the copyright owner. Further reproduction prohibited without permission.

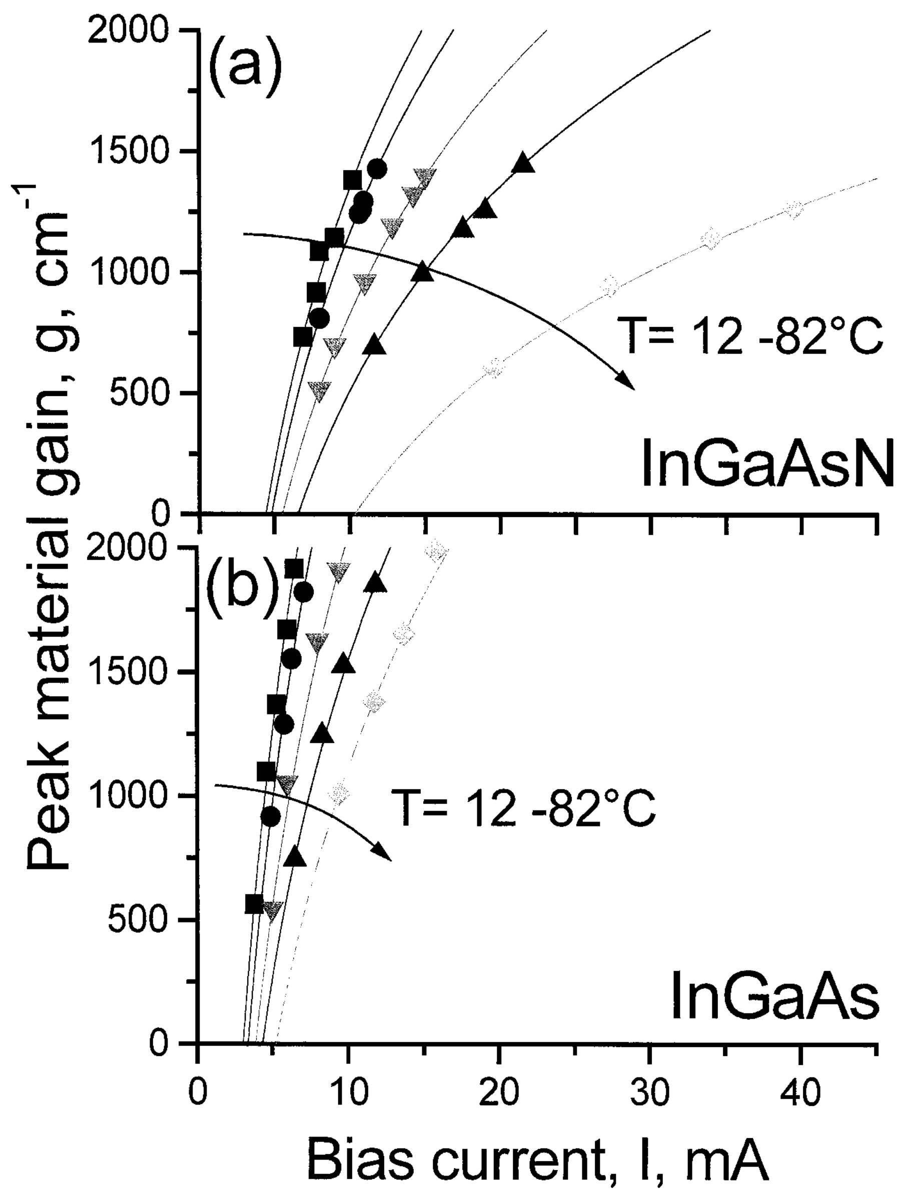

Figure 4.13.- Peak material gain traces, $g(I,T)$ obtained in InGaAsN and InGaAs SQW narrow-stripe lasers at T=12, 42 and 82°C.

Reproduced with permission of the copyright owner. Further reproduction prohibited without permission.

g_{0I} (T), 1000 cm^{-1}		
T, °C	InGaAsN	InGaAs
12	2.52	1.66
22	2.44	1.59
42	2.17	1.40
62	1.85	1.22
82	1.49	0.94

Table 4.1.- Peak material gain fit parameter g_i versus T in InGaAsN and InGaAs narrow-stripe lasers, according to equation (4.4). I_{tr} is the transparency current in (4.4) shown in Figure 4.14.

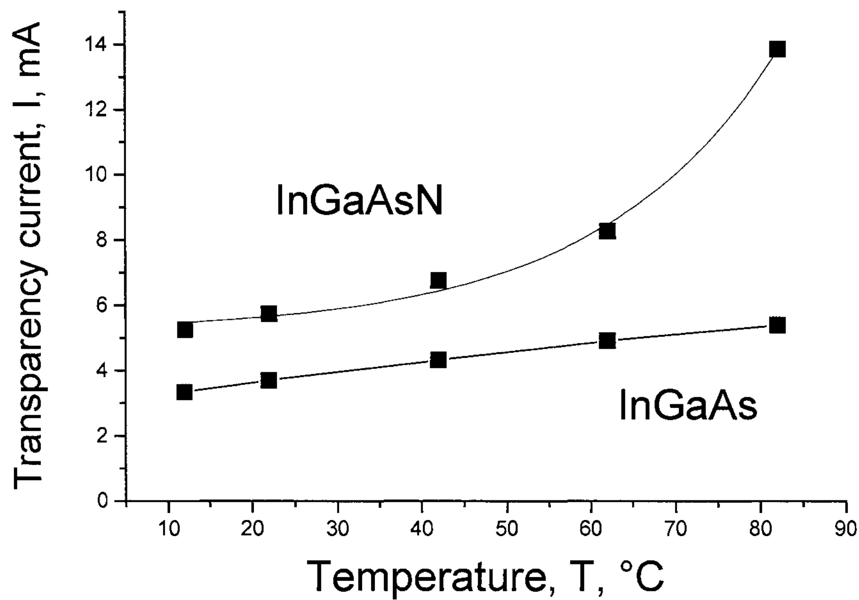

Figure 4.14.- Transparency bias current I_{tr} versus temperature in InGaAsN and InGaAs narrow-stripe SQW lasers from T=12°C to 82°C. I_{tr} in InGaAsN is 1.4-2.4 times larger than in InGaAs at T=12-82°C.

The device parameter dg/dI at threshold obtained from (4.4) is given by g_{0I} / I_{th} and plotted in Figure 4.15 versus T. A reduction in about 2.4 times in $dg/dI|_{th}$ in InGaAsN

Reproduced with permission of the copyright owner. Further reproduction prohibited without permission.

lasers is observed in the range T=12-62°C, with values at room temperature similar to those reported on Ref. [7]. A larger decrease is however observed in InGaAs lasers.

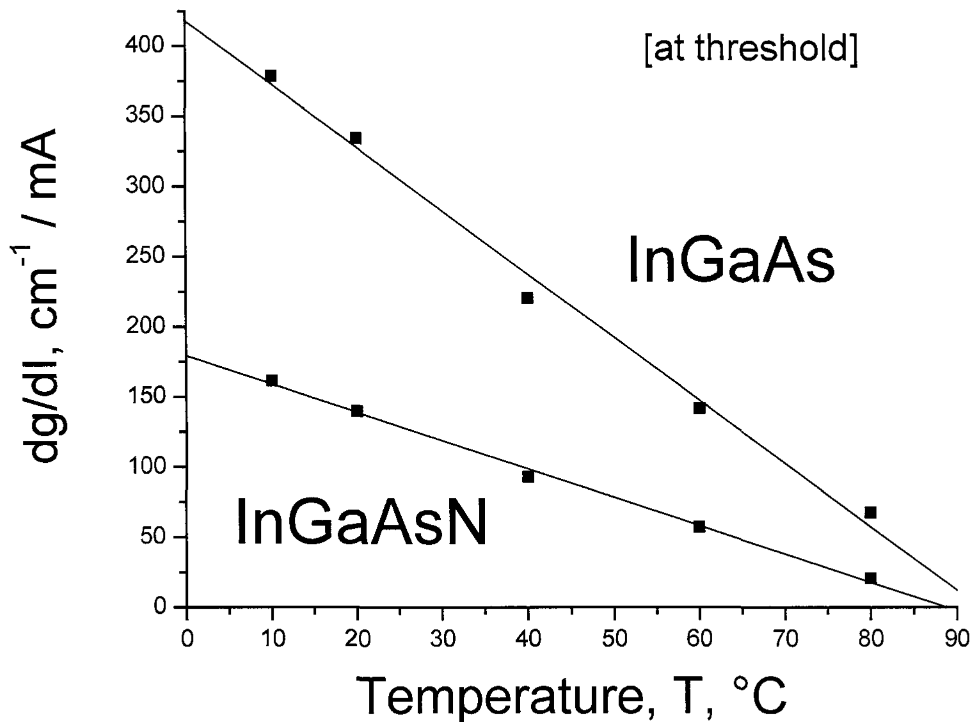

Figure 4.15.- Device threshold differential gain dg/dI versus T temperature in InGaAsN and InGaAs narrow-stripe SQW lasers from T=12°C to 82°C. Notice the ~2.4 (12-62°C) and 5.3 (82°C) times reduction in InGaAsN lasers.

At first sight, Figure 4.15 shows that $dg/dI|_{th}$ in InGaAsN lasers is significantly smaller than in InGaAs but it is yet less temperature sensitive. This analysis is however flawed as it is masked by the device behavior.

In order to decouple the device from the material behavior, the gain data must be expressed in terms of the carrier density as done next.

Reproduced with permission of the copyright owner. Further reproduction prohibited without permission.

4.4.3. Effective differential gain and transparency carrier density

This section performs the analysis of the peak gain traces versus effective carrier density. The experimental data is analyzed in a similar way as done on the previous section but having the laser bias given by N_{eff} instead of I. This implies using values of A_{eff}, B_{eff} and C_{eff} obtained in section 4.3.1 and considering that the injection efficiency, η, is the same in narrow and wide stripe lasers and equal to its threshold value. This analysis provides the framework to investigate the impact of nitrogen incorporation and temperature on InGaAsN and InGaAs materials and compare these findings with those from above threshold Chapter 5.

The peak net material gain versus N_{eff} is shown on Figure 4.16 for InGaAsN (a) and InGaAs (b) narrow-stripe SQW lasers, at the temperatures T=12 to 82°C.

Figure 4.16 shows a different behavior than in $g(I)$. First, we see that the slope of $g(N_{eff})$, reveals dg/dN_{eff} to be almost constant with temperature for both InGaAs and InGaAsN lasers, and slightly larger in InGaAs than in InGaAsN at all temperatures. N_{tr} is within the uncertainly of the analysis similar in both InGaAsN and InGaAs lasers.

The traces of Figure 4.16 were fitted with the logarithmic expression shown in (4.5), where N_{tr} denotes the effective transparency carrier density and g_{0N} is a fit constant. Keep in mind that N_{tr} and g_{0N} are effective parameters and are not equal to those in the exact analysis of Equation 1.12.

Reproduced with permission of the copyright owner. Further reproduction prohibited without permission.

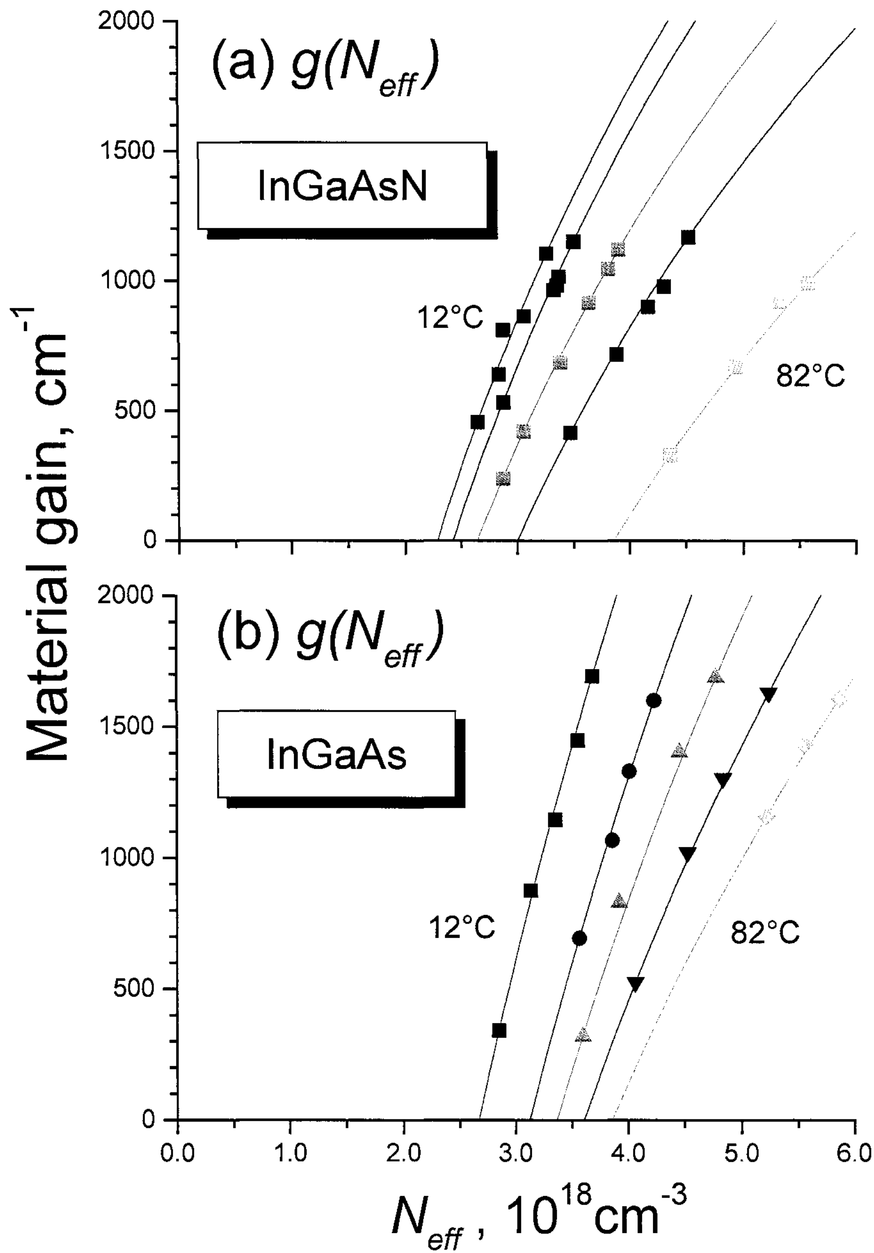

Figure 4.16.- Peak material gain $g(N_{eff})$, obtained in InGaAsN (a) and InGaAs (b) lasers at T=12°C to 82°C.

$$g = g_{0N} \ln(N_{eff} / N_{tr}) \tag{4.5}$$

Reproduced with permission of the copyright owner. Further reproduction prohibited without permission.

Tables 4.2 and 4.3 compile the parameters g_{0N} and N_{tr} with and without nitrogen incorporation as a function of temperature. The temperature behavior of N_{tr} is shown also in Figure 4.17 to highlight that within the error of the measurements, shown by the shaded region in the figure, N_{tr} is not affected by the increase in nitrogen content and furthermore, it is not a strongly dependent function of temperature.

$g_{0N}(T), 1000\ cm^{-1}$		
T, °C	***InGaAsN***	***InGaAs***
12	3.1	5.3
22	3.1	5.3
42	2.9	4.8
62	2.8	4.4
82	2.7	3.8

Table 4.2.- Peak material gain fit parameters g_{0N} versus T in InGaAsN and InGaAs narrow-stripe lasers, according to equation . N_{tr} is the transparency carrier density shown on Figure 4.17 and Table 4.3.

Effective $N_{tr}(T)$, $10^{18}\ cm^{-3}(\pm 20\%)$		
T, °C	***InGaAsN***	***InGaAs***
12	2.3	2.7
22	2.4	3.1
42	2.6	3.4
62	3.0	3.6
82	3.9	3.9

Table 4.3.- Effective transparency carrier density versus T, as shown on Figure 4.17 in InGaAsN and InGaAs narrow-stripe lasers.

Reproduced with permission of the copyright owner. Further reproduction prohibited without permission.

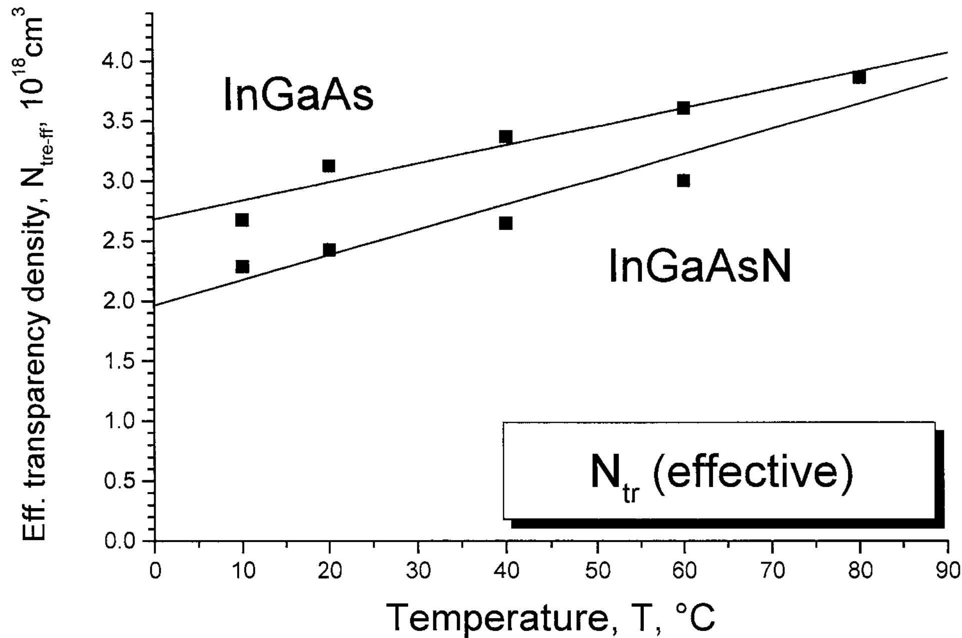

Figure 4.17.- Effective transparency carrier density N_{tr} versus temperature obtained in InGaAsN and InGaAs. The shaded area represents the estimated error bars.

Theoretical work previously developed on 1.3μm dilute nitrides lasers [13-15] predicted an increase in the transparency carrier density due to nitrogen incorporation, while at the same time predicted a reduction on the material differential gain at transparency and at threshold. We find however, that within the error bars N_{tr} is similar in InGaAsN and InGaAs materials as shown in Figure 4.18. Nevertheless, the results are not conclusive as N_w is not known and furthermore, this analysis assumes that η is the same for both wide and narrow stripe lasers and this may not be the case.

Figure 4.18 shows the effective differential gain $dg/dN_{eff}|_{th}$ at threshold in InGaAsN and InGaAs SQW laser structures versus temperature. The error in both traces is around ±25%. It is observed that $dg/dN_{eff\text{-}th}$ in InGaAsN devices is ~25-35% smaller than that in InGaAs in the full temperature range. We found $dg/dN_{eff\text{-}th}$ in InGaAs similar to

Reproduced with permission of the copyright owner. Further reproduction prohibited without permission.

$\sim 2 \cdot 10^{15}$cm^2 of 980 nm multiple quantum well InGaAs/GaAs lasers at room temperature [16]. On the other hand, $dg/dN_{eff\text{-}th}$ in InGaAsN at 22°C is about 20% smaller than $dg/dN_w \sim 10^{-15}$cm^2 in 1.3μm InAsP/InGaAsP lasers [17]. If R_{dc} in Section 2.5.1 were accurate, it could account for the previous difference.

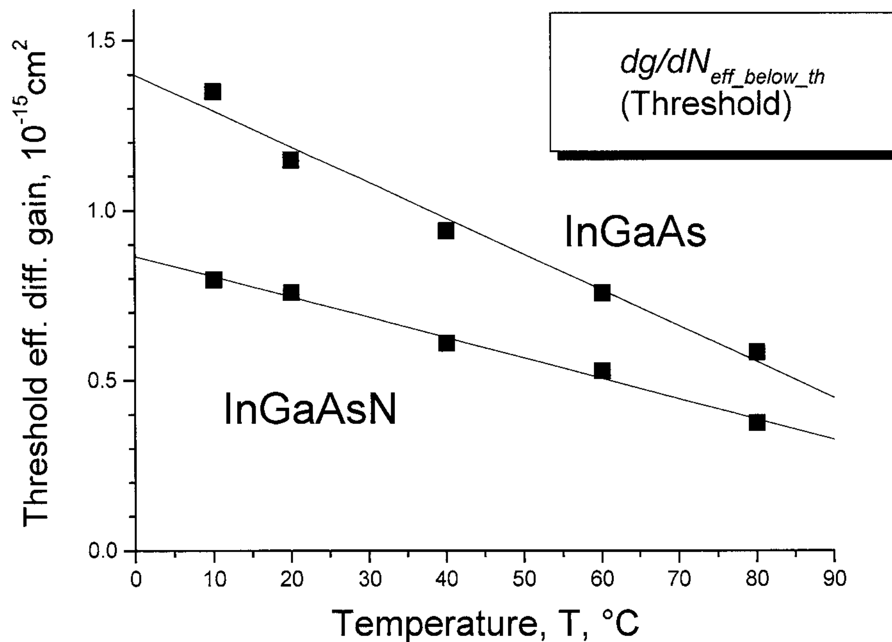

Figure 4.18.- Effective differential gain, dg/dN_{eff}, obtained at threshold in InGaAsN and InGaAs lasers from T=12°C to 82°C. Observe the reduction on dg/dN_{eff} due to nitrogen incorporation that is smaller than that on dg/dI.

The previous comparison has though, an inherent disadvantage, as the effective differential gain at threshold still depends on the device total optical losses, as shown on equations (1.10) and (1.12). The margin of error in this analysis is significant as the total losses were found different in InGaAsN than in InGaAs devices (Figure 4.16). It is therefore speculative to draw any conclusions on the material intrinsic parameters.

It is possible to speculate somewhat on the intrinsic material behavior by looking at the effective differential gain at transparency $dg/dN_{eff\text{-}tr}$ plotted in Figure 4.19 versus

Reproduced with permission of the copyright owner. Further reproduction prohibited without permission.

temperature. The figure shows a reduction of ~25% in $dg/dN_{eff\text{-}tr}$ in InGaAsN compared to InGaAs.

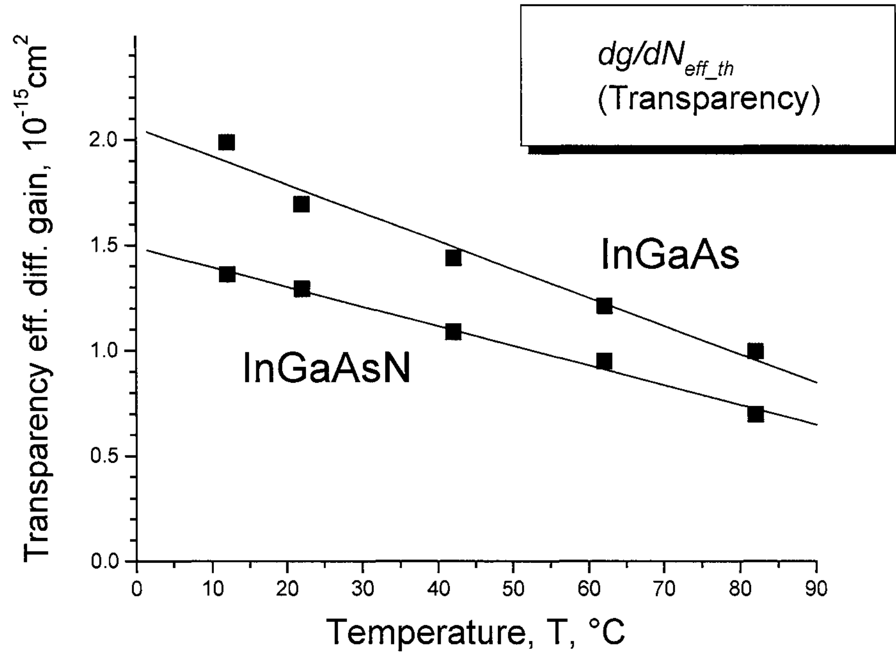

Figure 4.19.- Effective transparency differential gain $dg/dN_{eff} = g_{ON}/N_{tr}$ obtained in InGaAsN and InGaAs lasers from T=12°C to 82°C. A decrease of ~25-35% is observed due to nitrogen incorporation

In summary, our findings indicate a reduction of 25-35% in the effective differential gain at transparency in InGaAsN lasers due to the nitrogen incorporation. However, the analysis in Section 2.5 indicated that, by using the calculated values of R_{dc} from Figure 2.17, dg/dN_w could be 10-50% larger in InGaAsN than in InGaAs material. In similar way, we found that N_{tr} could be 30-50% smaller in InGaAsN than in their nitrogen free counterparts. In any case, we found that these values are contradictory to those predicted [9, 13-15], suggesting that the calculated values of R_{dc} in Figure 2.17 may be inaccurate. Therefore, we discarded this analysis and continue with effective analysis involving

Reproduced with permission of the copyright owner. Further reproduction prohibited without permission.

dg/dN_{eff} and $N_{tr\text{-}eff}$. Future work could be performed whenever R_{dc} were experimentally known.

4.4.4. Below and above threshold differential gain comparison

The threshold condition determines a differential gain dg/dN_{w_th} that is the same for the below and above threshold analyses, as is inferred for Chapters 1 and 2. The same assumption applies to the threshold effective differential gain dg/dN_{eff_th}, which implies R_{dc}=0. We compared the results obtained from the below threshold analysis above with those obtained from the frequency response analysis in Chapter 5. Figure 4.20 shows the dg/dN_{eff_th} traces from Figures 4.18 (solid lines and symbols) and from Chapter 5 (Figure 5.10, dotted lines and open symbols). As the absolute values were not identical, we normalized the values of dg/dN_{eff_th} to those of InGaAs at T=20°C to allow a direct comparison. From this comparison we observed, that within the experimental errors, (i) the reduction of dg/dN_{eff} due to the incorporation of nitrogen and (ii) the temperature behavior of dg/dN_{eff} in InGaAs and InGaAsN are similar. We consider these findings unprecedented for 1.3μm InGaAsN lasers, as the data is obtained from two very different experiments.

The differences in the absolute values of dg/dN_{eff_th} from Figures 4.18 and 5.10 can be accounted for by assuming a bias current spreading of ~1μm at each side of the stripes in narrow and wide stripe lasers. This current spreading is described in ref. [18], and it larger impact would occur below threshold causing a ~30-40% reduction in N_{eff} and consequently an increase in ~30-40% in dg/dN_{eff_th}. The change in the latter would make Figures 4.18 and 5.10 similar.

Reproduced with permission of the copyright owner. Further reproduction prohibited without permission.

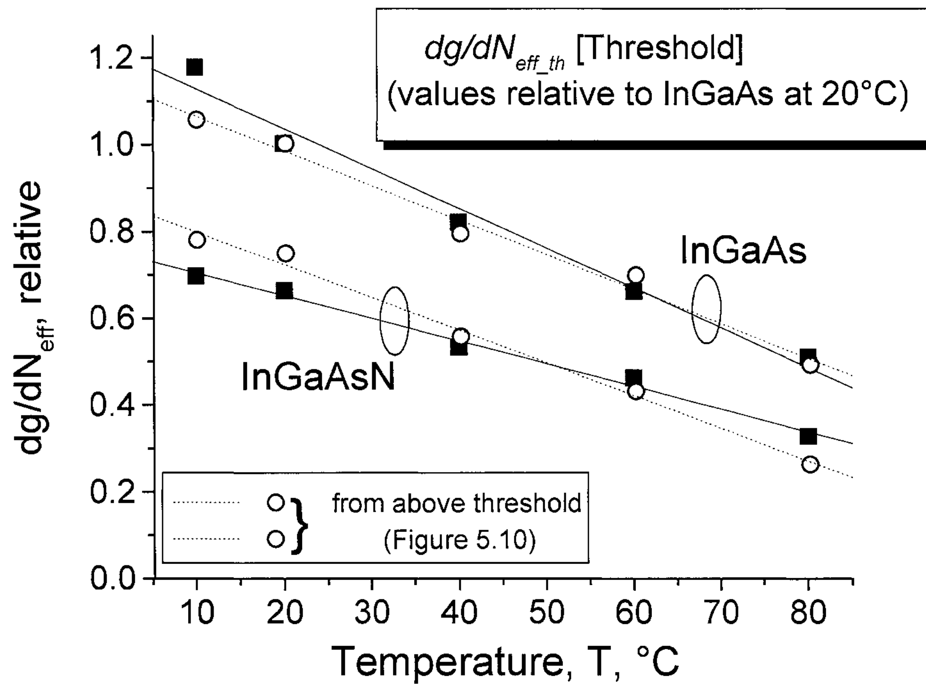

Figure 4.20.- Effective differential gain, $dg/dN_{eff\text{-}th}$ relative to InGaAs at 20°C, for InGaAsN and InGaAs lasers from T=12°C to 82°C, compared with the values obtained from Figure 5.10. Notice the similarity in their slopes with temperature and reduction from InGaAs to InGaAsN.

The results of the analysis of $dg/dN_{eff\text{-}th}$ are expected to yield larger values of $dg/dN_{w\text{-}th}$, depending on the values of R_{dc} calculated in Chapter 2. In other words, dg/dN_w could substantially exceed $10^{-15}cm^2$ found in InP compounds [17], allowing larger T_0's [19, 20] and broader bandwidths [21-23] in 1.3μm multiple quantum well InGaAsN lasers than in InP based lasers. However experimental work needs to be conducted to determine the exact values of R_{dc} and thus dg/dN_w.

4.5. Analysis of the threshold current and T_0

In this section we try to answer the question of what are the mechanisms affecting T_0 in 1.3μm InGaAsN lasers when nitrogen is incorporated. To find the answer we repeat the analysis of Section 2.5.1 with the experimental parameters found on previous

Reproduced with permission of the copyright owner. Further reproduction prohibited without permission.

sections. However, due to the unknown R_{dc}, the following study uses effective parameters which limits the scope of the conclusions.

We utilized the effective experimental gain and expansion parameters obtained in the previous sections plus those in Tables 3.1 and 3.3 for wide stripe InGaAsN lasers. We then simulate the threshold current I_{th} in 1.3μm InGaAsN wide-stripe lasers and extract from the fit I_{th}(22°C) and T_0.

Figure 4.21 shows the simulation of I_{th} versus T for wide-stripe laser diodes. The red squares represent the measured threshold current in InGaAsN laser from Table 3.3. We added for comparison I_{th} measured in InGaAs lasers (open squares). To complete the analysis, we performed a fit to the traces with I_{th}(22°C) and T_0, as it was previously done in section 2.5.1.1. I_{th}(22°C) and T_0 are summarized on Table 4.4.

We simulated the possible cases in which we completely suppressed the effects of either A_{eff}, B_{eff}, C_{eff}, or we changed g_{0N} or dg/N_{eff_tr}, one at a time. The trace in cyan (5) in Figure 4.21 shows the behavior of I_{th} when the gain parameter g_{0N} is fixed to g_{0N} (22°C), which showed no significant change on I_{th} (T). Conversely, we tried enlarging $dg/N_{eff\text{-}tr}$ (4) by 40%, which produced a great reduction in slope yielding T_0 ~125K, larger than in InGaAs. Still, $dg/N_{eff\text{-}tr}$ alone could not account for the increase of I_{th} in InGaAsN lasers.

Among the expansion coefficients, we found that the suppression of B_{eff} yielded a smaller I_{th} but yet led to a lower T_0 (2). On the other hand, the suppression of A_{eff} brought an important decrease in I_{th} (1) than in the previous case. This finding tells us about the nitrogen enhanced monomolecular recombination in InGaAsN lasers, which is consistent with our previous findings on Section 4.3.

Reproduced with permission of the copyright owner. Further reproduction prohibited without permission.

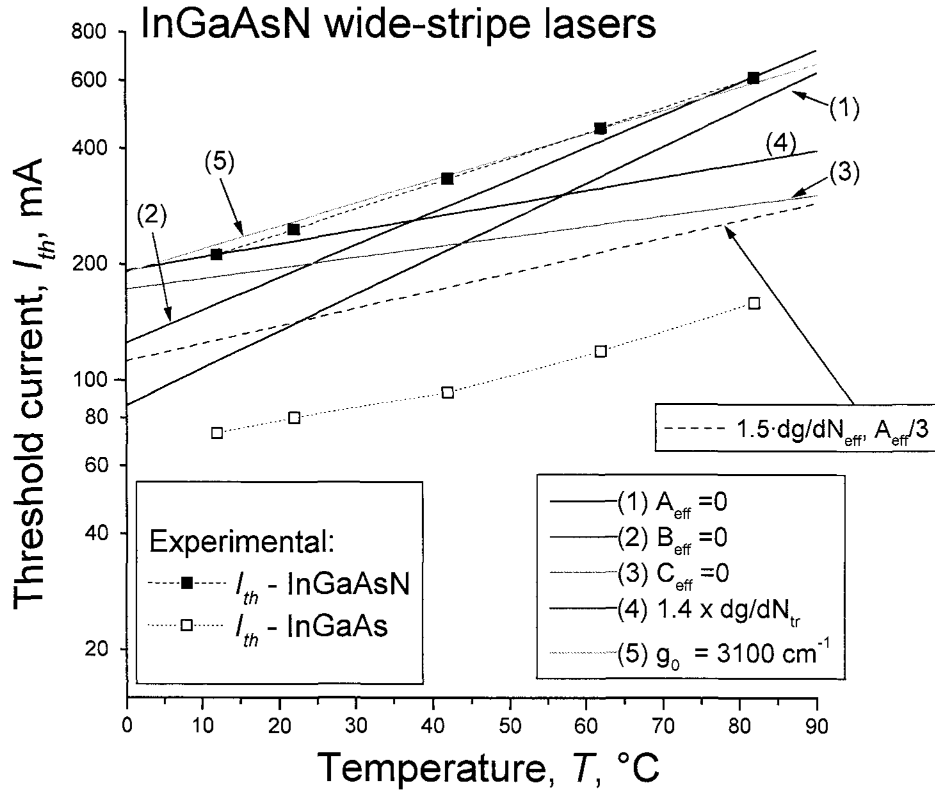

Figure 4.21.- Analysis of the sensitivity of I_{th} -T behavior to the suppression of the effects of either A_{eff}, B_{eff}, C_{eff} or to fixed N_{tr} or g_{0N} . The red squares show the measured I_{th} in InGaAsN (Table 3.3). For comparison open squares show the measured I_{th} in InGaAs.

Parameter changed	I_{th}, mA (22°C)	T_0 (K)
Measured	246	66
$A_{eff}=0$	134	45
$B_{eff}=0$	184	51
$C_{eff}=0$	195	160
$dg/dN_{eff\text{-}tr}$ x 1.4	225	125
g_0 fixed 3100 cm^{-1}(22°C)	251	72
$A_{eff}/3$, $dg/dN_{eff\text{-}tr}$ x 1.4	138	95

Table 4.4.- Parameter sensitivity of I_{th} (22°C) and T_0 in InGaAsN lasers. The last case retrieves T_0 similar to those in InGaAs lasers.

Reproduced with permission of the copyright owner. Further reproduction prohibited without permission.

The suppression of $C_{eff}\ N^3_{eff}$ (3), however, produced the largest simultaneous beneficial impact on I_{th} and T_0 along the full temperature range. This finding implies that C_{eff} is responsible for the increase of I_{th} and decrease of T_0 in InGaAsN material (Figure 4.9).

Summarizing our findings, we can only be certain about changes on the monomolecular recombination parameter and the effective differential gain at threshold. The former is accurately represented by A_{eff} and found to increase I_{th} but not to reduce T_0 in InGaAsN lasers. The latter was represented by $dg/dN_{eff\text{-}th}$ and its decrease was found to produce a reduction on T_0 in InGaAsN lasers. Moreover, the effective differential gain is more representative as underestimates dg/dN_w in an approximate 20%, as mentioned in Section 2.5.1.2.

In order to verify that T_0 in InGaAsN could approach that in InGaAs lasers, we simulated the joint effects of a 3-time reduction on A_{eff} and 40% increase on $dg/N_{eff\text{-}tr}$ at transparency. Interestingly, the simulation yielded a (gray-dashed) trace with T_0 ~95K and I_{th} close to those InGaAs. We found that by further assuming C_w of Figure 4.10 fixed at 22°C we obtain identical behavior than that in InGaAs lasers. By performing a further simulation assuming laser dimensions and mirror reflectivity as in ref. [24], we found that InGaAsN lasers can outperform high performance1.3μm AlInGaAs/InP QW lasers, as we obtained larger T_0's.

From these simulations we conclude that it would be possible to improve the temperature performance of InGaAsN lasers by (i) increasing dg/N_{eff}, (ii) reducing A_{eff} and (iii) fixing C_w to room temperature. Point (i) can be engineered by improving the barrier height [1, 25], p-dopping the quantum well [26] or growing multiple quantum

Reproduced with permission of the copyright owner. Further reproduction prohibited without permission.

wells as suggested by refs. [8, 27]. Point (ii) would require improving material quality and reducing dislocation density by changing the growing ramping temperature, the nitrogen sources [28] or even annealing temperature [29]. Although (iii) seems simple, C_{eff} lumps the combined effect of B_w, C_w, and R_{dc}. Still C_{eff} behavior could arise from an increase on C_w as shown in Figure 4.10, similar to what previously found in 1.3μm InAsP lasers [6].

4.6. Chapter summary

This chapter analyzed the results of the frequency response and amplified spontaneous emission measurements (ASE) below threshold in InGaAsN (λ=1.3μm) and InGaAs (λ=1.2μm) SQW lasers diodes as a function of temperature. Separately, the peak material gain was obtained from the analysis of ASE spectra versus temperature and bias current.

When combining the results of both, lifetime and gain analysis, the effective material parameters gain versus carrier density were obtained in InGaAsN and InGaAs at different temperatures. Analysis of these results retrieved the threshold effective differential gain and transparency carrier density versus temperature and for different nitrogen content. It was observed a ~25-35% reduction in the effective differential gain at threshold in InGaAsN compared to InGaAs lasers, which could be accounted in part by the experimentally unknown R_{dc}. Interestingly, we compared these findings with those from Chapter 5, which indicate a similar impact of temperature and nitrogen incorporation on the threshold differential gain. This is the first time that such comparison is done in the study of 1.3μm InGaAsN, revealing the impact of nitrogen incorporation in dg/dN_{eff}.

Reproduced with permission of the copyright owner. Further reproduction prohibited without permission.

From the effective recombination analysis we found a ~3 times increase in the monomolecular recombination due to nitrogen incorporation as well as a 2x increase on C_{eff}. Further, by using calculations on thermionic escape we found a 3x increase on C_w which can account for the reduction on T_0 in 1.3μm InGaAsN lasers.

As a further study utilizing the experimental parameters obtained in 1.3μm dilute nitride materials, we simulated an improved laser diode. A 60% reduction on monomolecular recombination and a 40% enhancement on the effective differential gain yielded T_0 ~95K, similar to that in InGaAs lasers. We found that by further adding a reduction on C_w we reproduced identical InGaAs threshold behavior, which indicated that C_{eff} enlarges due to nitrogen incorporation and plays a central role in the reduction of T_0.

Still, further studies need to measure R_{dc} to find dg/dN_w and confirm if InGaAsN 1.3 μm lasers could realize improved behavior over InP for high temperature and high speed 1.3μm laser diode applications.

The changes mentioned above could be accomplished with the engineering of the laser structure by careful changes in the structure design, i.e. multiple quantum wells, well doping, tuning of the growing temperatures and sources, as well as in the annealing conditions.

Reproduced with permission of the copyright owner. Further reproduction prohibited without permission.

References for Chapter 4

[1] N. Tansu and L. J. Mawst, "Current injection efficiency of InGaAsN quantum-well lasers," *Journal of Applied Physics*, vol. 97, 2005.

[2] G. P. Agrawal and N. K. Dutta, *Semiconductor Lasers*. New York: Van Nostrand Reinhold, 1993.

[3] J. J. Liou and F. A. Lindholm, "Capacitance of Semiconductor P-N-Junction Space-Charge Layers - an Overview," *Proceedings of the IEEE*, vol. 76, pp. 1406-1422, 1988.

[4] O. Anton, D. Patel, C. S. Menoni, J. Y. Yeh, T. T. Van Roy, L. Mawst, J. Pikal, and N. Tansu, "Frequency response of strain-compensated InGaAsN/GaAsP/GaAs SQW lasers," *IEEE Journal of Selected Topics in Quantum Electronics*, 2005.

[5] O. Anton, C. S. Menoni, J. Y. Yeh, L. J. Mawst, J. M. Pikal, and N. Tansu, "Increased monomolecular recombination in MOCVD grown 1.3-mu m InGaAsN-GaAsP-GaAs QW lasers from carrier lifetime measurements," *IEEE Photonics Technology Letters*, vol. 17, pp. 953-955, 2005.

[6] J. Pikal, "Temperature dependence of Carrier Lifetime, Recombination and Gain in 1.3μm InAsP/InGaAsP Multiple Quantum Well Lasers," in *Electrical Engineering*: Colorado State University, 1999.

[7] L. Shterengas, G. L. Belenky, J. Y. Yeh, L. J. Mawst, and N. Tansu, "Differential gain and linewidth-enhancement factor in dilute-nitride GaAs-based 1.3-mu m diode lasers," *IEEE Journal of Selected Topics in Quantum Electronics*, vol. 11, pp. 1063-1068, 2005.

[8] L. A. Coldren and S. W. Corzine, *Diode lasers and Photonic Integrated Circuits*: Wiley series in microwave and optical engineering, 1995.

[9] D. J. Palmer, P. M. Smowton, P. Blood, J. Y. Yeh, L. J. Mawst, and N. Tansu, "Effect of nitrogen on gain and efficiency in InGaAsN quantum-well lasers," *Applied Physics Letters*, vol. 86, 2005.

[10] A. Kaschner, T. Luttgert, H. Born, A. Hoffmann, A. Y. Egorov, and H. Riechert, "Recombination mechanisms in GaInNAs/GaAs multiple quantum wells," *Applied Physics Letters*, vol. 78, pp. 1391-1393, 2001.

[11] B. W. Hakki and T. L. Paoli, "Gain Spectra in Gaas Double-Heterostructure Injection Lasers," *Journal of Applied Physics*, vol. 46, pp. 1299-1306, 1975.

[12] M. Hofmann, A. Wagner, C. Ellmers, C. Schlichenmeier, S. Schafer, F. Hohnsdorf, J. Koch, W. Stolz, S. W. Koch, W. W. Ruhle, J. Hader, J. V. Moloney, E. P. O'Reilly, B. Borchert, A. Y. Egorov, and H. Riechert, "Gain spectra of (GaIn)(NAs) laser diodes for the 1.3-mu m- wavelength regime," *Applied Physics Letters*, vol. 78, pp. 3009-3011, 2001.

[13] S. Tomic and E. P. O'Reilly, "Gain characteristics of ideal dilute nitride quantum well lasers," *Physica E-Low-Dimensional Systems & Nanostructures*, vol. 13, pp. 1102-1105, 2002.

[14] S. T. Ng, W. J. Fan, Y. X. Dang, and S. F. Yoon, "Comparison of electronic band structure and optical transparency conditions of InxGa1-xAs1-yNy/GaAs

Reproduced with permission of the copyright owner. Further reproduction prohibited without permission.

quantum wells calculated by 10-band, 8-band, and 6-band k center dot p models," *Physical Review B*, vol. 72, 2005.

[15] J. M. Ulloa, J. L. Sanchez-Rojas, A. Hierro, J. M. G. Tijero, and E. Tournie, "Effect of nitrogen on the band structure and material gain of InyGa1-yAs1-xNx-GaAs quantum wells," *IEEE Journal of Selected Topics in Quantum Electronics*, vol. 9, pp. 716-722, 2003.

[16] L. F. Lester, S. D. Offsey, B. K. Ridley, W. J. Schaff, B. A. Foreman, and L. F. Eastman, "Comparison of the Theoretical and Experimental Differential Gain in Strained Layer Ingaas/Gaas Quantum-Well Lasers," *Applied Physics Letters*, vol. 59, pp. 1162-1164, 1991.

[17] J. M. Pikal, C. S. Menoni, H. Temkin, P. Thiagarajan, and G. Y. Robinson, "Carrier lifetime and recombination in long-wavelength quantum- well lasers," *IEEE Journal of Selected Topics in Quantum Electronics*, vol. 5, pp. 613-619, 1999.

[18] P. M. Smowton and P. Blood, "The differential efficiency of quantum-well lasers," *IEEE Journal of Selected Topics in Quantum Electronics*, vol. 3, pp. 491-498, 1997.

[19] N. Tansu, J. Y. Yeh, and L. J. Mawst, "Low-threshold 1317-nm InGaAsN quantum-well lasers with GaAsN barriers," *Applied Physics Letters*, vol. 83, pp. 2512-2514, 2003.

[20] N. Tansu, J. Y. Yeh, and L. J. Mawst, "High-performance 1200-nm InGaAs and 1300-nm InGaAsN quantum-well lasers by metalorganic chemical vapor deposition," *IEEE Journal of Selected Topics in Quantum Electronics*, vol. 9, pp. 1220-1227, 2003.

[21] B. Dagens, A. Martinez, D. Make, W. Le Gouezigou, J. G. Provost, V. Sallet, K. Merghem, J. C. Harmand, A. Ramdane, and B. Thedrez, "Floor free 10-Gb/s transmission with directly modulated GaInNAs-GaAs 1.35-mu m laser for metropolitan applications," *IEEE Photonics Technology Letters*, vol. 17, pp. 971-973, 2005.

[22] D. Gollub, S. Moses, and A. Forchel, "1.3 mu m double quantum well GaInNAs distributed feedback laser diode with 13.8 GHz small signal modulation bandwidth," *Electronics Letters*, vol. 40, pp. 1181-1182, 2004.

[23] A. Martinez, J. G. Provost, B. Dagens, V. Sallet, D. Jahan, K. Merghem, L. Ferlazzo, J. Landreau, O. Le Gouezigou, J. C. Harmand, and A. Ramdane, "9.7 GHz small-signal bandwidth of three-quantum well GaInNAs/GaAs laser diodes operating at 1.35 mu m," *Electronics Letters*, vol. 40, pp. 425-427, 2004.

[24] S. O. Slipchenko, A. V. Lyutetskii, N. A. Pikhtin, N. V. Fetisova, A. Y. Leshko, Y. A. Ryaboshtan, E. G. Golikova, and I. S. Tarasov, "Low-threshold-current 1.2-1.5 mu m laser diodes based on AlInGaAs/InP heterostructures," *Technical Physics Letters*, vol. 29, pp. 115-118, 2003.

[25] N. Tansu, A. Quandt, M. Kanskar, W. Mulhearn, and L. J. Mawst, "High-performance and high-temperature continuous-wave-operation 1300 nm InGaAsN quantum well lasers by organometallic vapor phase epitaxy," *Applied Physics Letters*, vol. 83, pp. 18-20, 2003.

[26] M. Oduncuoglu and B. Gonul, "A theoretical comparison of the 1.3 mu m doped InxGa1-xNyAs1-y/GaAs quantum well lasers for different x/y concentrations,"

Reproduced with permission of the copyright owner. Further reproduction prohibited without permission.

Physica E-Low-Dimensional Systems & Nanostructures, vol. 27, pp. 253-261, 2005.

[27] S. L. Chuang, *Physics of optoelectronic devices*, 1995.

[28] T. Takeuchi, Y. L. Chang, A. Tandon, D. Bour, S. Corzine, R. Twist, M. Tan, and H. C. Luan, "Low threshold 1.2 mu m InGaAs quantum well lasers grown under low As/III ratio," *Applied Physics Letters*, vol. 80, pp. 2445-2447, 2002.

[29] S. Nakatsuka, M. Kondow, M. Aoki, M. Kudo, T. Kitatani, and S. Tsuji, "Amplified spontaneous emission measurement of GaInNAs laser wafers with and without rapid thermal annealing," *Japanese Journal of Applied Physics Part 2-Letters*, vol. 42, pp. L1012-L1014, 2003.

Reproduced with permission of the copyright owner. Further reproduction prohibited without permission.

CHAPTER 5

Above threshold behavior of InGaAs(N) laser diodes

This chapter is dedicated to the study of the impact of nitrogen on the frequency response of 1.3 μm InGaAsN laser diodes above threshold. A comprehensive analysis of the results provides an insight into the material properties that determine the ultimate bandwidth that the laser devices can reach. Furthermore, the threshold effective differential gain and power compression factor, which rule over the laser bandwidth, are obtained and compared versus nitrogen incorporation and temperature.

Reproduced with permission of the copyright owner. Further reproduction prohibited without permission.

5.1. Introduction

A goal driving the research in 1.3μm dilute nitride lasers is to produce high speed devices that would replace the existent AlInGaAs/InP distributed feedback (DFB) transceivers with cheap VCSELs in high speed applications such as metropolitan area networks (MAN) and optical interconnects [1].

Two requirements are demanded in a high speed transceiver: gigabit data rate and broad temperature range of operation. These features are expected to be accomplished by a single laser diode, differently than in typical very long haul transceivers at 1.55μm in which the laser is mounted on thermoelectric cooler (TEC) and its beam is switched by an external modulator.

In order to explore the potential of dilute nitride lasers in fulfilling the requirements of 1.3μm telecom requirements, the speed performance versus temperature has to be characterized. More in depth, the physical mechanisms occurring in the laser structure and material which determine the speed in dilute nitride lasers must be identified in order to understand what is the ultimate bandwidth of the device. Several studies of direct modulation speed have been performed on 1.3μm QW InGaAsN lasers based on temporal eye diagrams [2, 3] and small signal frequency response measurements [4]. Contrarily to what was measured on 0.98-1μm InGaAs QW lasers [5, 6], it was found that the nitrogen containing 1.3μm devices have a reduced bandwidth. RIN measurements performed on identical single quantum well InGaAs and InGaAsN lasers similar to the ones used in this dissertation at room temperature, which indicated a reduction of ~1.6 times in the bandwidth versus emitted power due only to nitrogen incorporation in the quantum well [7].

Reproduced with permission of the copyright owner. Further reproduction prohibited without permission.

To explain the observed behavior, extensive theoretical work has modeled gain and carrier dynamics in the mid-infrared dilute nitride laser structures. Most of these works have predicted a reduction in the material gain with the incorporation of nitrogen to the InGaAs(N) material [8-12]. Using the results from gain simulations in which the differential gain dg/dN_w was obtained in combination with a rate equation analysis (Section 1.2.2), the laser frequency response was calculated and yielded bandwidths of about 37GHz at 27°C and 18GHz at 100°C [13]. These encouraging results predict that in theory the InGaAsN lasers would outperform AlInGaAs/InP technology. There are presently no experimental work that confirms these calculations. It is likely that the large bandwidth obtained in these calculations may be due to the result of only considering electron thermionic escape as the process ruling over the carrier dynamics in the active area. Nevertheless, recent theoretical and experimental studies have suggested hole thermionic escape may dominate the carrier dynamics in 1.3μm InGaAsN [14], therefore limiting the frequency response by enhancing carrier transport effects [15, 16].

This chapter is devoted to the analysis of frequency responses above threshold obtained by selective optical injection for the first time in 1.3 μm InGaAsN and 1.2 μm InGaAs SQW narrow-stripe lasers, and described in section 5.1. The frequency response was obtained in a temperature range T=10-80°C, and analyzed utilizing the model developed in Sections 2.4.1 and 2.5.2. The model analysis revealed changes in the material and device parameters with the incorporation of nitrogen.

Reproduced with permission of the copyright owner. Further reproduction prohibited without permission.

5.2. Results of optical modulation frequency response

The frequency response was measured in InGaAsN and InGaAs SQW narrow-stripe lasers by the experimental techniques described in Chapter 3. The selective optical modulation produced optical injection in the test laser QW and SCH when selecting the wavelength of the short pulse to source to λ=1070nm and λ=800nm, respectively.

The frequency response traces were obtained above threshold in the range below P_0 ~ 6mW per facet and at baseplate temperatures T=10, 20, 40, 60 and 80°C. Notice that Joule heating produced a maximum 2°C heating in the active area, that was considered as the error bars in Section 3.2.

The traces were obtained from the amplitude modulated frequency comb shown on Figure 3.14 by the algorithm described on Appendix 5.

Figure 5.1 compares the frequency response traces of narrow-stripe InGaAs and InGaAsN lasers with the two different excitations: OPO (λ =1070nm) and Ti:Sapp laser (λ=800nm). The traces are identical within the measurement uncertainty. The frequency response traces with Ti:Sapp and OPO excitations were simulated in Section 2.4 and described by equations (2.23) and (2.24), and described as SCH and QW-injection, respectively.

$$H_{opt-sch}(f) = H_{zp} \cdot \frac{dP_0 / dS_o\big|_{f\to 0}}{(1 + j2\pi f\tau_c)(f_r^2 - f^2 + jf\gamma)} \qquad (2.23)$$

$$H_{opt-w}(f) = H_{zp} \cdot \frac{dP_0 / dS_o\big|_{f\to 0}}{(f_r^2 - f^2 + jf\gamma)} \qquad (2.24)$$

Reproduced with permission of the copyright owner. Further reproduction prohibited without permission.

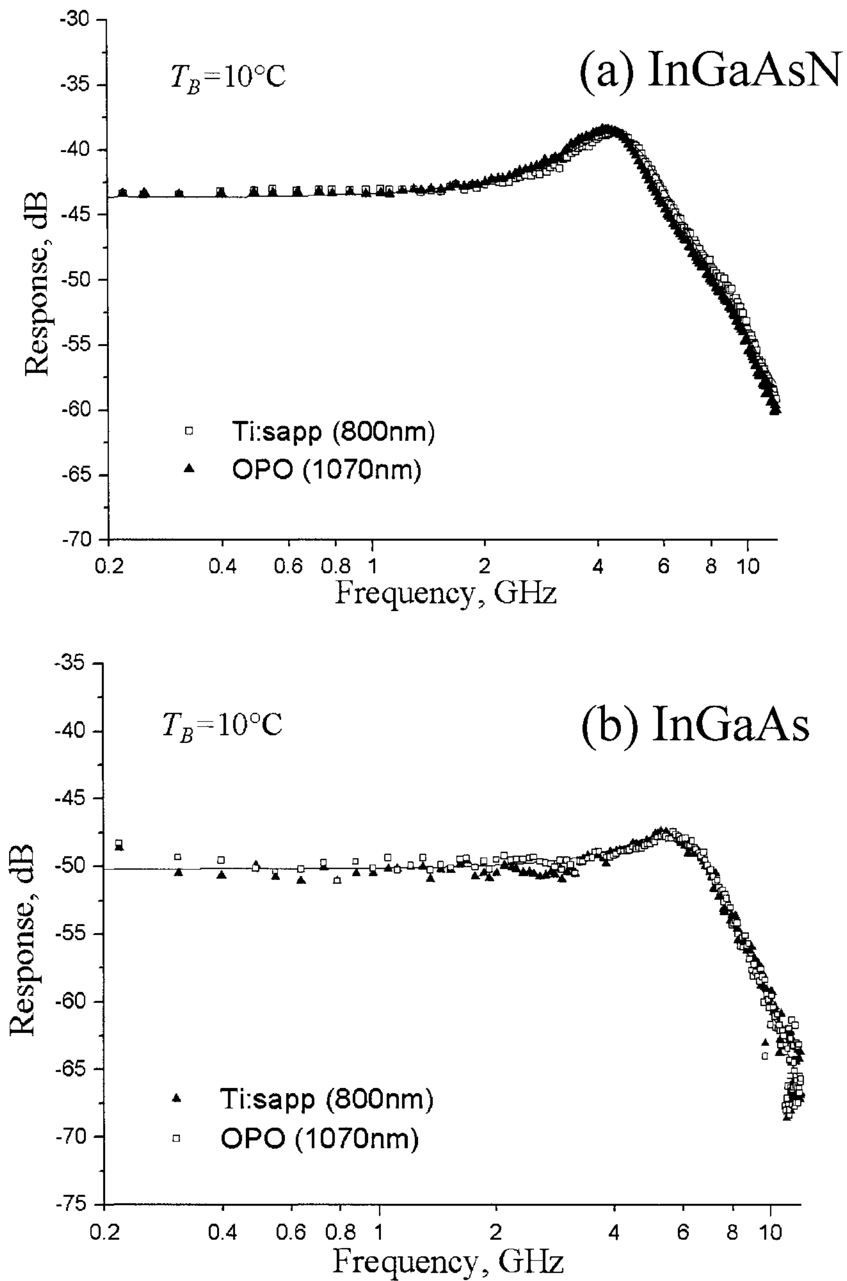

Figure 5.1.- Frequency responses of narrow-stripe InGaAsN (a) and InGaAs (b) lasers at P_0=0.76mW with two different excitations: OPO (λ =1070nm) and Ti:Sapp laser (λ=800nm). Notice that the traces are identical.

The frequency response traces with SCH excitation were fitted by (2.24) by the software shown in Appendix 7, whereas those from OPO excitation were fitted with

Reproduced with permission of the copyright owner. Further reproduction prohibited without permission.

(2.25). The fit yielded the same values of f_r and γ for the same laser and bias point and different excitation wavelength. The fit with (2.23) also retrieved values of τ_c in the order of 8ps ± 5ps. This value in both InGaAsN and InGaAs lasers is comparable to that used in the simulations of Section 2.4. This big uncertainty in τ_c is due to insufficient measurement bandwidth. In fact, the sole effect of assuming τ_c = 6.6ps in equation (2.23) would produce a difference of 1dB at f=12GHz (measurement bandwidth) with respect to (2.24).

Figure 5.2 shows optical frequency response traces at P_0=0.76mW and P_0=2.3mW obtained in InGaAsN and InGaAs devices with QW modulation produced by the OPO injection (λ =1070nm) at T=10 and 80°C. These results show that the 3dB bandwidths obtained in InGaAs are larger than those in InGaAsN SQW narrow-stripe lasers at all temperatures. In addition, it is observed that the frequency bandwidth in InGaAsN reduces more rapidly with temperature than in InGaAs lasers. The figure also compares the optical frequency response traces with those obtained with electrical modulation. Their differences are striking due to their significant role of the electrical parasitics in latter. These results highlight the strength of the optical modulation method we have developed.

Reproduced with permission of the copyright owner. Further reproduction prohibited without permission.

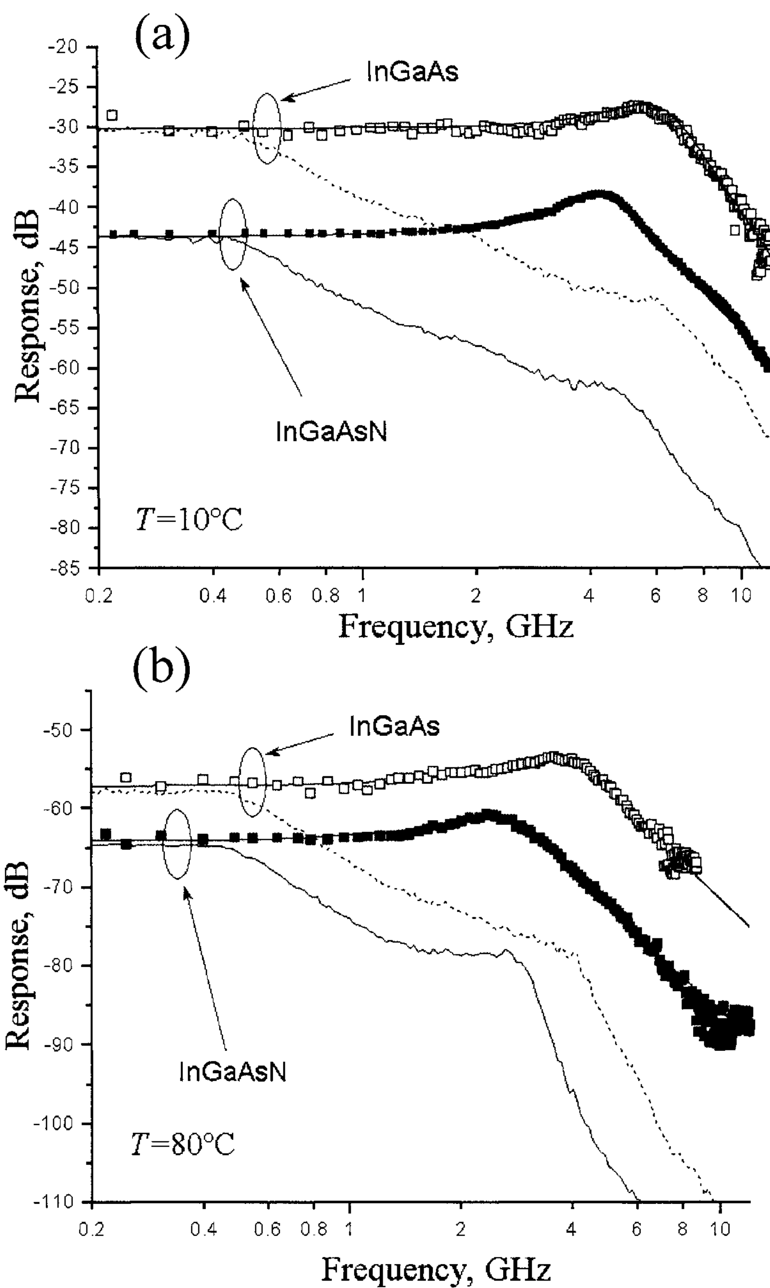

Figure 5.2.- Frequency responses of narrow-stripe InGaAs and InGaAsN lasers, for P_0=0.76mW and P_0=2.3mW, obtained with optical (solid lines) modulation at T=10°C (a) and 80°C (b). They are compared with electrical modulation response (dotted lines).

Reproduced with permission of the copyright owner. Further reproduction prohibited without permission.

5.3. Analysis of the device parameters

By fitting the experimental data using (2.25), the temperature and emitted power dependence of f_r^2 and γ were obtained. Shown in Figure 5.3 and Figure 5.4 is f_r^2 - P_0 for InGaAsN and InGaAs lasers, respectively. From their comparison it is observed that InGaAsN lasers feature: (i) Smaller values of f_r^2 at the same emitted power, and (ii) a more notorious reduction in the f_r^2–P_0 slope with temperature. In numbers, the slope f_r^2–P_0 reduces from 6.5 to 2.4 GHz^2/mW and from 10.6 to 5.6 GHz^2/mW in InGaAsN and InGaAs lasers, respectively, in the temperature range of T=10-80°C.

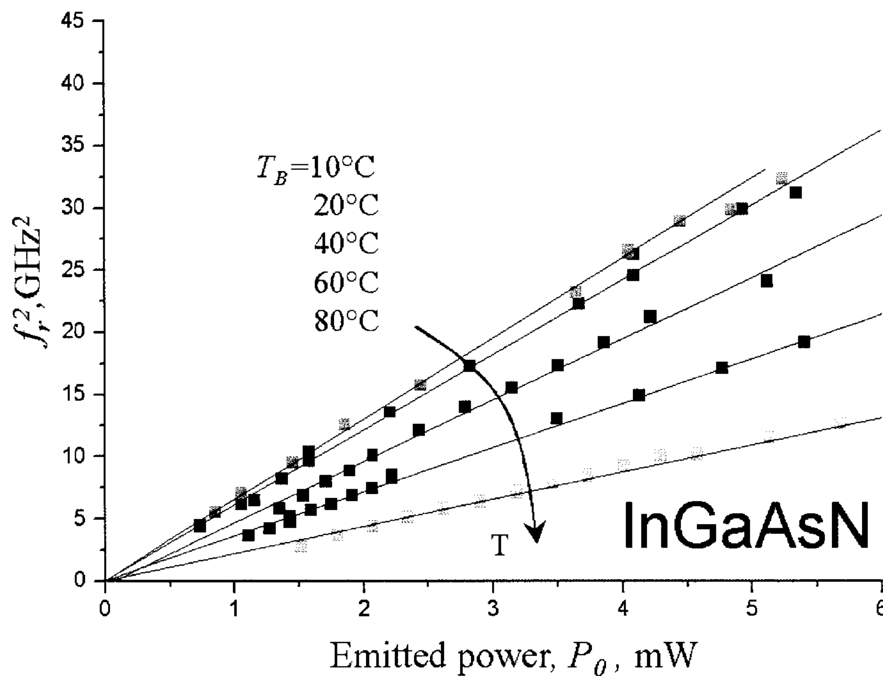

Figure 5.3.- Relaxation frequency squared, f_r^2, versus emitted power P_0 in InGaAsN SQW narrow-stripe lasers at T=10-80°C. Notice the reduction in slope f_r^2/P_0 as T increases.

Reproduced with permission of the copyright owner. Further reproduction prohibited without permission.

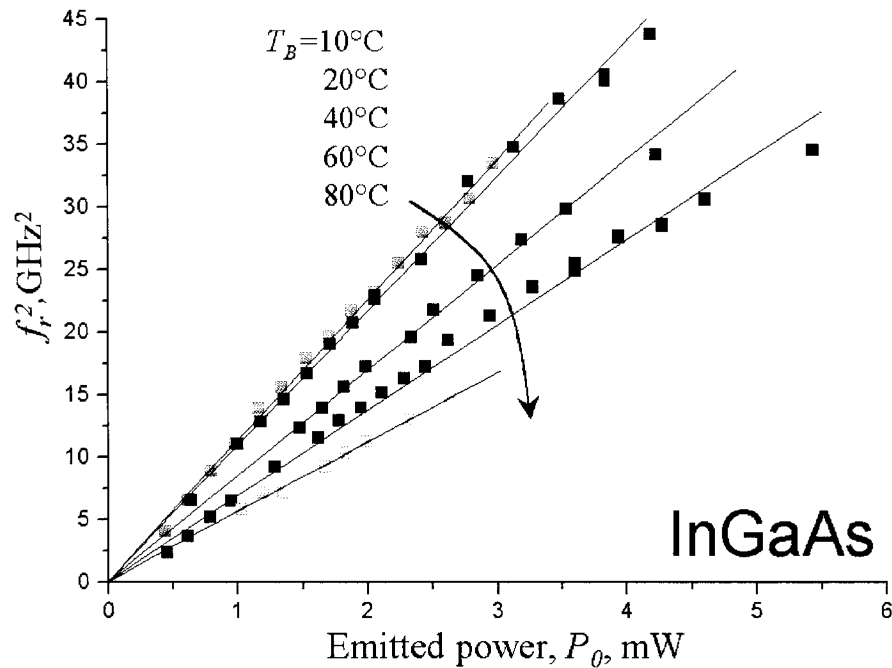

Figure 5.4.- Relaxation frequency squared, f_r^2, versus emitted power P_0 in InGaAs SQW narrow-stripe lasers at T=10-80°C. Notice the reduction in slope f_r^2/P_0 as T increases.

To analyze the damping γ we correct for the contributions from electrical parasitics by using equation (2.28) of Section 2.4.1. The effect of the parasitics is however different in InGaAs than in InGaAsN lasers. In the former, the bias currents are about one half than those in InGaAsN lasers, suggesting r_d is twice as large which in turn, according to equation 2.13 reduces χ. A smaller value of χ produces a larger coupling of parasitics into the active area in InGaAs lasers compared with InGaAsN.

The corrected parasitic-free values of γ versus P_0 at T=10, 40 and 80°C are shown on Figure 5.5 and Figure 5.6 in InGaAsN and InGaAs narrow-stripe lasers, respectively. Reductions in the damping of ~5% and ~20% at an emitted power P_0 = 4mW and between T=10 and 80°C are measured in InGaAsN and InGaAs lasers, respectively.

Reproduced with permission of the copyright owner. Further reproduction prohibited without permission.

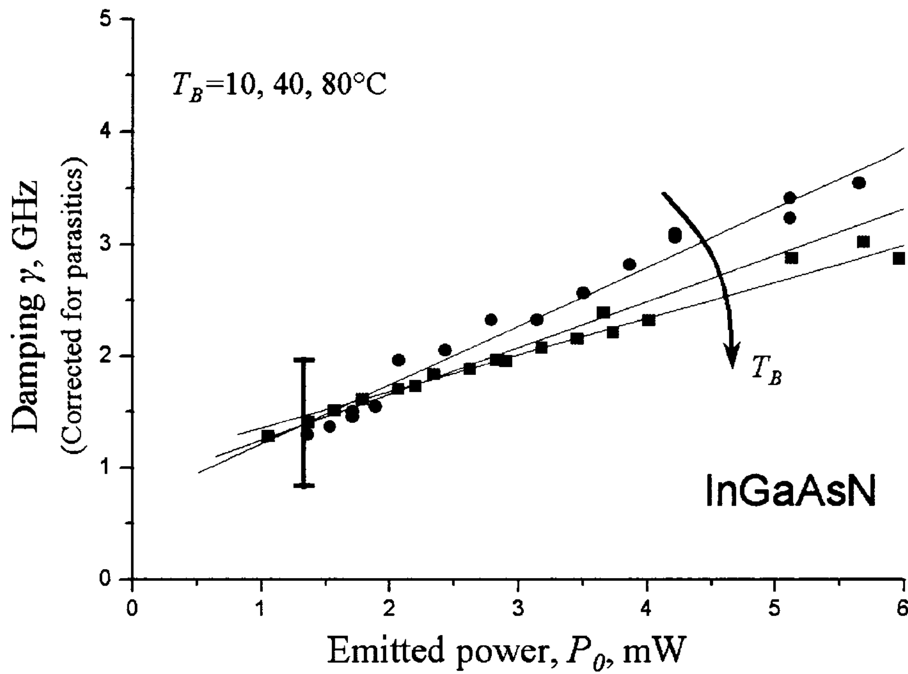

Figure 5.5.- Damping frequency γ versus emitted power P_0 in InGaAsN SQW narrow-stripe lasers at T=10, 40 and 80°C. The slope f_r^2/P_0 slightly increases with T.

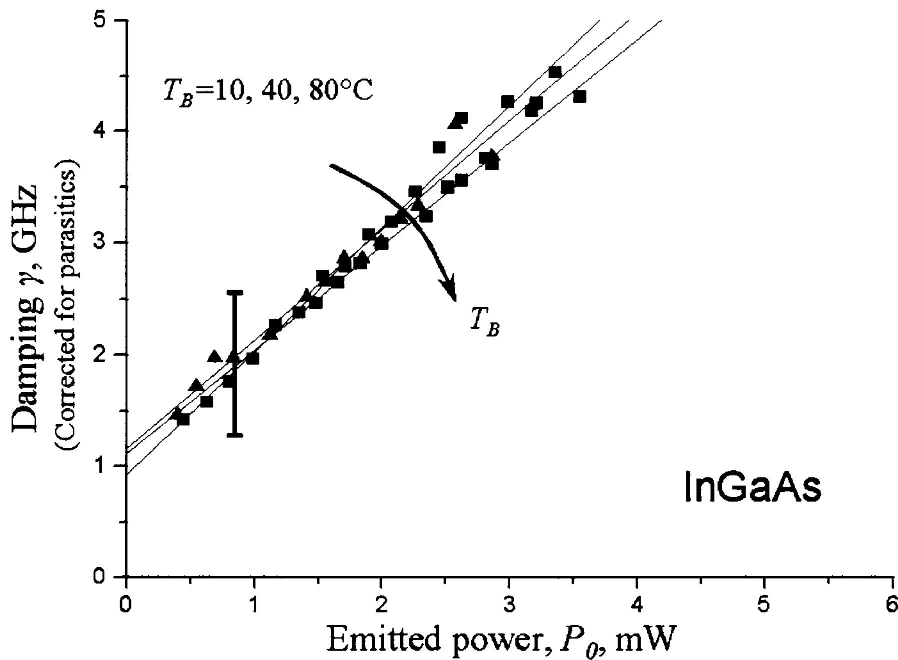

Figure 5.6.- Damping frequency γ versus emitted power P_0 in InGaAs SQW narrow-stripe lasers at T=10, 40 and 80°C. The slope f_r^2/P_0 slightly increases with T.

Reproduced with permission of the copyright owner. Further reproduction prohibited without permission.

The data of Figure 5.3-Figure 5.6 are combined to plot γ versus f_r^2 from which the *K*-factor defined as $2\pi \cdot d\gamma/df_r^2$ is obtained. As explained in Section 2.5, this parameter represents a bandwidth limit, defined mainly by gain compression. Figure 5.7 and Figure 5.8 show γ versus f_r^2 in InGaAsN and InGaAs SQW lasers, respectively. The values obtained in InGaAsN and InGaAs lasers are comparable to those measured in λ~980nm InGaAs/GaAs [17] and λ=1.3μm [18] and 1.55μm InGaAsP/InP [19] single and multiple quantum well lasers.

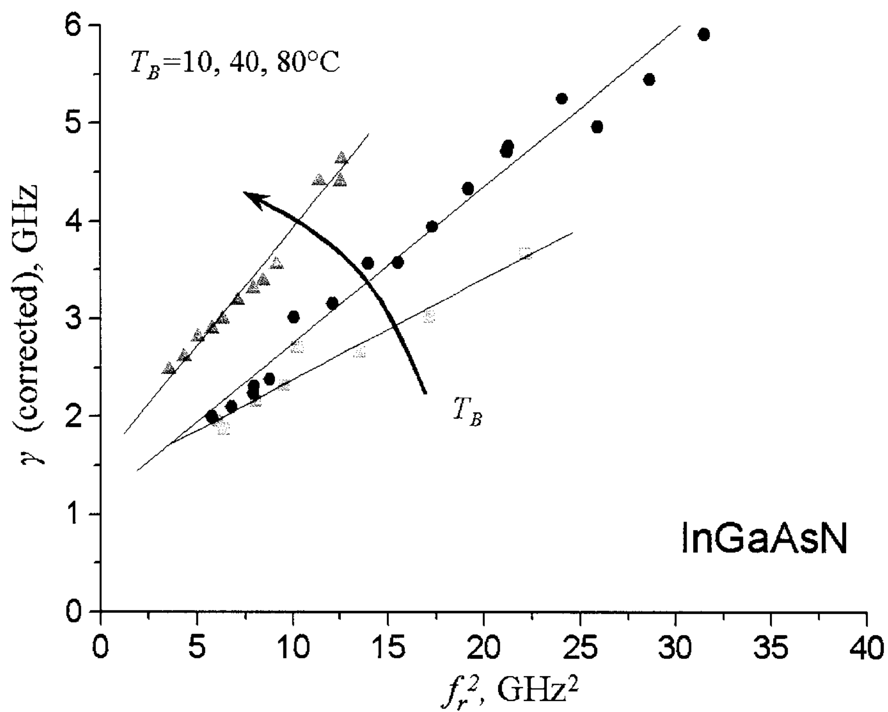

Figure 5.7.- Parasitic – free damping γ versus f_r^2 in InGaAsN SQW narrow-stripe lasers at T=10, 40 and 80°C. The slope represents the *K*-factor that increases with *T*.

Reproduced with permission of the copyright owner. Further reproduction prohibited without permission.

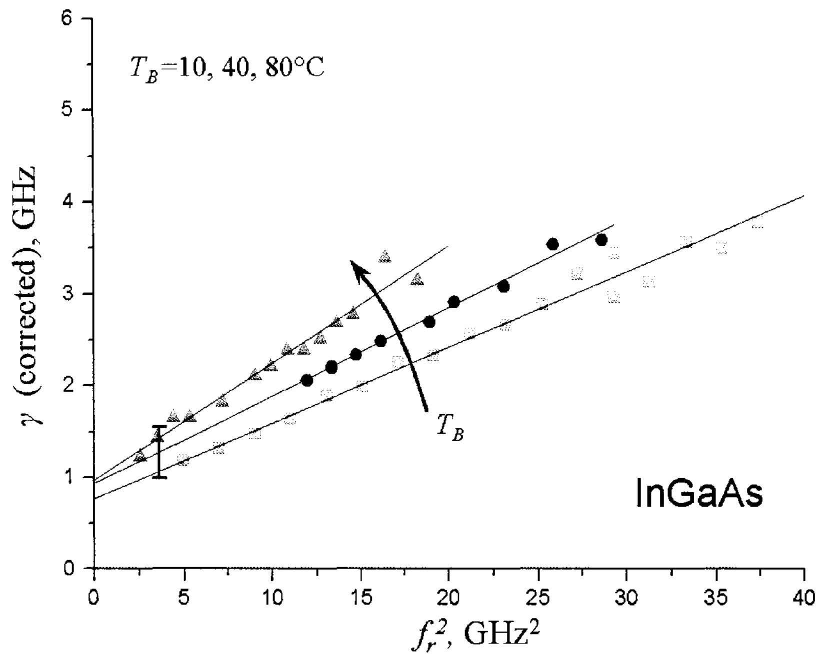

Figure 5.8.- Parasitic-free damping γ versus f_r^2 in InGaAs SQW narrow-stripe lasers in identical conditions as in Figure 5.7.

Figure 5.9 shows K versus T in InGaAsN and InGaAs lasers. The error bars of ±20% arise mainly from the uncertainty in the corrected γ. Although K is ~0.5ns in InGaAs lasers in the full temperature range, it increases from similar a value at T=10°C to 1.5ns at 80°C in InGaAsN. According to the expression in section 2.4, the K-limited bandwidth is 12GHz in InGaAs while it reduces from 12GHz down to 4GHz in InGaAsN lasers in the full temperature range T=20-80°C. In spite of the K-limited bandwidth reduction, 4GHz at T=80°C represents an unprecedented speed ever obtained in an as-cleaved single quantum well 1.3μm InGaAsN laser.

These results are very encouraging when compared with bandwidths obtained in multiple quantum well 1.3μm InGaAsN optimized devices [2, 4, 20], which suggest that

Reproduced with permission of the copyright owner. Further reproduction prohibited without permission.

by adding a second quantum well will enable our lasers to achieve bandwidths much larger than 10GHz [21, 22].

The analysis of the results just described allows to parameterize the laser in terms of the characteristic parameters of the frequency response. This behavior in turn has embedded material and device physics as discussed next.

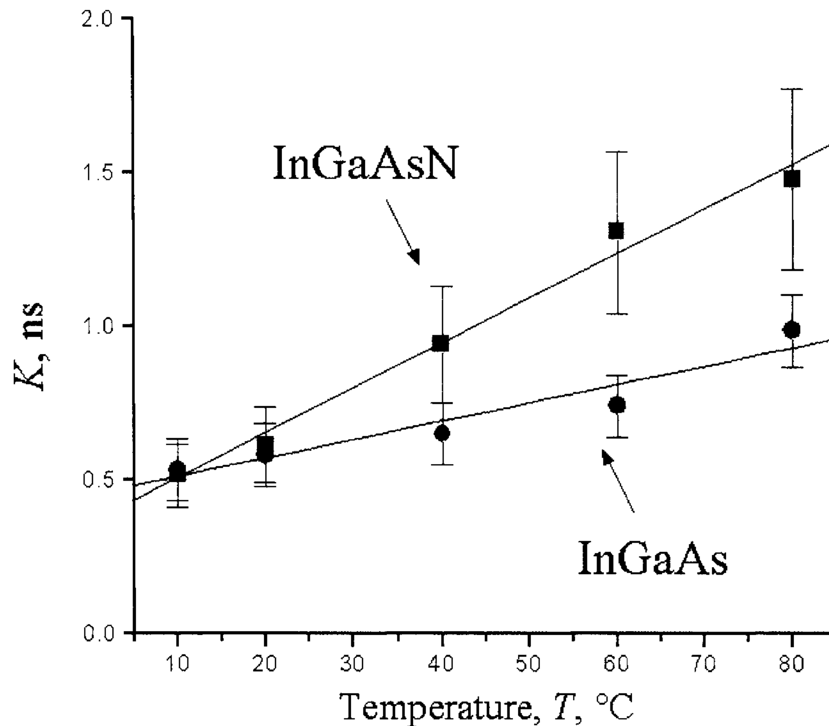

Figure 5. 9.- K-factor, $2\pi \cdot d\gamma/df_r^2$ in InGaAsN (solid) and InGaAs (dotted) SQW narrow-stripe lasers versus T from 10 to 80°C. The slope K-P_0 is ~35% smaller in InGaAs lasers.

5.4. Study of the device and material carrier dynamics

Further insight into the physics of the devices is based on the analysis of the K-factor and f_r^2–P_0 versus temperature in InGaAsN and InGaAs SQW narrow-stripe lasers. This analysis allowed to obtain the compression factor ε and the effective differential gain a_{eff} in the search for the parameter that is limiting f_{3dB} in InGaAsN lasers.

Reproduced with permission of the copyright owner. Further reproduction prohibited without permission.

Further studies on the contributions of the material differential gain dg/dN_w at threshold were speculated by using the calculated values of transport factor R_{ac} in Section 2.5.2.

The analysis of $f_r^2 – P_0$ versus T shown in Figure 5.3 and Figure 5.4 allowed to obtain the effective differential gain parameter a_{eff} versus temperature for InGaAsN and InGaAs laser diodes, as discussed in Section 2.4.1. We then obtained a_{eff} from the slope $f_r^2 – P_0$ .by using equation 2.25. Figure 5.10 shows a_{eff} versus T obtained for InGaAsN and InGaAs SQW narrow-stripe lasers by using (2.26) and the laser parameters on Table 2.1 and the $P_0 – I$ characteristics of Table 3.4. We found a_{eff} at T =20°C to be close to that predicted in InGaAs SQW structures [22, 23], however lower values than dg/dN_w predicted in InGaAsN structures [24]. Besides the experimental errors, the reduction on the latter can be attributed to transport effects (R_{ac}).

The results of Figure 5.10 show a reduction of 60% in the effective differential gain at threshold of the nitrogen-free laser structures over the temperature range T=10 to 80°C. A similar trend with temperature is observed in InGaAsN lasers, although the values are 20 to 50% lower than in InGaAs lasers. Previous RIN experiments have also reported ~2x reduction in the effective differential gain due to a similar incorporation of nitrogen [7]. This analysis was however restricted to room temperature only.

Reproduced with permission of the copyright owner. Further reproduction prohibited without permission.

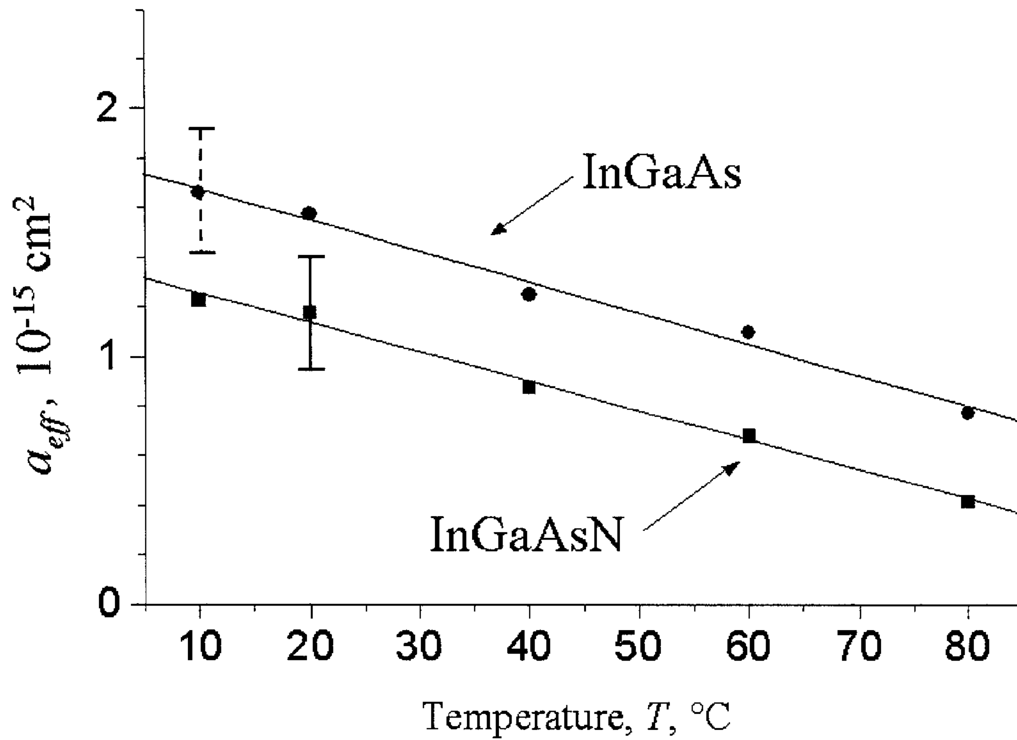

Figure 5.10.- Effective differential gain at threshold, a_{eff}, obtained in InGaAsN (solid) and InGaAs (dotted) SQW narrow-stripe lasers versus active area temperature T from 20 to 80°C. A reduction of ~35% in a_{eff} is observed in InGaAsN lasers at T=80°C.

The gain compression factor ε was obtained from the K factor and the effective differential gain a_{eff} versus temperature. Equation (5.1) shows the direct relationship between the device dependent K-factor and a_{eff}, and the intrinsic parameter ε. The latter was obtained by fitting with equation (5.1), obtained from (2.28), K obtained from the slope of the traces in Figure 5.9. Notice that the parasitics factor (1+U) in (2.28) does not appear in (5.1) as K is based on γ in Figure 5.5 and Figure 5.6, which was already corrected for parasitics.

$$K = 4\pi^2\tau_p\left[1+\Gamma\frac{g_{th}}{a_{eff}}\varepsilon\right] \tag{5.1}$$

Reproduced with permission of the copyright owner. Further reproduction prohibited without permission.

The factor $\Gamma \cdot g_{th}$ is the threshold modal gain given by the total losses $(\alpha_i+\alpha_m)$ obtained from gain measurements results presented on Section 4.3.1. N_{p0} is proportional to the emitted power P_0 as described in (1.13). Other parameters in equation (5.1) are given in Tables 2.1 and 4.1 (g_{th}).

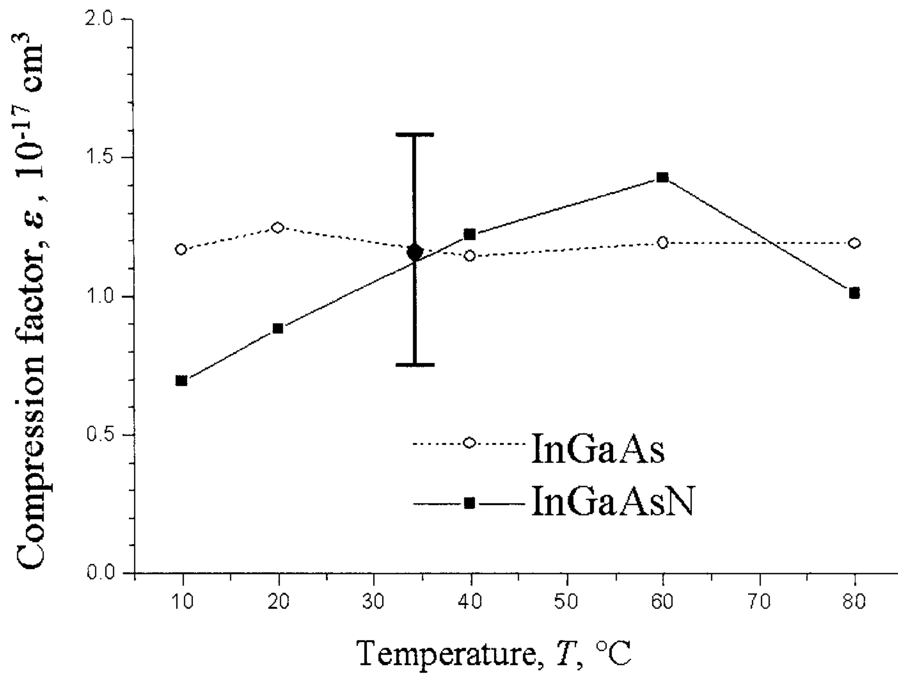

Figure 5.11.- Gain compression factor ε obtained in InGaAsN (solid) and InGaAs (dotted) SQW narrow-stripe lasers versus T.

Figure 5.11 shows the gain compression factor ε in InGaAsN and InGaAs lasers is not changing significantly with temperature within the analysis uncertainty ($\sim 1.2 \cdot 10^{-17}$ cm^3). We found ε similar to measured values for 980nm InGaAs multiple quantum well lasers [25]. This results allowed us to verify that the assumption previously adopted, $\varepsilon \cdot N_{p0} < 0.01$. According to equations (2.25-2.27), a negligible $\varepsilon \cdot N_{p0}$ could also be verified from the linear behavior of f_r^2 versus P_0 in Figure 5.3 and Figure 5.4. This finding

Reproduced with permission of the copyright owner. Further reproduction prohibited without permission.

indicated that ε is not a limiting factor to f_{3dB}, thus it pointed to a_{eff} to completely rule over f_{3dB} in InGaAsN and InGaAs lasers, as we studied next.

5.5. Mechanism causing the bandwidth reduction with temperature

The purpose of the study of the above threshold frequency response measurements is to investigate the effect of the incorporation of nitrogen in the QW into the temperature sensitivity of the laser 3dB bandwidth. In order to accomplish this objective, we use the tools developed in Section 2.5.2, in which we assume total losses of 30cm^{-1} that correspond to a typical as-cleaved 500μm laser and α_i=8cm^{-1}, in similar fashion to the study of T_0 in section 4.5 Chapter 4 and summarized Table 5.1.

Parameter (T=10-80°C)	Value, InGaAsN
α_i	8cm^{-1}
v_g	$7.1 \cdot 10^9$ cm/s
ε	$1.2 \cdot 10^{-17}$ cm^3
τ_p	4.66ps

Table 5.1 – Narrow-stripe diode laser parameters for the analysis of bandwidth versus temperature and nitrogen incorporation above threshold in narrow-stripe InGaAsN and InGaAs lasers.

Our findings from the previous section are summarized in Table 5.2 for InGaAsN and compared with those in InGaAs materials. We repeat the simulations performed in Section 2.5.2 to obtain f_{3dB} versus temperature for P_0=3mW and a_{eff} for InGaAsN, InGaAs equal to $1.66 \cdot 10^{-15} cm^2$ [24], as it would be expected for a temperature insensitive material.

Reproduced with permission of the copyright owner. Further reproduction prohibited without permission.

Figure 5.12 shows the simulated f_{3dB} versus T by assuming dilute nitride material, nitrogen free material and ideal case, whose traces are identified in ascending order. As expected, it is possible to obtain a temperature insensitive bandwidth by having temperature constant a_{eff}. However, observe that higher bandwidths will require more emitted power, for which the compression factor could become evident, as mentioned in the simulation Figure 2.27. However, this was not our case as we as $\varepsilon \cdot N_{p0} < 0.01$ in all the temperature range. Therefore, we conclude that a_{eff} is the only limiting factor to f_{3dB}.

T	InGaAsN		InGaAs	
	a_{eff} [10^{-15}cm^2]	ε [10^{17}cm^3]	a_{eff} [10^{-15}cm^2]	ε [10^{17}cm^3]
10	1.22	0.69	1.66	1.17
20	1.17	0.88	1.57	1.25
40	0.87	1.22	1.25	1.14
60	0.68	1.43	1.10	1.19
80	0.41	1.01	0.77	1.19

Table 5.2 – Summary of the experimental parameters obtained from the analysis of the frequency response measurements above threshold in narrow-stripe InGaAsN and InGaAs lasers.

Reproduced with permission of the copyright owner. Further reproduction prohibited without permission.

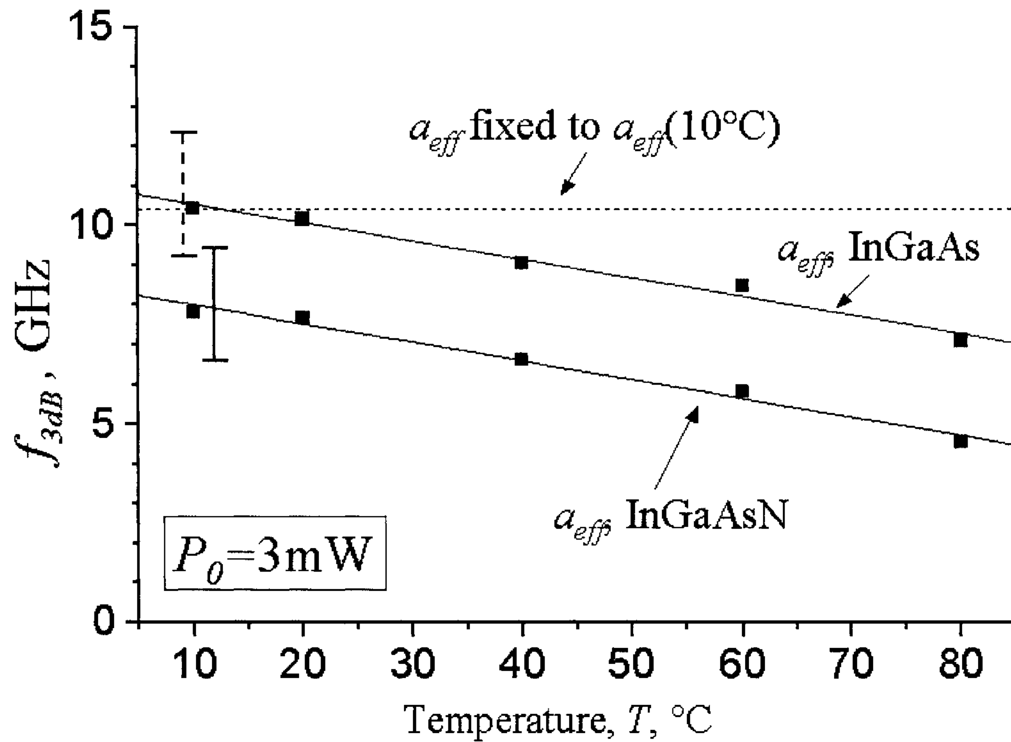

Figure 5.12.- Frequency bandwidth f_{3dB} versus T simulated in narrow-stripe InGaAsN, InGaAs and ideal lasers.

In conclusion, we have identified a_{eff} as responsible for the temperature reduction of f_{3dB} in InGaAsN lasers. In addition, and less notorious, InGaAs lasers suffer from the same temperature effect on a_{eff}.

We further speculated on whether the reduction of a_{eff} could arise from $dg/dN_{w\text{-}th}$ or from transport effects, we used the simulation in Figure 2.26 and the values of R_{ac} in Figure 2.21 to calculate $dg/dN_{w\text{-}th}$. Figure 5.13 shows $dg/dN_{w\text{-}th}$ versus temperature in InGaAsN and InGaAs laser structures.

Reproduced with permission of the copyright owner. Further reproduction prohibited without permission.

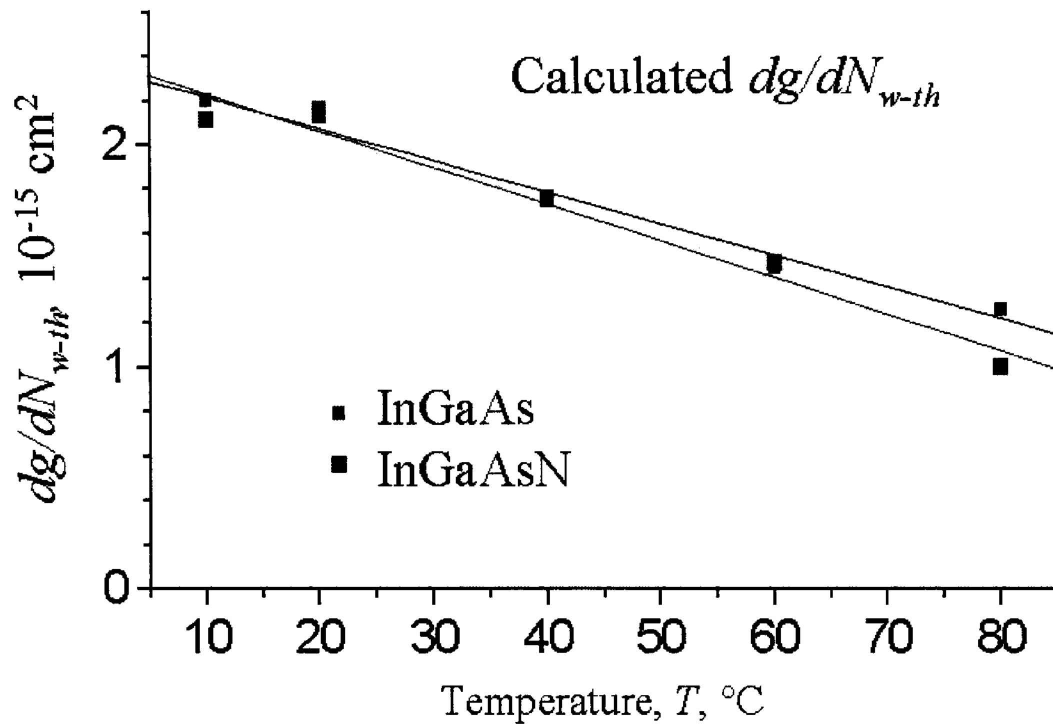

Figure 5.13.- Calculated differential gain at threshold, dg/dN_w, obtained in InGaAsN (solid) and InGaAs (dotted) SQW narrow-stripe lasers versus T from 20 to 80°C. A similar trend is observed in InGaAsN and InGaAs materials.

The results of Figure 5.11 reveal a similar trend in dg/dN_w at threshold with temperature in both laser materials. These results were compared with theoretical predictions by Tomic and O'Reilly [26] in single quantum well InGaAsN structures that show a similar behavior. These calculations are encouraging as they suggest that nitrogen incorporation may not alter significantly the material differential gain, allowing larger bandwidths in InGaAsN than in their counterparts 1.3μm AlInGaAs/InP at high temperature, as suggested by Figure 5.13. Experimental works have already reported significant improvements in high-frequency engineered lasers [4, 20, 27]. Further

Reproduced with permission of the copyright owner. Further reproduction prohibited without permission.

experimental work to determine R_{dc} is required to verify more accurately the values of $dg/dN_w|_{th}$.

5.6. Chapter summary

The objective of this chapter was to investigate, based on the analysis of the frequency response above threshold, the effect of nitrogen and temperature in the modulation response of 1.3μm InGaAsN QW lasers.

The solution of the rate equations model of Chapter 2 was utilized to analyze the optical modulation frequency responses on identical InGaAsN (λ=1.3μm) and InGaAs (λ=1.2μm) RGW lasers versus temperature. It was found that the frequency bandwidth of these lasers in a temperature range of T=10-80°C was limited by the effective differential gain at threshold, a_{eff}, whereas the gain compression factor was rather insensitive to the addition of nitrogen in InGaAsN lasers. Further, the latter did not produce significant effect on the frequency bandwidth of either InGaAsN or InGaAs lasers. The tools developed in Chapter 2 were instrumental to arrive to this conclusion, which otherwise would have yielded a gain compression factor that changed due to the laser electrical parasitic effects.

We found that the incorporation of nitrogen into the InGaAsN QW laser produced a reduction of 20 to 35% in threshold effective differential gain, between T= 10 and 80°C, respectively. Considering a ~20% experimental error in the analysis, these results resembled those obtained from the previous chapter below threshold. Similarly to Chapter 4, we could not neglect that the capture to escape ratio may play a significant role in causing the bandwidth reduction due to nitrogen incorporation and temperature.

Reproduced with permission of the copyright owner. Further reproduction prohibited without permission.

We took a step further and, based on the calculated R_{ac} assuming to be influenced mainly by thermionic escape, speculated on the material differential gain dg/dN_w at threshold. This analysis yielded similar values in both InGaAsN and InGaAs lasers at T=20-80°C, which outperforms the speed performance of existing 1.3μm InP-based lasers and justifies the measurement of the experimental capture to escape ratio. Thus, optimizing the heterostructure of InGaAsN QW lasers for minimizing the transport effect is crucial.

In conclusion, 1.3μm dilute nitride materials hold the potential high speed and high temperature operation. Steps to accomplish this goal are develop method for direct characterization of carrier transport followed by its reduction by engineering improved laser structures

Reproduced with permission of the copyright owner. Further reproduction prohibited without permission.

References for Chapter 5

[1] R. Michalzik, R. King, F. Mederer, M. Kicherer, G. Giaretta, and K. J. Ebeling, "Short-wavelength vertical-cavity surface-emitting laser applications: from high-throughput multimode fiber links to two-dimensional interchip interconnections," *Optical Engineering*, vol. 40, pp. 1179-1185, 2001.

[2] G. Steinle, F. Mederer, M. Kicherer, R. Michalzik, G. Kristen, A. Y. Egorov, H. Riechert, H. D. Wolf, and K. J. Ebeling, "Data transmission up to 10Gbit/s with 1.3 mu m wavelength InGaAsNVCSELs," *Electronics Letters*, vol. 37, pp. 632-634, 2001.

[3] A. W. Jackson, R. L. Naone, M. J. Dalberth, J. M. Smith, K. J. Malone, D. W. Kisker, J. F. Klem, K. D. Choquette, D. K. Serkland, and K. M. Geib, "OC-48 capable InGaAsN vertical cavity lasers," *Electronics Letters*, vol. 37, pp. 355-356, 2001.

[4] A. Martinez, J. G. Provost, B. Dagens, V. Sallet, D. Jahan, K. Merghem, L. Ferlazzo, J. Landreau, O. Le Gouezigou, J. C. Harmand, and A. Ramdane, "9.7 GHz small-signal bandwidth of three-quantum well GalnNAs/GaAs laser diodes operating at 1.35 mu m," *Electronics Letters*, vol. 40, pp. 425-427, 2004.

[5] S. Weisser, E. C. Larkins, K. Czotscher, W. Benz, J. Daleiden, I. Esquivias, J. Fleissner, J. D. Ralston, B. Romero, R. E. Sah, A. Schonfelder, and J. Rosenzweig, "Damping-limited modulation bandwidths up to 40 GHz in undoped short-cavity In0.35Ga0.65As-GaAs multiple-quantum-well lasers," *IEEE Photonics Technology Letters*, vol. 8, pp. 608-610, 1996.

[6] G. Morthier, R. Schatz, and O. Kjebon, "Extended modulation bandwidth of DBR and external cavity lasers by utilizing a cavity resonance for equalization," *IEEE Journal of Quantum Electronics*, vol. 36, pp. 1468-1475, 2000.

[7] L. Shterengas, G. L. Belenky, J. Y. Yeh, L. J. Mawst, and N. Tansu, "Differential gain and linewidth-enhancement factor in dilute-nitride GaAs-based 1.3-mu m diode lasers," *IEEE Journal of Selected Topics in Quantum Electronics*, vol. 11, pp. 1063-1068, 2005.

[8] X. Marie, J. Barrau, T. Amand, H. Carrere, A. Arnoult, C. Fontaine, and E. Bedel-Pereira, "Band structure and optical gain in InGaAsN/GaAs and InGaAsN/GaAsN quantum wells," *Iee Proceedings-Optoelectronics*, vol. 150, pp. 25-27, 2003.

[9] A. Lindsay, S. Tomic, and E. P. O'Reilly, "Derivation of a 10-band k center dot p model for dilute nitride semiconductors," *Solid-State Electronics*, vol. 47, pp. 443-446, 2003.

[10] M. M. E. Fahmi, A. Khan, J. A. Griffin, G. L. Harris, L. H. Robins, A. G. Birdwell, Y. S. Kang, D. J. Smith, T. Steiner, and S. N. Mohammad, "Nitrogen-activated bowing of dilute InyGa1-yAs1-xNx based on photoreflectance studies," *Journal of Applied Physics*, vol. 94, pp. 7576-7580, 2003.

[11] J. M. Ulloa, J. L. Sanchez-Rojas, A. Hierro, J. M. G. Tijero, and E. Tournie, "Effect of nitrogen on the band structure and material gain of InyGa1-yAs1-xNx-GaAs quantum wells," *IEEE Journal of Selected Topics in Quantum Electronics*, vol. 9, pp. 716-722, 2003.

Reproduced with permission of the copyright owner. Further reproduction prohibited without permission.

[12] R. Fehse, S. Tomic, A. R. Adams, S. J. Sweeney, E. P. O'Reilly, A. Andreev, and H. Riechert, "A quantitative study of radiative, Auger, and defect related recombination processes in 1.3-mu m GaInNAs-based quantum-well lasers," *IEEE Journal of Selected Topics in Quantum Electronics*, vol. 8, pp. 801-810, 2002.

[13] J. C. L. Yong, J. M. Rorison, M. Othman, H. D. Sun, M. D. Dawson, and K. A. Williams, "Simulation of gain and modulation bandwidths of 1300nm RWG InGaAsN lasers," *Iee Proceedings-Optoelectronics*, vol. 150, pp. 80-82, 2003.

[14] N. Tansu and L. J. Mawst, "The role of hole leakage in 1300-nm InGaAsN quantum-well lasers," *Applied Physics Letters*, vol. 82, pp. 1500-1502, 2003.

[15] C. Y. Tsai, Y. H. Lo, and R. M. Spencer, "Effects of Spectral Hole-Burning, Carrier Heating, and Carrier Transport on the Small-Signal Modulation Response of Quantum-Well Lasers," *Applied Physics Letters*, vol. 67, pp. 3084-3086, 1995.

[16] C. Y. Tsai, F. P. Shih, T. L. Sung, T. Y. Wu, and C. H. Chen, "A small-signal analysis of the modulation response of high- speed quantum-well lasers: Effects of spectral hole burning, carrier heating, and carrier diffusion-capture-escape," *IEEE Journal of Quantum Electronics*, vol. 33, pp. 2084-2096, 1997.

[17] M. Ishikawa, T. Fukushima, R. Nagarajan, and J. E. Bowers, "Temperature-Dependence of Damping in High-Speed Quantum-Well Lasers," *Applied Physics Letters*, vol. 61, pp. 396-398, 1992.

[18] R. Olshansky, P. Hill, V. Lanzisera, and W. Powazinik, "Frequency-Response of 1.3-Mu-M Ingaasp High-Speed Semiconductor-Lasers," *IEEE Journal of Quantum Electronics*, vol. 23, pp. 1410-1418, 1987.

[19] G. Liu and S. L. Chuang, "High-speed modulation of long-wavelength In1-xGaxAsyP1-y and In1-x-yGaxAlyAs strained quantum-well lasers," *IEEE Journal of Quantum Electronics*, vol. 37, pp. 1283-1291, 2001.

[20] D. Gollub, S. Moses, and A. Forchel, "1.3 mu m double quantum well GalnNAs distributed feedback laser diode with 13.8 GHz small signal modulation bandwidth," *Electronics Letters*, vol. 40, pp. 1181-1182, 2004.

[21] S. L. Chuang, *Physics of optoelectronic devices*, 1995.

[22] S. D. Offsey, W. J. Schaff, L. F. Lester, L. F. Eastman, and S. K. McKernan, "Strained-Layer Ingaas-Gaas-Algaas Lasers Grown by Molecular- Beam Epitaxy for High-Speed Modulation," *IEEE Journal of Quantum Electronics*, vol. 27, pp. 1455-1462, 1991.

[23] S. Shin, C. W. Lee, C. B. Su, J. Lacourse, W. Rideout, and R. B. Lauer, "Effective Differential-Gain and Modulation-Bandwidth Reduction in Quantum-Well Lasers Due to Confinement Factor Modulation," *IEEE Photonics Technology Letters*, vol. 5, pp. 145-147, 1993.

[24] S. Tomic and E. P. O'Reilly, "Optimization of material parameters in 1.3-mu m InGaAsN-GaAs lasers," *IEEE Photonics Technology Letters*, vol. 15, pp. 6-8, 2003.

[25] L. A. Coldren and S. W. Corzine, *Diode lasers and Photonic Integrated Circuits*: Wiley series in microwave and optical engineering, 1995.

[26] S. Tomic and E. P. O'Reilly, "Gain characteristics of ideal dilute nitride quantum well lasers," *Physica E-Low-Dimensional Systems & Nanostructures*, vol. 13, pp. 1102-1105, 2002.

Reproduced with permission of the copyright owner. Further reproduction prohibited without permission.

[27] B. Dagens, A. Martinez, D. Make, W. Le Gouezigou, J. G. Provost, V. Sallet, K. Merghem, J. C. Harmand, A. Ramdane, and B. Thedrez, "Floor free 10-Gb/s transmission with directly modulated GaInNAs-GaAs 1.35-mu m laser for metropolitan applications," *IEEE Photonics Technology Letters*, vol. 17, pp. 971-973, 2005.

Reproduced with permission of the copyright owner. Further reproduction prohibited without permission.

CHAPTER 6

Conclusions and future work

This work investigated the impact of nitrogen incorporation and temperature into the material parameters that affect the threshold current and frequency response of 1.3μm InGaAsN laser diodes. This task was accomplished by (a) a temperature study of the dependence of the laser material parameters through a complete model of the laser diode that contained intrinsic carrier dynamics as well as external parasitics associated with the diode device and (b) comprehensive measurements of the above and below threshold frequency responses and gain. The model was key to separate the role of parasitics and to obtain the effective carrier density below threshold. When combined with the gain measurements, the analysis of the transparency carrier density and differential gain was carried out. The impact of nitrogen incorporation in the laser active region was determined by comparing two identical structures with different nitrogen content, 0 and 0.5%.

The subthreshold lifetime experiments carried out in wide-stripe lasers and their analysis provided the information to obtain the relationship between the device current to carrier density. Innovative experimental setups were designed to overcome the difficulties imposed by the Joule heating at high bias and parasitics effects of the devices. The frequency response measurements were performed in broad area lasers that demanded pulsed bias operation to avoid device destruction. We thus built special biasing circuitry that combined the bias current and the RF modulation in the laser contacts. In addition we carried out impedance measurements on the devices. The analysis of the

Reproduced with permission of the copyright owner. Further reproduction prohibited without permission.

frequency responses and impedance responses was carried out with the support of the rate equation model. The simulation provided the platform to separate the effect of electrical parasitics, important at biases below 0.1 I_{th}, from intrinsic device processes. In addition, the model was used to extract the effective differential carrier lifetime. We carried out an effective analysis that retrieves the total carrier density in the laser active areas as the transport parameters are not known. Using the standard polynomial expansion in terms of A_{eff}, B_{eff} and C_{eff} parameters and assuming the injection efficiency constant and equal to its threshold value, the effective carrier density in the laser active region versus bias current was obtained. By utilizing calculated thermionic escape we further analyzed experimental results and obtained A_w, B_w and C_w parameters in the well. The results showed that in spite of the threshold current being three time larger in InGaAsN than in InGaAs lasers, the threshold effective carrier density is similar in InGaAsN in the full temperature range 10-80°C. The results also revealed that the A_{eff} coefficient is equivalent to monomolecular recombination A_w and is a factor of 3 larger in InGaAsN compared to InGaAs lasers in the whole temperature range. B_{eff} and C_{eff} were obtained with a much higher uncertainty, over 40%. Even within this confidence range, the C_{eff} parameter is a factor of 2 larger in InGaAsN than in InGaAs lasers in the 40-80°C, leading to C_w 3 times larger at 80°C. Within this framework, we found that the threshold current density in InGaAsN lasers is mainly affected by the A_w whereas C_w is mainly responsible for its high increased slope with temperature in the 10-80 °C range.

Separately, the analysis of amplified spontaneous emission measurements on narrow-stripe lasers allowed to evaluate the device-dependent gain versus current behavior in the 10-80 °C. This analysis revealed that dg/dI at threshold is lower and I_{tr} is larger than in

Reproduced with permission of the copyright owner. Further reproduction prohibited without permission.

InGaAs lasers. However, this analysis is structure dependent. To decouple the influence of the device contacts, and cladding layers we combined the effective carrier lifetime analysis and assuming the same injection efficiency of the wide stripe lasers, calculated the carrier density in the narrow stripe lasers. It was found that the net peak gain versus effective carrier density behavior is less temperature sensitive than that of the threshold current. The incorporation of nitrogen reduced the effective differential gain at threshold $dg/dN_{eff\text{-}th}$ by 25-35% when comparing InGaAsN and InGaAs. Moreover, within the accuracy of our analysis, the results showed that the effective transparency carrier density is not significantly affected by the 0.5% nitrogen incorporation.

Motivated by our findings from the experimental analysis below threshold, we studied the factors contributing to the characteristic temperature T_0 in dilute nitride lasers. We modeled a 1.3μm single quantum well InGaAsN laser with all the parameters experimentally obtained. However, we intentionally modified some coefficients in order to investigate which ones change by the addition of nitrogen and thus affect negatively to the device performance. In our simulations, we assumed a 40% enhancement on the effective differential gain and a 60% reduction in the monomolecular recombination. Interestingly, this study retrieved T_0 ~95K similar to 100K measured in InGaAs lasers. Further reduction on C_w retrieved T_0 even larger than that in InGaAs lasers. We further compared these results with T_0 obtained from 1.3μm AlInGaAs/InP quantum well lasers, which showed that InGaAsN can be less temperature sensitive than their InP-based counterparts, if further reduction on C_w were achieved. The most significant contribution of the subthreshold analysis in this dissertation to the field consists in showing that the incorporation of nitrogen reduces the effective differential gain and increases

Reproduced with permission of the copyright owner. Further reproduction prohibited without permission.

monomolecular recombination. These results can account for the majority of the reduction of T_0 in 1.3μm dilute nitride lasers. Separate determination of capture into and escape out of the well are needed to fully assess the material's behavior with and without nitrogen, as shown by the model developed in Chapter 2.

The study above threshold was implemented by measuring the frequency response of the laser diode by our previously developed technique of selective femtosecond optical injection. As an innovation to the setup, we obtained frequency responses under pulsed bias regime in order to avoid device damage at high currents. This scheme permitted to reach active area temperatures of 80°C in InGaAsN and InGaAs narrow-stripe lasers. The model analysis, that included parasitics, showed that the damping was indeed affected by parasitics even under optical modulation. This effect, which had been ignored until now, had a significant impact in our experimental results, which was more notorious in InGaAs lasers. After correcting for parasitics, the analysis of the damping permitted to find unprecedented bandwidths of 4GHz at 80°C for InGaAsN with a single quantum well. The fit of the experimental data by our model retrieved values of the gain compression factor and effective differential gain at threshold in both InGaAsN and InGaAs materials. We found that the gain compression factor was rather insensitive to the addition of nitrogen in InGaAsN lasers. Further, the incorporation of electrical parasitics in our model was instrumental in showing that the compression factor did not produce a significant effect on the frequency bandwidth of either InGaAsN or InGaAs lasers. Conversely, the analysis indicated the threshold effective differential gain $dg/dN_{eff\text{-}th}$ reduced in ~20-35% due to the addition of nitrogen. We found $dg/dN_{eff\text{-}th}$ to follow a similar trend with the increase in nitrogen content and temperature very similar to that

Reproduced with permission of the copyright owner. Further reproduction prohibited without permission.

determined in InGaAsN and InGaAs in the temperature range from 10°C to 80°C from the below threshold analysis. Again, by recalling our model analysis we investigated the laser frequency response and found that the bandwidth reduction in InGaAsN lasers is due to the reduction on the threshold effective differential gain. Further, bandwidths above 10GHz could be obtained at room temperature in 1.3μm InGaAsN lasers by increasing $dg/dN_{eff\text{-}th}$. There are two pathways for accomplishing this. If $dg/dN_{eff\text{-}th}$ is dominated by the material differential gain, then adding one or two additional wells to the structure would accomplish this goal. If instead $dg/dN_{eff\text{-}th}$ is transport dominated through R_{dc}, it would be necessary to engineer the quantum well and separate confinement regions to increase the effective carrier capture into the well. In this case knowledge of R_{dc} is instrumental. From the previous studies performed above and below threshold, we conclude that InGaAsN material has the potential to outperform AlInGaAs/InP in bandwidth and threshold current insensitivity. The improvements required for InGaAsN to achieve this goal are only left to improving the effective differential gain through the optimization of the laser heterostructure, which provides the motivation for continuing the research in producing better SCH's for mid-infrared dilute nitride laser diodes. It is important to note that transport effects play a significantly more important role in an InGaAsN QW, in comparison to that in an InGaAs QW. Thus, optimizing the heterostructure of InGaAsN QW lasers for minimizing the transport effect is crucial.

This dissertation provided the complete model for the future studies on dilute nitrides. This work must involve experimental measurements to determine the capture to escape times ratio as a function of temperature and carrier density in dilute nitride laser

Reproduced with permission of the copyright owner. Further reproduction prohibited without permission.

structures. By feeding these quantities in to the thesis model, the results will permit to separate material differential gain from the carrier transport and retrieve the carrier density N_w. In this way, this analysis will allow to monitor the changes in new lasers heterostructures and provide the feedback to the laser growth engineering team.

We foresee that improved InGaAsN laser structures will incorporate multiple quantum wells and higher bandgap barriers, as they are being developed during this thesis writing. In addition, we believe that a more refined control over the quantum well growth temperature and temperature ramping, device burn-in conditions and device annealing temperature are key in the process of optimizing the laser output behavior.

Reproduced with permission of the copyright owner. Further reproduction prohibited without permission.

Appendix 1 – Carrier lifetime analysis

This appendix section presents the numerical approach utilized to obtain the effective carrier density in the laser quantum well from the data $\tau(I)$ of Chapter 4. The analysis obtains first τ_{eff} from the experimental data. Figure A-1 shows τ_{eff} that is obtained from τ and parasitics r_d and C_p+C_j by using equation (2.18).

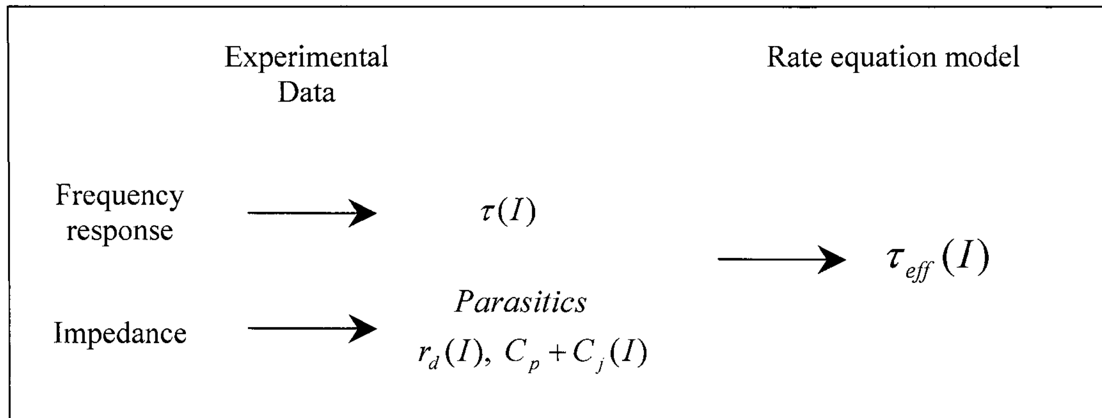

Figure A-1.- The effective differential carrier lifetime τ_{eff} is obtained from τ and parasitics r_d and C_p+C_j by using equation (2.18).

Following this, the trace $\tau_{eff} - I$ is simultaneously fitted by equations (2.33) and (2.34) to obtain A_{eff}, B_{eff} and C_{eff}. Figure A-2 shows the minimum squares fit method in which N_{eff} is obtained as an intermediate step. A_{eff}, B_{eff} and C_{eff} are within certain logical range. Once the minimum square error reaches its minimum, A_{eff}, B_{eff}, C_{eff} and N_{eff} are obtained.

Reproduced with permission of the copyright owner. Further reproduction prohibited without permission.

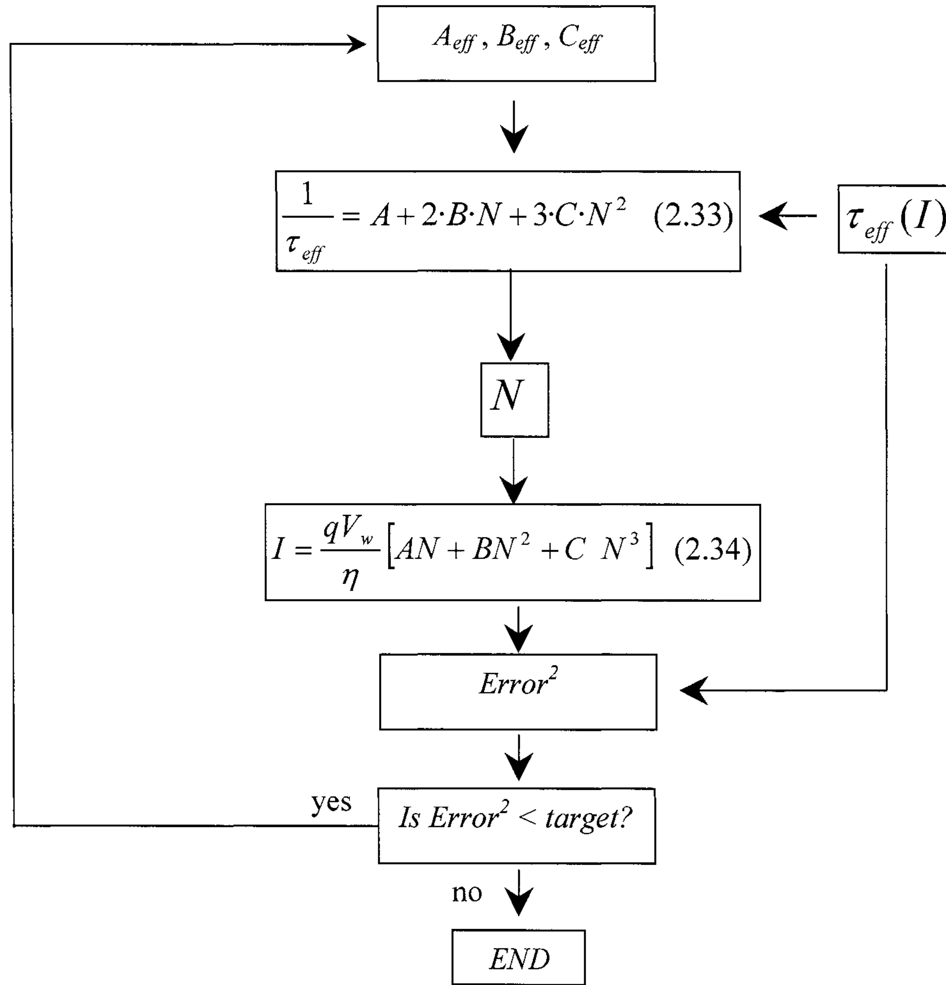

Figure A-2.- Flowchart summarizing the numerical method utilized to obtain $N_{eff} - I$ relationship and from the experimental traces of τ_{eff} - I.

The algorithm was then modified to obtain A_w , B_w , C_w and N_w based on the calculated ratio R_{dc}. Based on R_{dc} and equation (2.32), $N_s \approx \Gamma_q R_{dc} N_w$, N_s was obtained in parallel to N inside the loop Figure A-1. Equation (2.30) replaced (2.34) to calculate the device current with the incorporation of R_s,

$$I = \frac{qV}{\eta}\left[\Gamma_q\left(A_w N_w + B_w N_w^2 + C_w N_w^3\right) + (1 - \Gamma_q)\left(A_s N_s + B_s N_s^2 + C_s N_s^3\right)\right] \qquad (2.30)$$

Reproduced with permission of the copyright owner. Further reproduction prohibited without permission.

Appendix 2 – Frequency response and impedance below threshold

This appendix shows the matrix expressions that are solved to obtain the zero/pole transfer function that represents the electrical impedance, and the five pole transfer that defines the frequency response in Chapter 2.

By applying Crame's rule, the full model in (2.14) is solved to find the expression of electrical impedance versus frequency shown in (A-3).

$$
Z(j\omega)=\frac{\begin{vmatrix} \frac{r_d}{Q} & -1/(H_{21}C_p r_s) & 0 & 0 \\ 0 & j\omega+\frac{Q/r_s+\chi(1/\tau_{cap}+1/\tau_s)}{T+C_jQ} & \frac{-\Gamma_q}{\tau_{esc}(1+C_jQ/\chi)} & 0 \\ 0 & -1/(\Gamma_q\tau_{cap}) & j\omega+\left(1/\tau_w+1/\tau_{esc}\right) & -1/\Gamma\left(1/\tau_p\right) \\ 0 & 0 & -\beta/\tau_w & j\omega+1/\tau_p \end{vmatrix}}{\begin{vmatrix} j\omega+1/(C_p r_s) & -1/(H_{21}C_p r_s) & 0 & 0 \\ \frac{-Q}{r_s(1+C_jQ/\chi)} & j\omega+\frac{Q/r_s+\chi(1/\tau_{cap}+1/\tau_s)}{T+C_jQ} & \frac{-\Gamma_q}{\tau_{esc}(1+C_jQ/\chi)} & 0 \\ 0 & -1/(\Gamma_q\tau_{cap}) & j\omega+\left(1/\tau_w+1/\tau_{esc}\right) & -1/\Gamma\left(1/\tau_p\right) \\ 0 & 0 & -\beta/\tau_w & j\omega+1/\tau_p \end{vmatrix}} \qquad \text{(A-1)}
$$

In similar way, the frequency response was obtained as in (A-1). In both expressions, the poles and zeroes are obtained by factorizing the determinants.

Reproduced with permission of the copyright owner. Further reproduction prohibited without permission.

$$H_{sp}(j\omega)=\begin{vmatrix} j\omega+r_p/L_p & 1/L_p & 0 & 0 & 0 \\ -1/C_p & j\omega+1/(C_p r_s) & -1/(H_{21}C_p r_s) & 0 & 0 \\ 0 & \dfrac{-Q}{r_s(1+C_j Q/\chi)} & j\omega+\dfrac{Q/r_s+\chi(1/\tau_{cap}+1/\tau_s)}{T+C_j Q} & \dfrac{-\Gamma_q}{\tau_{esc}(1+C_j Q/\chi)} & 0 \\ 0 & 0 & -1/(\Gamma_q \tau_{cap}) & j\omega+(1/\tau_w+1/\tau_{esc}) & -1/\Gamma(1/\tau_p) \\ 0 & 0 & 0 & -\beta/\tau_w & j\omega+1/\tau_p \end{vmatrix}^{-1}$$

(A-2)

Reproduced with permission of the copyright owner. Further reproduction prohibited without permission.

Appendix 3 – Coupling factor χ (above threshold)

This appendix shows the matrix expressions that are solved to find the factor χ versus the model parameters and bias defined by P_0 and I above threshold. χ represents the coupling between the laser active region and the *p-n* junction and device contacts. Remember that $Cp+C_j$ and r_d depend on I while the intrinsic laser dynamics depend on P_0. Depending on whether the laser is InGaAsN or InGaAs, the different P_0 - I relationship dictates that the parasitics affect more the InGaAs lasers, due to larger r_d's, as experimentally demonstrated in Chapter 5. The coupling factor χ above threshold is numerically obtained from (A-3), which has been obtained from the 3x3 matrix of the parasitic-free model in Chapter 1 and from the full model above threshold in (2.18) .

$$\chi = \frac{Q}{r_d} \frac{\left. \begin{vmatrix} j\omega + (1/\tau_w + 1/\tau_{esc} + P) & -1/\Gamma(1/\tau_p + A_p P) \\ -\Gamma P & j\omega - A_p P \end{vmatrix} \right|_{j\omega=0}}{\left. \begin{vmatrix} j\omega + 1/\tau_{cap} + 1/\tau_s & \dfrac{-\Gamma_q}{\tau_{esc}} & 0 \\ 0 & j\omega + (1/\tau_w + 1/\tau_{esc} + P) & -1/\Gamma(1/\tau_p + A_p P) \\ 0 & -\Gamma P & j\omega - A_p P \end{vmatrix} \right|_{j\omega=0}} \tag{A-3}$$

The factor M in Chapter 2 was obtained from the ratio of (A-3) with the analytical expression of χ below threshold shown in (A-4) (Expression 2.13 with M=0).

$$\chi = \frac{Q}{r_d}\left[\frac{1}{\tau_s} + \frac{\tau_{cap}/\tau_{esc}}{(\tau_w + \tau_{esc})(1+M)}\right]^{-1} \tag{A-4}$$

Reproduced with permission of the copyright owner. Further reproduction prohibited without permission.

Appendix 4 – Damping γ versus parasitics: *U*-factor

The U factor relates the real laser damping including parasitics with the damping from a parasitic-free laser. The eigenvalues of the determinant of the 5x5 matrix in 2.18 are obtained as in (A-11), from which the two complex-conjugated poles $f=\alpha+j\beta$ and $f=\alpha-j\beta$ give rise to $f_r=\sqrt{\alpha^2+\beta^2}$ and $\gamma=2\alpha$. The determinant provided by (A-6) is the intrinsic laser equivalent to (A-11) when $\chi=\infty$ (total decoupling of intrinsic laser to parasitics), which retrieves the parasitic-free γ and f_r. From the comparison of γ - f_r from (A-11) and (A-6) we obtained $1+U=\gamma_1/\gamma_2$, where γ_1 is the real damping and γ_2 the parasitic free damping. In similar way, it is also verified the insensitivity of f_r to electrical parasitics, as $f_{r1}=f_{r2}$.

$$\Delta_2=\begin{vmatrix} j\omega+r_p/L_p & 1/L_p & 0 & 0 & 0 \\ -1/C_p & j\omega+1/(C_p r_s) & -1/(H_{21}C_p r_s) & 0 & 0 \\ 0 & \dfrac{-Q}{r_s(1+C_jQ/\chi)} & j\omega+\dfrac{Q/r_s+\chi(1/\tau_{cap}+1/\tau_s)}{\chi+C_jQ} & \dfrac{-\Gamma_q}{\tau_{esc}(1+C_jQ/\chi)} & 0 \\ 0 & 0 & -1/(\Gamma_q\tau_{cap}) & j\omega+(1/\tau_w+1/\tau_{esc}+P) & -1/\Gamma(1/\tau_p+A_pP) \\ 0 & 0 & 0 & -\Gamma P & j\omega-A_pP \end{vmatrix} \quad \text{(A-5)}$$

$$\Delta_1=\begin{vmatrix} j\omega+1/\tau_{cap}+1/\tau_s & \dfrac{-\Gamma_q}{\tau_{esc}} & 0 \\ 0 & j\omega+(1/\tau_w+1/\tau_{esc}+P) & -1/\Gamma(1/\tau_p+A_pP) \\ 0 & -\Gamma P & j\omega-A_pP \end{vmatrix} \quad \text{(A-6)}$$

Reproduced with permission of the copyright owner. Further reproduction prohibited without permission.

Appendix 5 – Electrical and Optical modulation frequency responses

The frequency response by electrical modulation consists in a transfer function with five poles which are the eigenvalues in obtained expression (2.18), as shown by (A-7).

$$\Delta = \begin{vmatrix} j\omega + r_p / L_p & 1/L_p & 0 & 0 & 0 \\ -1/C_p & j\omega + 1/(C_p r_s) & -1/(H_{21} C_p r_s) & 0 & 0 \\ 0 & \dfrac{-Q}{r_s(1+C_j Q/\chi)} & j\omega + \dfrac{Q/r_s + \chi(1/\tau_{cap} + 1/\tau_s)}{\chi + C_j Q} & \dfrac{-\Gamma_q}{\tau_{esc}(1+C_j Q/\chi)} & 0 \\ 0 & 0 & -1/(\Gamma_q \tau_{cap}) & j\omega + (1/\tau_w + 1/\tau_{esc} + P) & -1/\Gamma(1/\tau_p + A_p P) \\ 0 & 0 & 0 & -\Gamma P & j\omega - A_p P \end{vmatrix} \qquad \text{(A-7)}$$

The optical modulation frequency responses have the same poles from (A-7) but some are cancelled by zeros, which are provided by the eigenvalues of (A-8) or (A-9), depending whether the modulation occurs in the SCH or QW os the laser didoes, respectively.

$$\Delta_{sch} = \begin{vmatrix} j\omega + r_p / L_p & 1/L_p & 0 & 0 & 0 \\ -1/C_p & j\omega + 1/(C_p r_s) & 0 & 0 & 0 \\ 0 & \dfrac{-Q}{r_{clad}(1+C_j Q/\chi)} & \delta_{sch} & \dfrac{-\Gamma_q}{\tau_{esc}(1+C_j Q/\chi)} & 0 \\ 0 & 0 & 0 & j\omega + (1/\tau_w + 1/\tau_{esc} + P) & -1/\Gamma(1/\tau_p + A_p P) \\ 0 & 0 & 0 & -\Gamma P & j\omega - A_p P \end{vmatrix} \qquad \text{(A-8)}$$

$$\Delta_{QW} = \begin{vmatrix} j\omega + r_p / L_p & 1/L_p & 0 & 0 & 0 \\ -1/C_p & j\omega + 1/(C_p r_s) & -1/(H_{21} C_p r_s) & 0 & 0 \\ 0 & \dfrac{-Q}{r_s(1+C_j Q/\chi)} & j\omega + \dfrac{Q/r_s + \chi(1/\tau_{cap} + 1/\tau_s)}{\chi + C_j Q} & 0 & 0 \\ 0 & 0 & -1/(\Gamma_q \tau_{cap}) & \delta_{qw} & -1/\Gamma(1/\tau_p + A_p P) \\ 0 & 0 & 0 & 0 & j\omega - A_p P \end{vmatrix} \qquad \text{(A-9)}$$

Reproduced with permission of the copyright owner. Further reproduction prohibited without permission.

Appendix 6 – Optical gain

This section briefly describes the Matlab-based program that implements the Hakki-Paoli [ ] method to obtain the laser modal gain from the amplified spontaneous emission (ASE) spectrum. Figure A- 2 shows the program's console, in where the ASE file in *.txt or *.spe format is opened by the two top-left buttons with the file extension on their captions.

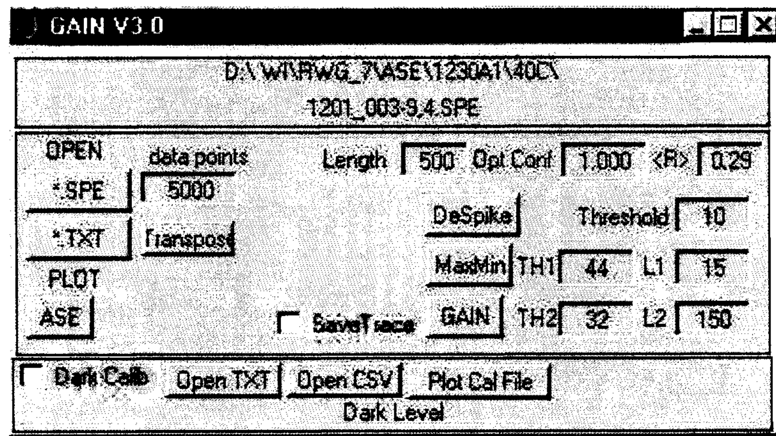

Figure A- 2. – Gain calculation program implemented in Matlab to calculate gain from ASE emission.

Laser length in microns, confinement Γ and mirror reflectivity are inputs into the program in the three top-right edit boxes. By pressing the button 'MaxMin', the program finds the Maxima/Minima curves shown on Figure A- 3, which serve as comparison functions to obtain the maxima and minima points of the ASE curves, respectively. the program also features other functions such as spike filters shows by the 'DeSpike' button. The oscillation period, ~5Å in the case of 500μm length lasers, is automatically obtained by the program from spectral analysis of the ASE trace. The modal gain is obtain from

Reproduced with permission of the copyright owner. Further reproduction prohibited without permission.

the ratio r=maxima/minima as shown below, where L, α_m and α_i are the laser length, mirror and internal losses respectively. L, α_m are inputs to the program, whereas α_i is retrieved by the software.

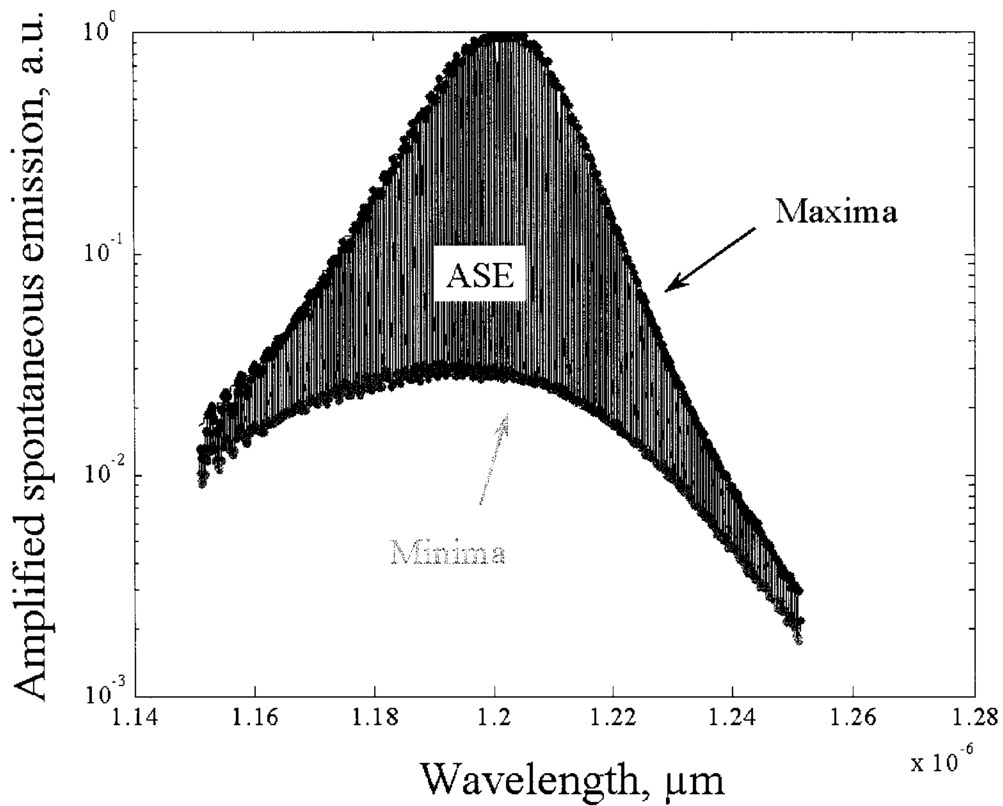

Figure A- 3. – (a) Gain calculation program implemented in Matlab to calculate gain from ASE emission. (b) Maxima/Minima auxiliary curves (red-green).

Reproduced with permission of the copyright owner. Further reproduction prohibited without permission.

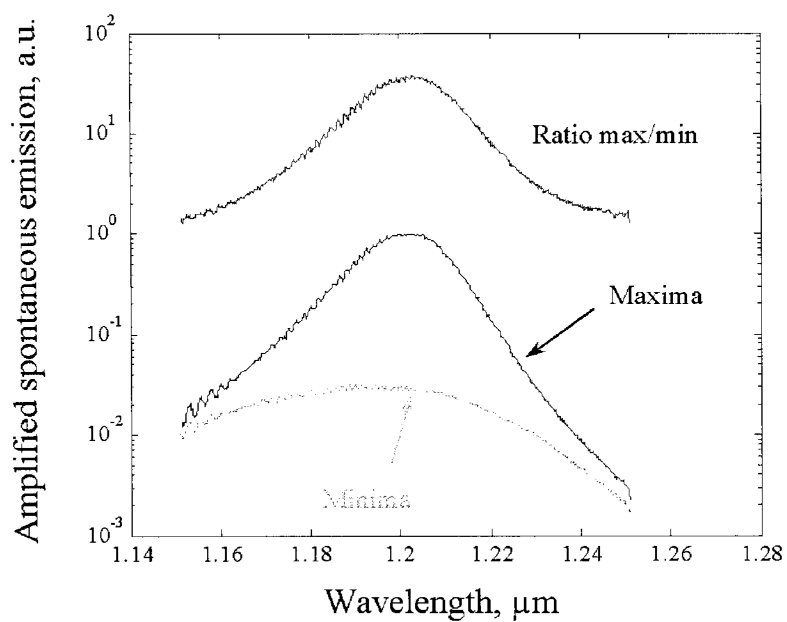

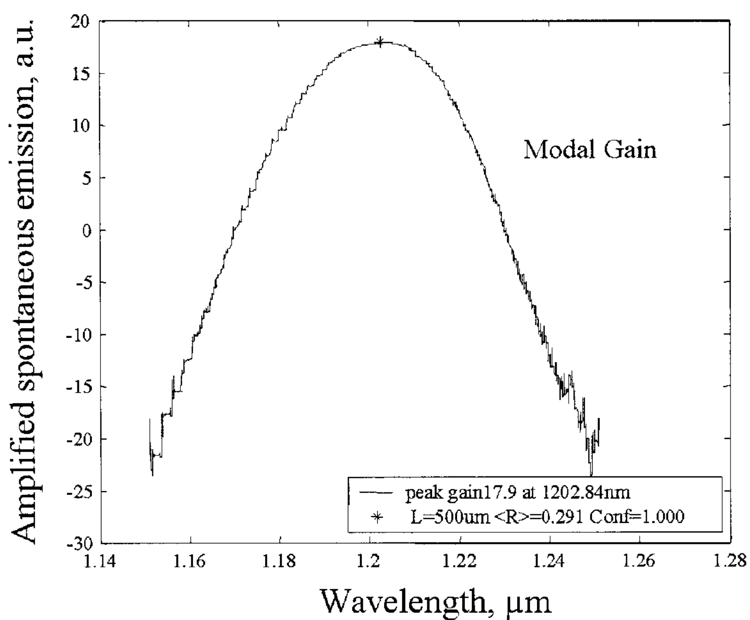

Figure A- 4. – (a) Maxima/Minima curves (red-green) and their ratio (blue) from which the gain is obtained. (b) Modal gain versus wavelength

The program also allows to save the obtained gain trace as *.txt file by checking into "save file" box.

Reproduced with permission of the copyright owner. Further reproduction prohibited without permission.

Appendix 7 – Fit of the frequency response

This section describes the program utilized to obtain the frequency response from the envelope of the comb spectrum of the laser diode under optical pulse modulation. Figure A- 5 shows the program's console, where the file is opened in '.txt' format as it is acquired from the spectrum analyzer. The log-frequency axis is generated by entering 'F1' and 'F2' in the panel, which in this work were 70MHz and 12GHz, respectively. The fit parameters are amplitude 'A' (dB), resonance frequency 'FR2' (GHz), damping Y2 (GHz) and transport pole T2 (ps). The fit is performed by hitting the button 'FIT'. The routine tries least squares fit within each variable's range specified on the right side boxes ('+/-'). The program allows to save the data (envelope) and fitted traces as '.txt.' by hitting 'save fit' button.

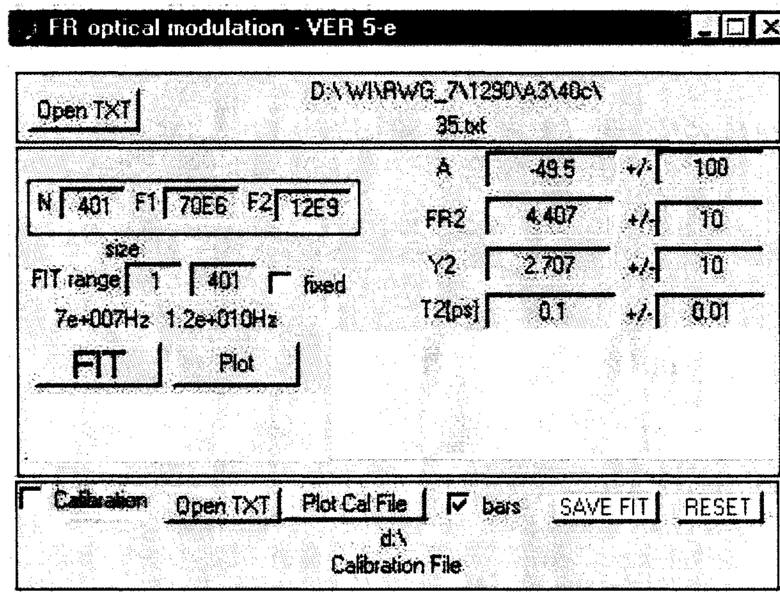

Figure A- 5. – Program implemented in Matlab to calculate the frequency response from the laser under pulse optical modulation.

Reproduced with permission of the copyright owner. Further reproduction prohibited without permission.

Figure A- 6 shows the ~81MHz frequency comb data, obtained by short-pulse optical modulation and fitted by the red trace, defined by resonance, damping and transport pole. Figure A- 7 shows the fitted data in log-frequency scale, where it can be seen a high-frequency asymptote of –40dB/dec is revealed.

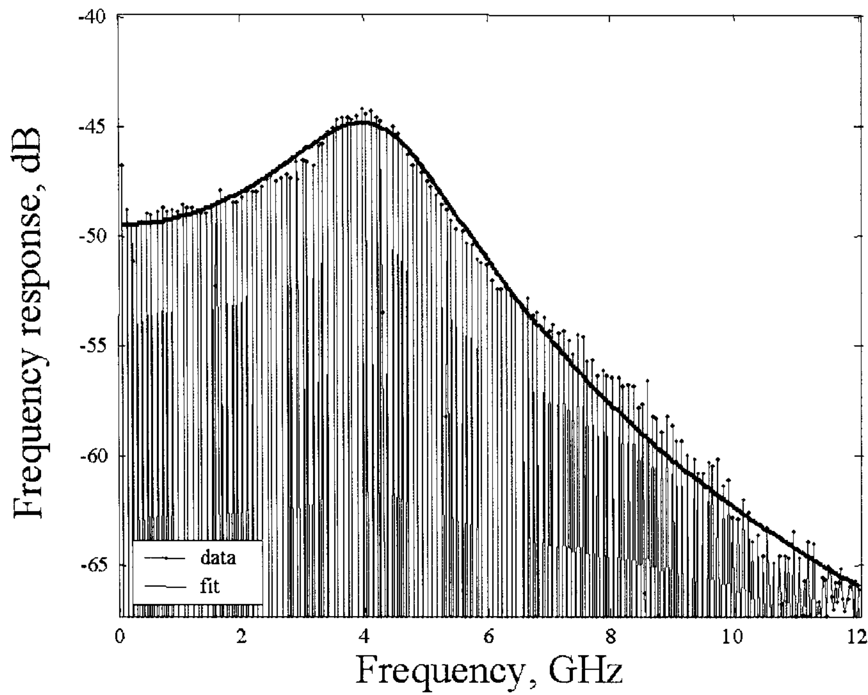

Figure A- 6. – Laser frequency comb spectrum (line-dot-blue), which contains the frequency reponse on its envelope and is fitted by a damped-resonance response (solid-red).

Reproduced with permission of the copyright owner. Further reproduction prohibited without permission.

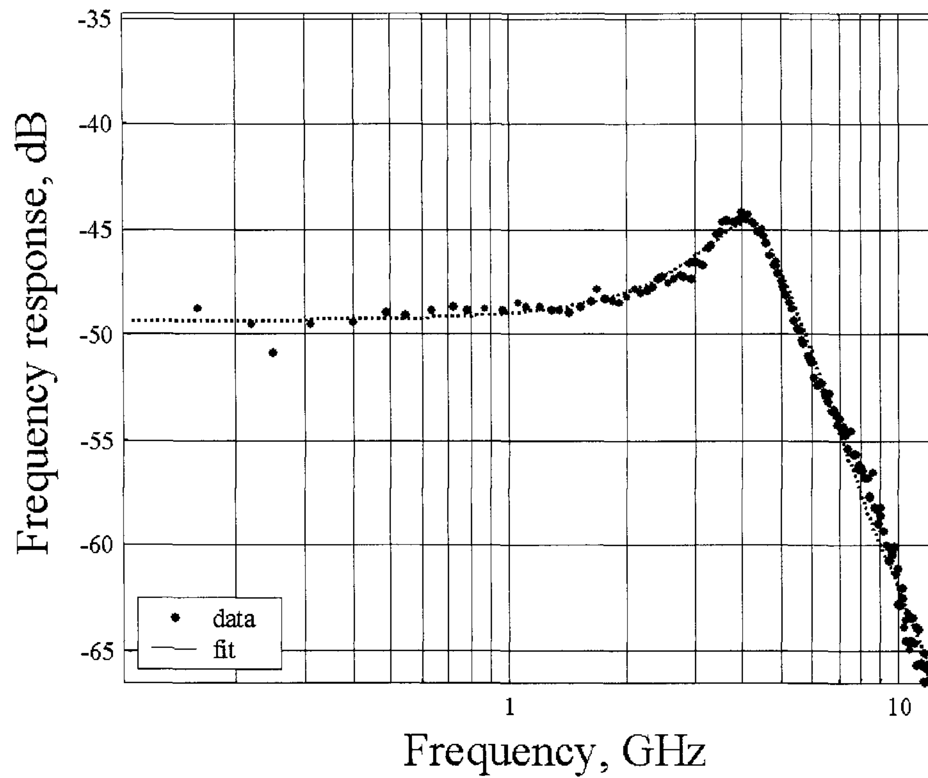

Figure A- 7. – Semilog representation of the fitted function, with a few point at low frequencies: ~80, 160, 240, 320, 400MHz....

Reproduced with permission of the copyright owner. Further reproduction prohibited without permission.